

701176
3.1.1749
701176

7149
3149
TR3149

**On the losses in a high-speed
permanent-magnet generator with rectifier
with special attention to the effect of a damper cylinder**

Stellingen

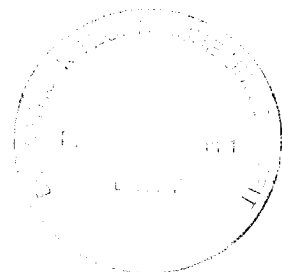
behorende bij het proefschrift van
Hendrik Polinder
getiteld

'On the losses in a high-speed permanent-magnet generator with rectifier
with special attention to the effect of a damper cylinder'

1. Het toepassen van een dempercilinder vermindert het blindvermogen dat een permanente-magneetmachine moet leveren bij gelijkrichterbelasting niet en is in het algemeen niet nodig om commutatie mogelijk te maken (dit proefschrift).
2. Zowel uit theoretisch als uit experimenteel werk blijkt dat de ijzerverliezen in gelamineerd ijzer bij frequenties boven 1000 Hz ruwweg evenredig zijn met de frequentie tot de macht anderhalf ([Buc 84], dit proefschrift) en niet met de frequentie in het kwadraat.
3. Het is onverstandig een dempercilinder in een permanente-magneetmachine dicht bij het statoroppervlak te plaatsen (dit proefschrift). Dit geldt ook als de stromen in de machine sinusvormig zijn.
4. Als stroomverdringing in de dempercilinder niet verwaarloosbaar is, kan dit eenvoudig in het in dit proefschrift beschreven model verwerkt worden door de dikte van de dempercilinder te vervangen door de indringdiepte in de dempercilinder.
5. Het is niet altijd waar dat een bovengrens voor de wervelstroomverliezen in de magneten van een permanente-magneetmachine verkregen wordt als de magneetblokjes in de berekening vervangen worden door een cilinder van magneetmateriaal (wat wel gesuggereerd wordt door Demel [Dem 87]).
6. De formulering voor de algemene oplossing van de vergelijking van Laplace die gegeven wordt in [Bin 92] en [Zhu 93a] is niet algemeen genoeg.
7. De perspectieven voor hybride voertuigen met een brandstofcel zijn veel beter dan die voor hybride voertuigen met een verbrandingsmotor omdat brandstofcellen een hoger rendement hebben en schoner zijn.
8. Natuurwetenschappen verklaren niets, ze beschrijven slechts hoe de dingen gewoonlijk gaan. Over eenmalige gebeurtenissen, zoals de Schepping en de Big Bang, kunnen natuurwetenschappen dus geen uitspraken doen.
9. God wil niet dat wij uit Zijn wetmatig handelen in de natuur concluderen dat Hij er niet is of dat wij onafhankelijk van Hem zijn, maar Hij wil hierdoor laten zien hoe betrouwbaar Hij is.

10. Volgens de gereformeerde leer is de mens van nature geneigd tot het kwaad. Daarom zouden gereformeerden zichzelf en elkaar zoveel mogelijk de gelegenheid moeten ontnemen het kwaad uit te leven. Dit gebeurt niet voldoende; teveel zaken worden in vertrouwen geregeld. De gevolgen bevestigen maar al te vaak de leer.
11. Als ouders van onvolwassen kinderen besluiten over hun taakverdeling thuis en hun carrière, en als de overheid besluit daarop invloed uit te oefenen, dient het belang van de opvoeding van die kinderen het zwaarst te wegen.
12. Het is onmenselijk uitgeprocedeerde asielzoekers die niet terug kunnen naar hun land van herkomst geen uitzicht te bieden op het opbouwen van een bestaan.
13. Bestuurders die ongehinderd door historische kennis allerlei vernieuwingen doorvoeren, creëren nogal eens situaties die eerder om goede redenen verlaten zijn.
14. De Nederlandse samenleving is in belangrijke mate verantwoordelijk voor de ontwikkeling van de varkenshouderij in de jaren 1960 tot 1990 en profiteert daar nog steeds van. Daarom behoort deze samenleving ook haar verantwoordelijkheid te nemen als ze tot het inzicht komt dat het anders moet.
15. Als een boer zijn dieren stuk voor stuk kent, is het onterecht zijn bedrijf bioindustrie te noemen.

**On the losses in a high-speed
permanent-magnet generator with rectifier
with special attention to the effect of a damper cylinder**



PROEFSCHRIFT

ter verkrijging van de graad van doctor
aan de Technische Universiteit Delft,
op gezag van de Rector Magnificus prof.ir. K.F. Wakker,
in het openbaar te verdedigen ten overstaan van een commissie,
door het College voor Promoties aangewezen,
op dinsdag 9 juni 1998 te 16.00 uur
door

Hendrik POLINDER

elektrotechnisch ingenieur
geboren te Nunspeet

Dit proefschrift is goedgekeurd door de promotor: Prof.Dr.-Ing. W. Deleroi

Toegevoegd promotor: Dr.ir. M.J. Hoeijmakers

Samenstelling promotiecommissie:

Rector Magnificus, voorzitter

Prof.Dr.-Ing. W. Deleroi, Technische Universiteit Delft, promotor

Dr.ir. M.J. Hoeijmakers, Technische Universiteit Delft, toegevoegd promotor

Prof.dr.ir. R. Belmans, Katholieke Universiteit Leuven

Prof.dr.ir. H. Blok, Technische Universiteit Delft

Prof.Dr.-Ing. W.-R. Canders, Technische Universiteit Braunschweig

Prof.dr. J.A. Ferreira, Technische Universiteit Delft

Dr.ir. L.J.J. Offringa, Technische Universiteit Eindhoven

ISBN 90-5651-041-X

Distributed by

EburonP&L

P.O.Box 2867

2601 CW Delft

The Netherlands

Printed by

Ponsen & Looijen BV

Wageningen

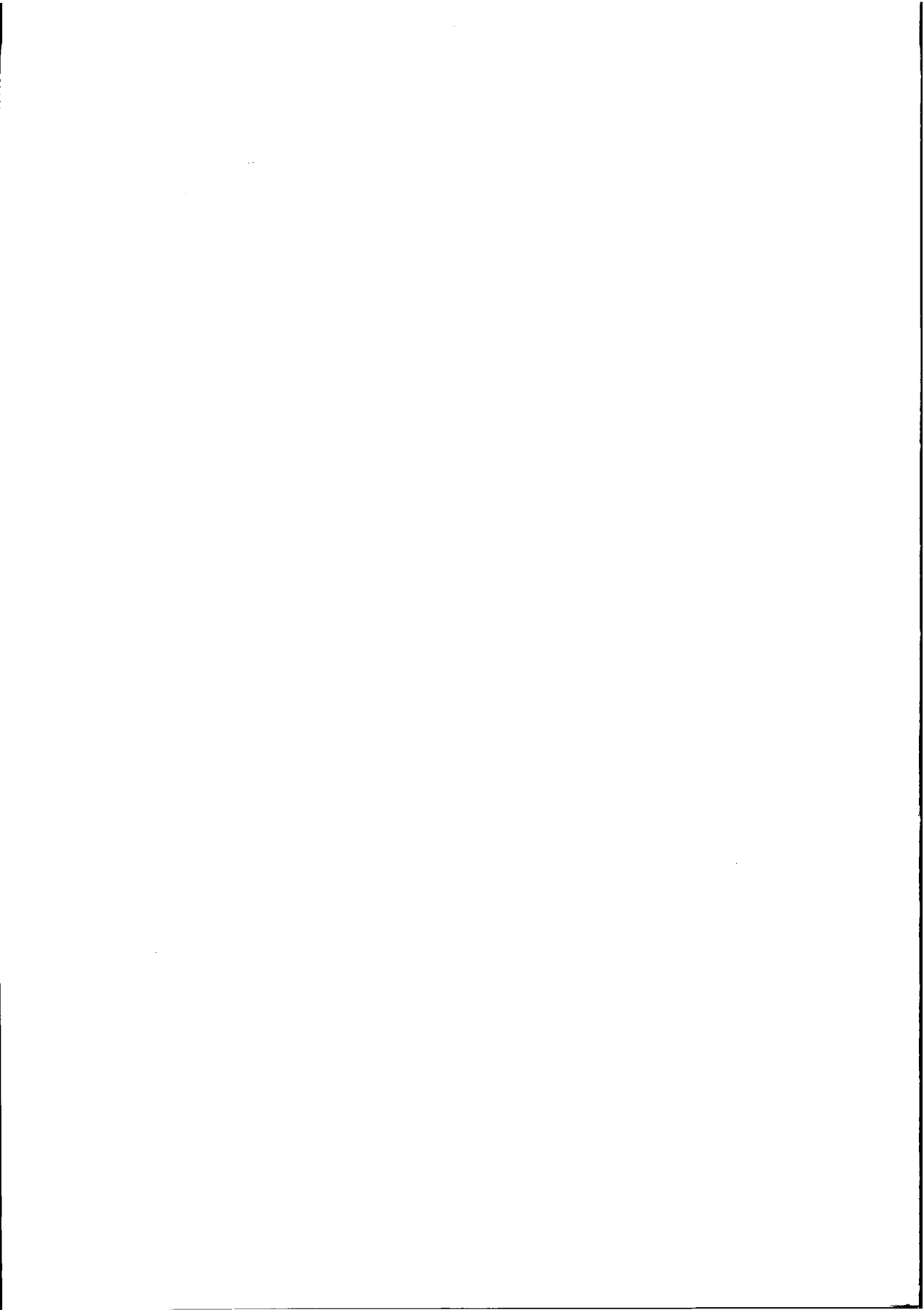
Copyright © 1998 by H. Polinder

All rights reserved. No part of the material protected by this copyright notice may be reproduced or utilized in any form or by any means, electronic or mechanical, including photocopying, recording or by any information storage and retrieval system without written permission of the publisher.

De vreze des HEEREN is het beginsel der wijsheid.
Psalm 111:10

The fear of the LORD is the beginning of wisdom.
Psalms 111:10

Voor mijn vrouw Clarisa
en onze kinderen Reinalt, Herbert en Minco



Dankwoord

Ieder die, op welke manier dan ook, heeft bijgedragen aan het tot stand komen van dit proefschrift wil ik daarvoor hartelijk danken. Zonder steun van mensen om mij heen, zowel thuis als op de universiteit, was het er niet gekomen. Een aantal bijdragen wil ik in het bijzonder noemen.

Het onderzoek dat tot dit proefschrift heeft geleid, is gedeeltelijk gefinancierd door de Novem (Nederlandse Onderneming voor Energie en Milieu).

Prof. Deleroi, mijn promotor, bood me de mogelijkheid een promotieonderzoek te doen bij de vakgroep Vermogenslektronica en Elektrische Machines, gaf hierin veel vrijheid en was altijd bereid om vragen in te gaan.

Martin Hoeijmakers, mijn dagelijks begeleider en toegevoegd promotor, gaf steeds grondig commentaar op zowel de grote lijnen als de details van het onderzoek en het proefschrift.

Lodewijk Offringa waarschuwde met enige regelmaat dat het werk niet te theoretisch mocht blijven en stelde praktische gegevens ter beschikking.

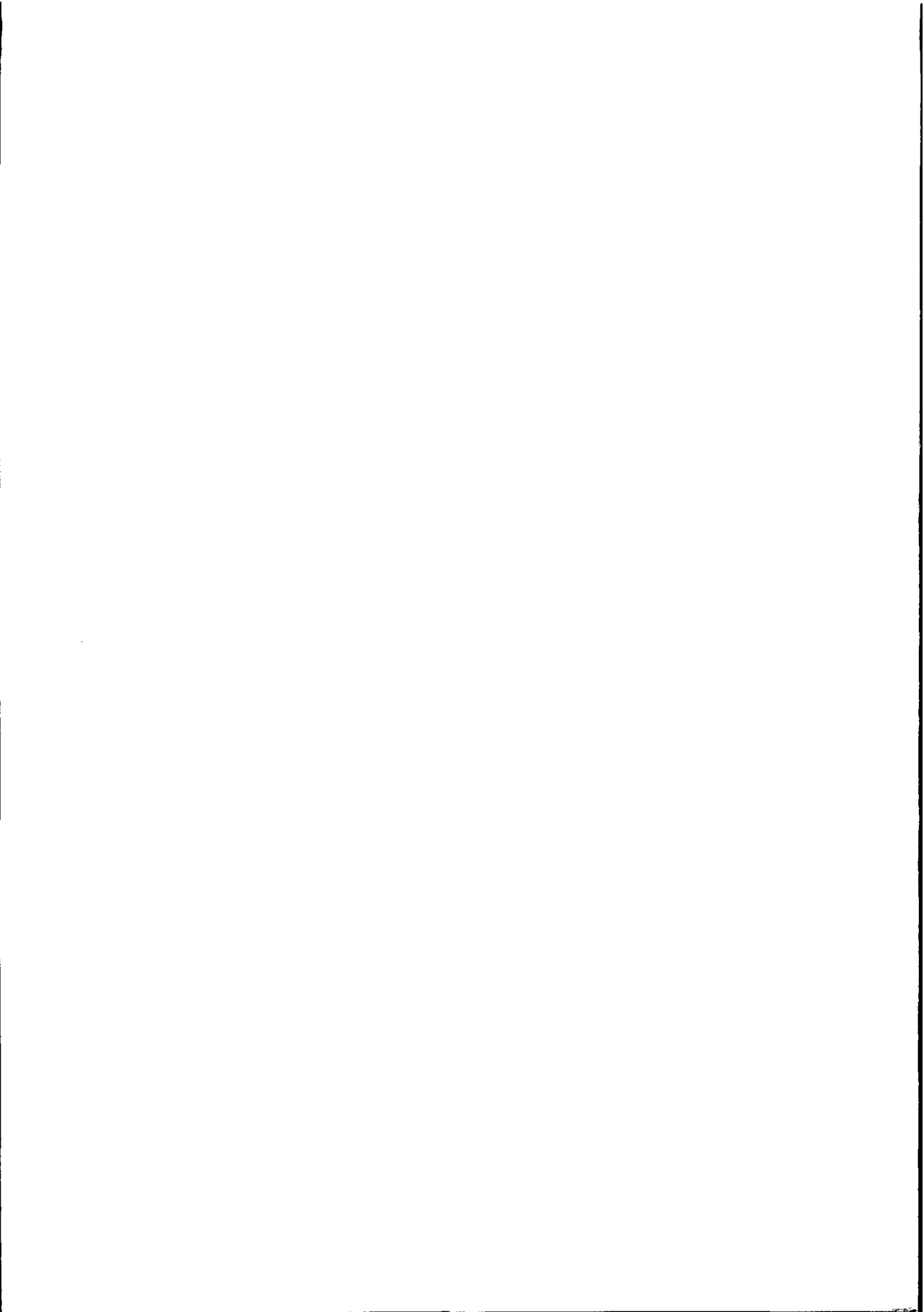
De andere leden van de promotiecommissie, Prof. Belmans, Prof. Blok, Prof. Canders en Prof. Ferreira, reageerden op het concept-proefschrift. Ik denk dat hun opmerkingen de kwaliteit van het uiteindelijke proefschrift ten goede gekomen zijn.

Kate Jansen-Bates voorzag mijn engels van het nodige commentaar.

Mijn ouders hebben mij gestimuleerd om mijn talenten te gebruiken en mij de mogelijkheden en de vrijheid gegeven om mijn weg te gaan.

Clarisa, mijn vrouw, heeft ervoor gezorgd dat ik me om een heleboel dingen niet druk hoefde te maken. Zij heeft, samen met Reinalt, Herbert en Minco, onze kinderen, mijn lichamelijke en (vaker) mentale afwezigheid verdragen. Omdat zij samen zorgen voor een stuk levensvreugde, draag ik dit proefschrift aan hen op.

Ik geloof dat heel mijn leven in Gods hand is, en dat daarom ook dit proefschrift aan Hem te danken is. Te weten dat Hij in Christus mijn God wil zijn, geeft een perspectief dat mijn wetenschappelijk werk overstijgt. Daarom geef ik dit proefschrift het motto 'De vreze des HEEREN is het beginsel der wijsheid' (Psalm 111:10).



Contents

Dankwoord	vii
List of symbols	xiii
1 Introduction	1
1.1 High-speed generator systems	1
1.2 Problem definition	4
1.3 Outline of the thesis	5
2 The magnetic field in the generator	7
2.1 Introduction	7
2.2 Derivation of a method to determine the magnetic field	12
2.2.1 The partial differential equation in cylindrical coordinates	12
2.2.2 The boundary conditions	14
2.2.3 Visualization of the magnetic field	16
2.3 The magnets	16
2.3.1 The permanent magnetization in cylindrical coordinates	16
2.3.2 The magnetic field of the magnets	19
2.4 The stator	24
2.4.1 The stator surface current density	24
2.4.2 The magnetic field of the stator currents	28
2.5 The damper cylinder	32
2.5.1 The surface current density of the damper cylinder	32
2.5.2 The magnetic field of the damper currents	34
2.6 Summary	36
3 The voltage equations of the generator	39
3.1 Introduction	39
3.2 The stator voltage equation	41
3.2.1 A general expression for the stator voltages	41
3.2.2 The leakage flux of the stator	42
3.2.3 The flux linkages of the stator windings	42

3.2.4	The no-load voltage	44
3.2.5	The stator flux linkages due to the stator currents	45
3.2.6	The stator flux linkages due to the damper currents	46
3.2.7	Summary	47
3.3	The damper voltage equation	47
3.3.1	Modelling of the damper cylinder	48
3.3.2	A general expression for the damper voltage equation	51
3.3.3	The flux linkages of the sinusoidally distributed damper windings	51
3.3.4	The damper resistance	53
3.3.5	The damper flux linkages due to the stator currents	53
3.3.6	The damper flux linkages due to the damper currents	54
3.3.7	Summary	54
3.4	Transformations of the voltage equations	55
3.4.1	Transformation into the stator-connected $\alpha\beta$ -system	55
3.4.2	Referring the damper quantities to the stator	60
3.4.3	Summary	61
3.5	Steady-state voltage equations	62
3.5.1	The rotor angular frequency and the slip	62
3.5.2	Equations for the rectifier-loaded machine	64
3.5.3	Equations for the locked-rotor tests	66
3.6	Experimental results of locked-rotor tests	68
3.7	Summary	70
4	The losses in the generator	71
4.1	Introduction	71
4.2	The stator copper loss	73
4.3	The iron loss	75
4.3.1	Introduction	75
4.3.2	The specific iron loss	75
4.3.3	The stator core loss	78
4.3.4	The rotor core loss	85
4.3.5	The stray loss	89
4.3.6	Locked-rotor tests of the test model	90
4.3.7	Concluding remarks	96
4.4	The eddy-current loss in the magnets	96
4.4.1	Introduction	96
4.4.2	The magnet loss due to space harmonics with a large pole angle	98
4.4.3	Magnet loss due to space harmonics with a small pole angle	101
4.4.4	Incorporating the magnet loss resistance in the machine model	104
4.4.5	Locked-rotor tests of the servomotor	107
4.4.6	Concluding remarks	110
4.5	The loss due to the stator slotting	111

4.5.1	Introduction	111
4.5.2	The pulsation of the magnetic flux density	112
4.5.3	The damper currents caused by the pulsation of the magnetic field	114
4.5.4	Concluding remarks	115
4.6	Summary	116
5	Calculation of the performance of the generator with rectifier	117
5.1	Introduction	117
5.2	Rough description of the generator with controlled rectifier load	119
5.2.1	The operating principles	119
5.2.2	The use of Fourier series	122
5.3	An infinitely large self-inductance in the direct-current circuit	123
5.3.1	Introduction	123
5.3.2	Forming an equation for the time derivative of the phase current	124
5.3.3	Solving the Fourier coefficients of the phase current	126
5.4	A finite self-inductance in the direct-current circuit	129
5.4.1	Introduction	129
5.4.2	Forming an equation for the time derivative of the phase current	130
5.4.3	Solving the Fourier coefficients of the phase current	133
5.5	The quantities in the direct-current circuit	134
5.5.1	The current in the direct-current circuit	134
5.5.2	The voltage across the direct-current circuit	136
5.6	On the choice of the external inductance	137
5.7	Concluding remarks	138
6	Experimental verification of the model of the generator with rectifier	139
6.1	Introduction	139
6.2	Machine model based on measured operational inductances	140
6.2.1	Introduction of the machine model with operational inductances	140
6.2.2	Determination of the operational inductances	142
6.2.3	The use of Fourier series in the machine model	144
6.3	Comparison of measured and calculated waveforms	145
6.3.1	Large self-inductance L_{dc} and small delay angle α_p	145
6.3.2	Large self-inductance L_{dc} and large delay angle α_p	148
6.3.3	Small self-inductance L_{dc} and small delay angle α_p	150
6.3.4	Small self-inductance L_{dc} and large delay angle α_p	151
6.4	Conclusions	153
7	On the design of permanent-magnet generators	155
7.1	Introduction	155
7.2	The effect of a damper cylinder	156
7.2.1	The voltage and current waveforms	156

7.2.2	The addition of a damper cylinder and the rotor losses	158
7.2.3	The damper radius and the rotor losses	160
7.2.4	Machines with solid rotor iron	161
7.3	Separation of the generator losses	161
7.4	Conclusions	164
8	Conclusions and recommendations	165
8.1	Conclusions	165
8.2	Recommendations for further research	168
References		169
Appendices		177
A	Machine parameters	177
A.1	Parameters of the test model	177
A.2	Parameters of the servomotor	178
A.3	Parameters of the Eindhoven machine	179
B	The number of turns of the space harmonics of a winding	180
B.1	The definition of the winding factor	180
B.2	Contributions to the winding factor	181
C	The effect of eddy currents on the air-gap field	183
C.1	Eddy currents in the iron	183
C.2	Eddy currents in the magnets	187
D	Conformal transformation for a stator slot	192
D.1	Introduction	192
D.2	The conformal transformation	192
D.3	The pulsation of the magnetic flux density	194
E	Derivation of equation (5.46)	198
Summary		201
Samenvatting		203
Curriculum vitae		207

List of symbols

Latin letters:

symbol	quantity	unit
\vec{A}	magnetic vector potential	Wb/m
b	width or breadth	m
\vec{B}	magnetic flux density	T
c_{Fe}	correction factor in the calculation of the iron loss	
C	closed contour	
C_{23}	matrix for the Clarke transformation	
$C_{rot,k}$	rotation matrix	
$C_{sign,k}$	matrix, which is combined with the rotation matrix	
$C_{r,k}$	$C_{rot,k} C_{sign,k}$	
e_p	induced voltage in no-load	V
e_s	internal voltage	V
\vec{E}	electric field strength	V/m
f	frequency	Hz
g	gap	m
h	height	m
h	pulse function	
\vec{H}	magnetic field strength	A/m
i	current	A
\vec{i}	unit vector	
\vec{J}	current density	A/m ²
k	counter, mainly for the space harmonics	
k	specific loss	W/kg or W/m ³
k_C	Carter factor	
k_w	winding factor	
K	surface current density (linear current density in [IEC 85])	A/m
l	counter	
l_s	stack length, active length of the machine	m
l_m	magnet length in the direction of the permanent magnetization	m
L	self-inductance	H
\underline{L}_o	operational inductance	H

m	mass	kg
M	mutual inductance	H
\vec{M}	magnetization	A/m
n	counter, mainly for the time harmonics	
n	rotational frequency	s^{-1}
n	winding distribution or number of conductors per radian	rad^{-1}
N	number of turns	
N	number	
p	number of pole pairs of the machine	
p	pulse function	
P	power	W
P	matrix for the park transformation	
q	number of slots per pole per phase	
r	radius	m
R	resistance	Ω
s	slip	
S	surface	m^2
S	Steinmetz constant	
t	time	s
T	period of the fundamental time harmonic	s
u	voltage	V
V	volume	m^3
Z	impedance	Ω

Greek letters:

symbol	quantity	unit
α	angular coordinate	rad
α	factor in the calculation of the eddy currents in appendix C	
β	angular coordinate	rad
γ	factor determining the amplitude of the pulsation due to the stator slotting	
δ	thickness	m
ε	angular coordinate	rad
θ	the rotor position angle	rad
κ	coupling factor	
μ	angle of overlap	rad
μ_r	relative magnetic permeability	
μ_0	magnetic permeability in vacuum	$4\pi 10^{-7}$ H/m
ξ	quantity in the calculation of the increase of the stator resistance	
ρ	resistivity	Ωm
Ψ	flux linkage	Wb
φ	phase angle	rad
Ω	(mechanical) angular velocity	rad/s

ω (electrical) angular frequency rad/s

Latin subscripts:

symbol	description
<i>a</i>	anomalous or excess loss
<i>a</i>	stator phase <i>a</i>
<i>av</i>	average
<i>b</i>	stator phase <i>b</i>
<i>b</i>	battery (in the battery voltage U_b)
<i>b</i>	blocks
<i>c</i>	stator phase <i>c</i>
<i>c</i>	conductor
<i>c</i>	cylinder
<i>chord</i>	chording or pitch
<i>C</i>	Carter (in the Carter factor k_C)
<i>C</i>	closed path <i>C</i>
<i>Cu</i>	copper
<i>d</i>	damper
<i>d</i>	direct axis of the rotor-connected <i>dq</i> -system
<i>dc</i>	direct-current circuit
<i>diss</i>	dissipation
<i>D</i>	damper after referring to the stator
<i>e</i>	eddy current loss
<i>e</i>	external
<i>ew</i>	end windings
<i>fth</i>	fundamental time harmonic
<i>fsh</i>	fundamental space harmonic
<i>Fe</i>	iron
<i>g</i>	gap
<i>h</i>	hysteresis loss
<i>hsh</i>	fundamental space harmonic
<i>hth</i>	fundamental time harmonic
<i>k</i>	integer, mainly for the space harmonics
<i>l</i>	integer
<i>m</i>	magnets
<i>m</i>	integer
<i>n</i>	integer, mainly for the time harmonics
<i>M</i>	the magnets after referring to the stator
<i>o</i>	operational (in the operational inductance L_o)
<i>p</i>	pole (in the no load voltage e_p , the pole angle $\alpha_{p,k}$, and the delay angle α_p)
<i>p</i>	permanent (in the permanent magnetization of the magnets)
<i>q</i>	quadrature axis of the rotor-connected <i>dq</i> -system

r	relative (in the magnetic permeability μ_r)
r	rotor
r	radial component
rr	rotor removed
R	rotor after referring to the stator
s	the stator
<i>skew</i>	skew
<i>skin</i>	skin in the skin depth δ_{skin}
<i>slot</i>	slot
<i>slotted</i>	slotted air gap
<i>smooth</i>	air gap without slots
so	slot opening
t	turn
t	tooth
tot	total
w	winding
x	x -component
y	yoke
y	y -component
z	(axial) z -component
0	zero component
0	at a given value

Greek subscripts:

symbol	description
α	tangential component
α	α -component of the stator connect $\alpha\beta$ -system
β	β -component of the stator connect $\alpha\beta$ -system
σ	leakage
σ	stray

Latin superscripts

symbol	description
$s0$	belongs to the three-dimensional stator-connected $\alpha\beta0$ -system
s	belongs to the two-dimensional $\alpha\beta$ -system without zero-component

Chapter 1

Introduction

1.1 High-speed generator systems

This thesis deals with the losses in a high-speed permanent-magnet generator, which is loaded with a rectifier. Such a generator system has several possible applications. The thesis originates from a research project into a gas turbine driven generator system for application in series hybrid vehicles. Therefore, this application is briefly introduced before other possible applications are mentioned. For discussions on the history, the technology, and the environmental effects of electric and hybrid vehicles, see [Cha 93], [Cha 97], [Wak 94], [IEA 93], the proceedings of the International Electric Vehicle Symposium (EVS), and the proceedings about electric and hybrid vehicles of the Society of Automotive Engineers (SAE).

Hybrid vehicles are vehicles with both a combustion engine and an electric drive system. They are used to overcome some of the main disadvantages of both normal combustion-engined vehicles and electric vehicles:

- 1) They enable driving without polluting emissions in urban areas using the electric drive system.
- 2) They enable the making of long journeys using the combustion engine.

In a parallel hybrid vehicle, the wheels can be driven both by the electric drive system and by the combustion engine. In a series hybrid vehicle, the wheels are driven electrically; the combustion engine drives a generator feeding into the electric system. The drive system of such a series hybrid vehicle is depicted in figure 1.1.

Compared to other combustion-engined vehicles, a series hybrid vehicle has three important advantages.

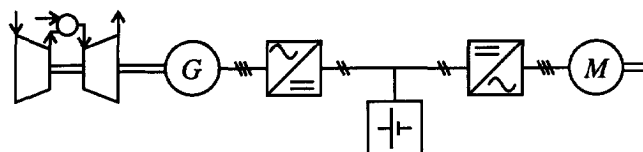


Figure 1.1: The drive system of a series hybrid vehicle, consisting of gas turbine, generator, rectifier, battery, inverter and AC traction motor.

- 1) The combustion engine can always work at its optimum (highest efficiency, lowest polluting emissions) at constant power and constant speed. This advantage compensates the disadvantage that many components of the drive system are connected in series, so that the efficiency from combustion engine to wheels is lower than the maximum efficiency of other combustion-engined vehicles.
- 2) The drive system is built up modularly.
- 3) A small combustion engine suffices because the power of the combustion engine can be limited to the average power consumption, which is usually about a quarter of the peak power consumption.

Furthermore, there are important arguments for using a gas turbine as a combustion engine with a generator mounted on the same shaft (figure 1.2) [Chu 96], [Chu 93], [Mac 94], [Krtü 94], [Pul 96]:

- 1) Because of the high speed, the unit may be small and light.
- 2) In principle, the system is very simple because it has only one moving part: the shaft with the rotors of the generator and the gas turbine.
- 3) A gas turbine has lower polluting emissions than a conventional internal-combustion engine.
- 4) A gas turbine is suitable for different kinds of fuel.

To obtain acceptable efficiency, a rather voluminous recuperator is necessary, which heats the incoming air from the exhaust gases. This recuperator reduces the advantage of the system being small, although it may remain light [Mac 94].

Generally, the high-speed generators in series hybrid vehicles are permanent-magnet machines, because of their high efficiency and power density. There are various opinions about the layout of the generator. Because of the high speed, an important consideration

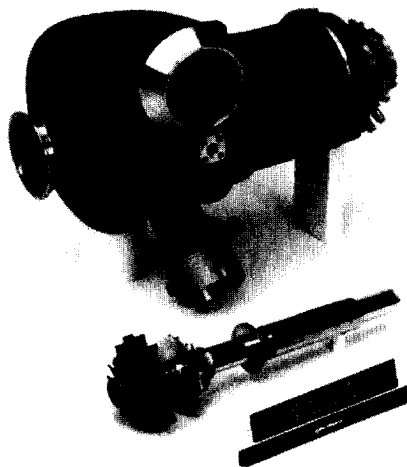


Figure 1.2: Stator and rotor of a gas turbine (left part) and generator (right part) developed by AlliedSignal, Inc., Torrance, California.

is the mechanical integrity of the rotor. In [Krü 94] and [Krü 92], surface-mounted magnets are kept in place by using an exterior rotor, which also functions as a flywheel to buffer short power peaks. In [Pul 96], the generator is of a disc type, because in this topology, the magnet containment structure is not in the magnetic circuit. In [Chu 93] and [Chu 96], the rotor is a cylindrical magnet encapsulated in a high strength cylinder and the stator is slotless.

In this thesis, a generator with a cylindrical rotor and surface-mounted magnets has been chosen. To make the generator mechanically strong enough, the use of a fibre bandage is proposed, as in [Off 96], [Vee 97], and [And 97]. In for example, [Bou 81], [And 87], and [Hen 94], a nonmagnetic metal cylinder is proposed. However, a serious disadvantage of such a cylinder is that the eddy-current loss in the cylinder due to the stator slotting may be very high.

To convert the ac voltage of the generator to the dc voltage of the battery, a six-pulse bridge rectifier is used. This rectifier is more efficient and more robust than other possible converters. A disadvantage of such a rectifier is that it needs reactive power, resulting in extra stator copper loss in the generator. However, converters which do not need reactive power, are less efficient and less robust. Moreover, six-pulse inverters used as rectifiers increase the harmonic content of the stator currents, while pulse width modulated rectifiers increase the rectifier loss further. For example, the efficiency of the pulse width modulated voltage source rectifier used in [Krü 92] is estimated at 91.8%. This is very low compared to the 96% efficiency of the generator systems (generator and converter) claimed in [Mac 94] and [Chu 96].

A thyristor bridge rectifier is used, because this enables to control the output voltage. In principle, a diode bridge rectifier also suffices when the generator only works at its optimum operating point and the battery voltage is constant. However, in practice, the battery voltage depends on the load of the battery, and therefore, it is advantageous to use a thyristor bridge rectifier. Another possibility is the use of a chopper between the diode bridge rectifier and the battery. If the effect of the chopper on the generator currents is negligible, this system may also be investigated with the methods described in this thesis, because the firing angle of the thyristor bridge rectifier can be made zero.

As mentioned earlier, the generator system described in this thesis is intended for use in series hybrid vehicles. However, the research has been done in such a way that the results may also be used for high-speed generator systems in other applications, for example, in aeroplanes [Vai 91], vessels, mobile ground power stations, total energy units [Off 96], [Vee 97], and expanders which recover power from compressed natural gas. Moreover, the results of the research may be used for permanent-magnet motors with load-commutated inverter [And 85], [And 87], [Blö 86], [And 97].

High-speed permanent-magnet machines are also used in flywheel systems [Can 82], [Gün 84], [Mee 88], [Krü 94], [Aca 96]. However, in this case, the machine layout is usually different from the layout considered in this thesis: exterior rotors integrated in the flywheel are used. Although such machines are beyond the scope of this thesis, they are in many respects comparable to the machines considered in the thesis.

1.2 Problem definition

The previous section describes the choice of the generator system consisting of a permanent-magnet generator with surface-mounted magnets and a controlled bridge rectifier. Figure 1.3 depicts a cross-section of such a machine with two poles.

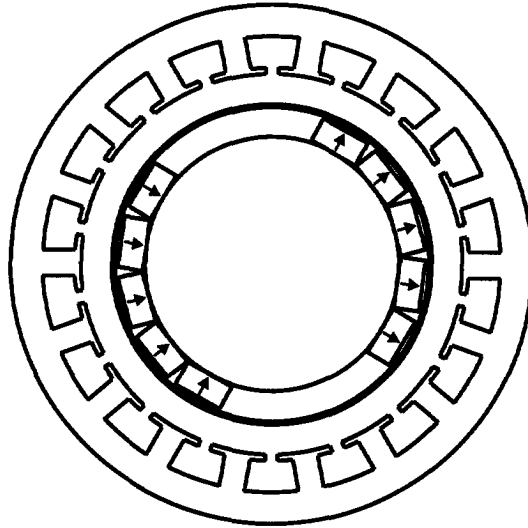


Figure 1.3: Cross-section of a two-pole permanent-magnet machine. The arrows in the magnet blocks indicate the direction of the magnetization. The thick line surrounding the magnets represents the damper cylinder.

The objective of the research described in this thesis is to derive a machine model suitable for the optimization of the generator design. Design optimization primarily means minimization of the losses. Such minimization is not only important for obtaining an efficient generator system applicable in a hybrid vehicle. It is mainly important because high rotor losses heat the rotor, which can only be cooled with difficulty, and the magnets may demagnetize if they become too hot. For example, there are permanent magnets (NdFeB) with a very high energy density that demagnetize at temperatures above approximately 120°C .

The most important aim of this thesis is to investigate the effect of a damper cylinder on the losses. On the one hand, a damper cylinder introduces extra losses. On the other hand, it shields the rotor, avoiding excessive eddy-current losses in the rotor iron and the magnets [Off 96], [Vee 97]. Investigation is done into whether applying a damper cylinder decreases the rotor losses or not. Therefore, the function of the damper cylinder in this study is not the damping of mechanical oscillations, but the shielding of the rotor.

To obtain a realistic comparison between machines with and without a damper

cylinder, the model of the machine without a damper cylinder must include the eddy-current loss in the magnets. Innovative research was called for to obtain a reasonable model of this loss, because an appropriate model was not available. By modelling the eddy-current loss in the permanent magnets, the usefulness of employing small permanent-magnet blocks, a way of decreasing the rotor losses [Hen 89], [Sch 97], is also investigated.

The model has to be suitable for optimizing the generator design. Therefore, the parameters of the machine model are derived from design parameters, such as the dimensions and the material properties of the generator.

In this thesis, only analytic methods are used. Compared to numerical methods as Finite Element Methods, analytic methods have the disadvantage of being unsuitable for complicated constructions and materials, so that they need more simplifying assumptions. However, they have the advantage that they result in analytic expressions for the relations between dimensions and parameters. This is a decisive argument, since the machine model is used for the optimization of the generator design.

The research described is restricted to the electromagnetic aspects of the rectifier-loaded generator. The gas turbine and the mechanical aspects of the generator are beyond the scope of this study. By implication, mechanical losses in the generator, such as friction and windage losses, are not considered either.

1.3 Outline of the thesis

This section gives an outline of the thesis including the most important methods and assumptions. The introduction of each chapter gives a more detailed description of the methods and assumptions.

In chapters 2 to 4, a machine model is derived. In the derivation, it is assumed that

- the damper cylinder is very thin,
- end effects in the machine are negligible, and
- nonlinear effects, such as hysteresis and saturation phenomena, are negligible.

The derivation of the machine model begins in chapter 2 with the calculation of the magnetic field in the air gap and the magnets. In this chapter, effects which hardly influence this magnetic field or influence it only locally are neglected. Therefore, this chapter is based on the assumptions that

- eddy-currents in the stator iron, the rotor iron and the magnets are negligible,
- the magnetic permeability of iron is infinite, and
- the stator slotting is negligible.

Under these assumptions, the magnetic field is caused by the permanent magnetization of the magnets, the stator currents, and the current density in the damper cylinder (if a damper cylinder is present). The magnetic field is calculated two-dimensionally and in a cylindrical coordinate system, which means that both the radial and the tangential

component are calculated. This is done because the effective air gap, which includes the magnets, is large and cylindrical. Space harmonics of the magnetic field are considered, because the losses they cause may be important. The calculated magnetic field is also visualized.

In chapter 3, the expressions for the magnetic field derived in chapter 2 are used to derive the voltage equations of the permanent-magnet generator. They form a model of the relation between the terminal voltages and the terminal currents of the machine. Furthermore, these voltage equations are transformed into a useful form, and they are partly verified by means of locked-rotor tests.

Although the derived voltage equations are suitable for the calculation of the terminal voltages and the terminal currents, they only consider a part of the losses in the machine, namely the copper loss. They neglect other important losses, such as

- the iron losses,
- the eddy-current loss in the magnets, and
- the losses due to the stator slotting.

Therefore, in chapter 4, these losses are modelled and incorporated in the voltage equations to obtain a machine model suitable for the optimization of the design. As far as possible, the models are verified by means of locked-rotor tests.

Then, in chapter 5, the derived model of the permanent-magnet generator is combined with a model of the controlled rectifier. The resulting equations are solved in the frequency domain to determine the steady-state performance of the rectifier-loaded permanent-magnet generator.

In chapter 6, the complete model of the machine and rectifier is verified by comparing measured and calculated line voltage and phase current waveforms.

In chapter 7, it is shown that the derived model can be used to optimize the machine design by calculating the losses in a rectifier-loaded permanent-magnet generator. The effect of a damper cylinder on the losses is explored by comparing the losses in the generator with and without a damper cylinder.

Conclusions are drawn and recommendations are given in chapter 8.

To avoid confusion, it is noted here that three machines are used in this thesis.

- 1) The so-called test model (described in section A.1 of appendix A), which consists of a three-phase stator, a removable cylindrical laminated rotor and a removable copper damper cylinder. This model is used for the verification of the model of the damper cylinder and for the verification of the model of the iron losses.
- 2) The so-called servomotor (described in section A.2 of appendix A), which is a permanent-magnet machine without a damper. This machine is used to verify the model for the eddy-current loss in the magnets and the calculation of the steady-state performance of the rectifier-loaded machine used as a generator.
- 3) The so-called Eindhoven machine (described in section A.3 of appendix A), which is a permanent-magnet machine. It is used as an example to illustrate that the derived model can be used for the optimization of the design of permanent-magnet machines in chapter 7.

Chapter 2

The magnetic field in the generator

2.1 Introduction

Objective

This chapter describes the first part of the modelling of the permanent-magnet generator, namely the calculation of the magnetic field. In later chapters, this magnetic field is used for the derivation of the voltage equations and for the modelling of the losses in the generator.

At this point, only the magnetic field in the air gap and the magnets is calculated, because this part of the magnetic field dominates the machine performance. In a machine without a damper cylinder, two sources of magnetic field are considered: the permanent magnetization of the magnets, and the stator currents. In a machine with a damper cylinder, the magnetic field produced by the current density in the damper cylinder is also considered.

The magnetic field is calculated two-dimensionally in a cylindrical coordinate system (figure 2.1), which means that both the radial and the tangential component of the field are calculated. Often, the air gap of an electrical machine is so small that the magnetic

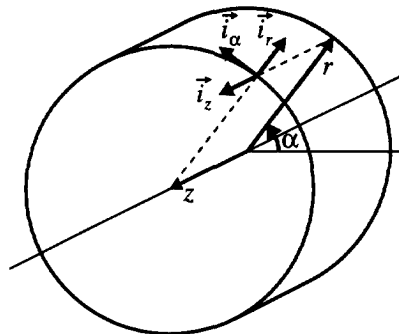


Figure 2.1: The cylindrical coordinate system, where \vec{i}_r , \vec{i}_α , and \vec{i}_z are the unit vectors in the radial, the tangential and the axial direction respectively, and r , α , and z are the radial, the angular, and the axial position respectively.

field may be assumed to cross the air gap perpendicularly (one-dimensional). However, a machine with surface-mounted magnets has a large effective air gap due to the low magnetic permeability of the magnets. Therefore, the magnetic field may not be assumed to cross the air gap perpendicularly, and the field is calculated two-dimensionally. A cylindrical coordinate system is used because the machine is cylindrical. Furthermore, space harmonics of the magnetic field are considered, because the losses they cause may be significant.

There are several publications about the two-dimensional calculation of magnetic fields in cylindrical coordinate systems. A few of the important ones are mentioned.

- 1) Hague wrote a book [Hag 29] containing the calculation of the two-dimensional field in cylindrical coordinates produced by a current in the air gap.
- 2) In his paper [Bou 85], Boules used Hague's book to calculate the no-load field of a permanent-magnet machine. He did not use the permanent magnetization of the magnets, but replaced it by a surface current density at the edges of the magnet.
- 3) Zhu wrote a series of papers about the calculation of the magnetic fields in permanent-magnet machines. In [Zhu 93a], the field of the magnet pole arcs is calculated. [Zhu 93b] describes the field of the stator currents and [Zhu 93c] the effect of stator slotting. The total field on load is calculated in [Zhu 93d]. These articles compare analytical two-dimensional calculations in cylindrical coordinates with finite element calculations. The agreement between these calculation methods is good. However, Zhu's articles deal with a machine without a damper.

The references mentioned all use the scalar magnetic potential to solve the equations for the magnetic field. Here, the magnetic vector potential is used for two reasons.

- 1) In subsection 4.4.3, the magnetic vector potential will be used to calculate eddy currents in the magnet material. If the scalar magnetic potential were used, it would be much more difficult to calculate these eddy currents.
- 2) Using the magnetic vector potential has the advantage that lines of magnetic flux density can easily be plotted as lines of constant magnetic vector potential. In this chapter, this is used to plot the lines of magnetic flux density in the air gap and the magnets of the machine.

The magnetic field of the stator currents causes a current density in the damper cylinder. It is possible to calculate the magnetic field and the current density in the damper cylinder two-dimensionally (as a function of the radial and the angular position) including skin effect by solving the Helmholtz equation, as is done, for example, in [Bou 81] and [Abu 97]. However, in this thesis, the damper cylinder is assumed to be so thin that skin effect is negligible for two reasons.

- 1) The damper cylinder does not function as a retainment sleeve, because a fibre bandage is applied when a retainment sleeve is necessary. For the shielding, a very thin damper cylinder is sufficient. For such a thin damper cylinder, skin effect is unimportant at the dominating frequencies. Skin effect is important at frequencies where the skin depth is smaller than the thickness of the damper cylinder. The skin depth δ_{skin} is given by [Sto 74] (equation (C.8) gives the skin depth in iron)

$$\delta_{skin} = \sqrt{\frac{\rho}{\pi \mu_0 \mu_r f}} \quad (2.1)$$

where

- ρ is the resistivity of the material,
- μ_0 is the magnetic permeability in vacuum,
- μ_r is the relative magnetic permeability of the material, and
- f is the frequency.

For example, for the copper damper cylinder of the test model with thickness $\delta_d = 0.5$ mm, skin effect is only important at frequencies above 18 kHz.

- 2) Considering skin effect in the damper cylinder would complicate the calculations of the magnetic field considerably. It would also make it more difficult to combine the machine model with a model of the rectifier to calculate the steady-state performance of the rectifier-loaded machine, as will be done in chapter 5.

In this chapter, the magnetic field produced by an arbitrary current density in the damper cylinder is calculated on the assumption that the damper cylinder is very thin. In chapter 3, the current density in the damper cylinder caused by the total magnetic flux density at the damper radius will be determined.

Outline of the chapter

This chapter first describes in section 2.2 how to derive the partial differential equation and the boundary conditions for the magnetic field from Maxwell's equations. It also explains how the magnetic field is visualized. In the next three sections, this is used to calculate and visualize the magnetic fields produced by the three sources of magnetic field, namely:

- 1) the permanent magnetization of the magnets (section 2.3),
- 2) the surface current density representing the stator currents (section 2.4), and
- 3) the surface current density of the damper cylinder (section 2.5).

The three sources of magnetic field are also described in the sections mentioned. Of course, in a machine without a damper cylinder, the third contribution is not present. The total magnetic field is a superposition of the different contributions, because of the assumption of the linear magnetic permeability of the magnetic circuit. Section 2.6 concludes with a summary.

Assumptions and starting-points

To obtain functional expressions for the magnetic field, it is necessary to use simplifying assumptions and to choose some starting-points. Many of the simplifying assumptions are neglects of effects which hardly influence the magnetic field or influence it only locally. The following assumptions and starting-points are used in this chapter.

- End effects are negligible, or in other words, the machine can be considered to be infinitely long. This implies that the magnetic field does not have a component in

the axial direction.

- The stator and the rotor of the machine are not skewed.
- The stator bore (radius r_s , figure 2.2) and the rotor iron (radius r_r , figure 2.2) are smooth and cylindrical: the effects of stator slots are neglected.
- The relative magnetic permeability of the iron μ_{rFe} is infinite. This implies that
 - * saturation and hysteresis phenomena are absent, and
 - * the magnetic field in the air gap is a superposition of the fields produced by the magnets, the stator currents, and the current density in the damper cylinder.
- The effect of eddy-currents in the stator and the rotor iron on the magnetic field in the air gap is negligible. This will be shown in section 4.3, where the assumption that the iron loss is negligible is reconsidered.
- The effect of eddy-currents in the magnets on the magnetic field in the air gap and the magnets is negligible. In section 4.4, this will be reconsidered.
- Although it is possible to incorporate the real magnetic permeability of the magnets ([Zhu 93a], [Abu 97]), here, the relative magnetic permeability of the magnets μ_m is assumed to be one. This is a reasonable assumption for the modern rare-earth magnets, which have relative magnetic permeabilities close to one.
- As is further explained in section 2.3, the magnet blocks with permanent magnetization M_{pm} of figure 1.3 can be replaced by the magnet pole arcs of figure 2.2. The permanent magnetization of these pole arcs has only a radial component, which is inversely proportional to the radius:

$$M_{pr} = M_{pm} \frac{r_r}{r} \quad (2.2)$$

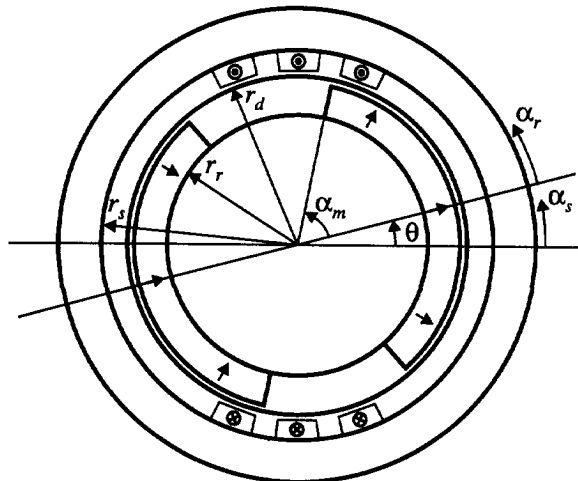


Figure 2.2: Cross-section of a two-pole permanent-magnet machine with a damper cylinder. An example of a winding distribution of stator phase a is depicted. The arrows in the magnet pole arcs indicate the direction of the magnetization.

Under the last three assumptions (concerning the magnets), the magnets have the same electromagnetic properties as air, except for their permanent magnetization.

- The stator has three symmetrical star- (or Y-)connected phases without star-point connection. The three windings are identical, except for an angular shift of the axes. Each of the three phase windings has p axes, where p is the number of pole pairs. The axes of stator phases a , b , and c on the interval $0 \leq \alpha_s < 2\pi/p$ are called the reference axes, and lay at stator coordinates $\alpha_a = 0$, $\alpha_b = 2\pi/(3p)$, and $\alpha_c = 4\pi/(3p)$ respectively. All turns of one stator phase are connected in series.
- The conductors in the stator slots can be replaced by a winding distribution with an infinitesimal thickness on the stator surface at the place of the slot openings. The blocks representing an example of a winding distribution in figure 2.2 do not mean that the winding distribution has a thickness. They indicate where the winding distribution has a value different from zero, which is at the place of the slot openings. The sign of the winding distribution is positive when a positive current results in a current flowing in the positive z -direction (from the plane of the drawing upwards, figure 2.1).
- The winding distribution (or the number of conductors per radian) of stator phase a $n_{sa}(\alpha_s)$ is symmetric in such a way that the following equations are valid:

$$n_{sa}(\alpha_s) = -n_{sa}(-\alpha_s) \quad (2.3)$$

and

$$n_{sa}(\alpha_s - \frac{\pi}{p}) = -n_{sa}(\alpha_s) \quad (2.4)$$

- The radius of the middle of the damper cylinder is the damper radius r_d (figure 2.2). The damper cylinder δ_d is so thin that the current density in the cylinder can be replaced by a surface current density at the damper radius r_d .
- Within the stack length of the machine l_s , the surface current density of the damper cylinder K_d only flows in the axial direction and

$$K_d(\alpha_r - \frac{\pi}{p}) = -K_d(\alpha_r) \quad (2.5)$$

is valid. As will be shown in subsection 3.3.1, this follows from the assumption that end effects are negligible.

It is possible to calculate the axial and the tangential component of the current density in the damper cylinder, which is longer than the stack length of the machine to provide a closing path for the damper currents. Comparable calculations have been done for screened rotor induction machines [Bol 69] and for linear induction machines [Mos 72], [Lan 73], [Gru 78], [Pol 80]. From these references, it can be concluded that it is reasonable to assume that the current density only flows in the axial direction within the stack length of the machine if the magnetic Reynold's number (or the Goodness [Bol 69]) is large. This is the case for the frequencies of the higher time harmonics in this thesis.

2.2 Derivation of a method to determine the magnetic field

This section considers a method for determining the magnetic field in the air gap and the magnets of a permanent-magnet machine. As explained in section 2.1, the magnetic field is calculated two-dimensionally and in cylindrical coordinates.

In subsection 2.2.1, a partial differential equation describing the magnetic field in the air gap and the magnets is derived. In this partial differential equation, the magnetic vector potential \vec{A} is used. To solve this equation, boundary conditions are required, which are derived in subsection 2.2.2. Subsection 2.2.3 describes how to use the magnetic vector potential to visualize the magnetic field. For a more detailed explanation of these derivations, see literature such as [Hau 89], and [Bin 92].

2.2.1 The partial differential equation in cylindrical coordinates

The magnetic field is characterized by Maxwell's equations. This section describes how to combine these equations to obtain one partial differential equation, from which the magnetic field in the air gap and the magnets can be solved.

The differential form of the first of Maxwell's equations (Ampere's law) for quasistatic fields is given by

$$\nabla \times \vec{H} = \vec{J} \quad (2.6)$$

where \vec{J} is the current density, and \vec{H} is the magnetic field strength.

The net magnetic flux out of any region enclosed by a surface must be zero. This magnetic flux continuity is expressed by

$$\nabla \cdot \vec{B} = 0 \quad (2.7)$$

where \vec{B} is the magnetic flux density.

The relation between the magnetic flux density \vec{B} and the magnetic field strength \vec{H} is given by

$$\vec{B} = \mu_0(\vec{H} + \vec{M}) \quad (2.8)$$

where μ_0 is the magnetic permeability in vacuum, and \vec{M} is the magnetization.

These three equations ((2.6), (2.7), and (2.8)) characterize the magnetic field, and form the basis for the derivation of the partial differential equation describing the magnetic field in the air gap and the magnets.

Using equation (2.8) in equation (2.6) results in

$$\nabla \times \vec{B} = \mu_0(\vec{J} + \nabla \times \vec{M}) \quad (2.9)$$

It is possible to combine equations (2.7) and (2.9) to obtain solvable partial differential equations for the radial and tangential components of the magnetic flux density. For example, in [Alg 65], this is done for the air spaces, where the magnetiza-

tion and the current density are zero. However, the equations become simpler when the magnetic vector potential \vec{A} is introduced. The relation between the magnetic flux density and the magnetic vector potential is given by

$$\vec{B} = \nabla \times \vec{A} \quad (2.10)$$

To determine the vector field \vec{A} completely, it is not enough only to define its rotation. Therefore, its divergence is also defined, and it is chosen as

$$\nabla \cdot \vec{A} = 0 \quad (2.11)$$

The magnetic vector potential of equation (2.10) always satisfies equation (2.7), because the divergence of a rotation is always zero.

Substitution of the magnetic flux density of equation (2.10) in equation (2.9) results in a partial differential equation for the magnetic vector potential \vec{A} :

$$\nabla \times (\nabla \times \vec{A}) = \nabla(\nabla \cdot \vec{A}) - \nabla^2 \vec{A} = -\nabla^2 \vec{A} = \mu_0(\vec{J} + \nabla \times \vec{M}) \quad (2.12)$$

In this equation, it is taken that the divergence of the magnetic vector potential is zero (equation (2.11)). This partial differential equation is a form of Poisson's equation.

On the right side of equation (2.12) two assumptions are used.

- 1) The stator currents and the current density in the damper have only a z-component.
- 2) The magnetization of the magnets has only a radial component, so that the rotation of this magnetization has only a z-component.

Because the right side of equation (2.12) has only a z-component, the magnetic vector potential \vec{A} also has only a z-component. With this, equation (2.12) can be written as

$$-\nabla^2 A_z(r, \alpha) = \mu_0 \left(J_z - \frac{1}{r} \frac{\partial M_r}{\partial \alpha} \right) \quad (2.13)$$

This equation must be solved in two regions, namely the magnet region ($r_r < r < r_m$) and the air-gap region ($r_m < r < r_s$). The solution of this equation in the magnet region is given in subsection 2.3.2. An expression for the general solution of this equation in the air spaces is given here, because it is used in the next three sections. In the air spaces, the magnetization and the current density are zero. Using this in equation (2.13) results in

$$\nabla^2 A_z(r, \alpha) = 0 \quad (2.14)$$

This well-known partial differential equation is a form of the potential equation or Laplace's equation. So, by taking that the magnetization and the current density as zero, Poisson's equation simplifies to Laplace's equation.

This partial differential equation is solved by means of separation of variables. For the magnetic vector potential in the air spaces considered in this thesis, a satisfying expression for the general solution is given by

$$\begin{aligned}
 A_z(r, \alpha) = & A_{1,0} + A_{2,0}\alpha + A_{3,0}\ln(r) + A_{4,0}\alpha\ln(r) \\
 & + \sum_{k=1}^{\infty} A_{1,k} r^k \sin(k\alpha) + A_{2,k} r^{-k} \sin(k\alpha) + A_{3,k} r^k \cos(k\alpha) + A_{4,k} r^{-k} \cos(k\alpha)
 \end{aligned} \quad (2.15)$$

where the constants $A_{1,k}$, $A_{2,k}$, $A_{3,k}$, and $A_{4,k}$ are determined from the boundary conditions.

2.2.2 The boundary conditions

To obtain the complete solution of the partial differential equation, boundary conditions are necessary, because the partial differential equation is not valid at the surface between two media. The number of required boundary conditions increases when the equation has to be solved in different regions separated by a surface current density or a surface between different media.

This subsection gives boundary conditions for the magnetic flux density and the magnetic field strength, and not for the magnetic vector potential. However, these boundary conditions are used to solve the partial differential equation for the magnetic vector potential. Equation (2.15) gives an expression for the general solution of the partial differential equation in the air-gap region. In subsection 2.3.2, an expression for the general solution of the partial differential equation in the magnet region will be derived. From the general solution, the magnetic flux density and the magnetic field strength are calculated by using equations (2.10) ($\vec{B} = \nabla \times \vec{A}$) and (2.8) ($\vec{B} = \mu_0(\vec{H} + \vec{M})$). In the resulting expressions for the magnetic flux density and the magnetic field strength, the boundary conditions are used.

There are two types of boundary conditions. The first is called Ampère's continuity condition, the second the magnetic flux continuity condition [Hau 89], [Bin 92].

Ampère's continuity condition

Ampère's continuity condition follows from the integral form of the first of Maxwell's equations (Ampère's law) for quasistatic fields:

$$\oint_C \vec{H} \cdot d\vec{s} = \iint_S \vec{J} \cdot d\vec{a} \quad (2.16)$$

where C is a closed contour, enclosing the surface S .

This equation is applied to the dashed closed contour C in figure 2.3. This contour C encloses a part of the surface between the two media. A surface current density K is located at the surface between the two media at radius r_1 . The length $r_3 - r_2$ of the two sides of the closed contour C is infinitesimal. Because the magnetic field strength is finite, these sides do not contribute to the line integral. With this, the result of applying Ampère's law to the closed contour C is

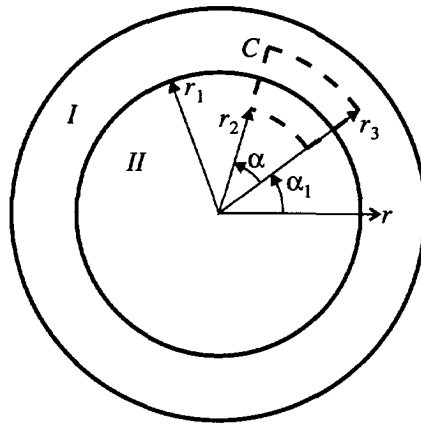


Figure 2.3: The closed contour C enclosing a part of the border between two media.

$$r_1 \int_{\alpha_1}^{\alpha_1+\alpha} H_{\alpha,I}(r_1, \alpha') d\alpha' - r_1 \int_{\alpha_1}^{\alpha_1+\alpha} H_{\alpha,II}(r_1, \alpha') d\alpha' = r_1 \int_{\alpha_1}^{\alpha_1+\alpha} K(\alpha') d\alpha' \quad (2.17)$$

Differentiating this equation to α and dividing it by r_1 results in Ampère's continuity condition:

$$H_{\alpha,I}(r_1, \alpha) - H_{\alpha,II}(r_1, \alpha) = K(\alpha) \quad (2.18)$$

When there is no surface current density at the surface between the two media, this boundary condition reduces to a well-known fact, namely that the component of the magnetic field strength parallel to a surface is continuous.

Often, the medium of one of the two regions is iron. Because the magnetic permeability of iron is assumed to be infinite, the magnetic field strength in iron is zero. In this case, the tangential component of the magnetic field strength at the other side of the surface is completely determined by this boundary condition.

Hence, Ampère's continuity condition gives a boundary condition for the tangential component of the magnetic field strength at every boundary.

The magnetic flux continuity condition

The magnetic flux continuity condition expresses that the component of the magnetic flux density perpendicular to a surface between two media is continuous. At a cylindrical surface at radius r_1 (figure 2.3), this means that the radial component of the magnetic flux density is continuous:

$$B_{r,II}(r_1, \alpha) = B_{r,I}(r_1, \alpha) \quad (2.19)$$

Often, the medium of one of the two regions is iron, the magnetic permeability of which was assumed infinite. In this case, it is impossible and unnecessary to use the magnetic flux continuity condition to determine the magnetic vector potential in the

other region. It is impossible because the magnetic flux density in the iron can not be determined. It is unnecessary because Ampère's continuity condition appears to be sufficient.

In conclusion, the magnetic flux continuity condition gives a boundary condition for the magnetic flux density at a surface between two media with a finite magnetic permeability.

2.2.3 Visualization of the magnetic field

A beautiful property of the magnetic vector potential is that it can be used to plot the lines of magnetic flux density, as shown in this subsection, and used in the next sections.

From the magnetic vector potential, the magnetic flux density follows with equation (2.10) ($\vec{B} = \nabla \times \vec{A}$). For a two-dimensional field, this equation can be worked out to

$$\vec{B} = -\vec{i}_z \times \nabla A_z \quad (2.20)$$

From this equation, it can be concluded that the lines of magnetic flux density are perpendicular to the gradient of A_z . Therefore, the lines of magnetic flux density can be plotted as the lines of constant magnetic vector potential (or the equipotential lines of the magnetic vector potential).

2.3 The magnets

This section describes the magnetic field produced by the magnets. This magnetic field is calculated, while the stator currents and the current density in the damper cylinder are zero.

A description of the permanent magnetization of the magnets in cylindrical coordinates is given in subsection 2.3.1. In subsection 2.3.2, this description is used to calculate the magnetic field of the magnets.

2.3.1 The permanent magnetization in cylindrical coordinates

This subsection describes the permanent magnetization of the magnets in cylindrical coordinates. Figure 2.4a shows a four-pole permanent-magnet machine ($p=2$), the rotor of which is partly covered with rectangular permanent-magnet blocks.

The permanent magnetization of the magnets is M_{pm} . To relate this permanent magnetization to the data provided by magnet manufacturers, it is mentioned that

- it is equal to the remanence of the magnets divided by the magnetic permeability in vacuum μ_0 , and

- for magnets with a relative magnetic permeability $\mu_{rm} = 1$ (as assumed in section 2.1), it is also equal to the coercivity or the coercive force of the magnets. For more information on the properties and the production of permanent magnet materials, see [Cam 94], [Mil 89] and [Ådn 91].

The magnets may be magnetized before they are placed in the machine, so that their permanent magnetization is perpendicular to the surface of the magnets. The magnets may also be magnetized after they are placed in the machine, which is easier with regard to the manufacturing of the machine. In this case, it is more difficult to find out the exact direction of the permanent magnetization, but its most important component is the radial component.

Because a cylindrical coordinate system is used, a description of the permanent magnetization in cylindrical coordinates is necessary. As mentioned in section 2.1, it is assumed that the magnet blocks can be represented by the magnet pole arcs of figure 2.4b. The magnet pole arcs are mounted on the rotor surface. The thickness of these magnet pole arcs is $l_m = r_m - r_r$. As expressed by equation (2.2), the permanent magnetization of the magnet pole arc is assumed to have only a radial component, and to be inversely proportional to the radius: $M_{pr} = M_{pm} r_r / r$.

The assumption that the rectangular magnet blocks can be replaced by these magnet pole arcs is reasonable, because the product of the magnet area of a pole and the permanent magnetization is equal in both situations. In the situation with magnet blocks (figure 2.4a), the area of the magnets of a pole and their permanent magnetization are both independent of the radius r (also inside the magnets). The product of the magnet area of a pole and the permanent magnetization is $2l_s r_r \alpha_m M_{pm}$, where l_s is the stack length of the machine. In the situation with the magnet pole arcs (figure 2.4b), the area of a pole arc is proportional to the radius, and the permanent magnetization is inversely

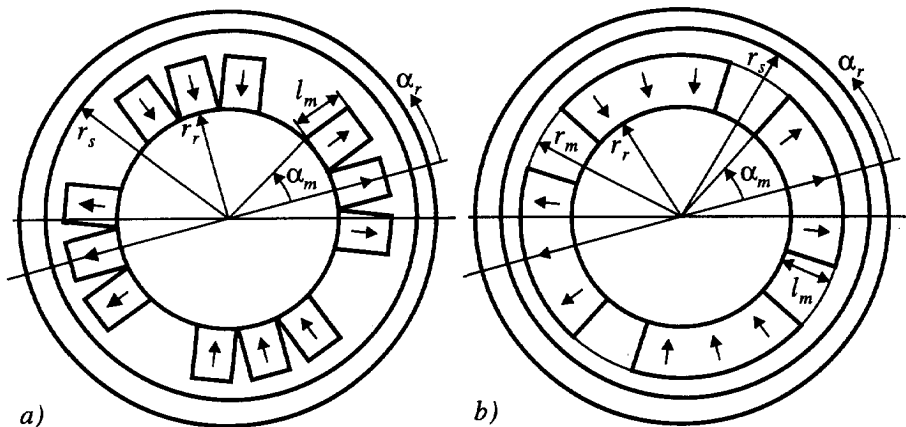


Figure 2.4: Section of a four-pole permanent-magnet machine a) with rectangular magnet blocks, and b) with magnet pole arcs. The arrows indicate the direction of the magnetization.

proportional to the radius. The product of the magnet area of a pole arc and the permanent magnetization of equation (2.2) is $2l_s r_r \alpha_m M_{pm}$, which is equal to the value of this product in the real situation.

By using these magnet pole arcs, the variation of the magnetic flux density at the stator surface resulting from the different magnet blocks is ignored.

Often, the magnet pole arcs do not cover the whole rotor surface. In this case, there are air spaces between the magnet pole arcs. These air spaces are treated as magnet arcs without magnetization. This is allowed, because magnets without magnetization are assumed to have the same electromagnetic properties as air.

On the interval $-\pi/(2p) < \alpha_r \leq 3\pi/(2p)$, the radial component of permanent magnetization $M_{pr}(r, \alpha_r)$ can be written as

$$M_{pr}(r, \alpha_r) = \begin{cases} M_{pm} \frac{r_r}{r} & \text{when } -\alpha_m < \alpha_r < \alpha_m \\ -M_{pm} \frac{r_r}{r} & \text{when } \frac{\pi}{p} - \alpha_m < \alpha_r < \frac{\pi}{p} + \alpha_m \\ 0 & \text{everywhere else on } -\pi/(2p) < \alpha_r \leq 3\pi/(2p) \end{cases} \quad (2.21)$$

In the next subsection, this permanent magnetization is used to calculate the magnetic field of the magnets. Because the solution of the partial differential equation for the magnetic vector potential has the form of a Fourier series, this permanent magnetization is also written as a Fourier series:

$$M_{pr}(r, \alpha_r) = \sum_{k=1,3,5,\dots}^{\infty} \hat{M}_{p,k} \frac{r_r}{r} \cos(kp\alpha_r) ; \quad (2.22)$$

$$\hat{M}_{p,k} = \frac{2p}{\pi} \int_{-\alpha_m}^{\alpha_m} M_{pm} \cos(pk\alpha) d\alpha = \frac{4}{k\pi} M_{pm} \sin(kp\alpha_m)$$

So, the permanent magnetization, which is a rectangular function of the rotor coordinate, is written as a series of permanent magnetizations, which are sinusoidal functions of the rotor coordinate. These sinusoidal functions are called space harmonics. The pole angle of these space harmonics $\alpha_{p,k}$ is introduced for use in the rest of this thesis as

$$\alpha_{p,k} = \frac{\pi}{pk} \quad (2.23)$$

Later in this chapter, time harmonics will also be introduced. These are present because of the rectifier. Furthermore, different references use different terms for the various components of Fourier series [Kwa 91], [IEC 85], [IEE 72]. To avoid confusion, it is noted here which terms are used in this thesis. A Fourier series of space harmonics is divided into a fundamental space harmonic ($k=1$) and higher space harmonics ($k \geq 2$). A Fourier series of time harmonics is divided into a constant component, a fundamental time harmonic and higher time harmonics.

2.3.2 The magnetic field of the magnets

This subsection describes the magnetic field which is produced by the magnets. The magnetic field is calculated by solving the partial differential equation for the magnetic vector potential in two regions:

- 1) the air-gap region, called region I ($r_m < r < r_s$), and
- 2) the magnet region, called region II ($r_r < r < r_m$).

Firstly, the permanent magnetization derived in subsection 2.3.1 is substituted into the partial differential equation for the magnetic field. Subsequently, the complete solution of the partial differential equation is calculated.

Substitution of the permanent magnetization

First, the permanent magnetization derived in the previous subsection (equation (2.22)) is substituted in the partial differential equation for the magnetic vector potential (equation (2.13)). It is also taken that the current density J_z in the magnets is zero. The result is

$$\nabla^2 A_z(r, \alpha_r) = \sum_{k=1,3,5,\dots}^{\infty} \frac{pk r_r}{r^2} \mu_0 \hat{M}_{p,k} \sin(pk \alpha_r) \quad (2.24)$$

It is noted that the Fourier series on the right side of this equation is not convergent. However, it is believed that the expressions derived in the rest of this section are reliable for the following reason. When the magnetic field is calculated by solving the partial differential equation for the scalar magnetic potential, it is not necessary to use non-converging Fourier series, and the results are the same. In this case, the right side of the partial differential equation does not contain the curl of the permanent magnetization (as equation (2.13)), but its divergence, which does not exist at a surface where a boundary condition is applied. Besides, this problem exists because the permanent magnetization is mathematically described as a discontinuous function of the rotor coordinate (in equation (2.21)), while in reality, it does not change so abrupt.

For the magnetic vector potential resulting from the magnets, a satisfying expression for the general solution is given by

$$A_z(r, \alpha_r) = \sum_{k=1,3,5}^{\infty} \left\{ A_{1,k} r^{pk} + A_{2,k} r^{-pk} + r_r \frac{\mu_0 \hat{M}_{p,k}}{pk} \right\} \sin(pk \alpha_r) \quad (2.25)$$

The constants $A_{1,k}$ and $A_{2,k}$ are determined from the boundary conditions.

As shown earlier, the magnetic vector potential in the air gap above the magnets is described by equation (2.14). Equation (2.15) gives a satisfying expression for the general solution of this partial differential equation.

The boundary conditions

Subsection 2.2.2 describes the boundary conditions. Ampère's continuity condition, expressed by equation (2.18), is applied to the three boundaries, namely the stator

surface, the rotor surface and the magnet surface. This results in three boundary conditions:

$$H_{am,I}(r_s, \alpha_r) = 0 \quad (2.26)$$

$$H_{am,II}(r_r, \alpha_r) = 0 \quad (2.27)$$

$$H_{am,I}(r_m, \alpha_r) = H_{am,II}(r_m, \alpha_r) \quad (2.28)$$

The magnetic flux continuity condition, expressed by equation (2.19), is applied to the magnet surface:

$$B_{m,II}(r_m, \alpha_r) = B_{m,I}(r_m, \alpha_r) \quad (2.29)$$

With these four boundary conditions, the partial differential equation can be solved.

The solution of the partial differential equation

The general solution of the partial differential equation is given by equation (2.15) for the air-gap region, and (2.25) for the magnet region. For both regions, the general solution is substituted in equation (2.10) ($\vec{B} = \nabla \times \vec{A}$) to determine the magnetic flux density. From this, the magnetic field strength is determined by using $\vec{B} = \mu_0 \vec{H}$ in the air-gap region, and $\vec{B} = \mu_0 (\vec{H} + \vec{M})$ (equation (2.8)) in the magnet region. In the resulting expressions for the magnetic flux density and the magnetic field strength, the four boundary conditions are used. The resulting expression for the magnetic vector potential in the air-gap region (region I) is given by

$$\begin{aligned} A_{zm,I}(r, \alpha_r) &= \sum_{k=1,3,5,\dots}^{\infty} \frac{(r_s^{2pk+r_s^{2pk}})(r_m^{2pk}-r_r^{2pk})r_r \mu_0 \hat{M}_{p,k}}{2(r_s^{2pk}-r_r^{2pk})r_m^{pk}r^{pk}} \sin(pk\alpha_r) \\ &= \sum_{k=1,3,5,\dots}^{\infty} \frac{\left(1 + \left(\frac{r}{r_s}\right)^{2pk}\right) \left(1 - \left(\frac{r_r}{r_m}\right)^{2pk}\right)}{\left(1 - \left(\frac{r_r}{r_s}\right)^{2pk}\right) \left(\frac{r}{r_m}\right)^{pk}} \frac{r_r \mu_0 \hat{M}_{p,k}}{2pk} \sin(pk\alpha_r) \end{aligned} \quad (2.30)$$

This equation and many other expressions in the rest of this thesis contain terms with radii to the power of pk or $2pk$. These expressions may be written in two different ways, as is done in this equation. In the rest of this thesis, the first form is used, but for the accurate numerical evaluation of these expressions, the second form has to be used.

Using equation (2.10) ($\vec{B} = \nabla \times \vec{A}$), the radial component of the magnetic flux density in the air-gap region is obtained from equation (2.30) as

$$B_{rm,I}(r, \alpha_r) = \sum_{k=1,3,5,\dots}^{\infty} \frac{(r_s^{2pk+r_s^{2pk}})(r_m^{2pk}-r_r^{2pk})r_r}{2(r_s^{2pk}-r_r^{2pk})r_m^{pk}r^{pk+1}} \mu_0 \hat{M}_{p,k} \cos(pk\alpha_r) \quad (2.31)$$

The magnetic vector potential in the magnet region (region II) is given by

$$A_{zm,II}(r, \alpha_r) = \sum_{k=1,3,5,\dots}^{\infty} \left(1 - \frac{(r_s^{2pk} + r_r^{2pk})(r_s^{2pk} - r_m^{2pk})}{2(r_s^{2pk} - r_r^{2pk})r_m^{pk}r^{pk}} \right) r_r \frac{\mu_0 \hat{M}_{p,k}}{pk} \sin(pk\alpha_r) \quad (2.32)$$

Using equation (2.10) ($\vec{B} = \nabla \times \vec{A}$), the radial component of the magnetic flux density in the magnet region is obtained as

$$B_{m,II}(r, \alpha_r) = \sum_{k=1,3,5,\dots}^{\infty} \left(1 - \frac{(r_s^{2pk} + r_r^{2pk})(r_s^{2pk} - r_m^{2pk})}{2(r_s^{2pk} - r_r^{2pk})r_m^{pk}r^{pk}} \right) r_r \mu_0 \hat{M}_{p,k} \cos(pk\alpha_r) \quad (2.33)$$

Only the radial component of the magnetic flux density is given explicitly, and not the tangential component. This is done because only the radial component is required in chapter 3, where the no-load voltages are calculated.

Figures 2.5, 2.6, and 2.7 illustrate the meaning of these equations for the magnetic field of the magnets. The fields in these pictures are calculated for the test model with the characteristics mentioned in appendix A, section A.1. Figure 2.5 depicts the radial component of the magnetic flux density in the air-gap region and the magnet region for one pole. Figure 2.6 gives the amplitudes of the space harmonics of the radial component of the magnetic flux density $\hat{B}_{m,k}$ at the rotor and the stator surface. Figure 2.7 depicts the lines of the magnetic flux density in the air gap and the magnets for one pole.

Three striking details in these figures are:

- 1) According to figure 2.5, the magnetic flux density at radius $r=r_r$ in the magnet is higher at the sides of the magnet than in the centre. This is also visible in figure 2.7, where there are more field lines at the sides of the magnets than in the centre. This is so because in the centre of the magnet, there is only flux crossing the air gap, while at the sides of the magnet, there is flux returning to the rotor besides the flux crossing the air gap, as can be seen in figure 2.7.
- 2) According to figure 2.5, the magnetic flux density at the stator surface is smooth, and the increase of the magnetic flux density at the sides of the magnets has disappeared, for the following reason. The flux paths of the space harmonics with small pole angles mainly close in the air gap, and do not reach the stator, because in this way, the flux paths are shorter than when they cross the air gap. Figure 2.6 affirms that the smaller the pole angle of a space harmonic of the magnetic field, the less it crosses the air gap.
- 3) In figure 2.5, near the sides of the magnet pole arc, a small ripple on the magnetic flux density is visible. In reality this ripple is not present, it is caused by the Gibb's phenomenon [Kwa 91]. This phenomenon says that near the discontinuities (so near the sides of the magnets), the Fourier series always has a truncation error.

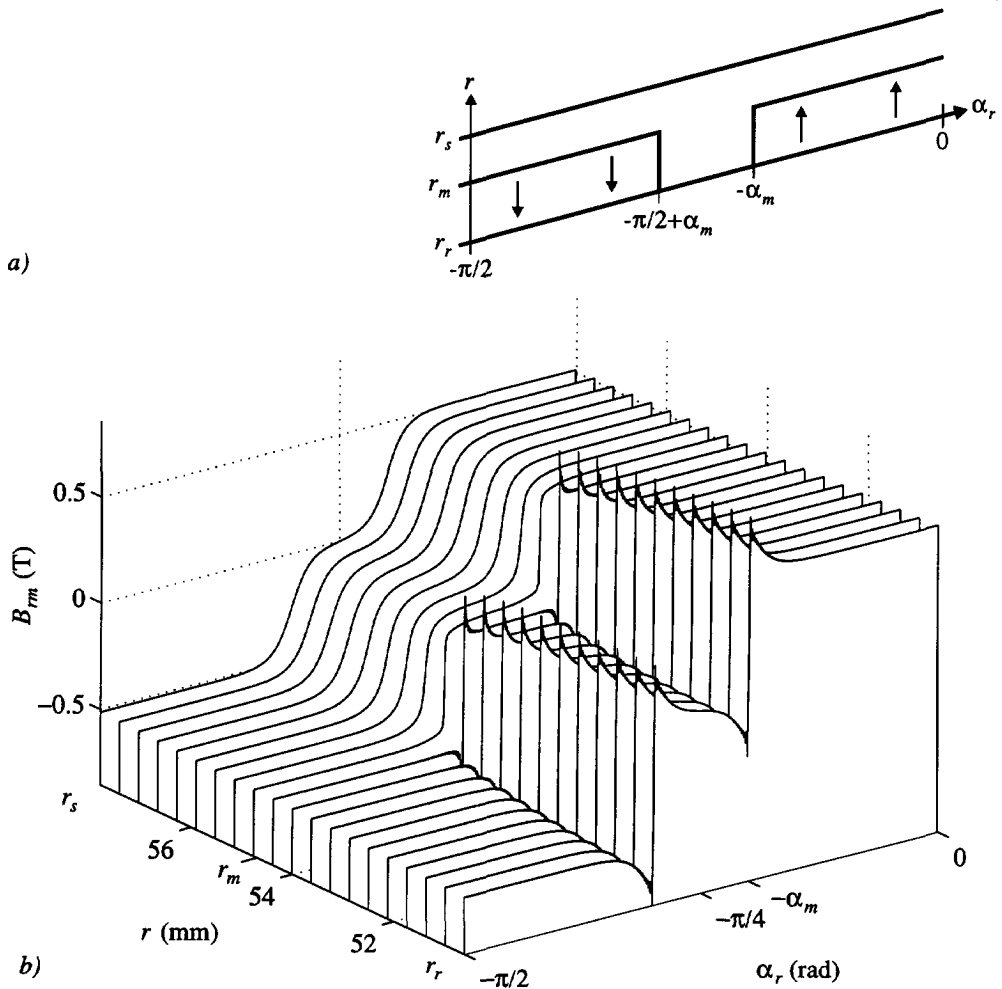


Figure 2.5: a) A pole pitch of the air gap and the magnets as a function of the rotor coordinate α_r . b) The radial component of the magnetic flux density produced by the magnets B_{rm} as a function of the rotor coordinate α_r , at different radii in the air gap of the test model ($p=2$) on the same pole pitch.

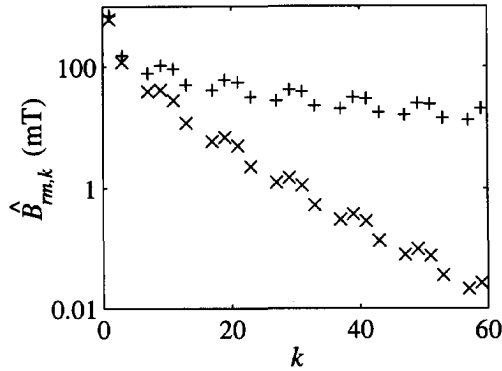


Figure 2.6: Amplitudes of the space harmonics of the radial component of the magnetic flux density produced by the magnets $\hat{B}_{rm,k}$ at the rotor surface (+) and at the stator surface (x) of the test model as a function of the space harmonic number k .

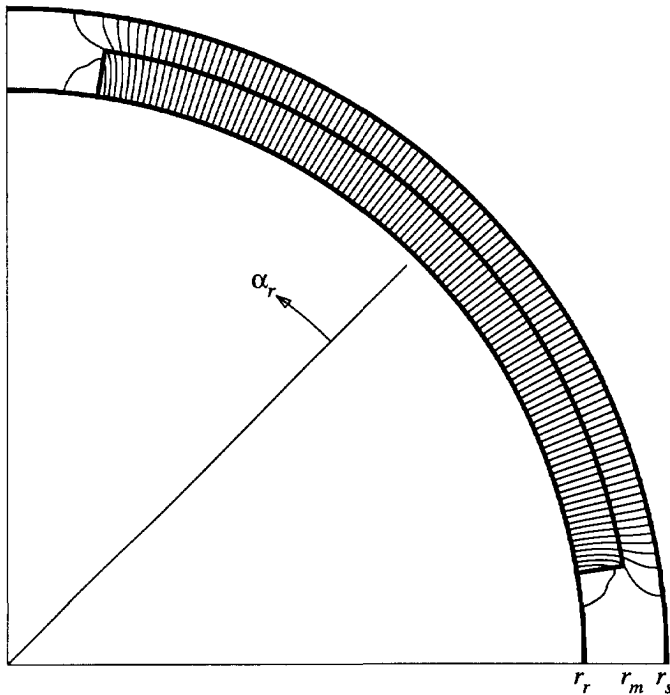


Figure 2.7: The lines of magnetic flux density produced by the magnets in the air gap and the magnet pole arc of the test model ($p=2$).

2.4 The stator

This section describes the magnetic field produced by the stator currents. This magnetic field is calculated, while the permanent magnetization of the magnets and the current density in the damper cylinder are zero.

To calculate the magnetic field of the stator currents, a description of the surface current density of the stator is necessary, which is given in subsection 2.4.1. In subsection 2.4.2, this is used to calculate the magnetic field.

2.4.1 The stator surface current density

This subsection describes the surface current density at the stator surface representing the stator currents. Firstly, the surface current density of stator phase a is derived. This is done by means of a description of the spatial distribution of the winding. Subsequently, the surface current density of a three-phase stator winding is calculated. It is also shown how travelling waves of surface current density arise.

The surface current density of stator phase a

To calculate the surface current density of phase a , first the winding distribution (or the number of conductors per radian, as introduced in [Sle 92]) of phase a n_{sa} is considered. The reference axis of this winding lays at stator coordinate $\alpha_a = 0$. As mentioned in section 2.1, it is assumed that this winding is distributed so that $n_{sa}(\alpha_s - \pi/p) = -n_{sa}(\alpha_s)$ and $n_{sa}(\alpha_s) = -n_{sa}(-\alpha_s)$ are valid. Under these assumptions, the winding distribution $n_{sa}(\alpha_s)$ can be expressed as the following Fourier series:

$$n_{sa}(\alpha_s) = \sum_{k=1,3,5,\dots}^{\infty} n_{sa,k}(\alpha_s); \quad (2.34)$$

$$n_{sa,k}(\alpha_s) = \frac{1}{2} N_{s,k} \sin(pk\alpha_s)$$

In this equation, $N_{s,k}$ is the number of turns of the k th space harmonic of the winding distribution, as appears from

$$pk \int_0^{\pi/(pk)} n_{sa,k}(\alpha_s) d\alpha_s = pk \int_0^{\pi/(pk)} \frac{1}{2} N_{s,k} \sin(pk\alpha_s) = N_{s,k} \quad (2.35)$$

As shown in appendix B, this number of turns of the k th space harmonic is related to the actual number of turns N by

$$N_{s,k} = \frac{4}{\pi} k_{w,k} N \sin\left(\frac{1}{2}k\pi\right) \quad (2.36)$$

where $k_{w,k}$ is the winding factor for the k th space harmonic of the actual winding.

It should be noted that the number of turns $N_{s,k}$ may be negative for some space harmonics. If the space harmonics of the winding distribution were expressed with different reference axes, all numbers of turns could be chosen as positive, because $N_{s,k} \sin(pk\alpha_s) = -N_{s,k} \sin(pk(\alpha_s - \pi/p))$ is valid for odd k . Some space harmonics would have the reference axis at $\alpha_a = 0$, others at $\alpha_a = \pi/p$. Because $\alpha_a = 0$ was chosen as the reference axis of all space harmonics of the winding distribution, the number of turns of the k th space harmonic $N_{s,k}$ may be negative. However, the use of negative numbers of turns does not change anything in the rest of the derivation.

The introduced winding distribution is negative at several places on the stator surface. The meaning of a negative winding distribution becomes clear after the calculation of the surface current density. When the winding distribution (or the number of conductors per radian) n_{sa} is divided by the stator radius r_s , the number of conductors per meter at the stator surface is obtained. Multiplication of this number of conductors per meter by the current i_{sa} results in the surface current density of phase a K_{sa} :

$$K_{sa}(\alpha_s) = n_{sa}(\alpha_s) \frac{i_{sa}}{r_s} = \sum_{k=1,3,5,\dots}^{\infty} K_{sa,k}(\alpha_s) ; \tag{2.37}$$

$$K_{sa,k}(\alpha_s) = \hat{K}_{sa,k} \sin(pk\alpha_s) = \frac{N_{s,k}}{2r_s} i_{sa} \sin(pk\alpha_s)$$

In this equation, the winding distribution of equation (2.34) was used. A positive surface current density flows in the positive z -direction, which means that the current flows from the plane of the drawing upwards. A negative surface current density means that the current flows in the opposite direction.

Figure 2.8a gives as an example the surface current density of a two-pole machine ($p = 1$). Figures 2.8b and 2.8c depict the fundamental space harmonic and the third space harmonic of this surface current density. Figure 2.8d depicts the sum of the fundamental space harmonic and the third space harmonic of the surface current density. If the sum of all space harmonics would be drawn, the result would be the surface current density of figure 2.8a.

It should be noted that the surface current density is an infinitesimal thin layer on the surface. So, the thickness of the blocks representing the surface current densities does not mean that the surface current density has a thickness, but it is an indication of the value of the surface current density at that stator coordinate.

The surface current density of a three-phase stator

When a current flows in more stator phases, the total surface current density can simply be calculated by adding the surface current densities of the different phases. The winding distributions of phases b and c are equal to the winding distribution of phase a , except for an angular shift of their reference axes, which lay at $\alpha_b = 2\pi/(3p)$ and $\alpha_c = 4\pi/(3p)$ respectively, as illustrated in figure 2.9.

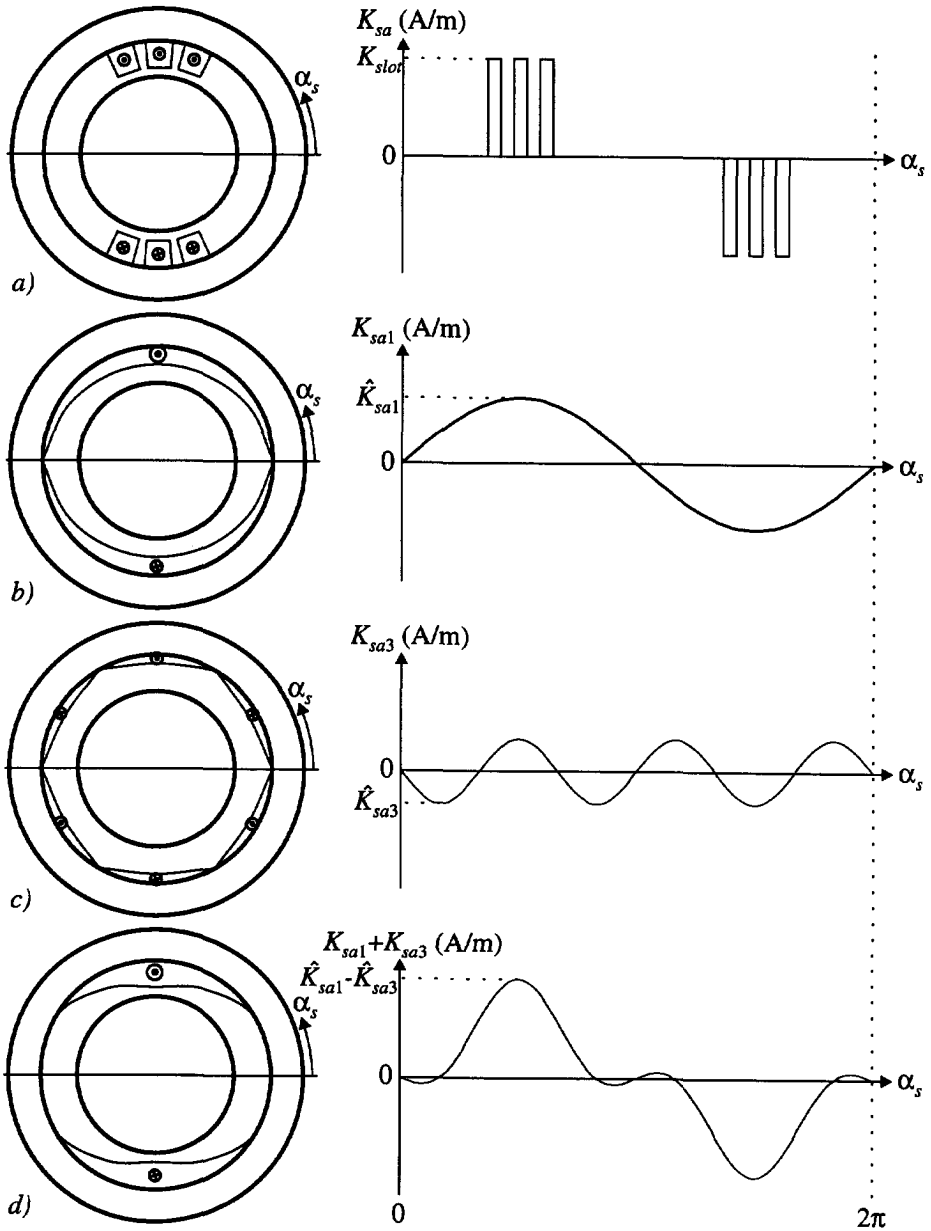


Figure 2.8: Surface current density of phase a, a) total, b) fundamental space harmonic, c) third space harmonic, d) sum of the fundamental and the third space harmonic. The surface current density is an infinitesimal thin layer on the stator surface.

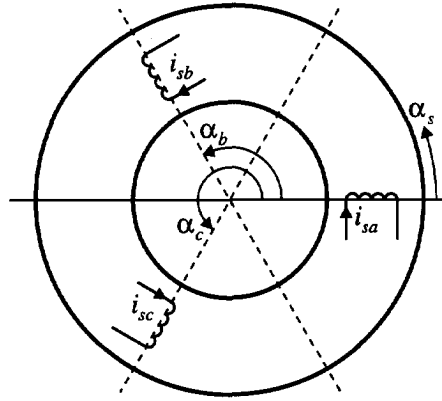


Figure 2.9: A schematic drawing of a three-phase stator with one pole pair ($p=1$).

Using this, the k th space harmonic of the surface current density of a three-phase stator is calculated as

$$\begin{aligned}
 K_{s,k}(\alpha_s) &= K_{sa,k}(\alpha_s) + K_{sb,k}(\alpha_s) + K_{sc,k}(\alpha_s) \\
 &= \frac{1}{r_s} \{ i_{sa} n_{sa,k}(\alpha_s) + i_{sb} n_{sb,k}(\alpha_s) + i_{sc} n_{sc,k}(\alpha_s) \} \\
 &= \frac{N_{s,k}}{2r_s} \left\{ i_{sa} \sin(pk\alpha_s) + i_{sb} \sin\left(pk\left(\alpha_s - \frac{2\pi}{3p}\right)\right) + i_{sc} \sin\left(pk\left(\alpha_s - \frac{4\pi}{3p}\right)\right) \right\}
 \end{aligned} \tag{2.38}$$

To clarify the meaning of the surface current density of equation (2.38), the surface current density of a three-phase stator is calculated. This is done for the set of stator currents flowing when the machine is in steady-state and when it is loaded with a rectifier. This set is written as a Fourier series:

$$\begin{bmatrix} i_{sa} \\ i_{sb} \\ i_{sc} \end{bmatrix} = \sum_{n=-\infty}^{\infty} \hat{i}_{s,6n+1} \begin{bmatrix} \cos((6n+1)\omega_1 t - \varphi_{6n+1}) \\ \cos((6n+1)(\omega_1 t - \frac{2\pi}{3}) - \varphi_{6n+1}) \\ \cos((6n+1)(\omega_1 t - \frac{4\pi}{3}) - \varphi_{6n+1}) \end{bmatrix} \tag{2.39}$$

where ω_1 is the electrical angular frequency of the fundamental time harmonic.

In this equation it was taken that the currents do not contain

- even time harmonics because there is half wave symmetry,
- time harmonics of which the harmonic number is an integer multiple of three because there is no star-point connection.

It should be noted that this equation is also meaningful for $n < 0$, because for a certain n , this equation represents the $|6n+1|$ th time harmonic.

The k th space harmonic of the surface current density of a three-phase stator is obtained by substitution of these currents in (2.38), and is given by

$$K_{s,k}(\alpha_s, t) = \sum_{n=-\infty}^{\infty} K_{s,k,6n+1}(\alpha_s, t) ;$$

$$K_{s,k,6n+1}(\alpha_s, t) = \begin{cases} \frac{3N_{s,k}}{4r_s} \hat{i}_{s,6n+1} \sin(pk\alpha_s - (6n+1)\omega_1 t + \varphi_{6n+1}) & \text{for } k=1,7,13,.. \\ 0 & \text{for } k=3,9,15,.. \\ \frac{3N_{s,k}}{4r_s} \hat{i}_{s,6n+1} \sin(pk\alpha_s + (6n+1)\omega_1 t - \varphi_{6n+1}) & \text{for } k=5,11,17,.. \end{cases} \quad (2.40)$$

For $k=3,9,15,..$, the space harmonics of this surface current density are zero. For these space harmonics, the arguments of the sinuses of the surface current densities of the three phases are equal, which is seen by substituting $k=3,9,15,..$ in equation (2.38). Therefore, the sum of the surface current densities of the three phases is zero when the sum of the stator currents is zero. This is the case for the stator currents of equation (2.39), and this is also the case if there is no star-point connection.

For $k=1,7,13,..$, the space harmonics of the surface current density of equation (2.40) are maximum when

$$pk\alpha_s - (6n+1)\omega_1 t + \varphi_{6n+1} = \frac{\pi}{2} \quad \Rightarrow \quad \alpha_s = \frac{(6n+1)\omega_1}{pk} t + \frac{\pi - 2\varphi_{6n+1}}{2pk} \quad (2.41)$$

This shows that these space harmonics rotate in the positive angular direction for $n \geq 0$, and in the negative angular direction for $n < 0$. This also shows that the angular velocity is inversely proportional to the space harmonic number k multiplied by the number of pole pairs p . These rotating space harmonics are called travelling waves.

In the same way, it can be seen that for $k=5,11,17,..$, the space harmonics form travelling waves rotating in the negative angular direction for $n \geq 0$, and in the positive angular direction for $n < 0$. Their angular velocity is also inversely proportional to the space harmonic number k multiplied by the number of pole pairs p .

It should be noted that this angular velocity is not equal to the electrical angular frequency experienced at a given place on the stator surface. At a given place at the stator surface at stator coordinate α_s , the angular frequency of the surface current density is $|6n+1|\omega_1$. This is seen if the stator coordinate in equation (2.40) is held constant.

2.4.2 The magnetic field of the stator currents

This subsection describes the magnetic field which is produced by the stator currents. It starts with the boundary conditions following from the surface current density derived in subsection 2.4.1. Next, it gives the complete solution of the partial differential equation.

To make this calculation, it is enough to consider one 'air-gap' region. It is not necessary to separate an air-gap region and a magnet region, because magnets without magnetization are assumed to have the same electromagnetic characteristics as air.

The boundary conditions

Subsection 2.2.2 describes the boundary conditions. Ampère's continuity condition, expressed by equation (2.18), is applied to the two boundaries, namely the stator surface, and the rotor surface:

$$H_{\alpha s}(r_r, \alpha_s) = 0 \tag{2.42}$$

$$H_{\alpha s}(r_s, \alpha_s) = -K_s(\alpha_s) \tag{2.43}$$

In this expression, the surface current density of equation (2.38) is used. With these two boundary conditions, the partial differential equation can be solved.

The solution of the partial differential equation

The general solution of the partial differential equation is given by equation (2.15). This equation is substituted in equation (2.10) ($\vec{B} = \nabla \times \vec{A}$) to determine the magnetic flux density. From this, the magnetic field strength is determined by using $\vec{B} = \mu_0 \vec{H}$. In the resulting expression for the magnetic field strength, the two boundary conditions are used. In this way, the magnetic vector potential is calculated as

$$A_{zs}(r, \alpha_s) = \sum_{k=1,3,5,\dots}^{\infty} \frac{(r^{2pk} + r_r^{2pk})r_s^{pk} \mu_0 N_{s,k}}{(r_s^{2pk} - r_r^{2pk})r^{pk} 2pk} \left\{ i_{sa} \sin(pk\alpha_s) + i_{sb} \sin\left(pk\left(\alpha_s - \frac{2\pi}{3p}\right)\right) + i_{sc} \sin\left(pk\left(\alpha_s - \frac{4\pi}{3p}\right)\right) \right\} \tag{2.44}$$

With equation (2.10) ($\vec{B} = \nabla \times \vec{A}$), the radial component of the magnetic flux density produced by the stator currents is obtained:

$$B_{rs}(r, \alpha_s) = \sum_{k=1,3,5,\dots}^{\infty} \frac{(r^{2pk} + r_r^{2pk})r_s^{pk} \mu_0 N_{s,k}}{(r_s^{2pk} - r_r^{2pk})r^{pk+1} 2} \left\{ i_{sa} \cos(pk\alpha_s) + i_{sb} \cos\left(pk\left(\alpha_s - \frac{2\pi}{3p}\right)\right) + i_{sc} \cos\left(pk\left(\alpha_s - \frac{4\pi}{3p}\right)\right) \right\} \tag{2.45}$$

Only the radial component of the magnetic flux density is given explicitly, because this component is required in chapter 3, where the inductances are calculated.

As at the end of subsection 2.4.1, travelling waves of magnetic flux density arise when a balanced set of three-phase currents flows in the stator phases.

Figures 2.10, 2.11 and 2.12 illustrate the meaning of the equations for the magnetic field of the stator currents. The fields in these figures are calculated for the test model with the characteristics mentioned in appendix A, section A.1. As an example that may occur during three-phase operation, a current of 5 A flows in stator phases *b* and *c*, which are connected in series ($i_{sb} = 5$ A, $i_{sc} = -5$ A), while the current in phase *a* is zero. Figure 2.10 depicts the radial component of the magnetic flux density in the air gap for one pole. Figure 2.11 gives the amplitudes of the space harmonics of the radial component of the magnetic flux density $\hat{B}_{rs,k}$ at the rotor and the stator surface. Figure 2.12 depicts the lines of magnetic flux density in the air gap for one pole.

The surface current density at the stator surface represents the current of six slots. In figure 2.10, this is visible from the six maxima of the magnetic flux density at the stator surface. In a machine with slot openings instead of a smooth stator surface, the magnetic field will be different, mainly for the space harmonics with a small pole angle.

Again it is seen that the space harmonics with a small pole angle hardly cross the air gap: at the rotor surface, the magnetic flux density is smooth.

Because the rotor-removed test is used in subsection 4.3.6, the solution for this situation is also mentioned. When the rotor is removed, only one boundary condition is valid, namely the boundary condition at the stator surface (equation (2.43)). The solution for this situation is obtained by substituting $r_r=0$ in the derived expression for the magnetic vector potential (equation (2.44)).

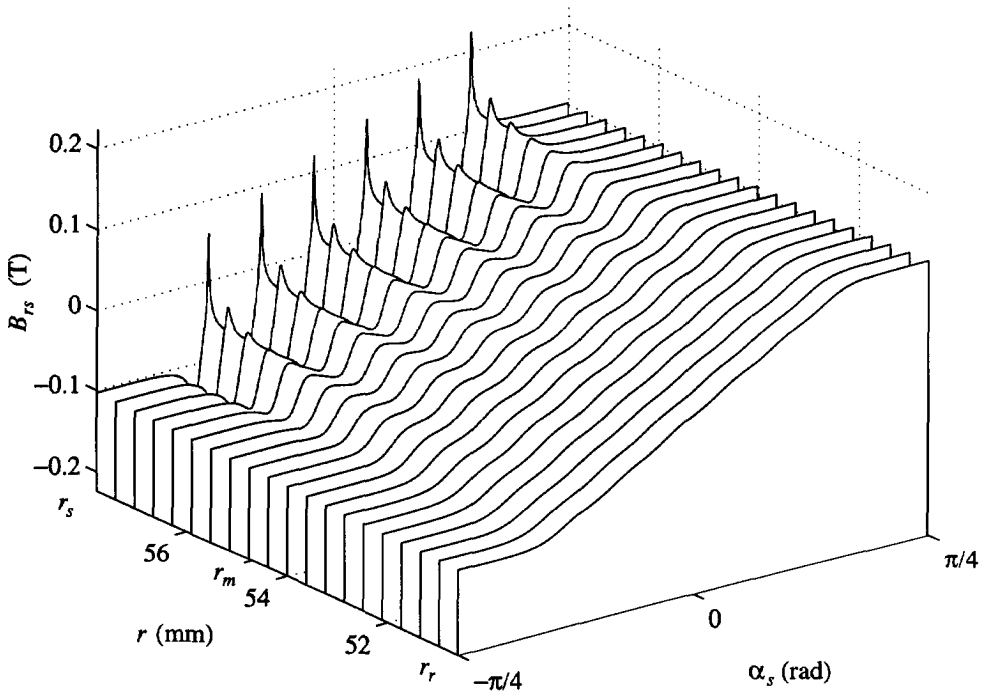


Figure 2.10: The radial component of the magnetic flux density produced by the stator currents B_{rs} as a function of the stator coordinate α_s at different radii. A current flows in stator phases b and c of the test model ($p=2$), while the current in phase a is zero. It can be seen that the surface current density represents the current of six slots.

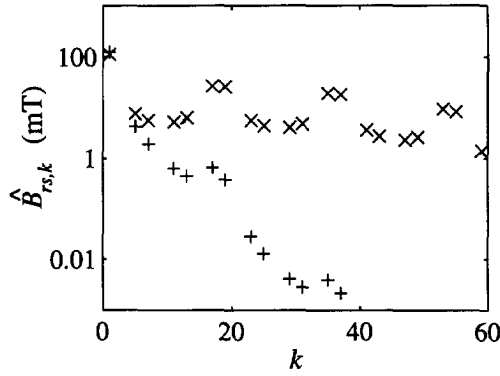


Figure 2.11: Amplitudes of the space harmonics of the radial component of the magnetic flux density produced by the stator currents $\hat{B}_{rs,k}$ at the rotor surface (+) and at the stator surface (x) of the test model as a function of the space harmonic number k .

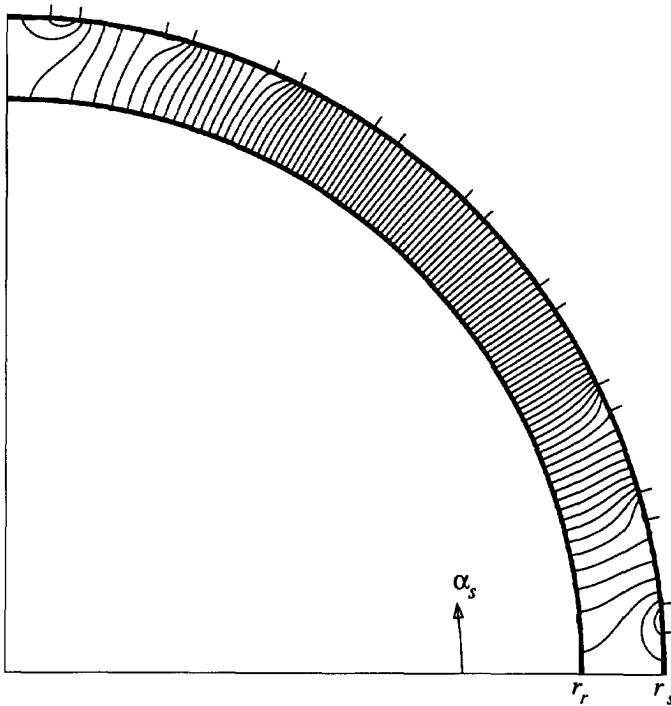


Figure 2.12: The lines of magnetic flux density produced by the stator currents in the air gap of the test model ($p=2$). At the stator surface, the place of the slots is indicated.

2.5 The damper cylinder

This section describes the magnetic field produced by the surface current density of the damper cylinder, which is of course only present in a machine with a damper cylinder. This magnetic field is calculated, while the stator currents and the permanent magnetization of the magnets are zero. The magnetic field is calculated for a given arbitrary surface current density. In section 3.3, the surface current density of the damper cylinder will be determined by deriving the voltage equations.

Before it is possible to make this calculation, a description of the surface current density is necessary, which is given in subsection 2.5.1. In subsection 2.5.2, this is used to calculate the magnetic field.

2.5.1 The surface current density of the damper cylinder

As mentioned in section 2.1, it is assumed that the damper cylinder is so thin that the current density in the damper cylinder can be replaced by a surface current density for the calculation of the magnetic field in the air gap. Furthermore, it is assumed that the surface current density of the damper cylinder K_d only flows in the axial direction, and that $K_d(\alpha_r - \pi/p) = -K_d(\alpha_r)$ is valid. Under these assumptions, the surface current density can be written as the following Fourier series:

$$K_d(\alpha_r) = \sum_{k=1,3,5,\dots}^{\infty} K_{d,k}(\alpha_r) ; \quad (2.46)$$

$$K_{d,k}(\alpha_r) = \hat{K}_{d,k} \sin(pk(\alpha_r - \gamma_k))$$

This surface current density of the damper cylinder can also be considered as a series of damper currents in a series of damper windings. In chapter 3, it will appear that this is useful when the damper voltage equations and the equivalent circuits are derived. To obtain the series of damper currents in the series of damper windings, the k th space harmonic of the surface current density of equation (2.46) is written as

$$K_{d,k}(\alpha_r) = \hat{K}_{d,k} \cos(pk\gamma_k) \sin(pk\alpha_r) - \hat{K}_{d,k} \sin(pk\gamma_k) \cos(pk\alpha_r) \quad (2.47)$$

The two terms on the right side of this equation can be considered as contributions of two sinusoidally distributed windings. For the k th space harmonic, the winding distributions of these two windings are given by

$$\begin{cases} n_{dd,k}(\alpha_r) = \frac{1}{2} N_{d,k} \sin(pk\alpha_r) \\ n_{dq,k}(\alpha_r) = -\frac{1}{2} N_{d,k} \cos(pk\alpha_r) = \frac{1}{2} N_{d,k} \sin(pk(\alpha_r - \frac{\pi}{2pk})) \end{cases} \quad (2.48)$$

The subscripts d and q are used, because the rotor-connected two-phase system is usually

called the dq -system, where d and q mean direct and quadrature respectively. The number of pole-pairs of these winding distributions is proportional to the space harmonic number k . The reference axes are chosen on the interval $0 \leq \alpha_r < 2\pi/(pk)$.

The direct-axis component of this winding distribution is called damper winding d,k . The current in this damper winding is called damper current $i_{dd,k}$. Its reference axis lays at rotor coordinate $\alpha_r = 0$. The quadrature-axis component of this winding distribution is called damper winding q,k . The current in this damper winding is called damper current $i_{dq,k}$. The windings q,k have different spatial reference axes for different k . As depicted in figure 2.13, the reference q -axis $\alpha_{q,k}$ of damper winding q,k lays at rotor coordinate

$$\alpha_{q,k} = \frac{\pi}{2kp} \tag{2.49}$$

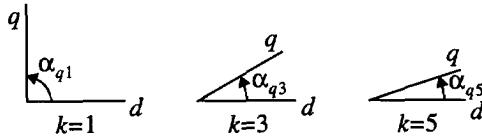


Figure 2.13: The real spatial angle between the reference direct axis and the reference quadrature axis of a two-pole machine ($p=1$) for different values of k .

With the introduced damper currents and damper windings, the surface current density of the damper cylinder can be written as

$$K_d(\alpha_r) = \sum_{k=1,3,5,\dots}^{\infty} K_{d,k}(\alpha_r); \tag{2.50}$$

$$K_{d,k}(\alpha_r) = \frac{N_{d,k}}{2r_d} \left\{ i_{dd,k} \sin(pk\alpha_r) + i_{dq,k} \sin\left(pk\left(\alpha_r - \frac{\pi}{2pk}\right)\right) \right\}$$

To obtain the surface current density of equation (2.46), the damper currents must be given by

$$\begin{bmatrix} i_{dd,k} \\ i_{dq,k} \end{bmatrix} = \frac{2r_d K_{d,k}}{N_{d,k}} \begin{bmatrix} \cos(pk\gamma_k) \\ \sin(pk\gamma_k) \end{bmatrix} \tag{2.51}$$

It should be noted that the number of conductors $N_{d,k}$ can be chosen arbitrarily, as long as the products $i_{dd,k}N_{d,k}$ and $i_{dq,k}N_{d,k}$ do not change.

So, the surface current density of the damper is described by means of a series of damper currents flowing in a series of sinusoidally distributed windings. This will appear to be useful when the damper voltage equations and the equivalent circuits are derived in chapter 3.

2.5.2 The magnetic field of the damper currents

This subsection describes the magnetic field produced by the series of currents in the series of damper windings. It starts with the boundary conditions following from the surface current density derived in subsection 2.5.1. Next, it gives the complete solution of the partial differential equation.

The partial differential equation for the magnetic vector potential has to be solved in two regions:

- 1) the region above the cylinder called region I, ($r_d < r < r_s$), and
- 2) the region below the cylinder called region II, ($r_r < r < r_d$).

It is not necessary to separate the region below the cylinder into two regions for air and magnets, because magnets without magnetization are assumed to have the same electromagnetic properties as air.

The boundary conditions

Subsection 2.2.2 describes the boundary conditions. Ampère's continuity condition, expressed by equation (2.18), is applied to the three boundaries, namely the stator surface, the rotor surface and the cylinder surface:

$$H_{ad,I}(\alpha_r, r_s) = 0 \quad (2.52)$$

$$H_{ad,II}(\alpha_r, r_r) = 0 \quad (2.53)$$

$$H_{ad,I}(\alpha_r, r_m) - H_{ad,II}(\alpha_r, r_m) = K_d(\alpha_r) \quad (2.54)$$

In this expression, the surface current density of equation (2.50) is used.

The magnetic flux continuity condition, expressed by equation (2.19), is applied to the cylinder surface:

$$B_{rd,II}(r_m, \alpha_r) = B_{rd,I}(r_m, \alpha_r) \quad (2.55)$$

With these four boundary conditions, the partial differential equation can be solved.

The solution of the partial differential equation

For both regions, the general solution of the partial differential equation is given by equation (2.15). This equation is substituted in equation (2.10) ($\vec{B} = \nabla \times \vec{A}$) to determine the magnetic flux density. From this, the magnetic field strength is determined by using $\vec{B} = \mu_0 \vec{H}$. In the resulting expressions for the magnetic flux density and the magnetic field strength, the four boundary conditions are used. In this way, the magnetic vector potential in the air gap above the damper cylinder (region I) is calculated as

$$A_{zd,I}(r, \alpha_r) = \sum_{k=1,3,5,\dots}^{\infty} \frac{(r^{2pk+r_s^{2pk}})(r_d^{2pk+r_r^{2pk}}) \mu_0 N_{d,k}}{2(r_s^{2pk}-r_r^{2pk})r_d^{pk}r_r^{pk}} \quad (2.56)$$

$$\left\{ i_{dd,k} \sin(pk\alpha_r) + i_{dq,k} \sin\left(pk\left(\alpha_r - \frac{\pi}{2pk}\right)\right) \right\}$$

With equation (2.10) ($\vec{B} = \nabla \times \vec{A}$), the radial component of magnetic flux density in this region is obtained:

$$B_{rd,I}(r, \alpha_r) = \sum_{k=1,3,5,\dots}^{\infty} \frac{(r_d^{2pk} + r_s^{2pk})(r_d^{2pk} + r_r^{2pk})}{2(r_s^{2pk} - r_r^{2pk})r_d^{pk}r_r^{pk+1}} \frac{\mu_0 N_{d,k}}{2} \left\{ i_{dd,k} \cos(pk\alpha_r) + i_{dq,k} \cos\left(pk\left(\alpha_r - \frac{\pi}{2pk}\right)\right) \right\} \quad (2.57)$$

Below the damper cylinder (region II), the magnetic vector potential is given by

$$A_{zd,II}(r, \alpha_r) = \sum_{k=1,3,5,\dots}^{\infty} \frac{(r_d^{2pk} + r_r^{2pk})(r_d^{2pk} + r_s^{2pk})}{2(r_s^{2pk} - r_r^{2pk})r_d^{pk}r_r^{pk}} \frac{\mu_0 N_{d,k}}{2pk} \left\{ i_{dd,k} \sin(pk\alpha_r) + i_{dq,k} \sin\left(pk\left(\alpha_r - \frac{\pi}{2pk}\right)\right) \right\} \quad (2.58)$$

With equation (2.10) ($\vec{B} = \nabla \times \vec{A}$), the radial component of magnetic flux density in this region is obtained:

$$B_{rd,II}(r, \alpha_r) = \sum_{k=1,3,5,\dots}^{\infty} \frac{(r_d^{2pk} + r_r^{2pk})(r_d^{2pk} + r_s^{2pk})}{2(r_s^{2pk} - r_r^{2pk})r_d^{pk}r_r^{pk+1}} \frac{\mu_0 N_{d,k}}{2} \left\{ i_{dd,k} \cos(pk\alpha_r) + i_{dq,k} \cos\left(pk\left(\alpha_r - \frac{\pi}{2pk}\right)\right) \right\} \quad (2.59)$$

It should be noted that the damper currents $i_{dd,k}$ and $i_{dq,k}$, flowing in the damper windings d,k and q,k , only cause the k th space harmonic of the magnetic flux density.

Only the radial component of the magnetic flux density is given explicitly, because this component is required in chapter 3, where the inductances are calculated.

The meaning of the derived equations is illustrated in figure 2.14. This figure depicts the radial component of the magnetic flux density produced by the damper currents in the air-gap region and the magnet region for one pole. It is calculated for the test model with the characteristics mentioned in appendix A, section A.1. The surface current density of the damper cylinder was chosen as equal to the surface current density at the stator surface when a stator current of 5 A flows through stator phases b and c , which are connected in series ($i_{sb} = 5$ A, $i_{sc} = -5$ A), while the current in phase a is zero. This surface current density was chosen for two reasons.

- 1) In this way, figure 2.14 is comparable to figure 2.10, where the same surface current density is used.
- 2) With this surface current density, figure 2.14 is illustrative. It is seen that the space harmonics with a small pole angle do not cross the air gap: they are present at the damper radius, but at the stator and rotor surface, the magnetic flux density is smooth. With, for example, a sinusoidal surface current density, this would not be visible.

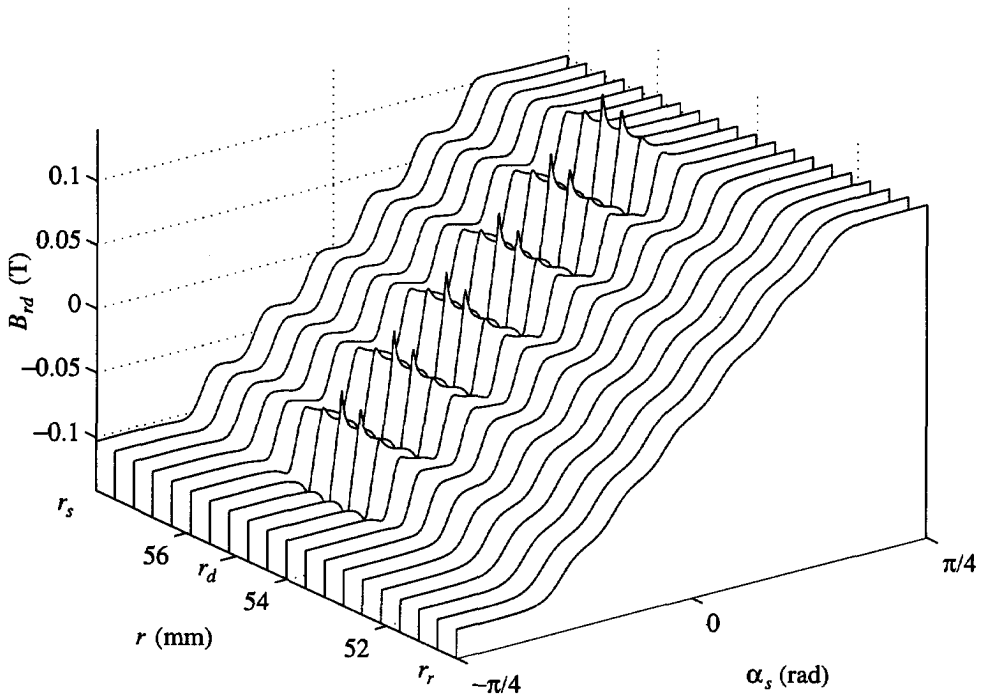


Figure 2.14: The radial component of the magnetic flux density B_{rd} produced by the surface current density of the damper as a function of the angular coordinate at different radii. The surface current density of the damper cylinder was chosen as equal to the surface current density at the stator surface if a current flows through stator phases b and c of the test model ($p=2$), while the current in phase a is zero (compare figure 2.10).

2.6 Summary

This chapter has described the first part of the modelling of the permanent-magnet generator, namely the calculation of the magnetic field in the air gap and the magnets. In later chapters, this magnetic field forms the basis for the derivation of the voltage equations of the generator and for the modelling of the losses in the generator.

To obtain functional expressions for the magnetic field, it has been necessary to use simplifying assumptions. These assumptions have mainly been neglects of effects that hardly influence the magnetic field and effects that influence the magnetic field only locally. The most important assumptions have been that

- the damper cylinder is very thin,
- end effects in the machine are negligible,

- nonlinear effects, such as hysteresis and saturation phenomena, are negligible,
- eddy-currents in the stator iron, the rotor iron and the magnets are negligible,
- the magnetic permeability of iron is infinite,
- the slotting of the stator is negligible, and
- the magnet blocks can be replaced by a magnet pole arc.

Based on these assumptions, the magnetic vector potential in the cylindrical air gap of the permanent-magnet machine has been calculated. This magnetic vector potential is a superposition of the magnetic vector potentials resulting from the permanent magnetization of the magnets, the stator currents, and the damper currents. From this magnetic vector potential, the magnetic field is calculated two-dimensionally.

In chapter 3, these expressions for the magnetic field are used in the derivation of the voltage equations. For this derivation, the radial component of the magnetic flux density at the stator surface and the damper surface is required. For convenience, the radial components of the magnetic flux density in the region between the stator surface and the damper surface are repeated here. The radial component of the magnetic flux density produced by the magnets between the magnet surface and the stator surface is given by equation (2.31):

$$B_{m,r}(r, \alpha_r) = \sum_{k=1,3,5,\dots}^{\infty} \frac{(r_s^{2pk} + r_r^{2pk})(r_m^{2pk} - r_r^{2pk})r_r}{2(r_s^{2pk} - r_r^{2pk})r_m^{pk}r^{pk+1}} \mu_0 \dot{M}_{p,k} \cos(pk\alpha_r) \quad (2.60)$$

The radial component of magnetic flux density of the stator currents is given by equation (2.45):

$$B_{rs}(r, \alpha_s) = \sum_{k=1,3,5,\dots}^{\infty} \frac{(r^{2pk} + r_s^{2pk})r_s^{pk}}{(r_s^{2pk} - r_r^{2pk})r^{pk+1}} \frac{\mu_0 N_{s,k}}{2} \left\{ i_{sa} \cos(pk\alpha_s) + i_{sb} \cos\left(pk\left(\alpha_s - \frac{2\pi}{3p}\right)\right) + i_{sc} \cos\left(pk\left(\alpha_s - \frac{4\pi}{3p}\right)\right) \right\} \quad (2.61)$$

If a damper cylinder is present, the radial component of magnetic flux density produced by the currents in the damper cylinder in the air-gap region is given by equation (2.57):

$$B_{rd,d}(r, \alpha_r) = \sum_{k=1,3,5,\dots}^{\infty} \frac{(r^{2pk} + r_s^{2pk})(r_d^{2pk} + r_r^{2pk})}{2(r_s^{2pk} - r_r^{2pk})r_d^{pk}r^{pk+1}} \frac{\mu_0 N_{d,k}}{2} \left\{ i_{dd,k} \cos(pk\alpha_r) + i_{dq,k} \cos\left(pk\left(\alpha_r - \frac{\pi}{2pk}\right)\right) \right\} \quad (2.62)$$

The current density of the damper is replaced by a series of damper currents flowing in a series of sinusoidally distributed damper windings, which will appear to be useful when the damper voltage equations and the equivalent circuits are derived in chapter 3.

From the illustrations of the calculated magnetic fields, it was concluded that the smaller the pole angle of a space harmonic of the magnetic field, the less it crosses the air gap.

Chapter 3

The voltage equations of the generator

3.1 Introduction

Objective

Chapter 2 has described the first part of the modelling of the generator, namely the calculation of the magnetic field in the air gap and the magnets of the generator. The next part of the derivation of the machine model is the derivation of the voltage equations, which is described in this chapter. In the following chapters, these voltage equations will be extended with models of the most important losses in order to obtain a machine model suitable for the analysis of the generator loaded with a rectifier.

The objective of this chapter therefore is the derivation of voltage equations relating the terminal currents and the terminal voltages of the permanent-magnet machine depicted in figure 3.1. The derivation is based on the expressions for the magnetic flux density derived in chapter 2 and on the machine dimensions and material properties.

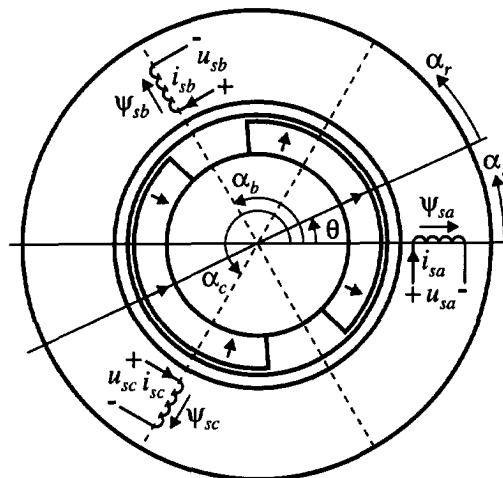


Figure 3.1: A two-pole three-phase permanent-magnet machine with a damper cylinder.

The voltage equations must be valid for the machine with and without a damper cylinder. Further, they must be suitable for the analysis of the machine in two situations:

- 1) during locked-rotor tests, which are used to verify the derived equations, and
- 2) during steady-state operation with rectifier load, which is investigated in this thesis.

Therefore, the voltage equations are transformed into forms which are useful for these two situations.

Outline of the chapter

This chapter starts with the derivation of the stator voltage equation in section 3.2. Next, section 3.3 describes the derivation of the voltage equations representing the damper cylinder. It is shown that useful damper voltage equations can be derived for the series of sinusoidally distributed damper windings introduced in subsection 2.5.1. In section 3.4, the voltage equations are transformed into the two-phase stator-connected $\alpha\beta$ -system and the damper quantities are referred to the stator. This is necessary to eliminate the dependence of the rotor position angle and to obtain simpler equations. Furthermore, in section 3.5, these voltage equations are worked out for the situations considered in the rest of the thesis, namely for steady-state operation with rectifier load and for the locked-rotor tests. Subsequently, section 3.6 describes some locked-rotor tests, which partly verify the derived voltage equations. Section 3.7 concludes with a summary of the results obtained.

Assumptions

The derivation of the voltage equations is based on the equations for the magnetic field derived in chapter 2, so that the assumptions mentioned in section 2.1 are also used in this chapter. Further, the work in this chapter is based on the following assumptions.

- Skin effect in the stator conductors is negligible.
- In section 2.1, it was assumed that end effects are negligible. Consequentially, the resistance and the leakage inductance of the end connections of the damper cylinder (the part of the damper cylinder outside the stack length of the machine l_s , providing a closing path for the damper currents) are neglected.
- For the magnetic flux density in the air gap and the magnets,

$$\vec{B}(r, \alpha_s - \frac{\pi}{p}) = -\vec{B}(r, \alpha_s) \quad (3.1)$$

is valid, as follows from the calculations of the magnetic field in chapter 2.

- The stator coordinate α_s is related to the rotor coordinate α_r by

$$\alpha_s = \alpha_r + \theta \quad (3.2)$$

where θ is the rotor position angle (see figure 3.1).

3.2 The stator voltage equation

In this section, the stator voltage equation is derived. Firstly, subsection 3.2.1 introduces a general expression for the stator voltage equation and a few separations between the contributions to the flux linkage in this equation. Next, subsection 3.2.2 gives an expression for a part of the leakage flux of the stator. Subsection 3.2.3 describes the flux linkages of the stator windings for an arbitrary magnetic flux density in the air gap along the stator surface. The obtained expression is used to calculate the flux linkages of the stator windings due to the magnetic fields of the magnets, the stator currents, and the damper currents in subsections 3.2.4, 3.2.5, and 3.2.6. Subsection 3.2.4 also gives an expression for the no-load voltage of a permanent-magnet machine. In summary, subsection 3.2.7 gives a valuable formulation of the stator voltage equation.

3.2.1 A general expression for the stator voltages

This subsection introduces a general equation for the stator voltages of a three-phase permanent-magnet machine. It also introduces separations between different contributions to the flux linkages in this stator voltage equation.

The general expression for the stator voltages, which follows from the second of Maxwell's equations (Faraday's law), can be written as

$$\vec{u}_s = R_s \vec{i}_s + \frac{d\vec{\Psi}_s}{dt} \quad (3.3)$$

where R_s is the resistance of a stator phase, and where vectors were introduced for the stator voltages, the stator currents and the stator flux linkages:

$$\vec{u}_s = \begin{bmatrix} u_{sa} \\ u_{sb} \\ u_{sc} \end{bmatrix}; \quad \vec{i}_s = \begin{bmatrix} i_{sa} \\ i_{sb} \\ i_{sc} \end{bmatrix}; \quad \vec{\Psi}_s = \begin{bmatrix} \Psi_{sa} \\ \Psi_{sb} \\ \Psi_{sc} \end{bmatrix} \quad (3.4)$$

The resistance R_s of a stator phase is constant when skin effect and effects of temperature are neglected. In section 4.2, the increase of the resistance R_s due to skin effect in the stator conductors will be reconsidered. Furthermore, this thesis does not pay attention to the calculation of this resistance, because it is calculated by conventional methods which are well described in, for example, [Ric 67].

The flux linkage $\vec{\Psi}_s$ of equation (3.3) is separated into two parts, namely:

- 1) the flux linkage due to the air-gap field, and
- 2) the flux linkage due to slot leakage and end-winding leakage fields $\vec{\Psi}_{sl}$.

It should be noted that the air-gap field also includes some leakage, because a part of the air-gap field does not cross the air gap. This leakage is included the air-gap field

calculated in chapter 2, because the magnetic field is calculated two-dimensionally. This leakage is called the air-gap leakage.

Chapter 2 described the air-gap field, which was separated into three contributions, which give three contributions to the flux linkage:

- 1) the flux linkage due to the field of the magnets Ψ_{sm} ,
- 2) the flux linkage due to the field of the stator currents Ψ_{ss} , and
- 3) the flux linkage due to the field of the damper currents Ψ_{sd} .

With the four separations (into flux linkage resulting from leakage, magnets, stator currents, and damper currents), the stator voltage equation is written as

$$\vec{u}_s = R_s \vec{i}_s + \frac{d\Psi_{sr}}{dt} + \frac{d\Psi_{sm}}{dt} + \frac{d\Psi_{ss}}{dt} + \frac{d\Psi_{sd}}{dt} \quad (3.5)$$

This voltage equation can also be used for a machine without damper cylinder; in this case, the flux linkage caused by the damper currents Ψ_{sd} is zero.

In the next subsections, this voltage equation is worked out and quantified.

3.2.2 The leakage flux of the stator

This subsection gives an expression for the flux linkage caused by slot leakage and end-winding leakage Ψ_{sr} . The air-gap leakage is included air-gap field.

Because of the symmetry of the stator and the air gap, the self-inductances of the stator phases due to the leakage fluxes are equal; they are called L_{sra} . For the same reason, the mutual inductances between the different phases due to the leakage fluxes are equal; they are called M_{sraab} . Hence, the leakage flux can be written as

$$\Psi_{sr} = \begin{bmatrix} L_{sra} & M_{sraab} & M_{sraab} \\ M_{sraab} & L_{sra} & M_{sraab} \\ M_{sraab} & M_{sraab} & L_{sra} \end{bmatrix} \vec{i}_s = L_{sr} \vec{i}_s \quad (3.6)$$

The thesis does not pay attention to the calculation of these inductances, because they are calculated with conventional methods, which are well described in, for example, [Ric 67].

3.2.3 The flux linkages of the stator windings

In this subsection, the stator flux linkages are calculated for an arbitrary magnetic flux density along the stator surface satisfying equation (3.1). Firstly, the flux linkage of stator phase a is calculated. Next, the flux linkages of the other stator phases are given.

To obtain an expression for the flux linkage of a stator winding, first the flux linkage of a full-pitch turn is calculated. The turn lays at the stator surface at radius r_s at stator coordinate α' , see figure 3.2. The flux linkage of this full-pitch turn $\Psi_l(\alpha')$ is

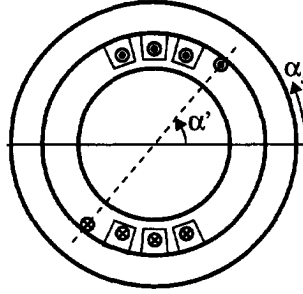


Figure 3.2: A winding distribution and a full-pitch turn at stator coordinate α' .

$$\Psi_i(\alpha') = \int_S \int \vec{B} \cdot d\vec{a} = \int_{\alpha' - \pi/p}^{\alpha'} B_r(r_s, \alpha_s) l_s r_s d\alpha_s \quad (3.7)$$

Equation (3.1) expresses that $\vec{B}(r, \alpha_s - \pi/p) = -\vec{B}(r, \alpha_s)$ is valid in the air gap. With this, the radial component of the magnetic flux density at the stator radius $B_r(r_s, \alpha_s)$ can be expressed as the following Fourier series:

$$B_r(r_s, \alpha_s) = \sum_{l=1,3,5,\dots}^{\infty} B_{r,l}(r_s, \alpha_s) ; \quad (3.8)$$

$$B_{r,l}(r_s, \alpha_s) = \hat{B}_{r,l}(r_s) \cos(pl(\alpha_s - \beta_l))$$

It should be noted that in general both the Fourier coefficient $\hat{B}_{r,l}(r_s)$ and the phase angle β_l of the space harmonics of the magnetic flux density are a function of time.

Using this Fourier series in the expression for the flux linkage of a full-pitch turn (equation (3.7)) results in

$$\Psi_i(\alpha') = 2l_s r_s \sum_{l=1,3,5,\dots}^{\infty} \frac{\hat{B}_{r,l}(r_s)}{pl} \sin(pl(\alpha' - \beta_l)) \quad (3.9)$$

Using this expression, the flux linkage of phase a Ψ_{sa} is calculated as

$$\Psi_{sa} = p \int_0^{\pi/p} n_{sa}(\alpha') \Psi_i(\alpha') d\alpha' \quad (3.10)$$

After substituting equation (2.34) for the winding distribution and equation (3.9) for the flux linkage of a full-pitch turn, this equation can be worked out to

$$\Psi_{sa} = \sum_{k=1,3,5,\dots}^{\infty} \sum_{l=1,3,5,\dots}^{\infty} \frac{l_s r_s N_{s,k}}{2l} \hat{B}_{r,l}(r_s) \int_0^{\pi/p} \cos((k+l)p\alpha' - pl\beta_l) + \cos((k-l)p\alpha' + pl\beta_l) d\alpha' \quad (3.11)$$

Because the harmonics in this equation are all even harmonics, the integral from 0 to π/p is 0, except if $k=l$ is valid. This means that a space harmonic of the magnetic flux density only links with the space harmonic of the winding distribution with the same

pole angle. Hence, the flux linkage of stator phase a Ψ_{sa} resulting from any magnetic flux density satisfying equation (3.1) is given by

$$\Psi_{sa} = \sum_{k=1,3,5,\dots}^{\infty} \Psi_{sa,k} = \sum_{k=1,3,5,\dots}^{\infty} \frac{\pi l_s r_s N_{s,k}}{2pk} \hat{B}_{r,k}(r_s) \cos(pk\beta_k) \quad (3.12)$$

where $\Psi_{sa,k}$ is introduced as the flux linkage of the k th space harmonic of the winding distribution of phase a .

The winding distributions of phases b and c are equal to the winding distribution of phase a , except for an angular shift of their axes, which lay at $\alpha_b = 2\pi/(3p)$ and $\alpha_c = 4\pi/(3p)$ respectively. Therefore, the flux linkages of these windings equal the flux linkage of phase a , except for the angular shift:

$$\Psi_s = \sum_{k=1,3,5,\dots}^{\infty} \Psi_{s,k} = \sum_{k=1,3,5,\dots}^{\infty} \frac{\pi l_s r_s N_{s,k}}{2pk} \hat{B}_{r,k}(r_s) \begin{bmatrix} \cos(pk\beta_k) \\ \cos(pk(\beta_k - \frac{2\pi}{3p})) \\ \cos(pk(\beta_k - \frac{4\pi}{3p})) \end{bmatrix} \quad (3.13)$$

This subsection shows that the flux linkage of the k th space harmonic of the winding distribution is maximum when the reference axis of this space harmonic of the winding distribution coincides with a maximum of the k th space harmonic of the magnetic flux density. In this case, the Fourier coefficient of the k th space harmonic of the magnetic flux density has to be multiplied by a factor $\pi l_s r_s N_{s,k}/(2pk)$ to obtain the flux linkage of the k th space harmonic of the winding distribution. The effect of a spatial angle between the reference axis of the k th space harmonic of the winding distribution and a maximum of the k th space harmonic of the magnetic flux density is the cosine of pk times this spatial angle. In the next three subsections, this is used to calculate the stator flux linkages resulting from the magnetic fields of the magnets, the stator currents, and the damper currents.

3.2.4 The no-load voltage

This subsection describes the stator flux linkages resulting from the magnetic field of the magnets and it introduces the no-load voltage.

In section 2.3, the magnetic flux density in the air gap produced by the magnets was calculated. The radial component of this magnetic flux density at the stator surface follows from equation (2.60) and is written as a function of the stator coordinate by using $\alpha_r = \alpha_s - \theta$ (equation (3.2)):

$$B_{m,r}(r_s, \alpha_s) = \sum_{k=1,3,5,\dots}^{\infty} \frac{(r_m^{2pk} - r_r^{2pk}) r_s^{pk-1} r_r}{(r_s^{2pk} - r_r^{2pk}) r_m^{pk}} \mu_0 \hat{M}_{p,k} \cos(pk(\alpha_s - \theta)) \quad (3.14)$$

In the same way as in subsection 3.2.3, the flux linkages of the stator phases are calculated as (compare equation (3.13))

$$\Psi_{sm} = \sum_{k=1,3,5,\dots}^{\infty} \frac{\pi l_s r_s N_{s,k}}{2pk} \frac{(r_m^{2pk} - r_r^{2pk}) r_s^{pk-1} r_r}{(r_s^{2pk} - r_r^{2pk}) r_m^{pk}} \mu_0 \hat{M}_{p,k} \begin{bmatrix} \cos(pk\theta) \\ \cos(pk(\theta - \frac{2\pi}{3p})) \\ \cos(pk(\theta - \frac{4\pi}{3p})) \end{bmatrix} \quad (3.15)$$

The permanent magnetization of the magnets is constant. Therefore, the flux linkage of the stator phases caused by the magnets Ψ_{sm} only depends on the position and the speed of the rotor. The time derivative of this flux is the no-load voltage \vec{e}_p :

$$\vec{e}_p = \frac{d\Psi_{sm}}{dt} = \begin{bmatrix} e_{pa} \\ e_{pb} \\ e_{pc} \end{bmatrix} = \sum_{k=1,3,5,\dots}^{\infty} \vec{e}_{p,k}; \quad \vec{e}_{p,k} = -\dot{\hat{e}}_{p,k} \begin{bmatrix} \sin(pk\theta) \\ \sin(pk(\theta - \frac{2\pi}{3p})) \\ \sin(pk(\theta - \frac{4\pi}{3p})) \end{bmatrix} \quad (3.16)$$

where

$$\hat{e}_{p,k} = \frac{(r_m^{2pk} - r_r^{2pk}) r_s^{pk} r_r}{(r_s^{2pk} - r_r^{2pk}) r_m^{pk}} \frac{\pi}{2} l_s \Omega N_{s,k} \mu_0 \hat{M}_{p,k} \quad (3.17)$$

In this equation, the mechanical angular velocity of the rotor Ω was introduced as

$$\Omega = \frac{d\theta}{dt} \quad (3.18)$$

3.2.5 The stator flux linkages due to the stator currents

In this subsection, the stator flux linkages which result from the magnetic field of the stator currents are calculated.

In section 2.4, the magnetic flux density in the air gap produced by the stator currents was calculated. The radial component of this magnetic flux density at the stator surface follows from equation (2.61), and is given by

$$B_{rs}(r_s, \alpha_s) = \sum_{k=1,3,5,\dots}^{\infty} \frac{r_s^{2pk} + r_r^{2pk}}{(r_s^{2pk} - r_r^{2pk}) r_s} \frac{\mu_0 N_{s,k}}{2} \left\{ i_{sa} \cos(pk\alpha_s) + i_{sb} \cos(pk(\alpha_s - \frac{2\pi}{3p})) + i_{sc} \cos(pk(\alpha_s - \frac{4\pi}{3p})) \right\} \quad (3.19)$$

In the same way as in subsection 3.2.3, the flux linkages of the stator phases are

calculated as (compare equation (3.13))

$$\Psi_{ss} = \sum_{k=1,3,5,\dots}^{\infty} L_{ss,k} \vec{i}_s ; \quad L_{ss,k} = L_{ss,k} \begin{bmatrix} 1 & \cos(pk\frac{2\pi}{3p}) & \cos(pk\frac{2\pi}{3p}) \\ \cos(pk\frac{2\pi}{3p}) & 1 & \cos(pk\frac{2\pi}{3p}) \\ \cos(pk\frac{2\pi}{3p}) & \cos(pk\frac{2\pi}{3p}) & 1 \end{bmatrix} \quad (3.20)$$

where the self-inductance of the stator $L_{ss,k}$ was introduced as.

$$L_{ss,k} = \frac{\mu_0 \pi l_s N_{s,k}^2 r_s^{2pk} + r_r^{2pk}}{4pk r_s^{2pk} - r_r^{2pk}} \quad (3.21)$$

It should be noted that a part of this flux is air-gap leakage.

3.2.6 The stator flux linkages due to the damper currents

This subsection describes the stator flux linkages resulting from the magnetic field of the damper currents.

In section 2.5, the magnetic flux density in the air gap produced by the damper currents was calculated. The radial component of this magnetic flux density at the stator surface follows from equation (2.62), and is written as a function of the stator coordinate by using $\alpha_r = \alpha_s - \theta$ (equation (3.2)):

$$B_{rd,l}(r_s, \alpha_r) = \sum_{k=1,3,5,\dots}^{\infty} \frac{(r_d^{2pk} + r_r^{2pk}) r_s^{pk-1} \mu_0 N_{d,k}}{(r_s^{2pk} - r_r^{2pk}) r_d^{pk} 2} \left\{ i_{dd,k} \cos(pk(\alpha_s - \theta)) + i_{dq,k} \cos(pk(\alpha_s - \theta - \frac{\pi}{2pk})) \right\} \quad (3.22)$$

In the same way as in subsection 3.2.3, the flux linkages of the stator phases are calculated as (compare equation (3.13))

$$\Psi_{sd} = \sum_{k=1,3,5,\dots}^{\infty} M_{sd,k} \vec{i}_{d,k} ; \quad M_{sd,k} = M_{sd,k} \begin{bmatrix} \cos(pk\theta) & \cos(pk(\theta + \frac{\pi}{2pk})) \\ \cos(pk(\theta - \frac{2\pi}{3p})) & \cos(pk(\theta - \frac{2\pi}{3p} + \frac{\pi}{2pk})) \\ \cos(pk(\theta - \frac{4\pi}{3p})) & \cos(pk(\theta - \frac{4\pi}{3p} + \frac{\pi}{2pk})) \end{bmatrix} \quad (3.23)$$

where the mutual inductance between stator and damper $M_{sd,k}$ was introduced as

$$M_{sd,k} = \frac{\mu_0 \pi l_s N_{s,k} N_{d,k} (r_d^{2pk} + r_r^{2pk}) r_s^{pk}}{4pk (r_s^{2pk} - r_r^{2pk}) r_d^{pk}} \quad (3.24)$$

For a two-pole machine ($p=1$), the angles between the axes of the stator windings and the damper windings are depicted in figure 3.3. The axis of damper winding q,k lays at rotor coordinate $\alpha_{q,k}$, as introduced in equation (2.49) and illustrated in figure 2.13.

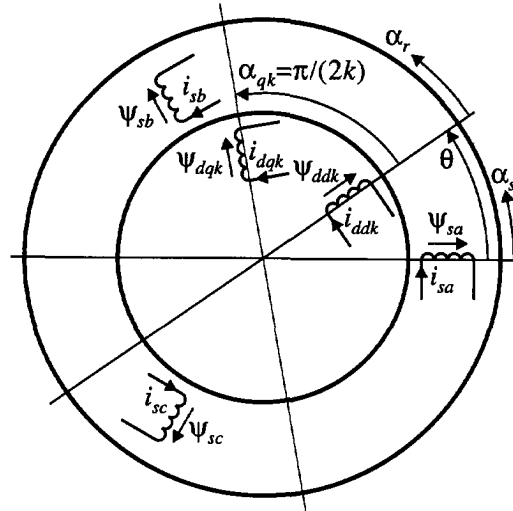


Figure 3.3: The real spatial angles between the axes of the stator and damper windings for a two-pole machine ($p=1$). The damper windings have $2kp$ poles.

3.2.7 Summary

In conclusion, using equations (3.6), (3.16), (3.20), and (3.23), the voltage equation of the stator (equation (3.5)) can be written as

$$\vec{u}_s = \vec{e}_p + R_s \vec{i}_s + L_{so} \frac{d\vec{i}_s}{dt} + \sum_{k=1,3,5,\dots}^{\infty} \left\{ L_{ss,k} \frac{d\vec{i}_s}{dt} + \frac{d}{dt} \{ M_{sd,k} \vec{i}_{d,k} \} \right\} \quad (3.25)$$

3.3 The damper voltage equation

The damper cylinder has no terminals of which the voltages have to be determined. However, the damper currents influence the stator voltages, as appears from stator voltage equation (3.25). Therefore, the aim of this section is to derive equations for the

damper currents which are useful in the calculation of the stator voltages.

First, subsection 3.3.1 shows that the damper cylinder can be modelled as a series of short-circuited sinusoidally distributed damper windings. Next, subsection 3.3.2 introduces a general expression for the voltage equation of these short-circuited sinusoidally distributed damper windings. In subsection 3.3.3, the flux linkages of the damper windings resulting from an arbitrary magnetic flux density along the damper surface are calculated. The expression obtained is used to calculate the resistance of the damper windings in subsections 3.3.4. This expression is also used to calculate the flux linkages of the damper windings due to the magnetic fields of the stator currents and the damper currents in subsections 3.3.5 and 3.3.6 respectively. Subsection 3.3.7 concludes with a valuable formulation of the damper voltage equation.

3.3.1 Modelling of the damper cylinder

In this subsection, the current density in the damper cylinder caused by an arbitrary magnetic flux density along the damper is calculated. From this current density, the damper currents in the sinusoidally distributed damper windings introduced in subsection 2.5.1 are calculated. The resulting expression shows that the damper cylinder can be modelled as a series of short-circuited sinusoidally distributed damper windings.

The current density in the damper cylinder

When the magnetic flux density in the damper cylinder changes, this causes a current density in the damper cylinder. As mentioned in section 2.1, it is possible to calculate the current density two-dimensionally, but here it is assumed that the damper cylinder is so thin that skin effect is negligible. The current density in the damper cylinder is calculated by means of the second of Maxwell's equations, which is given by

$$\nabla \times \vec{E} = -\frac{\partial \vec{B}}{\partial t} \quad (3.26)$$

where \vec{E} is the electric field strength.

In this equation, it is taken that $\vec{E} = \rho_d \vec{J}$, where \vec{J} is the current density, and ρ_d is the resistivity of the damper cylinder. Furthermore, the equation is divided by the resistivity ρ_d and written out for the components in the cylindrical coordinate system. The result is

$$\left\{ \begin{array}{l} \frac{1}{r} \frac{\partial J_z}{\partial \alpha} - \frac{\partial J_t}{\partial z} = -\frac{1}{\rho_d} \frac{\partial B_r}{\partial t} \\ \frac{\partial J_r}{\partial z} - \frac{\partial J_z}{\partial r} = -\frac{1}{\rho_d} \frac{\partial B_t}{\partial t} \\ \frac{1}{r} \frac{\partial(rJ_t)}{\partial r} - \frac{1}{r} \frac{\partial J_r}{\partial \alpha} = -\frac{1}{\rho_d} \frac{\partial B_z}{\partial t} \end{array} \right. \quad (3.27)$$

In this set of equations, two assumptions mentioned taken:

- 1) The z-component of the magnetic flux density is zero as mentioned in section 2.1.
- 2) As mentioned in section 3.1, end effects (the resistance and the inductance of the end connections of the damper cylinder) are neglected. Therefore, the current density in the damper cylinder has only a z-component.

With this, equation (3.27) simplifies to

$$\begin{cases} \frac{1}{r} \frac{\partial J_z}{\partial \alpha} = -\frac{1}{\rho_d} \frac{\partial B_r}{\partial t} \\ -\frac{\partial J_z}{\partial r} = -\frac{1}{\rho_d} \frac{\partial B_t}{\partial t} \end{cases} \quad (3.28)$$

Skin effect is assumed to be negligible. Therefore, the second equation of this set (representing skin effect) is omitted and the current density is not a function of the radial position. The current density in damper cylinder at radius r_d follows from the first equation of this set as

$$\frac{1}{r_d} \frac{\partial J_z(\alpha_r)}{\partial \alpha_r} = -\frac{1}{\rho_d} \frac{\partial B_r(r_d, \alpha_r)}{\partial t} \quad (3.29)$$

From this equation, the current density can be calculated as

$$J_z(\alpha_r) = -\int_{\rho_d}^{\alpha_r} \frac{r_d}{\rho_d} \frac{\partial B_r(r_d, \alpha')}{\partial t} d\alpha' = -\frac{r_d}{\rho_d} \frac{\partial}{\partial t} \int B_r(r_d, \alpha') d\alpha' \quad (3.30)$$

The second step in this equation is allowed because t and α_r are independent.

Equation (3.1) implies that $\vec{B}(r, \alpha_r - \pi/p) = -\vec{B}(r, \alpha_r)$ is valid in the air gap. With this, the radial component of the magnetic flux density at the damper radius $B_r(r_d, \alpha_r)$ can be expressed as the following Fourier series:

$$\begin{aligned} B_r(r_d, \alpha_r) &= \sum_{k=1,3,5,\dots}^{\infty} B_{r,k}(r_d, \alpha_r); \\ B_{r,k}(r_d, \alpha_r) &= \hat{B}_{r,k}(r_d) \cos(pk(\alpha_r - \beta'_k)) \end{aligned} \quad (3.31)$$

Substitution of this Fourier series in equation (3.30) results in

$$\begin{aligned} J_z(\alpha_r) &= -\frac{r_d}{\rho_d} \frac{\partial}{\partial t} \int \sum_{k=1,3,5,\dots}^{\infty} \hat{B}_{r,k}(r_d) \cos(pk(\alpha' - \beta'_k)) d\alpha' \\ &= -\sum_{k=1,3,5,\dots}^{\infty} \frac{r_d}{\rho_d pk} \frac{\partial}{\partial t} \{ \hat{B}_{r,k}(r_d) \sin(pk(\alpha_r - \beta'_k)) + C \} \end{aligned} \quad (3.32)$$

The time derivative of integration constant C in this equation must be zero, because the paths of the current density must close within the cylinder, so that it may be omitted. Furthermore, the rotor coordinate α_r is not considered as a variable, but as a constant. So, $J_z(\alpha_r)$ is the current density at the given position α_r . Therefore, the partial derivative

can be replaced by a normal derivative. With this, the current density can be written as

$$J_z(\alpha_r) = - \sum_{k=1,3,5,\dots}^{\infty} \frac{r_d}{\rho_d p k} \frac{d}{dt} \left\{ \hat{B}_{r,k}(r_d) (\cos(pk\beta'_k) \sin(pk\alpha_r) - \sin(pk\beta'_k) \cos(pk\alpha_r)) \right\} \quad (3.33)$$

According to this equation, the current density is the time derivative of a Fourier series of space harmonics. The time derivative of each space harmonic remains a space harmonic with the same pole angle, because only $\hat{B}_{r,k}(r_d)$ and β'_k are a function of time. This means that a space harmonic of the magnetic flux density causes a space harmonic of the current density with the same pole angle. Therefore, the current density of equation (3.33) can be written as

$$J_z(\alpha_r) = \sum_{k=1,3,5,\dots}^{\infty} J_{z,k}(\alpha_r); \quad (3.34)$$

$$J_{z,k}(\alpha_r) = - \frac{r_d}{\rho_d p k} \left\{ \sin(pk\alpha_r) \frac{d}{dt} (\hat{B}_{r,k}(r_d) \cos(pk\beta'_k)) - \cos(pk\alpha_r) \frac{d}{dt} (\hat{B}_{r,k}(r_d) \sin(pk\beta'_k)) \right\}$$

The currents in the damper cylinder

The space harmonics of the surface current density K_d of the damper cylinder can be calculated by multiplying the space harmonics of the current density $J_z(\alpha_r)$ of equation (3.34) by the thickness of the damper cylinder δ_d :

$$K_{d,k}(\alpha_r) = - \frac{\delta_d r_d}{\rho_d p k} \left\{ \sin(pk\alpha_r) \frac{d}{dt} (\hat{B}_{r,k}(r_d) \cos(pk\beta'_k)) - \cos(pk\alpha_r) \frac{d}{dt} (\hat{B}_{r,k}(r_d) \sin(pk\beta'_k)) \right\} \quad (3.35)$$

As in subsection 2.5.1, the two terms in the right side of this equation are considered as contributions of two damper windings. The winding distributions of these two damper windings are given by equation (2.48). To obtain the k th space harmonic of the surface current density of equation (3.35), the currents in these windings must be given by

$$\vec{i}_{d,k} = \begin{bmatrix} i_{dd,k} \\ i_{dq,k} \end{bmatrix} = - \frac{2\delta_d r_d^2}{\rho_d p k N_{d,k}} \frac{d}{dt} \left\{ \hat{B}_{r,k}(r_d) \begin{bmatrix} \cos(pk\beta'_k) \\ \sin(pk\beta'_k) \end{bmatrix} \right\} \quad (3.36)$$

This equation shows that the current in the damper windings d,k and q,k is only caused by the k th space harmonic of the magnetic flux density. This k th space harmonic of the magnetic flux density only induces a voltage in the damper windings d,k and q,k , because these damper windings are distributed sinusoidally. Therefore, this equation is a formulation of the voltage equation of the short-circuited damper windings d,k and q,k . This shows that the damper cylinder can be modelled as a series of short-circuited sinusoidally distributed damper windings.

Equation (3.36) could be used to calculate the damper currents. However, the rest of this section describes the derivation of a more useful formulation of the damper voltage equation using the flux linkage of the sinusoidally distributed damper windings.

3.3.2 A general expression for the damper voltage equation

This subsection introduces the voltage equation of the short-circuited sinusoidally distributed damper windings using the flux linkages. This voltage equation is given by

$$\vec{0} = \begin{bmatrix} 0 \\ 0 \end{bmatrix} = R_{d,k} \vec{i}_{d,k} + \frac{d\vec{\Psi}_{d,k}}{dt} \quad (3.37)$$

where $R_{d,k}$ is the resistance of the damper windings d,k and q,k .

In chapter 2, the air-gap field was separated into three contributions, which give three contributions to the flux linkage of equation (3.37):

- 1) the flux linkage due to the field of the magnets $\vec{\Psi}_{dm,k}$,
- 2) the flux linkage due to the field of the stator currents $\vec{\Psi}_{ds,k}$, and
- 3) the flux linkage due to the field of the damper currents $\vec{\Psi}_{dd,k}$.

The flux linkage of the damper windings caused by the magnets is constant, because the damper rotates with the same speed as the magnets. Therefore, the time derivative of this flux is zero, so that the corresponding contribution may be omitted.

Using the remaining two contributions, voltage equation (3.37) can be written as:

$$\vec{0} = R_{d,k} \vec{i}_{d,k} + \frac{d\vec{\Psi}_{ds,k}}{dt} + \frac{d\vec{\Psi}_{dd,k}}{dt} \quad (3.38)$$

In the following subsections, this voltage equation is worked out and quantified.

As already mentioned in subsection 3.3.1, the end-winding leakage of the damper windings is neglected. However, this does not mean that all damper leakage flux is neglected, because the air-gap field also includes some leakage flux, which does not cross the air gap. This leakage flux is included in the calculation of the air-gap field, because it is calculated two-dimensionally. This leakage flux contributes to the flux linkage caused by the damper currents $\vec{\Psi}_{dd,k}$.

3.3.3 The flux linkages of the sinusoidally distributed damper windings

In this subsection, the flux linkages of the damper windings resulting from any magnetic flux density satisfying equation (3.1) are calculated. Firstly, the flux linkage of damper winding d,k is calculated. Subsequently, the flux linkage of damper winding q,k is described. The flux linkage of the damper windings is calculated in the same way as the flux linkage of a stator winding (subsection 3.2.3).

First, the flux linkage of a full-pitch turn at the damper radius r_d is calculated, dependent on the angular position of this turn. The flux $\psi_r(\alpha')$ linked by this full-pitch turn at α' (figure 3.2 depicts a turn at the stator radius r_s) is calculated as

$$\psi_r(\alpha') = \int_S \vec{B} \cdot d\vec{a} = \int_{\alpha' - \pi/p}^{\alpha'} B_r(r_d, \alpha_r) l_s r_d d\alpha_r \quad (3.39)$$

For the magnetic flux density in this equation, equation (3.31) is substituted:

$$\begin{aligned}\Psi_{t,k}(\alpha') &= \sum_{k=1,3,5,\dots}^{\infty} \Psi_{t,k}(\alpha') ; \\ \Psi_{t,k}(\alpha') &= 2l_s r_d \frac{\hat{B}_{r,k}(r_d)}{pk} \sin(pk(\alpha' - \beta'_k))\end{aligned}\quad (3.40)$$

With this expression for the flux linkage of a full-pitch turn, the flux $\Psi_{dd,k}$ linked by damper winding d,k is calculated as

$$\Psi_{dd,k} = p \int_0^{\pi/p} n_{dd,k}(\alpha') \Psi_{t,k}(\alpha') d\alpha' \quad (3.41)$$

In this equation, it was taken that a sinusoidally distributed winding only links with the space harmonic of the magnetic flux density with the same pole angle. This follows from subsection 3.2.3, where it was shown that a space harmonic of the stator winding distribution only links with the space harmonic of the magnetic flux density with the same pole angle. It also follows from subsection 3.3.1, where it was shown that a space harmonic of the magnetic flux density only causes a space harmonic of the current density with the same pole angle.

In equation (3.41), the winding distribution of equation (2.48) and the k th space harmonic of the flux linkage of a full-pitch turn of equation (3.40) are substituted:

$$\Psi_{dd,k} = \frac{l_s r_d}{2k} N_{d,k} \hat{B}_{r,k}(r_d) \int_0^{\pi/p} \cos(pk\beta'_k) d\alpha' = \frac{\pi l_s r_d N_{d,k}}{2pk} \hat{B}_{r,k}(r_d) \cos(pk\beta'_k) \quad (3.42)$$

The winding distribution of damper winding q,k is equal to the winding distribution of damper winding d,k except for an angular shift of $\pi/(2pk)$. Therefore, the flux linkage of damper winding q,k is also equal to the flux linkage of damper winding d,k , except for an angular shift. With this, the flux vector $\Psi_{d,k}$ is given by

$$\Psi_{d,k} = \begin{bmatrix} \Psi_{dd,k} \\ \Psi_{dq,k} \end{bmatrix} = \frac{\pi l_s r_d N_{d,k}}{2pk} \hat{B}_{r,k}(r_d) \begin{bmatrix} \cos(pk\beta'_k) \\ \cos(pk(\beta'_k - \frac{\pi}{2pk})) \end{bmatrix} \quad (3.43)$$

This shows that the flux linkage of damper winding d,k or q,k is maximum when the reference axis of this damper winding coincides with a maximum of the k th space harmonic of the magnetic flux density. In this case, the Fourier coefficient of the k th space harmonic of the magnetic flux density has to be multiplied by a factor $\pi l_s r_d N_{d,k}/(2pk)$ to obtain the linked flux. The effect of a spatial angle between the reference axis of damper winding d,k or q,k and a maximum of the k th space harmonic of the magnetic flux density is the cosine of pk times this spatial angle. In subsections 3.3.5 and 3.3.6, this is used to calculate the flux linkages of the damper windings caused by the stator currents and the damper currents.

3.3.4 The damper resistance

This subsection introduces an expression for the damper resistance.

After substituting equation (3.43) for the flux linkages in the damper voltage equation (equation (3.37)), the damper currents are calculated as

$$\vec{i}_{d,k} = -\frac{1}{R_{d,k}} \frac{d\Psi_{d,k}}{dt} = -\frac{1}{R_{d,k}} \frac{\pi l_s r_d N_{d,k}}{2pk} \frac{d}{dt} \left\{ \hat{B}_{r,k}(r_d) \begin{bmatrix} \cos(pk\beta'_k) \\ \cos(pk(\beta'_k - \frac{\pi}{2pk})) \end{bmatrix} \right\} \quad (3.44)$$

Comparison of this equation with equation (3.36) affirms that the damper cylinder can be modelled as a series of short-circuited sinusoidally distributed damper windings if the resistance $R_{d,k}$ of the damper windings d,k and q,k is given by

$$R_{d,k} = \frac{\pi l_s \rho_d N_{d,k}^2}{4\delta_d r_d} \quad (3.45)$$

It should be noted that the number of turns of the winding distribution $N_{d,k}$ can be chosen arbitrarily, as indicated in subsection 2.5.1.

3.3.5 The damper flux linkages due to the stator currents

In this subsection, the damper flux linkages which result from the magnetic field of the stator currents are calculated.

In section 2.4, the magnetic flux density produced by the stator currents was calculated. The radial component of the magnetic flux density at the damper radius follows from equation (2.61), and is written as a function of the rotor coordinate by using $\alpha_s = \alpha_r + \theta$ (equation (3.2)):

$$B_{rs}(r_d, \alpha_r) = \sum_{k=1,3,5,\dots}^{\infty} \frac{(r_d^{2pk} + r_r^{2pk}) r_s^{pk} \mu_0 N_{s,k}}{(r_s^{2pk} - r_r^{2pk}) r_d^{pk+1} 2} \left\{ i_{sa} \cos(pk(\alpha_r + \theta)) + i_{sb} \cos(pk(\alpha_r + \theta - \frac{2\pi}{3p})) + i_{sc} \cos(pk(\alpha_r + \theta - \frac{4\pi}{3p})) \right\} \quad (3.46)$$

In the same way as in subsection 3.3.3, the flux linkages of the damper windings are calculated as (compare equation (3.43))

$$\Psi_{ds,k} = M_{sd,k}^T \vec{i}_s \quad (3.47)$$

In this equation, $M_{sd,k}^T$ is the transpose of the matrix $M_{sd,k}$ of equation (3.23), as expected because the mutual inductances between two linked coils are equal.

3.3.6 The damper flux linkages due to the damper currents

This subsection describes the calculation of the damper flux linkages which result from the magnetic field of the damper currents.

In section 2.5, the magnetic flux density in the air gap produced by the damper currents was calculated. The radial component of this magnetic flux density at the damper radius follows from equation (2.62), and is given by

$$B_{rd,k}(r_d, \alpha_r) = \sum_{k=1,3,5,\dots}^{\infty} \frac{(r_d^{2pk} + r_s^{2pk})(r_d^{2pk} + r_r^{2pk})}{2(r_s^{2pk} - r_r^{2pk})r_d^{2pk+1}} \frac{\mu_0 N_{d,k}}{2} \left\{ i_{dd,k} \cos(pk\alpha_r) + i_{dq,k} \cos\left(pk\left(\alpha_r - \frac{\pi}{2pk}\right)\right) \right\} \quad (3.48)$$

In the same way as in subsection 3.3.3, the flux linkages of the damper windings are calculated as (compare equation (3.43))

$$\Psi_{dd,k} = L_{dd,k} \begin{bmatrix} 1 & 0 \\ 0 & 1 \end{bmatrix} \vec{i}_{d,k} = L_{dd,k} \vec{i}_{d,k} \quad (3.49)$$

where the self-inductance of the damper winding $L_{dd,k}$ was introduced as

$$L_{dd,k} = \frac{\mu_0 \pi l_s N_{d,k}^2}{4pk} \frac{(r_d^{2pk} + r_s^{2pk})(r_d^{2pk} + r_r^{2pk})}{2(r_s^{2pk} - r_r^{2pk})r_d^{2pk}} \quad (3.50)$$

3.3.7 Summary

In conclusion, in section 3.3, expressions for the damper resistance and the flux linkages of the damper windings have been derived. These expressions (equations (3.45), (3.47), and (3.49)) are used in the damper voltage equation (equation (3.38)). For convenience, the damper voltage equation is combined with stator voltage equation (3.25):

$$\begin{cases} \vec{u}_s = \vec{e}_p + R_s \vec{i}_s + L_{ss} \frac{d\vec{i}_s}{dt} + \sum_{k=1,3,5,\dots}^{\infty} \left\{ L_{ss,k} \frac{d\vec{i}_s}{dt} + \frac{d}{dt} \{ M_{sd,k} \vec{i}_{d,k} \} \right\} \\ \vec{0} = R_{d,k} \vec{i}_{d,k} + \frac{d}{dt} \{ M_{sd,k}^T \vec{i}_s \} + L_{dd,k} \frac{d\vec{i}_{d,k}}{dt} \quad \text{for } k=1,3,5,\dots \end{cases} \quad (3.51)$$

It should be noted that there is a damper voltage equation for each space harmonic. The damper windings are coupled with the stator windings, but not with each other.

3.4 Transformations of the voltage equations

In this section, the voltage equations (equation (3.51)) are transformed into a useful form. This is necessary to eliminate the dependence of the rotor position angle θ and to obtain simpler equations. Firstly, in subsection 3.4.1, the voltage equations are transformed into a two-phase stator-connected reference system, the $\alpha\beta$ -system. Subsequently, in subsection 3.4.2, the damper quantities are referred to the stator. It should be noted that the result is not a two-phase machine, but a set of two-phase equations describing a three-phase machine.

3.4.1 Transformation into the stator-connected $\alpha\beta$ -system

The aim of this subsection is to transform the stator and the damper quantities into a two-phase stator-connected reference system, the $\alpha\beta$ -system. The stator quantities are transformed into this system in order to decrease the number of equations. When the zero-component is considered, the number of equations remains three. However, the zero-component can often be omitted because it is zero, for example, when there is no star-point connection. The damper quantities are transformed into this system to eliminate the dependence of the rotor position θ .

Transformation of the stator quantities

The stator quantities are transformed into the $\alpha\beta 0$ -system by means of the well-known Clarke-transformation [Cla 43], [Kra 95], which is given by

$$\vec{i}_s^{s0} = \begin{bmatrix} i_{s\alpha} \\ i_{s\beta} \\ i_{s0} \end{bmatrix} = C_{23} \vec{i}_s^- ; \quad \vec{u}_s^{s0} = \begin{bmatrix} u_{s\alpha} \\ u_{s\beta} \\ u_{s0} \end{bmatrix} = C_{23} \vec{u}_s^- ; \quad \vec{\Psi}_s^{s0} = \begin{bmatrix} \Psi_{s\alpha} \\ \Psi_{s\beta} \\ \Psi_{s0} \end{bmatrix} = C_{23} \vec{\Psi}_s^- ; \quad (3.52)$$

$$\vec{e}_p^{s0} = \begin{bmatrix} e_{p\alpha} \\ e_{p\beta} \\ e_{p0} \end{bmatrix} = C_{23} \vec{e}_p^- ; \quad C_{23} = \frac{1}{\sqrt{6}} \begin{bmatrix} 2 & -1 & -1 \\ 0 & \sqrt{3} & -\sqrt{3} \\ \sqrt{2} & \sqrt{2} & \sqrt{2} \end{bmatrix}$$

The transformation matrix C_{23} is orthogonal. The superscript $s0$ of the vectors denotes that the vector belongs to the three-dimensional stator-connected $\alpha\beta 0$ -system. The superscript s is used for the two-dimensional $\alpha\beta$ -system without zero-component:

$$\vec{u}_s^s = \begin{bmatrix} u_{s\alpha} \\ u_{s\beta} \end{bmatrix} ; \quad \vec{e}_p^s = \begin{bmatrix} e_{p\alpha} \\ e_{p\beta} \end{bmatrix} ; \quad \vec{i}_s^s = \begin{bmatrix} i_{s\alpha} \\ i_{s\beta} \end{bmatrix} ; \quad \vec{\Psi}_s^s = \begin{bmatrix} \Psi_{s\alpha} \\ \Psi_{s\beta} \end{bmatrix} \quad (3.53)$$

Rotation of the damper quantities

The dependence of the rotor position θ is eliminated from the voltage equations by rotating the damper quantities from the rotating two-phase rotor-connected dq -system to the two-phase stator-connected $\alpha\beta$ -system.

First, it is explained how the rotation matrix might be derived. The damper winding distribution can be transformed into the stator reference system by substituting $\alpha_r = \alpha_s - \theta$ in the equation for the damper winding distribution (equation (2.48)). The result is

$$\begin{bmatrix} n_{dd,k}(\alpha_r) \\ n_{dq,k}(\alpha_r) \end{bmatrix} = \frac{N_{dk}}{2} \begin{bmatrix} \sin(pk(\alpha_s - \theta)) \\ \sin(kp(\alpha_s - \theta) - \frac{1}{2}\pi) \end{bmatrix} = \frac{N_{dk}}{2} C_{rot,k} \begin{bmatrix} \sin(pk\alpha_s) \\ \sin(kp\alpha_s - \frac{1}{2}\pi) \end{bmatrix} \quad (3.54)$$

where the rotation matrix $C_{rot,k}$ is introduced as

$$C_{rot,k} = \begin{bmatrix} \cos(pk\theta) & -\sin(pk\theta) \\ \sin(pk\theta) & \cos(pk\theta) \end{bmatrix} \quad (3.55)$$

Using this transformation results in voltage equations with signs dependent on the space harmonic number k . To prevent this, the rotation is combined with a transformation, the transformation matrix of which is given by

$$C_{sign,k} = \begin{cases} \begin{bmatrix} 1 & 0 \\ 0 & 1 \end{bmatrix} & \text{for } k=1,3,7,9,13,.. \\ \begin{bmatrix} 1 & 0 \\ 0 & -1 \end{bmatrix} & \text{for } k=5,11,17,.. \end{cases} \quad (3.56)$$

The transformation matrix for the damper quantities $C_{r,k}$ is the multiplication of this matrix with the rotation matrix. Therefore, the transformation of the damper quantities to the $\alpha\beta$ -system is given by

$$\begin{bmatrix} \bar{i}_{dk}^s \\ \bar{i}_{\beta k}^s \end{bmatrix} = \begin{bmatrix} i_{d\alpha,k} \\ i_{d\beta,k} \end{bmatrix} = C_{r,k} \bar{i}_{dk}^r ; \quad \begin{bmatrix} \Psi_{d\alpha,k}^s \\ \Psi_{d\beta,k}^s \end{bmatrix} = \begin{bmatrix} \Psi_{d\alpha,k} \\ \Psi_{d\beta,k} \end{bmatrix} = C_{r,k} \Psi_{dk}^r ; \quad (3.57)$$

$$C_{r,k} = C_{sign,k} C_{rot,k}$$

The transformation matrix $C_{r,k}$ is orthogonal. Also here, the superscript s is used for vectors in the two-dimensional $\alpha\beta$ -system.

Incorporating the transformations into the voltage equations

These transformations are incorporated into voltage equations (3.51):

$$\begin{cases} \bar{u}_s^{s0} = \bar{e}_p^{s0} + R_s \bar{i}_s^{s0} + C_{23} \left\{ L_{sv} \frac{d}{dt} (C_{23}^T \bar{i}_s^{s0}) + \sum_{k=1,3,5,..}^{\infty} \left\{ L_{ss,k} \frac{d}{dt} (C_{23}^T \bar{i}_s^{s0}) + \frac{d}{dt} (M_{sd,k} C_{r,k}^T \bar{i}_{dk}^s) \right\} \right\} \\ \bar{0} = R_{dk} \bar{i}_{dk}^s + C_{r,k} \left\{ \frac{d}{dt} (M_{sd,k}^T C_{23}^T \bar{i}_s^{s0}) + L_{dd,k} \frac{d}{dt} (C_{r,k}^T \bar{i}_{dk}^s) \right\} \quad \text{for } k=1,3,5,.. \end{cases} \quad (3.58)$$

The matrix multiplications in these equations are worked out:

$$C_{23}L_{s\sigma}C_{23}^T = \begin{bmatrix} L_{s\sigma} & 0 & 0 \\ 0 & L_{s\sigma} & 0 \\ 0 & 0 & L_{s\sigma} + 3M_{s\sigma ab} \end{bmatrix} \quad (3.59)$$

where the leakage inductance $L_{s\sigma}$ was introduced as

$$L_{s\sigma} = L_{s\sigma a} - M_{s\sigma ab} \quad (3.60)$$

$$C_{23}L_{ss,k}C_{23}^T = \begin{cases} \frac{3}{2}L_{ss,k} \begin{bmatrix} 1 & 0 & 0 \\ 0 & 1 & 0 \\ 0 & 0 & 0 \end{bmatrix} & \text{for } k=1,5,7,11,.. \\ 3L_{ss,k} \begin{bmatrix} 0 & 0 & 0 \\ 0 & 0 & 0 \\ 0 & 0 & 1 \end{bmatrix} & \text{for } k=3,9,15,.. \end{cases} \quad (3.61)$$

$$C_{23}M_{sd,k}C_{r,k}^T = \begin{cases} \sqrt{\frac{3}{2}}M_{sd,k} \begin{bmatrix} 1 & 0 \\ 0 & 1 \\ 0 & 0 \end{bmatrix} & \text{for } k=1,5,7,11,.. \\ \sqrt{3}M_{sd,k} \begin{bmatrix} 0 & 0 \\ 0 & 0 \\ 1 & 0 \end{bmatrix} & \text{for } k=3,9,15,.. \end{cases} \quad (3.62)$$

$$\begin{aligned} C_{r,k} \frac{d}{dt} (M_{sd,k}^T C_{23}^T \bar{i}_s^{\bar{s}0}) &= C_{r,k} M_{sd,k}^T C_{23}^T \frac{d\bar{i}_s^{\bar{s}0}}{dt} + C_{r,k} \frac{dM_{sd,k}^T}{dt} C_{23}^T \bar{i}_0^{\bar{s}0} \\ &= C_{r,k} M_{sd,k}^T C_{23}^T \frac{d\bar{i}_s^{\bar{s}0}}{dt} + kp\Omega G_k C_{r,k} M_{sd,k}^T C_{23}^T \bar{i}_0^{\bar{s}0} \end{aligned} \quad (3.63)$$

where $C_{r,k} M_{sd,k}^T C_{23}^T$ is the transpose of the matrix $C_{23} M_{sd,k} C_{r,k}^T$ of equation (3.62), and the matrix G_k is given by

$$G_k = \begin{cases} \begin{bmatrix} 0 & 1 \\ -1 & 0 \end{bmatrix} & \text{for } k=1,3,7,9,13,.. \\ \begin{bmatrix} 0 & -1 \\ 1 & 0 \end{bmatrix} & \text{for } k=5,11,17,.. \end{cases} \quad (3.64)$$

$$C_{r,k} \frac{d}{dt} (C_{r,k} \bar{i}_{d,k}^{\bar{s}}) = C_{r,k} \frac{dC_{r,k}}{dt} \bar{i}_{d,k}^{\bar{s}} + \frac{d\bar{i}_{d,k}^{\bar{s}}}{dt} = kp\Omega G_k \bar{i}_{d,k}^{\bar{s}} + \frac{d\bar{i}_{d,k}^{\bar{s}}}{dt} \quad (3.65)$$

In this equation, the matrix G_k is given in equation (3.64).

The resulting voltage equations

The elaborated expressions are used in the set of voltage equations (equations (3.58)). To obtain useful voltage equations, the zero-component is separated from the $\alpha\beta$ -components. For the zero-component, the set of voltage equations becomes

$$\left\{ \begin{array}{l} u_{s0} = e_{p0} + R_s i_{s0} + (L_{sr} + 3M_{soab}) \frac{di_{s0}}{dt} + \sum_{k=3,9,15,\dots}^{\infty} \left\{ 3L_{ssk} \frac{di_{s0}}{dt} + \sqrt{3}M_{sd,k} \frac{di_{da,k}}{dt} \right\} \\ \vec{0} = R_{dk} \vec{i}_{dk} + \sqrt{3}M_{sd,k} \frac{d}{dt} \begin{bmatrix} i_{s0} \\ 0 \end{bmatrix} + L_{dd,k} \frac{d\vec{i}_{dk}^s}{dt} \\ \quad + kp\Omega \left\{ \sqrt{3}M_{sd,k} \begin{bmatrix} 0 \\ -i_{s0} \end{bmatrix} + L_{dd,k} \begin{bmatrix} i_{d\beta,k} \\ -i_{d\alpha,k} \end{bmatrix} \right\} \end{array} \right. \quad \text{for } k=3,9,15,\dots \quad (3.66)$$

It should be noted that the stator quantities in this equation are the scalar zero-components, and not vectors. In this voltage equation, only damper currents appear of which the space harmonic number k is an integer multiple of three: $k=3,9,15,\dots$. This means that the zero-component only causes these damper currents and these space harmonics of the (surface) current density in the damper cylinder.

For the $\alpha\beta$ -components, the set of voltage equations (equation (3.58)) becomes

$$\left\{ \begin{array}{l} \vec{u}_s^s = \vec{e}_p^s + R_s \vec{i}_s^s + L_{sr} \frac{d\vec{i}_s^s}{dt} + \sum_{k=1,5,7,11,\dots}^{\infty} \left\{ \frac{3}{2}L_{ssk} \frac{d\vec{i}_s^s}{dt} + \sqrt{\frac{3}{2}}M_{sd,k} \frac{d\vec{i}_{dk}^s}{dt} \right\} \\ \vec{0} = R_{dk} \vec{i}_{dk}^s + \sqrt{\frac{3}{2}}M_{sd,k} \frac{d\vec{i}_s^s}{dt} + L_{dd,k} \frac{d\vec{i}_{dk}^s}{dt} \\ \quad + kp\Omega G_k \left\{ \sqrt{\frac{3}{2}}M_{sd,k} \vec{i}_s^s + L_{dd,k} \vec{i}_{dk}^s \right\} \end{array} \right. \quad \text{for } k=1,5,7,11,\dots \quad (3.67)$$

The stator quantities in this set of equations are written as two-dimensional vectors with an α - and a β -component, as in equation (3.53). In set of voltage equations, no damper currents appear of which the space harmonic number k is an integer multiple of three. This means that the $\alpha\beta$ -components do not cause these damper currents and these space harmonics of the (surface) current density in the damper cylinder.

The equivalent circuit representing the α -component of this voltage equation, is depicted in figure 3.4. In this equivalent circuit, the first, the fifth and the seventh space harmonic are visible. For the other space harmonics, the equivalent circuit can be extended in the same way. This figure uses the flux linkage of the damper Ψ_{dk}^s , which is given by

$$\Psi_{dk}^s = \sqrt{\frac{3}{2}}M_{sd,k} \vec{i}_s^s + L_{dd,k} \vec{i}_{dk}^s \quad (3.68)$$

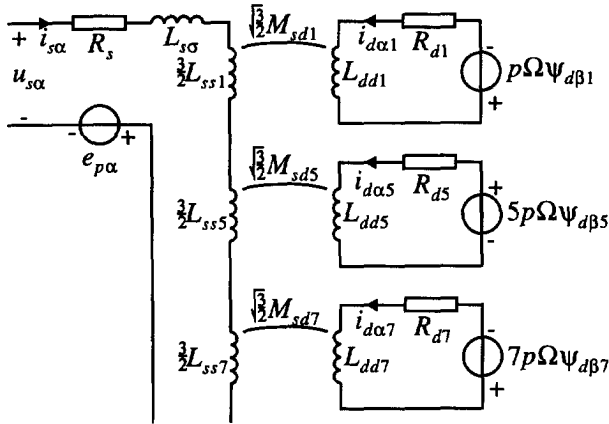


Figure 3.4: Equivalent circuit for the α -component of the voltage equation.

The coupling factor κ_k between the stator and the damper windings is given by

$$\kappa_k = \frac{\sqrt{\frac{3}{2}} M_{sd,k}}{\sqrt{\frac{3}{2}} L_{ss,k} L_{dd,k}} = \sqrt{\frac{2(r_d^{2pk} + r_r^{2pk}) r_s^{2pk}}{(r_s^{2pk} + r_r^{2pk})(r_d^{2pk} + r_s^{2pk})}} \quad (3.69)$$

For the test model (described in appendix A, section A.1), this coupling factor κ_k is depicted in figure 3.5 for two values of the damper radius. If the distance between the stator surface and the damper surface decreases, the coupling factor increases. Because the coupling factor decreases quickly with increasing space harmonic number k , it is not necessary to consider many space harmonics. This again illustrates that the space harmonics with small pole angles hardly cross the air gap.

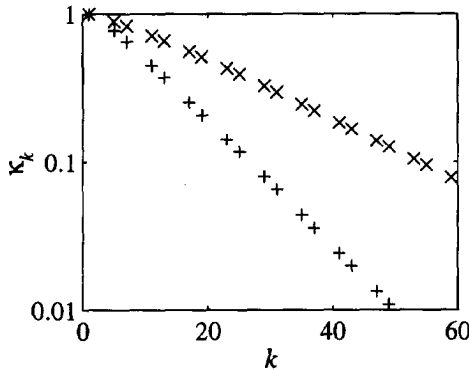


Figure 3.5: Coupling factor κ_k between stator and damper windings as a function of the space harmonic number k for $r_d = 55.0$ mm (+) and $r_d = 56.4$ mm (x) (test model).

3.4.2 Referring the damper quantities to the stator

In the transformation introduced in this subsection, the damper quantities are referred to the stator to simplify the voltage equations. This is done for the $\alpha\beta$ -components, and not for the zero-component, because the zero-component is not used in the rest of the thesis.

The transformation which refers the damper quantities to the stator is given by

$$\vec{i}_{D,k}^s = \begin{bmatrix} i_{D\alpha,k} \\ i_{D\beta,k} \end{bmatrix} = \sqrt{\frac{2}{3}} \frac{L_{dd,k}}{M_{sd,k}} \vec{i}_{d,k}^s ; \quad \Psi_{D,k}^s = \begin{bmatrix} \Psi_{D\alpha,k} \\ \Psi_{D\beta,k} \end{bmatrix} = \sqrt{\frac{3}{2}} \frac{M_{sd,k}}{L_{dd,k}} \Psi_{d,k}^s \quad (3.70)$$

The subscript D in these vectors denotes that this quantity is referred to the stator.

This transformation is incorporated into the set of voltage equations for the α - and the β -components (equation (3.67)). The result is

$$\begin{cases} \vec{u}_s^s = \vec{e}_p^s + R_s \vec{i}_s^s + L_{so} \frac{d\vec{i}_s^s}{dt} + \sum_{k=1,5,7,11,\dots}^{\infty} \left\{ \frac{3}{2} L_{ss,k} \frac{d\vec{i}_s^s}{dt} + \frac{3}{2} \frac{M_{sd,k}^2}{L_{dd,k}} \frac{d\vec{i}_{d,k}^s}{dt} \right\} \\ \vec{0} = \frac{3M_{sd,k}^2}{2L_{dd,k}^2} R_{d,k} \vec{i}_{D,k}^s + \frac{3M_{sd,k}^2}{2L_{dd,k}} \frac{d}{dt} (\vec{i}_s^s + \vec{i}_{D,k}^s) \\ \quad \quad \quad + kp\Omega \frac{3M_{sd,k}^2}{2L_{dd,k}} \mathbf{G}_k (\vec{i}_s^s + \vec{i}_{D,k}^s) \quad \text{for } k=1,5,7,11,\dots \end{cases} \quad (3.71)$$

After introducing

$$R_{D,k} = \frac{3M_{sd,k}^2}{2L_{dd,k}^2} R_{d,k} = \frac{6r_s^{2pk} r_d^{2pk}}{(r_d^{2pk} + r_s^{2pk})^2} \frac{\pi l_s \rho_d N_{s,k}^2}{4r_d \delta_d} \quad (3.72)$$

$$L_k = \frac{3M_{sd,k}^2}{2L_{dd,k}} = \frac{3}{2} \kappa_k^2 L_{ss,k} = \frac{(r_d^{2pk} + r_s^{2pk}) r_s^{2pk}}{(r_d^{2pk} + r_s^{2pk})(r_s^{2pk} - r_r^{2pk})} \frac{3\mu_0 \pi l_s N_{s,k}^2}{4pk} \quad (3.73)$$

$$L_\sigma = L_{so} + \sum_{k=1,5,7,11,\dots}^{\infty} L_{go,k} ;$$

$$L_{go,k} = \frac{3}{2} L_{ss,k} - L_k = \frac{3}{2} (1 - \kappa_k^2) L_{ss,k} = \frac{r_s^{2pk} - r_d^{2pk}}{r_s^{2pk} + r_d^{2pk}} \frac{3\mu_0 \pi l_s N_{s,k}^2}{8pk} \quad (3.74)$$

the set of voltage equations of equation (3.71) can be written as

$$\begin{cases} \vec{u}_s^s = \vec{e}_p^s + R_s \vec{i}_s^s + L_\sigma \frac{d\vec{i}_s^s}{dt} + \sum_{k=1,5,7,11,..}^\infty L_k \frac{d}{dt}(\vec{i}_s^s + \vec{i}_{D,k}^s) \\ 0 = R_{D,k} \vec{i}_{D,k}^s + L_k \frac{d}{dt}(\vec{i}_s^s + \vec{i}_{D,k}^s) + kp\Omega L_k G_k(\vec{i}_s^s + \vec{i}_{D,k}^s) \end{cases} \quad \text{for } k=1,5,7,11,.. \quad (3.75)$$

The equivalent circuit representing the α -component of this voltage equation is depicted in figure 3.6. In this equivalent circuit, the first, the fifth and the seventh space harmonic are visible. For the other space harmonics, the equivalent circuit can be extended in the same way. This figure uses the flux linkage of the damper $\Psi_{D,k}^s$, which is given by

$$\Psi_{D,k}^s = L_k(\vec{i}_s^s + \vec{i}_{D,k}^s) \quad (3.76)$$

Figure 3.7 depicts the resistance $R_{D,k}$ and the inductance L_k of the test model (described in appendix A, section A.1). Both parameters decrease very quickly with increasing k . For all space harmonics higher than the 19th, $R_{D,k}$ is smaller than 0.2 % of $R_{D,1}$. L_k decreases even faster: for all higher space harmonics, L_k is smaller than 0.2 % of L_1 . This shows again that it is not necessary to consider many space harmonics.

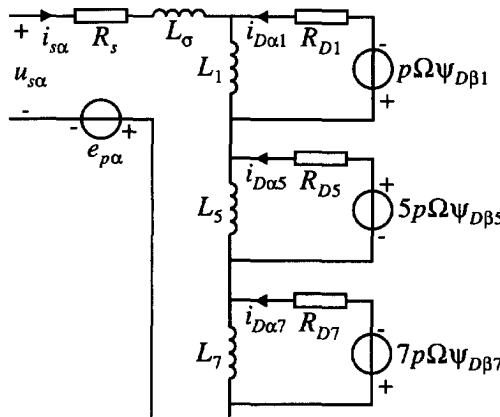


Figure 3.6: Equivalent circuit for the α -component of the voltage equation, where the damper quantities are referred to the stator.

3.4.3 Summary

In this section, the voltage equations of the stator and the rotor have been transformed into a useful set of voltage equations. This has been done for any (varying) speed of the rotor, and for any form of the stator currents and stator voltages. For the zero-component, the voltage equations are given in expression (3.66). This equation is not

used in the rest of the thesis, because this component is zero when there is no star-point connection. For the $\alpha\beta$ -components, the voltage equations are given by equation (3.75). In the next section, this set of equations is worked out for the situations considered in the rest of the thesis.

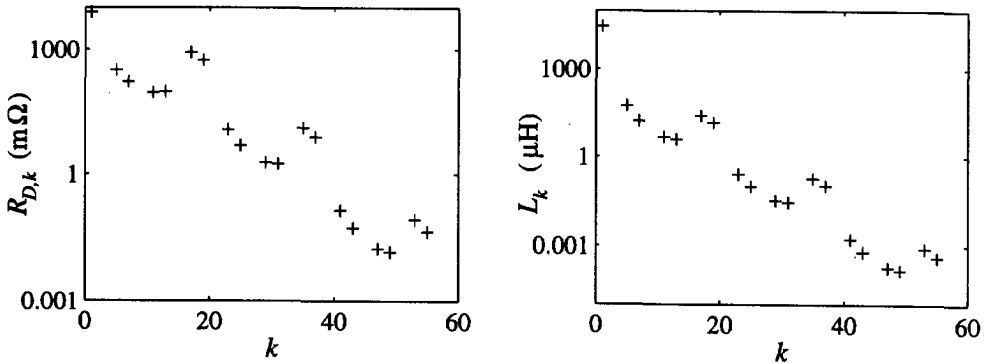


Figure 3.7: The damper resistance $R_{D,k}$ and the inductance L_k as a function of the harmonic number k (test model).

3.5 Steady-state voltage equations

Until now, the derived voltage equations are valid for any form of the stator currents and for any (varying) speed of the rotor. In this section, the voltage equations are worked out for the two situations considered in the rest of the thesis:

- 1) In subsection 3.5.2, the voltage equations are worked out for steady-state operation with rectifier load. These equations are used in the rest of this thesis where the steady-state performance of the rectifier-loaded machine is considered.
- 2) In subsection 3.5.3, the voltage equations are worked out for the locked-rotor tests. These tests are used for the verification of the derived voltage equations (in section 3.6) and the equations for the losses (in chapter 4).

Before the voltage equations are worked out, the slip and the rotor angular frequency are introduced in subsection 3.5.1, because they are useful in the next subsections.

3.5.1 The rotor angular frequency and the slip

In this thesis, the slip is defined for steady-state situations, while the stator currents form a balanced set of three-phase currents, and while there is no star-point connection. This means that the angular speed of the rotor Ω is constant, and that the stator currents can be written as in equation (2.39).

As explained in section 2.4, the currents of equation (2.39) cause travelling waves of magnetic flux density. These travelling waves have the same speed and pole angle as the surface current density. The angular frequency experienced by the stator from the $|6n+1|$ th time harmonic of the magnetic flux density is $|6n+1|\omega_1$. The angular frequency experienced by the rotor differs from the angular frequency experienced by the stator because of the rotation of the rotor, and is calculated below.

Equation (3.2) expresses that $\alpha_s = \alpha_r + \theta$. The rotor position angle θ can be written as a function of the angular speed of the rotor Ω by using equation (3.18):

$$\theta = \int_0^t \Omega dt' = \Omega t + \theta_0 = \Omega t - \frac{\pi}{2p} \quad (3.77)$$

where θ_0 is the rotor position on time $t=0$, which is chosen as $\theta_0 = -\pi/(2p)$, because in this way, the induced voltage in no-load of phase a e_{pa} is cosinusoidal.

Substituting $\alpha_s = \alpha_r + \theta$ and this value of θ in the harmonics of the surface current density of equation (2.40) gives

$$K_{s,k,6n+1}(\alpha_r, t) = \begin{cases} \frac{3N_{s,k}}{4r_s} \hat{i}_{s,6n+1} \sin(pk(\alpha_r + \Omega t + \theta_0) - (6n+1)\omega_1 t + \varphi_{6n+1}) & \text{for } k=1,7,13,.. \\ \frac{3N_{s,k}}{4r_s} \hat{i}_{s,6n+1} \sin(pk(\alpha_r + \Omega t + \theta_0) + (6n+1)\omega_1 t - \varphi_{6n+1}) & \text{for } k=5,11,17,.. \end{cases} \quad (3.78)$$

$$= \begin{cases} \frac{3N_{s,k}}{4r_s} \hat{i}_{s,6n+1} \sin(pk(\alpha_r + \theta_0) - s_{k,6n+1}(6n+1)\omega_1 t + \varphi_{6n+1}) & \text{for } k=1,7,13,.. \\ \frac{3N_{s,k}}{4r_s} \hat{i}_{s,6n+1} \sin(pk(\alpha_r + \theta_0) + s_{k,6n+1}(6n+1)\omega_1 t - \varphi_{6n+1}) & \text{for } k=5,11,17,.. \end{cases}$$

In this equation, the slip $s_{k,6n+1}$ for the travelling wave resulting from the combination of the k th space harmonic and the $|6n+1|$ th time harmonic was introduced as

$$s_{k,6n+1} = \begin{cases} \frac{(6n+1)\omega_1 - kp\Omega}{(6n+1)\omega_1} & \text{for } k=1,7,13,.. \\ \frac{(6n+1)\omega_1 + kp\Omega}{(6n+1)\omega_1} & \text{for } k=5,11,17,.. \end{cases} \quad (3.79)$$

In words, the slip is defined as the difference between the speed of a travelling wave and the speed of the rotor, divided by the speed of the travelling wave. This means that the slip for a travelling wave is zero when the rotor rotates at the same speed as the travelling wave. Usually in machine theory, the slip is defined as the difference between the synchronous speed and the actual speed of the rotor divided by the synchronous speed [Kra 95]. This agrees with the slip introduced in equation (3.79) for the travelling

wave resulting from the combination of the fundamental space harmonic ($k=1$) and the fundamental time harmonic ($n=0$).

From equation (3.78), it can be concluded that the angular frequency ω experienced by the rotor from the k th space harmonic of the winding distribution and the $|6n+1|$ th time harmonic of the stator current is given by

$$\omega = |s_{k,6n+1}(6n+1)\omega_1| \quad (3.80)$$

When the rotor is locked ($\Omega=0$), the slip $s_{k,6n+1}$ is one for all combinations of time and space harmonics. In this case, the angular frequency ω experienced by the rotor from the k th space harmonic of the winding distribution and the $|6n+1|$ th time harmonic of the stator current is equal to the angular frequency experienced by the stator.

3.5.2 Equations for the rectifier-loaded machine

In this subsection, the voltage equations are worked out for the rectifier-loaded machine in steady state. Using equation (3.77), the relations between the rotor position angle θ , the angular speed of the rotor Ω and the angular frequency of the fundamental time harmonic ω_1 during steady-state operation with rectifier can be written as

$$\Omega = \frac{\omega_1}{p} ; \quad \theta = \frac{\omega_1}{p} t - \frac{\pi}{2p} \quad (3.81)$$

This is used in the expression for the no-load voltage (equation (3.16)). Furthermore, the time harmonics of which the harmonic number is an integer multiple of three are omitted, because they are not present in the line voltages. Using a complex representation, this expression for the no-load voltage can be written as

$$\bar{e}_p = \sum_{n=-\infty}^{\infty} \text{Re} \left\{ \hat{e}_{p,6n+1} e^{j(6n+1)\omega_1 t} \begin{bmatrix} 1 \\ e^{-j\frac{2}{3}\pi} \\ e^{-j\frac{4}{3}\pi} \end{bmatrix} \right\} \quad (3.82)$$

The Clarke-transformation (equation (3.52)) transforms these voltages into the $\alpha\beta$ -system:

$$\bar{e}_p^s = \sqrt{\frac{3}{2}} \sum_{n=-\infty}^{\infty} \text{Re} \left\{ \hat{e}_{p,6n+1} e^{j(6n+1)\omega_1 t} \begin{bmatrix} 1 \\ -j \end{bmatrix} \right\} \quad (3.83)$$

Furthermore, the currents form a balanced set of three-phase currents without even time harmonics and without time harmonics of which the harmonic number is an integer multiple of three, as in equation (2.39). Using a complex representation, this set of currents can be written as

$$\vec{i}_s = \sum_{n=-\infty}^{\infty} \operatorname{Re} \left\{ \hat{i}_{s,6n+1} e^{j(6n+1)\omega_1 t} \begin{bmatrix} 1 \\ e^{-j\frac{2}{3}\pi} \\ e^{-j\frac{4}{3}\pi} \end{bmatrix} \right\} \quad (3.84)$$

The Clarke-transformation (equation (3.52)) transforms these currents into the $\alpha\beta$ -system:

$$\vec{i}_s^s = \sqrt{\frac{3}{2}} \sum_{n=-\infty}^{\infty} \operatorname{Re} \left\{ \hat{i}_{s,6n+1} e^{j(6n+1)\omega_1 t} \begin{bmatrix} 1 \\ -j \end{bmatrix} \right\} \quad (3.85)$$

When this set of currents is substituted in the damper voltage equation (the second expression of the set of equations (3.75)), the damper currents can be solved as

$$\vec{i}_{D,k}^s = -\sqrt{\frac{3}{2}} \sum_{n=-\infty}^{\infty} \operatorname{Re} \left\{ \frac{j(6n+1)\omega_1 L_k}{R_{D,k} + j(6n+1)\omega_1 L_k} \hat{i}_{s,6n+1} e^{j(6n+1)\omega_1 t} \begin{bmatrix} 1 \\ -j \end{bmatrix} \right\} \quad (3.86)$$

Substitution of equations (3.83), (3.85), and (3.86) in the stator voltage equation (the first equation of the set of (3.75)) results in

$$\vec{u}_s^s = \sqrt{\frac{3}{2}} \sum_{n=-\infty}^{\infty} \operatorname{Re} \left\{ \hat{u}_{s,6n+1} e^{j(6n+1)\omega_1 t} \begin{bmatrix} 1 \\ -j \end{bmatrix} \right\} \quad (3.87)$$

where

$$\hat{u}_{s,6n+1} = \hat{e}_{p,6n+1} + Z_{6n+1} \hat{i}_{s,6n+1}; \quad (3.88)$$

$$Z_{6n+1} = R_s + j(6n+1)\omega_1 L_\sigma + \sum_{k=1,5,7,11,\dots}^{\infty} \frac{j(6n+1)\omega_1 L_k R_{D,k}}{R_{D,k} + j(6n+1)\omega_1 L_k}$$

The equivalent circuit for the $|m|$ th ($m = 6n+1$) time harmonic is depicted in figure 3.8.

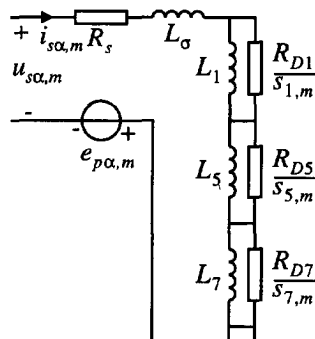


Figure 3.8: Equivalent circuit of the machine for the $|m|$ th time harmonic ($m = 6n+1$).

Application of the inverse Clarke-transformation (the transpose of equation (3.52)) to equation (3.87) results in

$$\vec{u}_s = \sum_{n=-\infty}^{\infty} \operatorname{Re} \left\{ \vec{u}_{s,6n+1} e^{j(6n+1)\omega_1 t} \begin{bmatrix} 1 \\ e^{-j\frac{2}{3}\pi} \\ e^{-j\frac{4}{3}\pi} \end{bmatrix} \right\} \quad (3.89)$$

This shows that the equivalent circuit for the three machine phases is the same as the equivalent circuit in the $\alpha\beta$ -system.

3.5.3 Equations for the locked-rotor tests

In this subsection, the impedance of the machine with locked rotor is calculated. The resistance and the inductance of this impedance depend on the frequency because of currents in the damper cylinder and eddy currents in the iron. This impedance is called the reflected impedance.

Figure 3.9 depicts the measurement circuit during the locked-rotor tests. The circuit is excited by an amplifier with a voltage u_{amp} . At low frequencies, the capacitance C is omitted. At high frequencies, the variable capacitance C is used to bring the circuit in resonance in order to reach sufficiently high voltages and currents. Often, locked-rotor tests are performed with symmetrical three-phase voltages. This is not done here, because with the single-phase system, it is possible to reach much higher frequencies and voltages.

Because phases b and c are connected in series (as depicted in figure 3.9), $i_{sc} = -i_{sb}$ and $u_{sb} - u_{sc} = u_{sbc}$ are valid. With the Clarke-transformation (equation (3.52)), the $\alpha\beta 0$ -components of the currents and voltages are calculated as

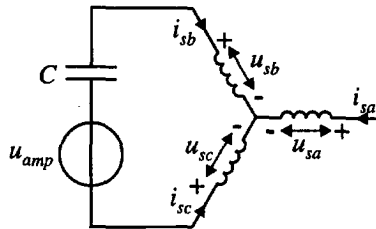


Figure 3.9: The measurement circuit. At low frequencies the variable capacitance C is omitted, while at high frequencies, it is used to bring the circuit in resonance.

$$\begin{bmatrix} i_{s\alpha} \\ i_{s\beta} \\ i_{s0} \end{bmatrix} = C_{23} \begin{bmatrix} 0 \\ i_{sb} \\ -i_{sb} \end{bmatrix} = \sqrt{2} \begin{bmatrix} 0 \\ i_{sb} \\ 0 \end{bmatrix} \tag{3.90}$$

$$\begin{bmatrix} u_{s\alpha} \\ u_{s\beta} \\ u_{s0} \end{bmatrix} = C_{23} \begin{bmatrix} 0 \\ u_{sb} \\ u_{sc} \end{bmatrix} = \frac{1}{2}\sqrt{2} \begin{bmatrix} 0 \\ u_{sb} - u_{sc} \\ 0 \end{bmatrix} = \frac{1}{2}\sqrt{2} \begin{bmatrix} 0 \\ u_{sbc} \\ 0 \end{bmatrix} \tag{3.91}$$

When it is used in the voltage equations (equation (3.75)) that the angular speed of the rotor Ω is zero, the voltage equations are given by

$$\begin{cases} \vec{u}_s^s = R_s \vec{i}_s^s + L_\sigma \frac{d\vec{i}_s^s}{dt} + \sum_{k=1,5,7,11,\dots}^{\infty} L_k \frac{d}{dt} (\vec{i}_s^s + \vec{i}_{D,k}^s) \\ 0 = R_{Dk} \vec{i}_{D,k}^s + L_k \frac{d}{dt} (\vec{i}_s^s + \vec{i}_{D,k}^s) \quad \text{for } k=1,5,7,11,\dots \end{cases} \tag{3.92}$$

The equivalent circuit representing the β -component of the voltage equations is depicted in figure 3.10. In this equivalent circuit, the first, the fifth, and the seventh space harmonic are depicted. For the other space harmonics, the equivalent circuit can be extended in the same way.

This equivalent circuit is equal to the equivalent circuit for a higher time harmonic (figure 3.8) if for the slip $s_{k,6n+1} = 1$ is used. This value for the slip follows when $\Omega = 0$ is substituted in the equation for the slip (equation (3.79)). So, when the rotor is locked, the voltage equation of equation (3.87) is not only valid for the balanced set of currents of equation (3.84), but also for a single-phase current. This is so because when the rotor is locked, the α - and the β -component of the voltage equation are completely independent, as can be seen from equation (3.92).

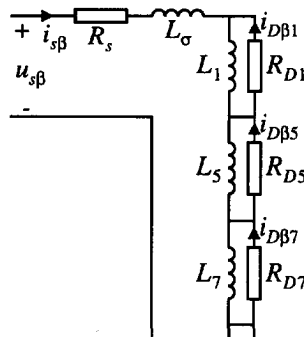


Figure 3.10: Equivalent circuit of the β -component of the voltage equation of the machine with locked rotor.

From the equivalent circuit of figure 3.10, it is concluded that the reflected impedance $Z(\omega)$ during the locked-rotor test is given by

$$Z(\omega) = \frac{\hat{u}_{sbc}(\omega)}{\hat{i}_{sb}(\omega)} = \frac{\sqrt{2}\hat{u}_{s\beta}(\omega)}{\frac{1}{2}\sqrt{2}\hat{i}_{s\beta}(\omega)} = 2 \left\{ R_s + j\omega L_\sigma + \sum_{k=1,5,7,11,\dots}^{\infty} \frac{j\omega L_k R_{Dk}}{R_{Dk} + j\omega L_k} \right\} \quad (3.93)$$

where equations (3.90) and (3.91) were used for the relation between the phase quantities and the quantities in the $\alpha\beta$ -system.

The reflected resistance is the real part of the impedance $Z(\omega)$, and the reflected inductance is the imaginary part divided by ω :

$$R(\omega) = \text{Re}(Z(\omega)) \quad ; \quad L(\omega) = \frac{1}{\omega} \text{Im}(Z(\omega)) \quad (3.94)$$

3.6 Experimental results of locked-rotor tests

This section describes some measurements, which partly verify the derived voltage equations. Firstly, this section describes the measurements of inductance and resistance. Next, the measurements are compared to the calculations of subsection 3.5.3, from which a conclusion is drawn.

The measurements

For the measurements, the test model (described in appendix A, section A.1) was used. The resistance and the inductance of this test model were measured as a function of the angular frequency ω in the following way. A sinusoidal voltage was supplied to phases b and c of the test model, which were connected in series (figure 3.9). The voltage U_{sbc} over the terminals of the test model, the current I_{sb} flowing through the phases of the test model, and the power P dissipated in the test model were measured. This was done for a wide frequency range. From the measured voltages, currents and powers, the resistance R and the inductance L are calculated as

$$R = \frac{P}{I_{sb}^2} \quad ; \quad L = \frac{1}{\omega} \sqrt{\left(\frac{U_{sbc}}{I_{sb}}\right)^2 - R^2} \quad (3.95)$$

At each frequency, the measurement was done with different root-mean-square values of the current, because hysteresis may cause non-linear behaviour.

Comparison of calculations and measurements

Figure 3.11 depicts the measured resistance and inductance as a function of the frequency. Also values calculated according to subsection 3.5.3 are depicted. In figure 3.11a and b, the value of the damper resistance of equation (3.72) is used.

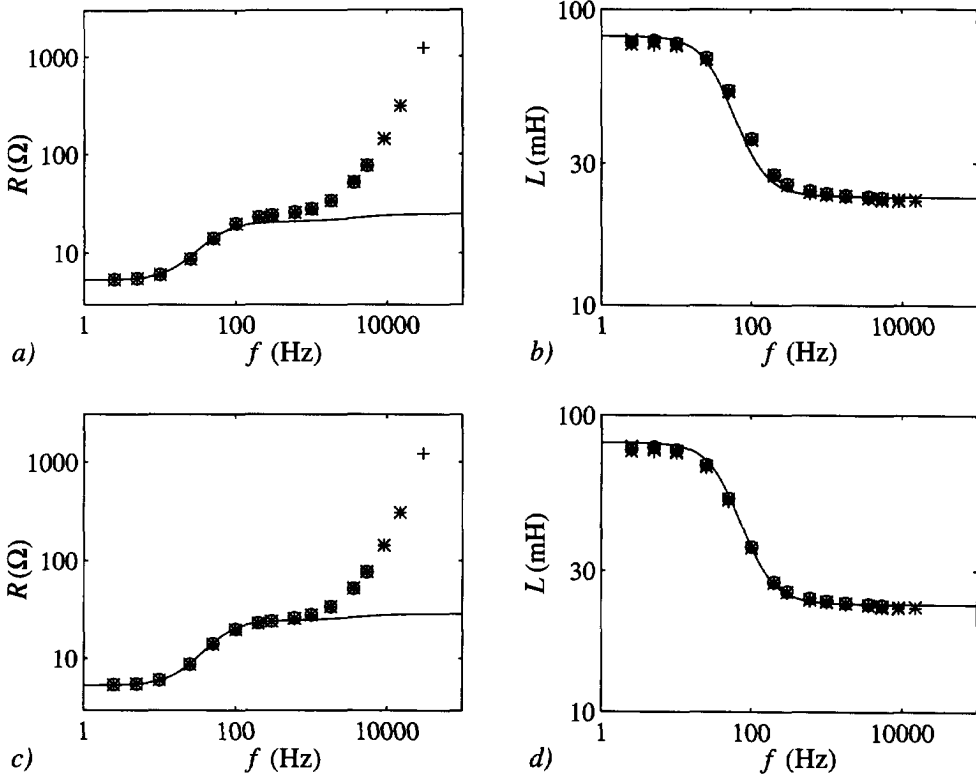


Figure 3.11: Resistance and inductance of the test model using a), c) the calculated and b), d) the (because of end connections) 25 % larger value of the damper resistance — : calculated, and +, x, *, o : measured with $I_{sb}=0.1A$, $I_{sb}=0.2A$, $I_{sb}=0.5A$, $I_{sb}=1A$, and $I_{sb}=2A$.

Comparison of the measured and calculated resistance shows a reasonable correlation at frequencies below 1 kHz. Above 1 kHz, the differences are much larger. Probably, this is caused by the iron losses and the increase of the stator resistance, as will be shown in chapter 4. Comparison of the measured and calculated inductance shows a reasonable correlation at all frequencies. This may seem strange, because the inductance is calculated with equation (3.95), using a value for the resistance which does not correlate at high frequencies. However, at these frequencies, the voltage across the resistance (RI_{sb}) is very small compared to the voltage across the terminals (U_{sbc}), so that the value of the resistance hardly effects the determination of the inductance.

Below 1 kHz, the correlation is reasonable, but there are differences. These differences are probably caused by the neglect of the resistance of the end connections. That the resistance of the end connections is the cause of this difference, is seen in figure 3.11c and d, where the correlation is very good. In these calculations, the resistance of the damper winding for the fundamental space harmonic is increased by

25 %. This is reasonable because of the form and the dimensions of the end connections.

This figure only tells something about the fundamental space harmonic, because the decrease of the inductance of the higher space harmonics is negligible and not visible in figure 3.11b and d. As a result of the higher space harmonics, there is a very small increase in the calculated resistance at frequencies above 1 kHz, as can be seen in figure 3.11a and c. However, above 1 kHz, the difference between the calculated and the measured resistance is so large, that the measurements do not verify the calculations. In the calculations, the first 19 space harmonics have been considered.

It can be concluded that the measurements of resistance and inductance verify the derived voltage equations for the fundamental space harmonic. Herewith, the derivation of L_1 and $R_{D,1}$ is verified. For the higher space harmonics, the voltage equations are neither verified, nor refuted.

3.7 Summary

In this chapter, the voltage equations of a permanent-magnet machine have been derived. This derivation was based on the assumptions used in chapter 2, and the expressions for the magnetic flux density derived in chapter 2, as summarized in section 2.6.

The voltage equations for the stator and the damper windings have been derived. It has been shown that the damper cylinder can be modelled as a series of short-circuited sinusoidally distributed damper windings. Next, the voltage equations have been transformed into the stator-connected $\alpha\beta$ -system, and the rotor quantities have been referred to the stator. The result is a set of voltage equations for the zero component (equation (3.66)) and for the $\alpha\beta$ -components (equation (3.75)) valid for any (varying) speed of the rotor and for any form of the stator currents.

These voltage equations were then transformed and worked out for the two situations which are considered in the rest of the thesis:

- 1) Subsection 3.5.2 has described the steady-state voltage equations of the rectifier-loaded machine. In chapter 4, the voltage equations will be extended with models of several kinds of losses to obtain a machine model suitable for the optimization of the design. In further chapters, this machine model will be combined with a model of the rectifier and it will be used for the analysis of the steady-state performance of the rectifier-loaded generator.
- 2) Subsection 3.5.3 has given the voltage equations for the locked-rotor tests. In section 3.6, these tests have been used to verify the derived voltage equations. In chapter 4, the machine model will be extended by including models of several kinds of losses, and these locked-rotor tests will be used to verify the models.

The derived voltage equations can also be used for a machine without a damper cylinder by making the damper currents zero.

Chapter 4

The losses in the generator

4.1 Introduction

Objective

In chapter 3, the voltage equations of the permanent-magnet generator have been derived, based on the two-dimensional calculation of the magnetic field in chapter 2. In this chapter, the calculated magnetic field and the derived voltage equations are used to derive a machine model including the most important losses in the generator. In later chapters, this machine model will be used for the analysis of the steady-state performance of the rectifier-loaded machine.

The voltage equations derived in chapter 3 form a model of the relation between the terminal voltages and the terminal currents of the machine. However, these voltage equations are not suitable for the optimization of the design of the generator, because losses that hardly influence the voltage equations have been ignored:

- In chapter 2, effects that hardly influence the magnetic field, such as eddy currents in the iron and the magnets and the slotting of the stator, have been neglected. However, the losses due to these effects may be significant.
- In chapter 2 and 3, skin effect in the stator conductors and the damper cylinder has been neglected, but skin effect may increase the copper loss considerably.

Therefore, in this chapter, the voltage equations are extended with models of the most important losses in the machine to obtain a machine model suitable for the optimization of the design. Five kinds of losses are considered:

- 1) the damper copper loss caused by the stator currents,
- 2) the stator copper loss,
- 3) the iron loss,
- 4) the eddy-current loss in the magnets caused by the stator currents, and
- 5) the loss in the damper cylinder and the magnets due to the stator slotting.

As explained in section 2.1, skin effect in the damper cylinder is neglected.

Often, the iron loss in an electric machine is represented by 'iron loss resistances' connected in parallel to inductances in the equivalent circuit of the machine. In this way, the dependence of the iron loss on the magnetic flux density is replaced by a dependence

on the voltage across an inductance, which has two advantages:

- 1) The calculation of voltages in an equivalent circuit is easier than the calculation of a magnetic field, which is a summation of contributions of different sources of magnetic field.
- 2) Iron loss resistances provide more insight than a number representing the iron loss. This approach is followed here, not only for the iron loss, but also for the eddy-current loss in the magnets. Hence, the models of the iron loss and the eddy-current loss in the magnets are worked out in such a way that they can be represented by resistances in an equivalent circuit.

It should be noted that in a machine with rectifier load, there are losses because of travelling waves, which are combinations of space harmonics and time harmonics.

In this chapter, the losses are only calculated for the two situations mentioned in section 3.5, namely steady-state operation with rectifier load and locked-rotor tests. Locked-rotor tests are considered, because as far as possible, they are used to verify the models derived in this chapter.

Outline of the chapter

Section 4.2 describes the frequency-dependence of the stator resistance because of skin effect. Next, in section 4.3, expressions for the iron loss are derived and partly verified by means of locked-rotor tests. Section 4.4, describes the derivation of expressions for the eddy-current loss in the magnets. These expressions are also partly verified by means of locked-rotor tests. Subsequently, section 4.5 describes the losses due to the stator slotting. In conclusion, section 4.6 summarizes the results obtained. Because the derivation of each model requires its own assumptions, these assumptions are discussed in the section where the model is derived.

In the last part of this section, it is shown that the losses caused by a travelling wave can be calculated as the superposition of the losses caused by two pulsating fields. This is shown here, because it is used in sections 4.3 and 4.4.

Losses because of travelling waves and pulsating fields

A travelling wave (compare equation (2.40)) of magnetic flux density can be written as the sum of two pulsating fields in two perpendicular axes:

$$\hat{B}_{r,k} \cos(pk\alpha - \omega t) = \hat{B}_{r,k} \cos(pk\alpha) \cos(\omega t) + \hat{B}_{r,k} \sin(pk\alpha) \sin(\omega t) \quad (4.1)$$

When the travelling wave is written as a function of the stator coordinate, the perpendicular axes are the α - and the β -axis; when the travelling wave is written as a function of the rotor coordinate, the perpendicular axes are the direct and the quadrature axis.

In sections 4.3 and 4.4, it is shown that the iron loss and the eddy-current loss in the magnets are

- proportional to the square of the magnetic flux density, and
- calculated by integration over the angular coordinate α .

Integrating the square of the left side of equation (4.1) results in

$$\int_0^{2\pi} (\hat{B}_{r,k} \cos(pk\alpha - \omega t))^2 d\alpha = \pi \hat{B}_{r,k}^2 \quad (4.2)$$

Integrating the square of the right side of equation (4.1) results in

$$\begin{aligned} \int_0^{2\pi} (\hat{B}_{r,k} \cos(pk\alpha) \cos(\omega t) + \hat{B}_{r,k} \sin(pk\alpha) \sin(\omega t))^2 d\alpha \\ = \hat{B}_{r,k}^2 \int_0^{2\pi} \cos^2(pk\alpha) \cos^2(\omega t) + \sin^2(pk\alpha) \sin^2(\omega t) \\ + \cos(pk\alpha) \cos(\omega t) \sin(pk\alpha) \sin(\omega t) d\alpha \\ = \hat{B}_{r,k}^2 \int_0^{2\pi} \cos^2(pk\alpha) \cos^2(\omega t) + \sin^2(pk\alpha) \sin^2(\omega t) d\alpha = \pi \hat{B}_{r,k}^2 \end{aligned} \quad (4.3)$$

The second is-equal-to sign in this equation is valid because the average of the product of a sinus and a cosinus is zero, and therefore, the integral from 0 to 2π is zero.

The results of both integrations are equal. This shows that the losses caused by travelling waves can be calculated as the sum of the losses caused by two pulsating fields in perpendicular axes, which is used in sections 4.3 and 4.4.

4.2 The stator copper loss

This section describes how the stator resistance depends on the frequency because of skin effect. Often, skin effect in the stator conductors is neglected. If it is not neglected, Richter's expressions [Ric 67] are usually used, as is done, for example, in [Dem 87] and [Buc 79]. Here, these expressions are also used.

A part of the stator windings lays in slots, the other part, the end windings, is situated in air. It is assumed that the increase of the resistance of the end windings is negligible compared to the increase of the resistance of the part of the windings laying in the stator slots, because the magnetic field in the slots is higher than the magnetic field in the end winding regions.

In rectangular slots with rectangular conductors, the ratio of the resistance at angular frequency ω to the resistance at angular frequency zero is (see [Ric 67] and [Dem 87])

$$k_{slot} = \xi \frac{\sinh(2\xi) + \sin(2\xi)}{\cosh(2\xi) - \cos(2\xi)} + \frac{m_{slot}^2 - 1}{3} 2\xi \frac{\sinh(\xi) - \sin(\xi)}{\cosh(\xi) + \cos(\xi)} \quad (4.4)$$

where

$$\xi = h_c \sqrt{\frac{\mu_0 n_{slot} b_c \omega}{2 b_{slot} \rho_{Cu}}} \quad (4.5)$$

where (see figure 4.1)

- m_{slot} is the number of layers of conductors above each other in a slot,
 n_{slot} is the number of rows of conductors next to each other in a slot,
 b_{slot} is the slot width,
 h_c is the height of a rectangular stator conductor,
 b_c is the width of a rectangular stator conductor, and
 ρ_{Cu} is the resistivity of the stator copper.

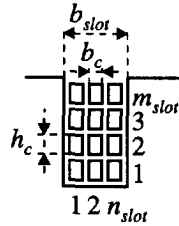


Figure 4.1: A rectangular slot with rectangular conductors.

To calculate the increase of the stator resistance, two facts have to be considered.

- 1) For conductors which are not rectangular, the expression has to be corrected. The correction factor is called k_{shape} , and it has the value 0.46 for round conductors [Dem 87], [Ric 15].
- 2) This increase of the stator resistance is only present in the part of the stator winding laying in slots. In the other part of the winding, consisting of end windings, the increase of the resistance was assumed to be negligible.

Herewith, the stator resistance at angular frequency ω is given by

$$R_s(\omega) = \left(1 + \frac{l_s}{l_{ew} + l_s} k_{shape} (k_{slot}(\omega) - 1) \right) R_s(0) \quad (4.6)$$

where the ratio $l_s / (l_{ew} + l_s)$ is the part of the length of the stator windings that lays in slots, with l_s the stack length of the machine, and l_{ew} the length of the end windings.

For the stator resistance during locked-rotor tests, this expression suffices. For the stator resistance during steady-state operation with rectifier load, it is written as

$$R_{s,6n+1} = R_s(|6n+1| \omega_1) = \left(1 + \frac{l_s}{l_{ew} + l_s} k_{shape} (k_{slot}(|6n+1| \omega_1) - 1) \right) R_s(0) \quad (4.7)$$

4.3 The iron loss

4.3.1 Introduction

Objective

The aim of this section is to derive expressions for the iron loss in the laminated stator and the laminated rotor of a permanent-magnet machine. Chapter 7 will discuss machines with solid rotor iron. The calculation of the iron loss is based on the expressions for the magnetic flux density in the air gap and the magnets derived in chapters 2 and 3. These magnetic fields were calculated on the assumption of a smooth stator surface. Although the real machine has stator slots, the expressions for the field derived for a machine without slots can be used, as is shown in this section.

Throughout the section, it is assumed that the effect of eddy currents in the iron on the magnetic field in the air gap is negligible, as shown in appendix C, section C.1.

Outline of this section

The iron loss is divided into three parts, namely the core loss in the stator, the core loss in the rotor and the stray load loss. Firstly, subsection 4.3.2 describes an expression for the specific iron loss, starting from the literature. In the next three subsections (4.3.3, 4.3.4, and 4.3.5) the three parts of the iron loss are quantified. These subsections also explain which assumptions are used to obtain the resulting expressions. Next, subsection 4.3.6 describes some locked-rotor tests, which partly verify the derived expressions. Concluding remarks are made in subsection 4.3.7.

4.3.2 The specific iron loss

This subsection gives an expression for the specific iron loss. In literature, the iron loss in laminated cores is calculated in different ways. Firstly, the classical and the modern literature is discussed. Next, a description is given of how the expression for the specific iron loss used in this thesis is obtained.

Classical literature

The most commonly used model for the iron loss separates the hysteresis loss $P_{Fe,h}$ and the eddy-current loss $P_{Fe,e}$ [Ric 67], [Cul 72], [Sen 89], [Wah 91], [Sle 90], [Hen 94]:

$$P_{Fe} = P_{Fe,h} + P_{Fe,e} \quad (4.8)$$

In this equation, the hysteresis loss $P_{Fe,h}$ is given by

$$P_{Fe,h} \propto \omega \hat{B}^S \quad (4.9)$$

where S is the Steinmetz constant, which lays between 1.5 and 2.3 ($1.5 < S < 2.3$) dependent on the material. Often a value of $S=2$ is used.

When the magnetic flux density does not vary sinusoidally, the hysteresis loss can not be calculated as the sum of the hysteresis losses produced by the different time harmonics. In this case, [Lav 78] describes how to calculate the hysteresis loss, but this is fairly complicated. Mathematical descriptions of hysteresis are mainly based on the Preisach model [Pre 35], [May 86], [Zhu 96].

At low frequencies (up to about 1 kHz), the effect of eddy currents on the magnetic field in the laminations is negligible, and the eddy-current loss is proportional to ω^2 . At high frequencies (above about 1 kHz), the effect of eddy currents on the magnetic field in the laminations is not negligible, and the eddy-current loss is proportional to $\omega^{1.5}$. Hence, the eddy-current loss $P_{Fe,e}$ is given by

$$P_{Fe,e} \propto \begin{cases} \omega^2 \hat{B}^2 & \text{at low frequencies} \\ \omega^{1.5} \hat{B}^2 & \text{at high frequencies} \end{cases} \quad (4.10)$$

as shown in appendix C, section C.1, and in many books, for example, [Ric 67], [Sto 74]. For magnetic flux densities with higher time harmonics, the contributions caused by the different time harmonics can be added, because eddy currents are linear.

Modern literature

The commonly used model considering hysteresis and eddy-current loss is not completely satisfactory, because the measured iron loss is much higher than theoretically calculated. This is so because it assumes a homogenous magnetization of the laminations, which is not a valid representation of what happens during the magnetization process. Therefore, a better model of the iron loss is obtained by considering magnetic domains, the magnetic domain walls (Bloch walls) of which move when the magnetic flux density changes. The loss caused by the movements of the magnetic domain walls is higher than the loss calculated with the commonly used model.

The difference between measured and calculated loss is called the excess loss or the anomalous loss $P_{Fe,a}$. Sometimes, this anomalous or excess loss is considered as a third contribution to the iron loss [Pry 58], [Cul 72], [Ber 88], [Pfü 91], [Zhu 93e], [Ami 95]. With this third contribution, the iron loss is given by

$$P_{Fe} = P_{Fe,h} + P_{Fe,e} + P_{Fe,a} \quad (4.11)$$

Great efforts have been made to calculate this excess loss, as indicated in, for example, [Ber 88], [Pfü 91], and [Zhu 93e]. Because of the complexity of the domain patterns and the domain wall movements, success has been limited until now. However, many authors find that Bertotti [Ber 88], [Ber 92] derived a satisfying model for the calculation of the excess loss. It is based on a dynamic generalization of the Preisach model for hysteresis. In [Fio 90b], this theory is worked out to a simple expression for the excess loss $P_{Fe,a}$, which is given by

$$P_{Fe,a} \propto \frac{1}{T} \int \left| \frac{dB}{dt} \right|^{1.5} dt \quad (4.12)$$

This expression is used, for example, in [Fio 90a], [Zhu 93e], [Zhu 96], [Ata 94], [Jil 94], and [Ama 95]. When the magnetic flux density varies sinusoidally, the excess loss is proportional to $\omega^{1.5} \hat{B}^{1.5}$ (compare equation (4.12)). For other waveforms, the calculation of the excess loss is a complicated subject.

As already mentioned, for non-sinusoidal waveforms, the calculation of the hysteresis loss and the excess loss is fairly complicated. However, even with these complicated models, the results of the prediction of the iron loss in electrical machines are poor. Two important reasons for this are mentioned.

- 1) The punching of the laminations strongly influences the material properties.
- 2) It is hard to predict the magnetic flux density distribution in the teeth and yokes. There are several ways to solve this problem.
 - 1) Empirical correction factors are inserted into the equations for the losses [Ric 67].
 - 2) The equations for the losses are used in combination with Finite Element Methods, which give an approximation of the magnetic flux density distribution. In, for example, [Ber 91], [Zhu 92] and [Ata 94], quite accurate results are reported.

This thesis

From this brief literature survey, it can be concluded that it is not possible to derive simple and exact analytical expressions for the iron loss in an electric machine. Besides, it is not the aim of this thesis to make a detailed investigation of the iron loss. Therefore, in this study, a simple expression for the specific iron loss (the loss per unit of mass) is used, which is comparable to the expression used in [Buc 84]:

$$k_{Fe} = c_{Fe} k_{Fe,0} \left(\frac{\omega}{\omega_0} \right)^{1.5} \left(\frac{\hat{B}}{\hat{B}_0} \right)^2 \quad (4.13)$$

where

$k_{Fe,0}$ is the specific iron loss (dimension: W/kg) at a given angular frequency ω_0 and magnetic flux density \hat{B}_0 provided by the manufacturer, and

c_{Fe} is a dimensionless empirical correction factor.

To obtain accurate results, the specific iron loss $k_{Fe,0}$ should be given at the fundamental frequency, because the major part of the iron loss arises at this frequency. The empirical correction factor c_{Fe} includes effects of material processing and flux density distribution. Often, for example, in [Ric 67], different correction factors are used for the losses in the teeth (where the field mainly pulsates) and the yokes (where the field also rotates). However, in this thesis, one empirical correction factor c_{Fe} is used, because from measurements, it is difficult to separate the iron loss into loss in the yokes and loss in the teeth. Furthermore, in this thesis, only values for the product $c_{Fe} k_{Fe,0}$ are used.

The claim that equation (4.13) is a reliable expression for the iron loss, can be made plausible by comparing it to the equations for the hysteresis, the eddy-current and the

excess loss:

- 1) At high frequencies, the iron loss is dominated by the eddy-current loss and the excess loss, because they increase faster with the frequency than the hysteresis loss and at 100 Hz they are comparable. At high frequencies, the eddy-current loss and the excess loss both increase with $\omega^{1.5}$.
- 2) At medium frequencies, equation (4.13) is an approximation of the sum of the three contributions.
- 3) At low frequencies, equation (4.13) is not satisfactory. However, in high-speed permanent-magnet machines, this is unimportant.

The measurements reported in [Buc 84] and in subsection 4.3.6 verify this equation for frequencies above approximately 300 Hz.

It is assumed that the iron loss is linear, which means that the total loss can be calculated by adding the losses caused by the different time harmonics. Later, it will be seen that on particular assumptions this is also valid for the space harmonics. Although it is not valid for the hysteresis and excess loss, this assumption is reasonable, because at the frequencies of the higher time harmonics, the eddy-current loss is the major part.

4.3.3 The stator core loss

In this subsection, the core loss in the stator is calculated. Firstly, there is a description of which space harmonics are neglected. Next, the core loss in the stator teeth and in the stator yoke is calculated. This is done for a sinusoidally pulsating field in the α -axis. From the calculated loss, a core loss resistance is calculated. The same could be done for a pulsating field in the β -axis. However, the result would be the same because of the symmetry of the machine. Therefore, the resistance calculated for the α -axis is also used for the β -axis.

For the description of the magnetic flux density in the stator iron, figure 4.2 is used. The number of slots per pole per phase q of this machine is 3. With this, the number of teeth of a three phase stator is calculated as $6pq$. The stator teeth are numbered from 1 to $6pq$, and the axis of the l th stator tooth lays at stator coordinate $\alpha_{st,l}$, where the subscript st stands for stator tooth. The slot angle is given by

$$\beta_{slot} = \frac{\pi}{3pq} \quad (4.14)$$

Neglect of core loss caused by space harmonics

This subsection is based on the following assumptions.

- 1) The stator core loss due to the space harmonics of the magnetic flux density with a pole angle $\alpha_{p,k}$ (introduced in equation (2.23)) smaller than or equal to a slot angle β_{slot} is negligible compared to the loss due to the fundamental space harmonic. This assumption is reasonable, because for the fundamental space

harmonic, the magnetic field goes through the stator teeth and the stator yoke, causing loss in the whole stator iron. The magnetic fields with a very small pole angle hardly enter the stator teeth, because the field lines close in the surface of the teeth. Therefore, these space harmonics with a small pole angle hardly cause any loss.

As long as the pole angle of the space harmonics is larger than the slot angle, the fields flow through the stator teeth and the stator yoke. Therefore, in this thesis, the loss caused by these space harmonics is considered. For these harmonics, the pole angle (equation (2.23)) is larger than the slot angle (equation (4.14)):

$$\alpha_{p,k} > \beta_{slot} \rightarrow \frac{\pi}{pk} > \frac{\pi}{3pq} \rightarrow k < 3q \quad (4.15)$$

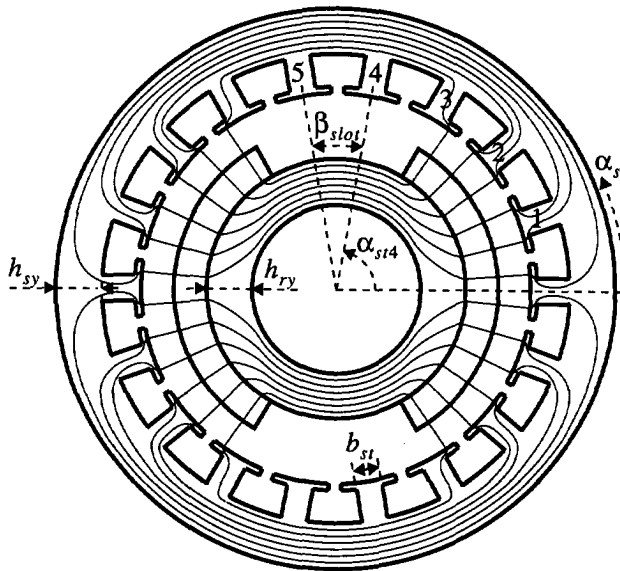


Figure 4.2: Sketch of the flux lines in the permanent-magnet machine.

- 2) The stator core loss caused by the higher space harmonics of the fields of the stator and the damper currents is negligible compared to the loss caused by the fundamental space harmonic of this field.
- This assumption is reasonable for a permanent-magnet machine without a damper cylinder, as can be concluded from figure 2.11. This figure shows that the amplitudes of the higher space harmonics of the magnetic flux density produced by the stator currents at the stator surface $\hat{B}_{rs,k}(r_s)$ are small compared to the amplitude of the fundamental space harmonic $\hat{B}_{rs,1}(r_s)$. Therefore, the loss resulting from these higher space harmonics is negligible compared to that resulting from the fundamental space harmonic.

- This assumption is also reasonable for a permanent-magnet machine with damper cylinder. In this case, the sum of the magnetic fields of the stator currents and the damper currents is smaller than that of the stator currents alone, because of the damping of the damper cylinder. Therefore, the loss due to the higher space harmonics of the fields of the stator and the damper currents remains negligible compared to the loss due to the fundamental space harmonic.

When the rotor rotates, the core loss caused by the higher space harmonics of the magnetic field of the magnets is not negligible (as also shown in [Sle 90]). As can be seen in figure 2.6, the amplitude of the k th space harmonic $\hat{B}_{m,k}(r_s)$ of the magnetic flux density is smaller than or equal to $\hat{B}_{m,1}(r_s)/k$. The angular frequency ω_k experienced by the stator from the k th space harmonic of the magnetic flux density produced by the magnets is proportional to k . (This is not the case for the frequency experienced by the stator from the space harmonics of the stator currents, which all have the same frequency.) With this, the ratio of the loss caused by the k th space harmonic to that caused by the fundamental space harmonic is given by

$$\frac{P_{sFe,k}}{P_{sFe,1}} = \frac{\hat{B}_{m,k}^2(r_s) \omega_k^{1.5}}{\hat{B}_{m,1}^2(r_s) \omega_1^{1.5}} \leq \frac{1}{\sqrt{k}} \quad (4.16)$$

It should be noted that, in contrast to the field of the stator currents, the field of the magnets also contains space harmonics of which the harmonic number k is an integer multiple of three, as can be seen in equation (2.60).

The core loss in the stator teeth caused by a pulsating field

The stator core loss is calculated for a field in the α -axis pulsating sinusoidally with angular frequency ω . $\vec{B}(r, \alpha_s - \pi/p) = -\vec{B}(r, \alpha_s)$ (equation (3.1)) is also valid. Furthermore, only the loss produced by the space harmonics with a pole angle larger than the slot angle are considered: $k < 3q$ (as expressed by equation (4.15)). With this, the radial component of the magnetic flux density at the stator surface can be written as the following Fourier series:

$$B_{r\alpha}(r_s, \alpha_s, t) = \sum_{k=1,3,5,\dots}^{3q-1} \hat{B}_{r\alpha,k}(r_s) \cos(pk\alpha_s) \sin(\omega t) \quad (4.17)$$

The magnetic flux density in the l th stator tooth $B_{st,l}(t)$ is calculated from the radial component of the magnetic flux density in the air gap at the stator surface $B_{r\alpha}(r_s, \alpha_s, t)$. The following assumptions are used.

- The tooth width b_{st} is not a function of the radius, as indicated in figure 4.2.
- The magnetic flux density $B_{st}(\alpha_s, t)$ has only a component parallel to the sides of the stator teeth, other components are neglected.
- The number of stator slots is high.
- The pole angle $\alpha_{p,k}$ of the space harmonics is large compared to the slot angle

β_{slot} .

The flux flowing through one slot pitch $\beta_{slot} r_s$ at the stator surface has to flow through a tooth with width b_{st} . Because the pole angle $\alpha_{p,k}$ is large compared to the slot angle β_{slot} , the magnetic flux density in the l th stator tooth is calculated as

$$B_{st,l}(t) = \frac{\beta_{slot} r_s}{b_{st}} B_{ra}(r_s, \alpha_{st,l}, t) = \sum_{k=1,3,5,\dots}^{3q-1} \frac{\beta_{slot} r_s}{b_{st}} \hat{B}_{ra,k}(r_s) \cos(pk\alpha_{st,l}) \sin(\omega t) \quad (4.18)$$

The amplitude of this magnetic flux density is used in equation (4.13) to calculate the specific iron loss in the l th stator tooth:

$$k_{Fe,l} = c_{Fe} k_{Fe,0} \left(\frac{\omega}{\omega_0} \right)^{1.5} \left(\sum_{k=1,3,5,\dots}^{3q-1} \frac{r_s \beta_{slot}}{b_{st}} \frac{\hat{B}_{ra,k}(r_s)}{\hat{B}_0} \cos(pk\alpha_{st,l}) \right)^2 \quad (4.19)$$

Multiplication of this expression by the mass of a stator tooth $m_{st}/(6pq)$ (where m_{st} is the mass of all $6pq$ stator teeth together) gives the iron loss in the l th stator tooth. Summation over all stator teeth results in the total iron loss in the stator teeth:

$$\begin{aligned} P_{stFe}(\omega) &= \sum_{l=1}^{6pq} \frac{m_{st}}{6pq} k_{Fe,l} \\ &= \frac{m_{st}}{6pq} c_{Fe} k_{Fe,0} \left(\frac{\omega}{\omega_0} \right)^{1.5} \sum_{l=1}^{6pq} \left(\sum_{k=1,3,5,\dots}^{3q-1} \frac{r_s \beta_{slot}}{b_{st}} \frac{\hat{B}_{ra,k}(r_s)}{\hat{B}_0} \cos(pk\alpha_{st,l}) \right)^2 \\ &\approx m_{st} c_{Fe} k_{Fe,0} \left(\frac{\omega}{\omega_0} \right)^{1.5} \frac{1}{2\pi} \int_0^{2\pi} \left(\sum_{k=1,3,5,\dots}^{3q-1} \frac{r_s \beta_{slot}}{b_{st}} \frac{\hat{B}_{ra,k}(r_s)}{\hat{B}_0} \cos(pk\alpha_s) \right)^2 d\alpha_s \end{aligned} \quad (4.20)$$

The approximation in the last step of this equation is based on the assumption that the number of stator slots is large. If the series between the parentheses is written out and squared, the result is a series of products of cosinusoidal functions of the stator coordinate. The integral from 0 to 2π of these products is only different from zero if the sinusoidal functions have the same harmonic number k . Therefore, the total iron loss in the stator teeth is given by

$$P_{stFe}(\omega) = m_{st} c_{Fe} k_{Fe,0} \left(\frac{\omega}{\omega_0} \right)^{1.5} \frac{1}{2} \sum_{k=1,3,5,\dots}^{3q-1} \left(\frac{r_s \beta_{slot}}{b_{st}} \right)^2 \left(\frac{\hat{B}_{ra,k}(r_s)}{\hat{B}_0} \right)^2 \quad (4.21)$$

This shows that the iron loss in the stator teeth can be calculated as a superposition of the losses caused by the different space harmonics.

The core loss in the stator yoke due to a pulsating field

The magnetic flux density in the stator yoke $B_{sy}(\alpha_s, t)$ (where the subscript sy stands for stator yoke) is calculated from the radial component of the magnetic flux density in the air gap at the stator surface $B_{ra}(r_s, \alpha_s, t)$. The flux density in the stator yoke $B_{sy}(\alpha_s, t)$ is assumed to have only a tangential component; radial components are neglected. The

air-gap flux flowing through the stator surface between the stator coordinates 0 and α_s , has to flow through the stator yoke with height h_{sy} at stator coordinate α_s , as illustrated in figure 4.2:

$$B_{sy}(\alpha_s, t) = \frac{1}{h_{sy}} \int_0^{\alpha_s} B_{ra}(r_s, \alpha', t) r_s d\alpha' = \sum_{k=1,3,5,\dots}^{3q-1} \frac{r_s}{pkh_{sy}} \hat{B}_{ra,k}(r_s) \sin(pk\alpha_s) \sin(\omega t) \quad (4.22)$$

In the stator yoke, the magnetic flux density has its maximum at another place than in the air gap, as also appears from figure 4.2.

The amplitude of this magnetic flux density is used in equation (4.13). In this way, the specific iron loss in the stator yoke is calculated as

$$k_{Fe}(\alpha_s) = c_{Fe} k_{Fe,0} \left(\frac{\omega}{\omega_0} \right)^{1.5} \left(\sum_{k=1,3,5,\dots}^{3q-1} \frac{\hat{B}_{ra,k}(r_s)}{\hat{B}_0} \frac{r_s}{pkh_{sy}} \sin(pk\alpha_s) \right)^2 \quad (4.23)$$

This expression is only a function of the stator coordinate α_s , and not of the axial and the radial position. When this specific loss is averaged over the stator coordinate, and multiplied by the mass of the stator yoke m_{sy} , the iron loss in the stator yoke is calculated:

$$\begin{aligned} P_{sFe}(\omega) &= m_{sy} c_{Fe} k_{Fe,0} \left(\frac{\omega}{\omega_0} \right)^{1.5} \frac{1}{2\pi} \int_0^{2\pi} \left(\sum_{k=1,3,5,\dots}^{3q-1} \frac{\hat{B}_{ra,k}(r_s)}{\hat{B}_0} \frac{r_s}{pkh_{sy}} \sin(pk\alpha_s) \right)^2 d\alpha_s \\ &= m_{sy} c_{Fe} k_{Fe,0} \left(\frac{\omega}{\omega_0} \right)^{1.5} \frac{1}{2} \sum_{k=1,3,5,\dots}^{3q-1} \left(\frac{\hat{B}_{ra,k}(r_s)}{\hat{B}_0} \right)^2 \left(\frac{r_s}{pkh_{sy}} \right)^2 \end{aligned} \quad (4.24)$$

Again, the second step in this equation is valid, because the square of a series of sinusoidal functions is a series of products of sinusoidal functions, and the integral from 0 to 2π of these products is only different from zero if both sinusoidal functions have the same harmonic number k . And again, this shows that the iron loss can be calculated as a superposition of the losses caused by the different space harmonics.

The total stator core loss is calculated by adding the contributions of the stator teeth (equation (4.21)) and the stator yoke (equation (4.24)):

$$\begin{aligned} P_{sFe}(\omega) &= \sum_{k=1,3,5,\dots}^{3q-1} P_{sFe,k}(\omega) \\ P_{sFe,k}(\omega) &= \frac{1}{2} c_{Fe} k_{Fe,0} \left(\frac{\omega}{\omega_0} \right)^{1.5} \left(\frac{\hat{B}_{r,k}(r_s)}{\hat{B}_0} \right)^2 \left\{ m_{st} \left(\frac{\beta_{slot} r_s}{b_{st}} \right)^2 + m_{sy} \left(\frac{r_s}{pkh_{sy}} \right)^2 \right\} \end{aligned} \quad (4.25)$$

The stator core loss resistance

For reasons mentioned in section 4.1, it is useful to represent the stator core loss by core loss resistances, which are placed in equivalent circuits. However, this is only

useful for the fundamental space harmonic, and not for the higher space harmonics because the core loss caused by the higher space harmonics of the fields of the stator and the damper currents is neglected. So, this loss is independent of the stator currents; it only depends on the geometry of the machine and the speed of the rotor. Therefore, only the stator core loss caused by the fundamental space harmonic of the magnetic flux density is represented by a core loss resistance. The loss resulting from the space harmonics of the magnetic flux density produced by the magnets are calculated with equation (4.25).

To calculate the stator core loss resistance, first, the flux linkages of the fundamental space harmonic of the winding distributions of the three stator phases resulting from the magnetic flux density of equation (4.17) are calculated. This is done in the same way as in subsection 3.2.3. The result is (compare equation (3.13); there still is only a component in the α -axis)

$$\Psi_{s,1} = \frac{\pi l_s r_s N_{s,1}}{2p} \hat{B}_{ra,1}(r_s) \frac{1}{2} \begin{bmatrix} 2 \\ -1 \\ -1 \end{bmatrix} \sin(\omega t) \quad (4.26)$$

With the Clarke transformation (equation (3.52)), this flux linkage is transformed to the stator-connected $\alpha\beta 0$ -system. The time derivative of this flux linkage is the voltage in the $\alpha\beta 0$ -system, which has only an α -component:

$$u_{RsFe} = \frac{d\Psi_{s\alpha,1}}{dt} = \sqrt{\frac{3}{2}} \frac{\pi l_s r_s N_{s,1}}{2p} \hat{B}_{ra,1}(r_s) \omega \cos(\omega t) = \hat{u}_{RsFe} \cos(\omega t) \quad (4.27)$$

When this voltage is indicated in the equivalent circuit of figure 3.4, the equivalent circuit of figure 4.3 results. In this figure, the no-load voltage is divided into the contributions induced in the different space harmonics of the winding distribution. The voltage induced in the fundamental space harmonic of the winding distribution consists of the contributions of the magnets, the stator currents and the damper currents. The contribution of the magnets is represented by the no-load voltage.

The stator core loss resistance is connected across the voltage u_{RsFe} . Therefore, the power dissipated in this resistance is

$$P_{sFe,1}(\omega) = \frac{\hat{u}_{RsFe}^2}{2R_{sFe}(\omega)} \Rightarrow R_{sFe}(\omega) = \frac{\hat{u}_{RsFe}^2}{2P_{sFe,1}(\omega)} \quad (4.28)$$

There is a factor 2 in the denominator because in the numerator, the amplitude of the voltage is used.

The stator core loss resistance $R_{sFe}(\omega)$ must have such a value that the average loss dissipated in this resistance is equal to the stator core loss. Therefore, the value of this resistance follows when equations (4.25) and (4.27) are used in equation (4.28):

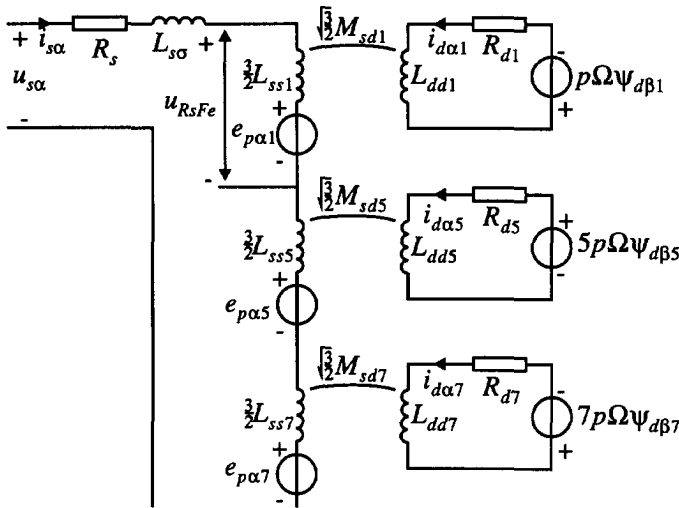


Figure 4.3: The equivalent circuit with an indication of the voltage u_{RsFe} .

$$R_{sFe}(\omega) = \frac{3\pi^2 l_s^2 N_{s,1}^2 \sqrt{\omega}}{8c_{Fe} k_{Fe,0} \left(\frac{1}{\omega_0}\right)^{1.5} \left(\frac{1}{\hat{B}_0}\right)^2 \left\{ m_{st} \left(\frac{p\beta_{slot}}{b_{st}}\right)^2 + m_{sy} \left(\frac{1}{h_{sy}}\right)^2 \right\}} \quad (4.29)$$

When this core loss resistance is depicted in an equivalent circuit, it should be noted that the resistance is frequency dependent. Therefore, this core loss resistance can only be used in equivalent circuits which represent one frequency.

Adding this resistance to the equivalent circuits of figure 3.10 results in the equivalent circuit of figure 4.4c. Adding this resistance to the equivalent circuit of figure 3.8 results in the equivalent circuit of figure 4.4a for the fundamental time harmonic and in the equivalent circuit of figure 4.4b for the higher time harmonics, as will be explained further. The travelling wave resulting from the fundamental time harmonic of the stator currents and the fundamental space harmonic of the winding distribution rotates with the same speed as the rotor. Therefore, it does not cause currents in the damper cylinder, and the damper resistance $R_{D,1}$ in figure 3.8 has been omitted in figure 4.4a. Furthermore, during steady-state operation with rectifier load, the no-load voltage induced in the fundamental space harmonic of the winding distribution has the fundamental frequency. Therefore, it appears in the equivalent circuit for the fundamental time harmonic (figure 4.4a), and it does not appear in the equivalent circuit for the higher time harmonics (figure 4.4b).

The core loss resistance is not only connected in parallel to L_1 , but also in parallel to a part of the inductance L_σ , for two reasons:

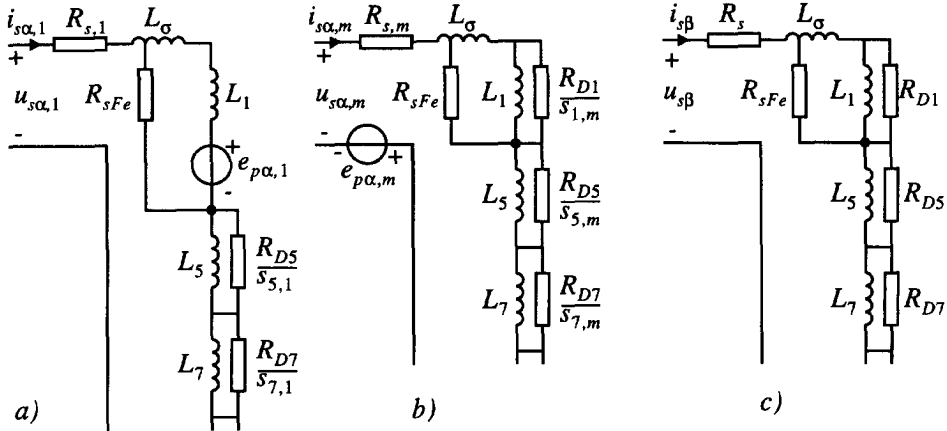


Figure 4.4: The equivalent circuit including the stator core loss, a) for the fundamental time harmonic and b) for the higher time harmonics during steady-state operation with rectifier ($m = 6n + 1$), and c) for the locked-rotor tests.

- 1) When the damper quantities are referred to the stator (as in subsection 3.4.2), a part of the inductance $3/2L_{ss,1}$ (in figure 4.3) is included in the inductance L_{σ} , namely the part $L_{g\sigma,1}$ introduced in equation (3.74).
- 2) The magnetic flux density in the stator iron is further increased by the slot leakage. This slot leakage is represented by a part of inductance $L_{s\sigma}$ in figure 4.3, and by a part of inductance L_{σ} in figure 4.4.

In the literature about induction machines, the stator core loss is often modelled as a resistance parallel to only the main inductance [Ven 82], [Mur 83], [Uda 89], [Sou 92], [Eld 95]. In induction machines, this results in a very small error, because the leakage inductance is very small compared to the main inductance. However, in permanent-magnet machines, the leakage inductance is not negligible compared to the main inductance because of the large effective air gap. In the literature about permanent-magnet machines, the core loss is sometimes represented by a resistance connected in parallel to the whole machine inductance [Col 87], [Mor 93]. However, not all leakage flux contributes to the field in the stator iron. In this thesis, it is assumed that $2/3$ of the leakage inductance $L_{s\sigma}$ contributes to the stator core loss, which is only a rough estimate. Therefore, the resistance R_{sFe} is connected across the series connection of the inductances L_1 , $L_{g\sigma,1}$, and $2/3L_{s\sigma}$.

4.3.4 The rotor core loss

In this subsection, the core loss in the rotor is calculated. This loss is not zero because the stator currents contain time harmonics because of the rectifier load. Firstly, this subsection describes why the loss produced by the higher space harmonics is neglected.

Next, the rotor core loss is calculated. This is done for a sinusoidally pulsating field in the direct axis. From the calculated loss, a core loss resistance is calculated. The same could be done for a pulsating field in the quadrature axis. However, the result would be the same because it is assumed that the relative magnetic permeability of the magnets is one ($\mu_m = 1$), so that the machine is symmetric. Therefore, the resistance derived for the direct axis is also used for the quadrature axis.

Neglecting loss caused by higher space harmonics

In this subsection, it is assumed that the rotor core loss due to the higher space harmonics is negligible compared to the loss due to the fundamental space harmonic. This is a reasonable assumption, because the loss in the rotor yoke is caused by the magnetic field of the stator currents and the space harmonics of this magnetic field hardly cross the air gap, as can be seen in figure 2.11.

Calculation of the rotor core loss due to a pulsating field

The core loss is calculated for a field in the direct axis pulsating sinusoidally with angular frequency ω . (It should be noted that the frequency experienced by the rotor may be different from that experienced by the stator.) $\vec{B}(r, \alpha_r - \pi/p) = -\vec{B}(r, \alpha_r)$ is also valid, as follows from equation (3.1). The loss produced by the higher space harmonics of this field is ignored, as explained above. With this, the component of the magnetic flux density causing losses in the rotor iron can be written as

$$B_{rd,1}(r_d, \alpha_r, t) = \hat{B}_{rd,1}(r_d) \cos(p\alpha_r) \sin(\omega t) \quad (4.30)$$

The magnetic flux density in the rotor yoke $B_{ry}(\alpha_r, t)$ (where the subscript ry stands for rotor yoke) is calculated from the radial component of the magnetic flux density in the air gap at the damper radius $B_{rd,1}(r_d, \alpha_r, t)$. It is assumed that all flux linked by the damper windings flows through the rotor yoke, which is a reasonable assumption for the fundamental space harmonic if the number of pole pairs is small. The magnetic flux density at the damper radius is taken, because the resulting rotor core loss resistance can easily be placed in the equivalent circuit. Furthermore, it is assumed that the magnetic flux density in the rotor yoke $B_{ry}(\alpha_r, t)$ has only a tangential component; other components are neglected. The flux flowing through the rotor surface between the rotor coordinates 0 and α_r has to flow through the rotor yoke with height h_{ry} at rotor coordinate α_r , as illustrated in figure 4.2:

$$B_{ry}(\alpha_r, t) = -\frac{1}{h_{ry}} \int_0^{\alpha_r} B_{rd,1}(r_d, \alpha', t) r_d d\alpha' = -\frac{r_d}{ph_{ry}} \hat{B}_{rd,1}(r_d) \sin(p\alpha_r) \sin(\omega t) \quad (4.31)$$

In the rotor yoke, the magnetic flux density has its maximum at another place than in the air gap, as illustrated in figure 4.2.

The amplitude of this magnetic flux density is used in equation (4.13). In this way, the specific iron loss in the stator yoke is calculated as

$$k_{Fe}(\alpha_r) = c_{Fe} k_{Fe,0} \left(\frac{\omega}{\omega_0} \right)^{1.5} \left(\frac{\hat{B}_{rd,1}(r_d)}{\hat{B}_0} \frac{r_d}{ph_{ry}} \sin(p\alpha_r) \right)^2 \quad (4.32)$$

This expression is only a function of the rotor coordinate α_r , and not of the axial and the radial position. When this specific loss is averaged over the rotor coordinate and multiplied by the mass of the rotor yoke m_{ry} , the iron loss in the rotor yoke is calculated:

$$\begin{aligned} P_{rFe}(\omega) &= m_{ry} c_{Fe} k_{Fe,0} \left(\frac{\omega}{\omega_0} \right)^{1.5} \left(\frac{1}{\hat{B}_0} \right)^2 \frac{1}{2\pi} \int_0^{2\pi} \left(-\frac{r_d}{ph_{ry}} \hat{B}_{rd,1}(r_d) \sin(p\alpha_r) \right)^2 d\alpha_r \\ &= \frac{1}{2} m_{ry} c_{Fe} k_{Fe,0} \left(\frac{\omega}{\omega_0} \right)^{1.5} \left(\frac{\hat{B}_{rd,1}(r_d)}{\hat{B}_0} \right)^2 \left(\frac{r_d}{ph_{ry}} \right)^2 \end{aligned} \quad (4.33)$$

The rotor core loss resistance

For reasons mentioned in section 4.1, it is useful to represent the rotor core loss by a rotor core loss resistance, which is placed in the equivalent circuits.

To calculate the rotor core loss resistance, firstly, the flux linkage of the damper windings resulting from the pulsating magnetic flux density of equation (4.30) is calculated. This is done in the same way as in subsection 3.3.3. The resulting flux linkage (compare equation (3.43)) has only a component in damper winding $d,1$:

$$\Psi_{d,1} = \begin{bmatrix} \Psi_{dd,1} \\ \Psi_{dq,1} \end{bmatrix} = \frac{\pi l_s r_d N_{d,1}}{2p} \hat{B}_{rd,1}(r_d) \sin(\omega t) \begin{bmatrix} 1 \\ 0 \end{bmatrix} \quad (4.34)$$

The voltage induced in damper winding $d,1$ is the time-derivative of the flux linked by this damper winding:

$$u_{dd,1} = \frac{d\Psi_{dd,1}}{dt} = \frac{\pi l_s r_d N_{d,1}}{2p} \omega \hat{B}_{rd,1}(r_d) \cos(\omega t) = \hat{u}_{dd,1} \cos(\omega t) \quad (4.35)$$

The rotor core loss resistance $R_{rFe}(\omega)$ is connected in parallel to the inductances representing damper windings $d,1$ and $q,1$. Therefore, the dissipation in this resistance caused by the magnetic flux density of equation (4.30) is given by

$$P_{rFe}(\omega) = \frac{\hat{u}_{dd,1}^2}{2R_{rFe}(\omega)} \Rightarrow R_{rFe}(\omega) = \frac{\hat{u}_{dd,1}^2}{2P_{rFe}(\omega)} \quad (4.36)$$

There is a factor 2 in the denominator, because in the numerator, the amplitude of the voltage is used.

The rotor core loss resistance $R_{rFe}(\omega)$ must have such a value that the average loss dissipated in this resistance is equal to the rotor core loss. Therefore, the value of this resistance follows when equations (4.33) and (4.35) are used in equation (4.36):

$$R_{rFe}(\omega) = \frac{\pi^2 l_s^2 \sqrt{\omega}}{4c_{Fe} k_{Fe,0} \left(\frac{1}{\omega_0}\right)^{1.5} \left(\frac{1}{\hat{B}_0}\right)^2 m_{ry} \left(\frac{1}{h_{ry}}\right)^2} \quad (4.37)$$

Before this resistance can be used in the equivalent circuits of figures 3.8 and 3.10, it must be rotated to the stator-connected $\alpha\beta$ -system and it must be referred to the stator. Because in section 3.4 the same was done with the damper resistance R_{dk} , this is not extensively repeated here. The rotation to the stator-connected $\alpha\beta$ -system is done by means of equation (3.57). This rotation does not effect the value of the resistance. However, it should be noted that the angular frequency experienced by the rotor is different from the angular frequency experienced by the stator, as expressed by equation (3.80). The rotor quantities are referred to the stator by means of equation (3.70). The value of the rotor core loss resistance is calculated as (compare equation (3.72))

$$R_{RFe}(\omega) = \frac{3M_{sd,1}^2}{2L_{dd,1}^2} R_{rFe}(\omega) = \frac{6r_s^{2p} r_d^{2p}}{(r_s^{2p} + r_d^{2p})^2} \frac{\pi^2 l_s^2 N_{s,1}^2 \sqrt{\omega}}{4c_{Fe} k_{Fe} \left(\frac{1}{\omega_0}\right)^{1.5} \left(\frac{1}{\hat{B}_0}\right)^2 m_{ry} \left(\frac{1}{h_{ry}}\right)^2} \quad (4.38)$$

As the damper resistance R_{Dk} , this rotor core loss resistance $R_{RFe}(\omega)$ must be divided by the slip $s_{1,m}$ when it is used in the equivalent circuit of figure 3.10. It is connected in parallel to the inductance L_1 , as depicted in figure 4.5 for the higher time harmonics during steady-state operation with rectifier load and for the locked-rotor tests. The fundamental time harmonic of the magnetic flux density produced by the stator currents does not cause core loss in the rotor, because it rotates with the same speed as the rotor. Therefore, figure 4.4a remains valid for the fundamental time harmonic.

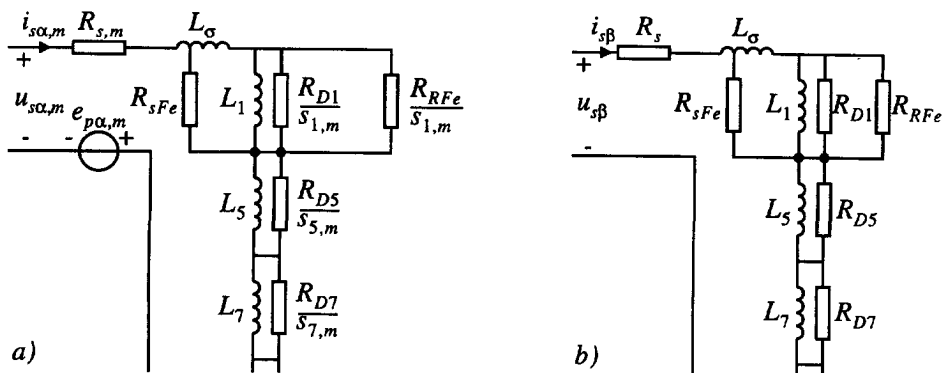


Figure 4.5: The equivalent circuit including the stator and rotor core loss, a) for the higher time harmonics during steady-state operation with rectifier ($m = 6n+1$), and b) for the locked-rotor tests.

Chapters 2 and 3 introduced sinusoidally distributed damper windings to describe the linear current density of the damper cylinder. The damper loss was represented by damper resistances in parallel to these damper windings. At first sight, the introduction of these damper windings seems to be meaningless for a machine without a damper cylinder. However, these damper windings appear to be useful in this case also, because the rotor iron loss can be represented by an iron loss resistance connected in parallel to the introduced damper windings. In this case, the radius of these damper windings is chosen at the magnet radius r_m .

4.3.5 The stray loss

The stray loss represents a group of losses [Alg 59], [Sch 64], [Eld 95], [Gle 98]. Which ones belong to this group, is not clearly defined. Contributions are:

- the eddy-current loss in the end regions induced by leakage fluxes, and
- the loss due to the higher space harmonics of the field of the stator currents.

Further, there is little agreement in the literature about the models for the calculation of the stray loss. According to Glew [Gle 98], this subject is a challenge to academia; Williamson [Wil 97] even calls it a residue of ignorance.

In this thesis, the different contributions to the stray loss are not separated, but treated as a whole, as in [Sou 92]. The stray loss is represented by a stray loss resistance $R_{\sigma Fe}$ connected in parallel to the inductance L_{σ} , because the fields causing this loss are mainly leakage fields. This is illustrated in figure 4.6.

It is assumed that the stray loss resistance is the same function of the angular frequency as the core loss resistance, because, as the core loss, the stray loss is basically due to hysteresis, eddy currents and excess loss effects. Therefore, the stray loss is assumed to be proportional to $i^2 \omega^{1.5}$. This roughly agrees with the literature, where loss due to end-winding leakage is reported to be proportional to between $i^2 \omega$ and $i^2 \omega^{1.5}$ [Alg 59], [Cha 68], [Lar 70], [Buc 78], [Mur 83], [Eld 95].

Several authors report that for the higher time harmonics in an induction machine, the loss due to end-winding leakage fields is comparable to or higher than the regular core loss [Cha 68], [Lar 70], [Buc 78], [Mur 83], [Buc 84]. The same is probably true for a permanent-magnet machine with a damper cylinder. From this, a conclusion can be drawn about the relation between the stray loss resistance $R_{\sigma Fe}$ and the stator core loss resistance R_{sFe} . For the higher time harmonics, the voltage across these resistances is comparable,

- because the voltage across the inductance L_1 is negligible compared to the voltage across the inductance L_{σ} , and
- because both the stator core loss resistance and the stray loss resistance are connected across a large part of the inductance L_{σ} .

Therefore, the value of the stray loss resistance $R_{\sigma Fe}$ is comparable to or smaller than the value of the stator core loss resistance R_{sFe} .

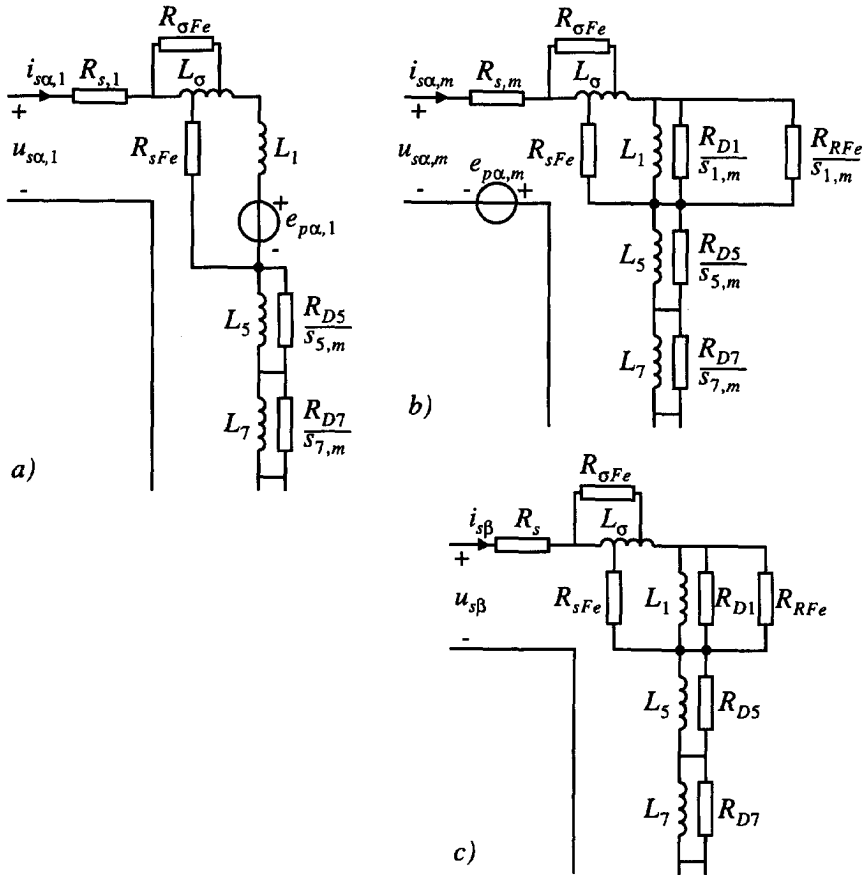


Figure 4.6: The equivalent circuit including stator and rotor core loss and stray loss, a) for the fundamental time harmonic and b) for the higher time harmonics during steady-state operation with rectifier ($m = 6n + 1$), and c) for the locked-rotor tests.

In a permanent-magnet machine without a damper cylinder, the stray loss is less important, because in this case, the regular time harmonic fields are not reduced by the damper currents and therefore, the regular core loss is probably dominant.

4.3.6 Locked-rotor tests of the test model

This subsection describes some locked-rotor tests, which partly verify the derived expressions for the iron loss. Firstly, the configurations of the test model are described. Next, the measured and calculated resistance and inductance are compared.

Configurations

The locked-rotor test (as described in section 3.6) was applied to the test model (described in appendix A, section A.1) in three configurations, namely:

- 1) with the rotor and with the damper cylinder (as in section 3.6),
- 2) with the rotor and without the damper cylinder, and
- 3) without the rotor and without the damper cylinder (rotor-removed).

The equivalent circuits for the first two configurations are given in figure 4.7a and 4.7b. The inductance during the rotor-removed test is different from the inductance in the first and the second configuration. At the end of subsection 2.4.2, it was shown that the magnetic flux density during the rotor-removed test was obtained by substituting $r_r=0$ in the expression for the magnetic flux density. Using this magnetic flux density in subsection 3.2.5 results in an expression for the self-inductance of the stator $L_{ss,k}$ during the rotor-removed test, which is called $L_{rr,k}$ (where the subscript rr stands for rotor-removed):

$$L_{rr,k} = \frac{\mu_0 \pi l_s \hat{N}_{s,k}^2}{4pk} \tag{4.39}$$

This inductance is used in the stator voltage equation (3.25) and the Clarke transformation described in subsection 3.4.1 is applied. Further, it is taken that the no-load voltage is zero, and the damper currents are absent. The result is (compare equation (3.67))

$$\vec{u}_s^s = R_s \vec{i}_s^s + L_{s\sigma} \frac{d\vec{i}_s^s}{dt} + \sum_{k=1,5,7,11,\dots}^{\infty} \frac{3}{2} L_{rr,k} \frac{d\vec{i}_s^s}{dt} \tag{4.40}$$

If the stator core loss resistance and the stray loss resistance are added to the equivalent circuit representing the β -component of this voltage equation, figure 4.7c results.

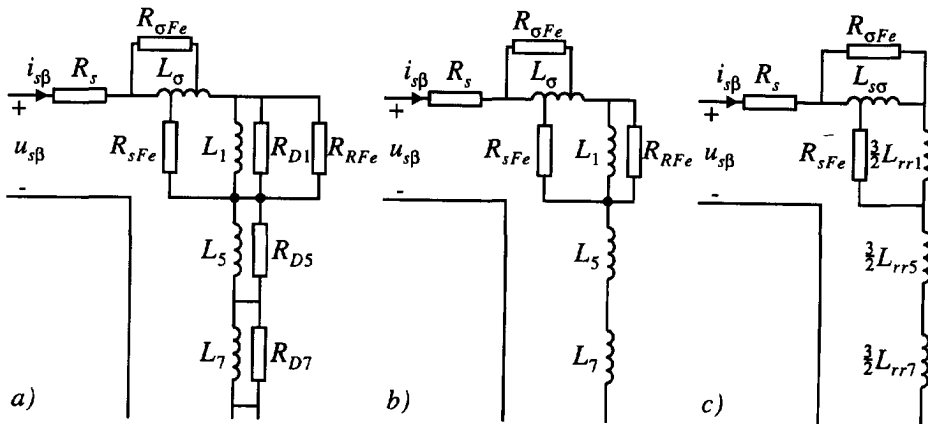


Figure 4.7: The equivalent circuits of the test model during the locked-rotor tests, a) with the rotor and the damper cylinder, b) with the rotor and without the damper cylinder, and c) without the rotor and the damper cylinder.

The stray loss resistances $R_{\sigma Fe}$ in these three equivalent circuits are different, because the end-winding fields are different for the different configurations. However, the order of magnitude of this resistance is the same in the three different configurations. Therefore, a first indication of the stray loss resistance $R_{\sigma Fe}$ is obtained when this resistance is assumed to be equal in the three configurations.

Measured and calculated resistance

Figures 4.8, 4.9, and 4.10 depict the resistance measured at the terminals of the test model during the locked rotor tests together with the calculated values. Also the contributions (iron loss, stator copper loss and damper loss) to this resistance are given.

The resistance of the stator winding was calculated as in section 4.2. For the damper resistance, equation (3.72) was used. The resistance for the fundamental space harmonic was increased by 25% because of the end connections as discussed in section 3.6.

The values of the specific iron loss multiplied by the empirical correction factor $c_{Fe} k_{Fe,0}$ and of the stray loss resistance $R_{\sigma Fe}$ are obtained from curve fitting to the measurements. The resulting values are given by $c_{Fe} k_{Fe,0} = 6$ W/kg (at $\omega_0 = 100\pi$ rad/s and $\hat{B}_0 = 1$ T), and $R_{\sigma Fe} = R_{sFe}/3$. The same values are used in the three configurations. That $R_{\sigma Fe} = R_{sFe}/3$ is valid, means that the larger part of the iron loss caused by higher time harmonics in a machine with a damper cylinder is stray loss. This agrees with what is said in the literature about induction machines, as mentioned in subsection 4.3.5. When the rotor is removed, the core loss and the stray loss are comparable. In the configuration with the rotor and without the damper cylinder, the core loss forms the major part of the iron loss.

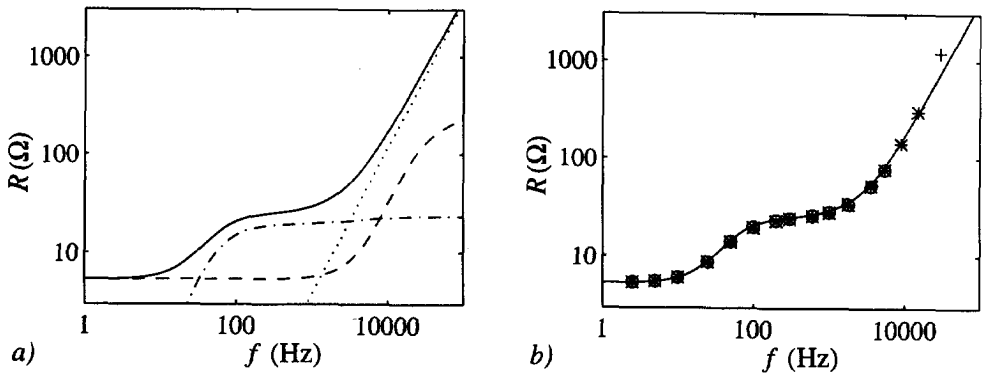


Figure 4.8: Resistance of the test model with the rotor and the damper cylinder as a function of the frequency. a) Calculated resistance (—) and contributions of iron loss (\cdots), damper loss ($- \cdot -$), and stator copper loss ($- -$). b) Calculated (—), and measured ($+$, \times , $*$, \circ , \cdot with $I_{sb} = 0.1$ A, $I_{sb} = 0.2$ A, $I_{sb} = 0.5$ A, $I_{sb} = 1$ A, $I_{sb} = 2$ A respectively) resistance.

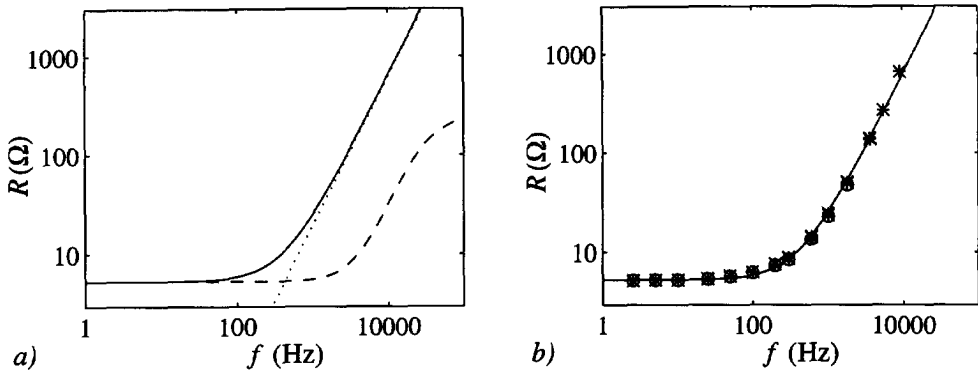


Figure 4.9: Resistance of the test model with the rotor and without the damper cylinder as a function of the frequency. a) Calculated resistance (—) and contributions of iron loss (\cdots), and stator copper loss (---). b) Calculated (—), and measured (+, \times , *, \circ , \cdot with $I_{sb}=0.1$ A, $I_{sb}=0.2$ A, $I_{sb}=0.5$ A, $I_{sb}=1$ A, $I_{sb}=2$ A) resistance.

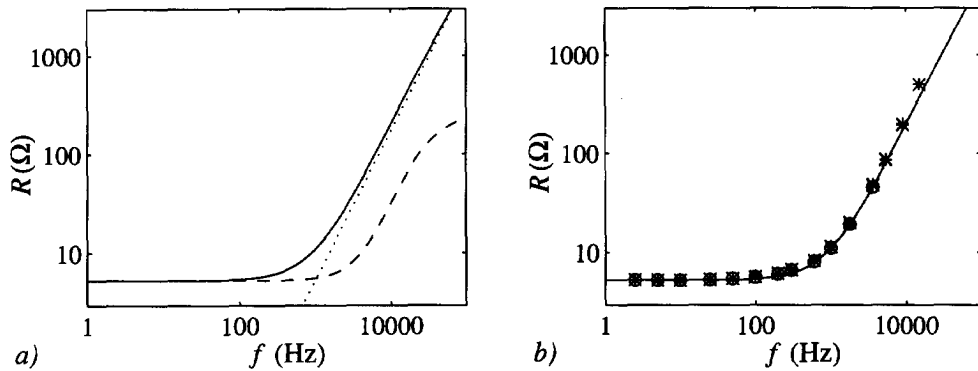


Figure 4.10: Resistance of the test model without the rotor and the damper cylinder as a function of the frequency. a) Calculated resistance (—) and contributions of iron loss (\cdots) and stator copper loss (---). b) Calculated (—), and measured (+, \times , *, \circ , \cdot with $I_{sb}=0.1$ A, $I_{sb}=0.2$ A, $I_{sb}=0.5$ A, $I_{sb}=1$ A, $I_{sb}=2$ A respectively) resistance.

In subsection 4.3.2, it was assumed that the iron loss is proportional to $\omega^{1.5}$. The measurements at very high frequencies suggest that the exponent of the angular frequency might be a little larger than 1.5. However, this was not incorporated in the model for two reasons.

- 1) At the highest frequencies, the measurements are not very reliable because of resonance phenomena. These phenomena appear from the increase of the measured inductance in figure 4.11 at the highest frequencies. The parasitic capacity of the stator windings was neglected in the machine model. However, it probably causes resonances in combination with the machine inductance at the highest frequency.
- 2) In the theory about iron loss, no indications were found that the iron loss might

increase with an exponent larger than 1.5.

The measured and calculated resistances neither verify nor refute the calculated increase of the stator resistance described in section 4.2, because the extra loss due to the increase of the stator resistance is small compared to the other losses.

In the calculations which produced the figures in this subsection, only the loss caused by the fundamental space harmonic was considered; that caused by the space harmonics was neglected. Therefore, this subsection does not verify the calculation of the iron loss caused by the higher space harmonics of the magnetic field of the magnets.

The good correlation between the measured and calculated resistances indicates that the proposed model for the iron loss is useful for the fundamental space harmonic and for frequencies above approximately 300 Hz. Below this frequency, the iron loss forms such a small part of the losses, that the model is neither verified nor refuted.

Measured and calculated inductance

Figure 4.11 depicts the measured and the calculated inductance of the test model without the damper cylinder and with and without the rotor. In figure 3.11d, the inductance of the test model with the damper cylinder and the rotor was already given.

The measured inductance depends on the amplitude of the current: the larger the current, the larger the measured inductance. The explanation of this effect is illustrated in figure 4.12, which depicts some sketched BH -curves of iron. The figure shows that with an increasing amplitude of the current, the relative magnetic permeability of iron may increase at low values of the magnetic flux density. During these tests, the amplitude of the magnetic flux density is smaller than 0.1 T (compare figure 2.10). For the test model with the rotor and without the damper, this effect is strong, because the major part of the flux is the main flux, which flows through the iron. For the test model with the rotor and the damper cylinder, this effect is small, because the major part of the flux is leakage flux.

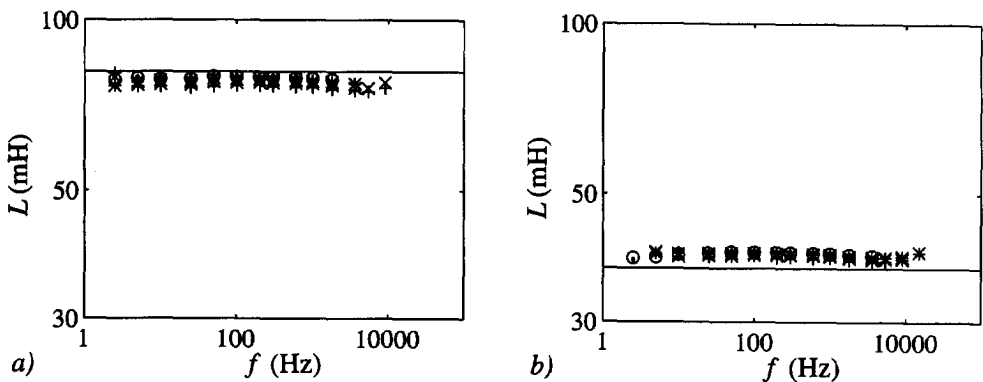


Figure 4.11: Calculated (—) and measured (+, ×, *, ○, · with $I_{sb}=0.1$ A, $I_{sb}=0.2$ A, $I_{sb}=0.5$ A, $I_{sb}=1$ A, $I_{sb}=2$ A) inductance of the test model without the damper cylinder, a) with and b) without the rotor as a function of the frequency.

The inductances were calculated on the assumption that the relative magnetic permeability of iron is infinite. This explains why the calculated inductance of the test model with the rotor and without the damper cylinder is a little larger than the measured inductance. However, the inductance measured during the rotor-removed test is larger than the calculated inductance, which may be explained in the following way. The inductance is calculated on the assumption that the magnetic field in the machine has only a radial and a tangential component. However, during the rotor-removed test, the magnetic field in the end regions may also have a considerable axial component; the magnetic field spreads over a larger length than stack length of the machine l_s . This results in a larger flux and therefore, in a larger measured inductance.

The measured inductance in figure 4.11 hardly depends on the frequency; only at very high frequencies does the inductance decrease slightly. This means that the effect of eddy currents in the iron on the magnetic field in the air gap is very small. In appendix C, section C.1, it is shown that the very small decrease of the inductance at very high frequencies is probably caused by the eddy currents in the iron. The small increase of the inductance measured at the highest frequency is probably caused by the resonance phenomena discussed earlier in this subsection.

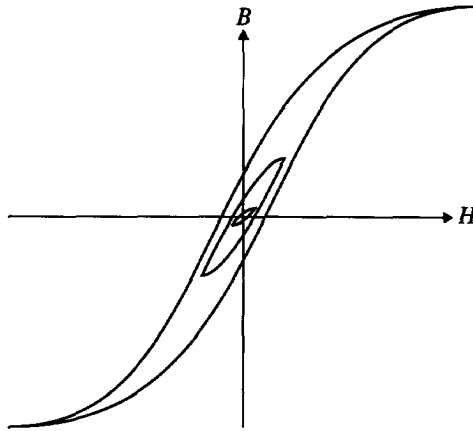


Figure 4.12: Sketch of BH-curves of iron, illustrating that the relative magnetic permeability of iron may increase with increasing magnetic field strength at low values of the magnetic flux density.

4.3.7 Concluding remarks

In this section, a model for the iron loss has been derived. The model is mainly based on the assumption that the specific iron loss is proportional to $\omega^{1.5} B^2$. Using this, expressions for a stator core loss resistance and a rotor core loss resistance have been derived. The stray loss has been modelled by a resistance connected in parallel to the leakage inductance L_{sr} .

For the verification of the derived model, locked-rotor tests were used. The good correlation between measurements and calculations verifies the proposed model for the iron loss for the fundamental space harmonic and for frequencies above approximately 300 Hz. For the higher space harmonics of the magnetic field of the magnets, the model was verified nor refuted.

The effect of eddy currents in the iron on the magnetic field in the air gap is negligible. This is shown in appendix C, section C.1, and this is affirmed by the experimental results. Therefore, it is possible to use the voltage equations without iron loss resistances (given in section 3.5) for the calculation of the terminal voltages and the terminal currents. Afterwards, the voltages over the iron loss resistances and the loss in these resistances can be calculated.

4.4 The eddy-current loss in the magnets

4.4.1 Introduction

Objective

The aim of this section is to model the eddy-current loss in the magnets of a permanent-magnet machine and to represent this loss by magnet loss resistances in the equivalent circuits. This loss is not zero because the generator is loaded with a rectifier, which produces time harmonics in the stator currents. Here, the eddy-current loss in the magnets is called the magnet loss.

The calculation of the magnet loss is mainly important for sintered rare-earth magnets which have a relatively low resistivity. The resistivity of plastic bonded and ferrite magnets is usually so high that the magnet loss is negligible.

Usually, eddy currents in the magnets are neglected. However, there are a few indications in the literature that this is not allowed for high-speed high-frequency machines. Henneberger and Schleuter [Hen 89] report on high-speed permanent-magnet machines with large magnets that became too hot because of eddy currents in the magnets, although the machines were without load. Van der Meer and Rietema [Mee 88] state that the loss in the magnets and the iron loss in the solid rotor of their high-speed permanent-magnet machine are in the same order of magnitude.

Some authors consider the magnet loss in permanent-magnet machines [Bou 80],

[Bou 81], [Wes 83], [Dem 87], [Abu 97], [Sch 97]. However, they all replace the magnets with a cylinder of magnet material. This does not give realistic results when the magnets are divided into small magnet blocks to reduce the eddy-current loss [Hen 89], [Sch 97]. Therefore, in this thesis, the eddy-current loss in permanent-magnet blocks is modelled. In such a way, the usefulness of applying small permanent-magnet blocks is also investigated.

Sebastian and Slemon [Seb 89] represented the effect of eddy currents in the magnets by a resistance in the equivalent circuit. They concluded that the effect of this resistance on the transient performance was negligible. However, they did not study the loss in this resistance.

Outline of this section

In this section, a resistance representing the magnet loss is calculated. It is done for space harmonics with a large pole angle in subsection 4.4.2, and for space harmonics with a small pole angle in subsection 4.4.3. Next, in subsection 4.4.4, the magnet loss resistance is incorporated in the machine model, and the loss is calculated for the space harmonics with pole angles which are neither large nor small. Subsection 4.4.5 describes some locked-rotor tests, which partly verify the derived expressions. Concluding remarks are made in subsection 4.4.6.

Assumptions

The derivations in this section are based on the following assumptions.

- The effect of eddy currents in the magnets on the magnetic field in the air gap is negligible: the loss is resistance-limited. Although this assumption is not valid at high frequencies, the derived expressions are useful, as will be explained in subsection 4.4.5 and in appendix C, section C.2.
- The rotor of the machine is completely covered with magnets. Therefore, eddy currents in the direct and the quadrature axis are equal and the magnet loss resistances in the direct and the quadrature axis are also equal. In [Pol 97], the magnet loss caused by the fundamental space harmonic is calculated without using this assumption. Subsection 4.4.6 gives a method to approximate the loss in the magnets of a machine the rotor of which is not completely covered with magnets.
- End effects are negligible. Therefore, the current density \vec{J} and the electric field strength \vec{E} in the magnets have only a z -component. Considering end effects would increase the resistance and decrease the loss, because the loss is resistance-limited. Therefore, this assumption results in an overrating of the magnet loss.

Because of the last assumption, it cannot be expected that the magnet loss is calculated very accurately. However, it is expected that the results form a much better approximation, than the results calculated assuming a cylinder of magnet material.

In subsections 4.4.2 and 4.4.3, the magnet loss is calculated for a pulsating field in the direct axis. From the calculated loss, a magnet loss resistance is calculated. The same could be done for a pulsating field in the quadrature axis. However, the result would be

the same because it is assumed that the rotor is completely covered with magnets, so that the machine is symmetric. Therefore, the resistance derived for the direct axis is also used for the quadrature axis.

4.4.2 The magnet loss due to space harmonics with a large pole angle

This subsection describes the calculation of the magnet loss produced by the space harmonics of the magnetic flux density with a large pole angle.

Specific magnet loss

Figure 4.13a depicts a cross-section of the permanent-magnet machine. Figure 4.13b depicts a cross-section of a magnet in a rectangular coordinate system, in which the x -, y -, and z -component agree with the tangential, the radial and the axial component. Both figures are used to explain the calculation of the eddy currents in the magnets.

This subsection is based on the assumptions mentioned in subsection 4.4.1, and on two assumptions, which are only used in this subsection:

- 1) The magnetic flux density in the magnets has only a radial component, which is not a function of the radius. In figure 4.13b, this means that the magnetic flux density has only an y -component, and is not a function of y . That the magnetic flux density is not a function of the radius is a reasonable assumption for the fundamental space harmonic, but not for the higher space harmonics, as is seen from figure 2.11. The amplitudes of the higher space harmonics of the magnetic flux density in the magnets decrease with decreasing radius. Therefore, this assumption results in an overrating of the magnet loss for the higher space harmonics.

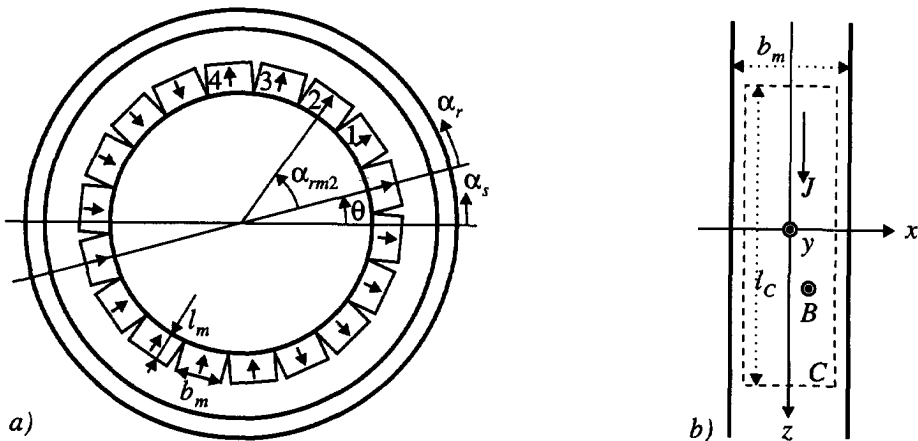


Figure 4.13: a) Section of the permanent-magnet machine, and b) cross-section of a magnet in a rectangular coordinate system.

2) The magnet width b_m is so small compared to the pole pitch of the space harmonics $\alpha_{p,k}r$ (where $r_r < r < r_m$), that the magnetic flux density can be considered constant over the magnet width. In figure 4.13b, this means that the magnetic flux density is not a function of x . Consequently, the electric field strength and the current density are odd functions of x . For the fundamental space harmonic, this assumption is reasonable, because the pole pitch is much larger than the magnet width b_m . For the higher space harmonics, this assumption is questionable.

The current density in the magnets is calculated with the integral form of the second of Maxwell's equations (Faraday's law):

$$\oint_C \vec{E} \cdot d\vec{s} = -\frac{d}{dt} \int_S \vec{B} \cdot d\vec{a} \tag{4.41}$$

This equation is applied to the dashed closed path C in figure 4.13b. In the z -direction, this closed path has length l_C . Because the electric field strength has only a z -component, the two sides of this closed path parallel to the x -axis do not contribute to the line integral. Furthermore, it is taken that the magnetic flux density is not a function of x . The result is

$$-l_C E_z(x) + l_C E_z(-x) = -l_C \frac{d}{dt} \int_{-x}^x B dx' = -2l_C x \frac{dB}{dt} \tag{4.42}$$

In this equation, it is taken that

- the electric field strength is an odd function of x : $E_z(-x) = -E_z(x)$, and
- the electric field strength is the current density multiplied by the resistivity of the magnet: $E_z(x) = \rho_m J_z(x)$.

The resulting expression for the current density is given by

$$J_z(x) = \frac{x}{\rho_m} \frac{dB}{dt} \tag{4.43}$$

Herewith, the specific magnet loss (the eddy-current loss per unit of magnet volume) k_m is calculated as

$$k_m = \frac{1}{b_m} \int_{-b_m/2}^{b_m/2} \rho_m J_z^2(x) dx = \frac{b_m^2}{12\rho_m} \left(\frac{dB}{dt} \right)^2 \tag{4.44}$$

Comparable expressions are derived, for example, in [Küp 84], [Ric 67] and [Sto 74] for the specific eddy-current loss in laminated iron.

Calculation of the magnet loss

The loss in the magnets is calculated for a pulsating field in the direct axis. $\vec{B}(r, \alpha_r, -\pi/p) = -\vec{B}(r, \alpha_r)$ is also valid, as follows from equation (3.1). With this, the radial component of this magnetic flux density at the damper radius can be written as the

following Fourier series:

$$B_{rd}(r_d, \alpha_r, t) = \sum_{k=1,3,5,\dots}^{\infty} \hat{B}_{rd,k}(r_d, t) \cos(pk\alpha_r) \quad (4.45)$$

The magnet blocks are numbered 1 to N_m (figure 4.13a), where N_m is the number of magnet blocks around the rotor circumference. The axis of l th magnet lays at rotor coordinate $\alpha_{m,l}$. As mentioned at the beginning of this subsection, the magnetic flux density is assumed not to be a function of the radius and to be constant over the magnet width. With this, the magnetic flux density in the l th magnet block can be written as

$$B_{m,l}(t) = B_{rd}(r_d, \alpha_{m,l}, t) = \sum_{k=1,3,5,\dots}^{\infty} \hat{B}_{rd,k}(r_d, t) \cos(pk\alpha_{m,l}) \quad (4.46)$$

If this magnetic flux density is used in equation (4.44), the eddy-current loss per unit of magnet volume in the l th magnet block is calculated as

$$\begin{aligned} k_{m,l} &= \frac{b_m^2}{12\rho_m} \left(\frac{d}{dt} \left\{ \sum_{k=1,3,5,\dots}^{\infty} \hat{B}_{rd,k}(r_d, t) \cos(pk\alpha_{m,l}) \right\} \right)^2 \\ &= \frac{b_m^2}{12\rho_m} \left(\sum_{k=1,3,5,\dots}^{\infty} \frac{d\hat{B}_{rd,k}(r_d, t)}{dt} \cos(pk\alpha_{m,l}) \right)^2 \end{aligned} \quad (4.47)$$

Multiplication of this expression by the volume of the magnet V_m/N_m (where V_m is the volume of all magnets together) gives the eddy-current loss in the l th magnet. Summation over all magnets results in the total magnet loss:

$$\begin{aligned} P_m &= \sum_{l=1}^{N_m} \frac{V_m}{N_m} k_{m,l} = \frac{V_m}{N_m} \sum_{l=1}^{N_m} \frac{b_m^2}{12\rho_m} \left(\sum_{k=1,3,5,\dots}^{\infty} \frac{d\hat{B}_{rd,k}(r_d, t)}{dt} \cos(pk\alpha_{m,l}) \right)^2 \\ &\approx V_m \frac{b_m^2}{12\rho_m} \frac{1}{2\pi} \int_0^{2\pi} \left(\sum_{k=1,3,5,\dots}^{\infty} \frac{d\hat{B}_{rd,k}(r_d, t)}{dt} \cos(pk\alpha_r) \right)^2 d\alpha_r \end{aligned} \quad (4.48)$$

The approximation in the last step of this equation is based on the assumption that the number of magnets is large.

If the series between the parentheses of this equation is written out and squared, the result is a series of products of cosinusoidal functions of the rotor coordinate. The integral from 0 to 2π of these products is only different from zero if the sinusoidal functions have the same harmonic number k . This implies that the magnet loss can be calculated as the sum of the losses caused by the different space harmonics:

$$\begin{aligned} P_m &= \sum_{k=1,3,5,\dots}^{\infty} P_{m,k} ; \\ P_{m,k} &= \frac{V_m b_m^2}{24\pi\rho_m} \int_0^{2\pi} \left(\frac{d\hat{B}_{rd,k}(r_d, t)}{dt} \right)^2 \cos^2(pk\alpha_r) d\alpha_r = \frac{V_m b_m^2}{24\rho_m} \left(\frac{d\hat{B}_{rd,k}(r_d, t)}{dt} \right)^2 \end{aligned} \quad (4.49)$$

Comparable expressions are derived, for example, in [Küp 84] and [Sto 74] for the eddy-current loss in laminated iron.

Representing the magnet loss by a resistance

For reasons mentioned in section 4.1, it is useful to represent the magnet loss by magnet loss resistances, which are placed in the equivalent circuits.

To calculate the magnet loss resistances, first, the flux linkage $\Psi_{d,k}$ of the damper windings d,k and q,k resulting from the magnetic flux density of equation (4.45) is calculated. This is done in the same way as in subsection 3.3.3. The resulting flux linkage $\Psi_{d,k}$ (compare equation (3.43)) has only a component in the direct axis:

$$\Psi_{d,k} = \begin{bmatrix} \Psi_{dd,k} \\ \Psi_{dq,k} \end{bmatrix} = \frac{\pi l_s r_d N_{d,k}}{2pk} \hat{B}_{r,k}(r_d, t) \begin{bmatrix} 1 \\ 0 \end{bmatrix} \tag{4.50}$$

The voltage induced in damper winding d,k is the time-derivative of the flux linkage of this damper winding:

$$u_{dd,k} = \frac{d\Psi_{dd,k}}{dt} = \frac{\pi l_s r_d N_{d,k}}{2pk} \frac{d\hat{B}_{r,k}(r_d, t)}{dt} \tag{4.51}$$

The magnet loss resistance for the k th space harmonic $R_{mb,k}$ is connected in parallel to the inductance representing the damper windings d,k and q,k . The magnet loss resistance $R_{mb,k}$ must have such a value that the loss dissipated in this resistance is equal to the magnet loss. Therefore,

$$P_{m,k} = \frac{u_{dd,k}^2}{R_{mb,k}} \Rightarrow R_{mb,k} = \frac{u_{dd,k}^2}{P_{m,k}} \tag{4.52}$$

Substitution of equations (4.49) and (4.51) in this equation results in

$$R_{mb,k} = \frac{6 \rho_m \pi^2 r_d^2 l_s^2 N_{d,k}^2}{V_m p^2 k^2 b_m^2} \tag{4.53}$$

For the fundamental space harmonic, the loss calculated with this magnet loss resistance is a realistic approximation, although the loss may be overrated a little, because of the used assumptions. For the higher space harmonics, the assumptions used probably result in a significant overrating of the loss.

4.4.3 Magnet loss due to space harmonics with a small pole angle

In this subsection, the magnet loss produced by the space harmonics of the magnetic flux density with a small pole angle is calculated.

The loss in a cylinder of magnet material

This subsection is based on the assumptions mentioned in subsection 4.4.1. Furthermore, in this subsection, it is assumed that the pole pitch of the space harmonics $\alpha_{p,k}r$ (where $r_r < r < r_m$) is so small compared to the magnet width b_m , that for the calculation of the eddy currents, the magnets can be replaced with a cylinder of magnet material.

For the space harmonics with a small pole angle, the magnetic flux density strongly depends on the radius, as can be seen in figure 2.11. Therefore, the loss is calculated two-dimensionally, namely as a function of the angular coordinate and as a function of the radius in the cylindrical coordinate system.

The current density in the cylinder of magnet material is calculated by means of the differential form of the second of Maxwell's equations (equation (3.26)), in which the magnetic vector potential is used. Substituting equation (2.10) ($\vec{B} = \nabla \times \vec{A}$) in the second of Maxwell's equations results in

$$\nabla \times \vec{E} = -\frac{\partial}{\partial t} \{\nabla \times \vec{A}\} \quad (4.54)$$

In this equation, it is taken that $\vec{E} = \rho_m \vec{J}$, and that the magnetic vector potential and the current density have only a z-component. The result is written out for the three components of the cylindrical coordinate system:

$$\begin{cases} \frac{\rho_m}{r} \frac{\partial J_z}{\partial \alpha} = -\frac{1}{r} \frac{\partial}{\partial t} \frac{\partial A_z}{\partial \alpha} \\ -\rho_m \frac{\partial J_z}{\partial r} = \frac{\partial}{\partial t} \frac{\partial A_z}{\partial r} \\ 0 = 0 \end{cases} \quad (4.55)$$

From this, the current density is calculated as

$$J_z = -\frac{1}{\rho_m} \frac{\partial A_z}{\partial t} + C \quad (4.56)$$

where C is an integration constant.

According to equations (2.44) and (2.58), the z-components of the magnetic vector potentials resulting from the stator currents and the damper currents in the magnet region are the same function of the radius: they are both proportional to $r_r^{-pk} r^{pk} + r_r^{pk} r^{-pk}$. With this function of the radius, the z-component of the magnetic vector potential belonging to a field in the direct axis is given by

$$A_z(r, \alpha_s, t) = \sum_{k=1,3,5,\dots}^{\infty} \hat{A}_{z,k}(r_d, t) (r_r^{-pk} r^{pk} + r_r^{pk} r^{-pk}) \sin(pk\alpha_s) \quad (4.57)$$

With equation (4.56), the current density resulting from the magnetic vector potential is calculated as

$$J_z(r, \alpha_r) = - \sum_{k=1,3,5,\dots}^{\infty} \frac{1}{\rho_m} (r_r^{-pk} r_m^{pk} + r_r^{pk} r_m^{-pk}) \sin(pk\alpha_r) \frac{d\hat{A}_{z,k}(r_d, t)}{dt} + C \quad (4.58)$$

The integration constant C in this equation must be zero, because the paths of the current density must close within the cylinder of magnet material.

From the current density, the magnet loss is calculated as

$$\begin{aligned} P_m &= \int_{r_r}^{r_m} \int_0^{2\pi} \int_0^{l_s} \rho_m J_z^2(r, \alpha_r) r dz d\alpha_r dr \\ &= \frac{l_s}{\rho_m} \int_{r_r}^{r_m} \int_0^{2\pi} \left(\sum_{k=1,3,5,\dots}^{\infty} (r_r^{-pk} r_m^{pk} + r_r^{pk} r_m^{-pk}) \sin(pk\alpha_r) \frac{d\hat{A}_{z,k}(r_d, t)}{dt} \right)^2 r d\alpha_r dr \end{aligned} \quad (4.59)$$

As in earlier sections, if the summation between the parentheses of this equation is written out and squared, an infinite series of products of two cosinusoidal functions results. The integral from 0 to 2π of these products of two cosinusoidal functions is only different from zero if these two functions have the same the harmonic number k . Therefore, the magnet loss can also be calculated as the sum of the losses caused by the different space harmonics:

$$\begin{aligned} P_m &= \sum_{k=1,3,5,\dots}^{\infty} P_{m,k} ; \\ P_{m,k} &= \frac{l_s}{\rho_m} \int_{r_r}^{r_m} \int_0^{2\pi} (r_r^{-pk} r_m^{pk} + r_r^{pk} r_m^{-pk})^2 \sin^2(pk\alpha_r) \left(\frac{d\hat{A}_{z,k}(r_d, t)}{dt} \right)^2 r d\alpha_r dr \\ &= \frac{\pi l_s}{\rho_m} \left(\frac{r_r^{-2pk} r_m^{2pk+2} - r_r^2}{2pk+2} + r_m^2 - r_r^2 - \frac{r_r^{2pk} r_m^{-2pk+2} - r_r^2}{2pk-2} \right) \left(\frac{d\hat{A}_{z,k}(r_d, t)}{dt} \right)^2 \end{aligned} \quad (4.60)$$

The magnet loss resistance

For reasons mentioned in section 4.1, it is useful to represent the magnet loss by magnet loss resistances, which are placed in the equivalent circuits.

To calculate the magnet loss resistances, first, the flux linkage $\Psi_{d,k}$ of the damper windings d,k and q,k resulting from the magnetic vector potential of equation (4.57) is calculated. The magnetic flux density belonging to this magnetic vector potential is calculated with $\vec{B} = \nabla \times \vec{A}$ (equation (2.10)). At the damper radius, this magnetic flux density is given by

$$B_r(r_d, \alpha_r, t) = \frac{1}{r} \frac{\partial A_z(r_d, \alpha_r, t)}{\partial \alpha_r} = \sum_{k=1,3,5,\dots}^{\infty} \hat{A}_{z,k}(r_d, t) (r_r^{-pk} r_d^{pk-1} + r_r^{pk} r_d^{-pk-1}) pk \cos(pk\alpha_r) \quad (4.61)$$

The flux linkage $\Psi_{d,k}$ of the damper windings d,k and q,k resulting from this magnetic flux density is calculated in the same way as in subsection 3.3.3 (compare equation

(3.43)), and it has only a component in damper winding d,k :

$$\Psi_{d,k} = \begin{bmatrix} \Psi_{dd,k} \\ \Psi_{dq,k} \end{bmatrix} = \frac{\pi l_s r_d N_{d,k}}{2pk} \hat{A}_{r,k}(r_d, t) (r_r^{-pk} r_d^{pk} + r_r^{pk} r_d^{-pk-1}) pk \begin{bmatrix} 1 \\ 0 \end{bmatrix} \quad (4.62)$$

The voltage induced in damper winding d,k is the time-derivative of the flux linkage of this damper winding:

$$u_{dd,k} = \frac{d\Psi_{dd,k}}{dt} = \frac{1}{2} \pi l_s N_{d,k} (r_r^{-pk} r_d^{pk} + r_r^{pk} r_d^{-pk-1}) \frac{d\hat{A}_{r,k}(r_d, t)}{dt} \quad (4.63)$$

The magnet loss resistance for the k th space harmonic $R_{mb,k}$ is connected in parallel to the inductance representing the damper windings d,k and q,k . The magnet loss resistance $R_{mb,k}$ must have such a value that the loss dissipated in this resistance is equal to the magnet loss. Therefore,

$$P_{m,k} = \frac{u_{dd,k}^2}{R_{mc,k}} \Rightarrow R_{mc,k} = \frac{u_{dd,k}^2}{P_{m,k}} \quad (4.64)$$

Substitution of equations (4.60) and (4.63) in this equation results in

$$R_{mc,k} = \frac{\rho_m \pi l_s N_{d,k}^2 (r_r^{-pk} r_d^{pk} + r_r^{pk} r_d^{-pk})^2}{4 \left(\frac{r_r^{-2pk} r_m^{2pk+2} - r_r^2}{2pk+2} + r_m^2 - r_r^2 - \frac{r_r^{2pk} r_m^{-2pk+2} - r_r^2}{2pk-2} \right)} \quad (4.65)$$

For the space harmonics with a small pole angle, the loss calculated with this magnet loss resistance is a realistic approximation, although the loss is overrated a little, because the 'lamination' of the magnets is ignored. For the space harmonics with a large pole angle, the magnet loss is overrated significantly, because the 'lamination' of the magnets results in an important reduction of the eddy currents.

4.4.4 Incorporating the magnet loss resistance in the machine model

In this subsection, the magnet loss resistances are incorporated in the machine model, and the loss is calculated for the space harmonics with a pole pitch which is neither large nor small.

Before the magnet loss resistances derived in subsections 4.4.2 and 4.4.3 can be used in the equivalent circuits of figures 3.8 and 3.10, they must be rotated to the stator-connected $\alpha\beta$ -system and they must be referred to the stator. Because in section 3.4 the same was done with the damper resistance $R_{d,k}$, this is not extensively repeated here. The rotation to the stator-connected $\alpha\beta$ -system by means of equation (3.57) does not effect the value of the resistances. The rotor quantities are referred to the stator by means of equation (3.70); the resulting values of the magnet loss resistances are

calculated as (compare equation (3.72))

$$R_{Mb,k} = \frac{3M_{sd,k}^2}{2L_{dd,k}^2} R_{mb,k} ; R_{Mc,k} = \frac{3M_{sd,k}^2}{2L_{dd,k}^2} R_{mc,k} ; \frac{3M_{sd,k}^2}{2L_{dd,k}^2} = \frac{6r_s^{2pk} r_d^{2pk}}{(r_s^{2pk} + r_d^{2pk})^2} \frac{N_{s,k}^2}{N_{d,k}^2} \quad (4.66)$$

In this equation, the capital M in the subscript denotes that the resistance is referred to the stator.

The magnet loss resistance $R_{Mb,k}$ was calculated for space harmonics with a pole pitch much larger than the magnet width. The magnet loss resistance $R_{Mc,k}$ was calculated for space harmonics a pole pitch much smaller than the magnet width. In figure 4.14a, the two calculated magnet loss resistances are given as a function of the space harmonic number k for the test model (described in appendix A, section A.1).

For the fundamental space harmonic, the magnet loss resistance $R_{Mb,1}$ is larger than the magnet loss resistance $R_{Mc,1}$. Since the loss is resistance-limited, the magnet loss resistance $R_{Mb,1}$ results in lower loss. This was already expected at the end of subsection 4.4.3, where it was explained that the loss caused by the space harmonics with a large pole angle is overrated when it is calculated with the magnet loss resistance $R_{Mc,k}$.

For the space harmonics with a small pole angle, the magnet loss resistance $R_{Mc,k}$ is larger than the magnet loss resistance $R_{Mb,k}$. Since the loss is resistance-limited, the magnet loss resistance $R_{Mc,k}$ results in a lower loss. This shows that for the space harmonics with a small pole angle, the loss is overrated when it is calculated with the magnet loss resistance $R_{Mb,k}$, as already expected at the end of subsection 4.4.2.

Because both expressions for the magnet loss result in an overrating of the magnet loss, the magnet loss resistance resulting in the lowest loss is used:

$$R_{m,k} = \max(R_{mb,k}, R_{mc,k}) ; R_{M,k} = \max(R_{Mb,k}, R_{Mc,k}) \quad (4.67)$$

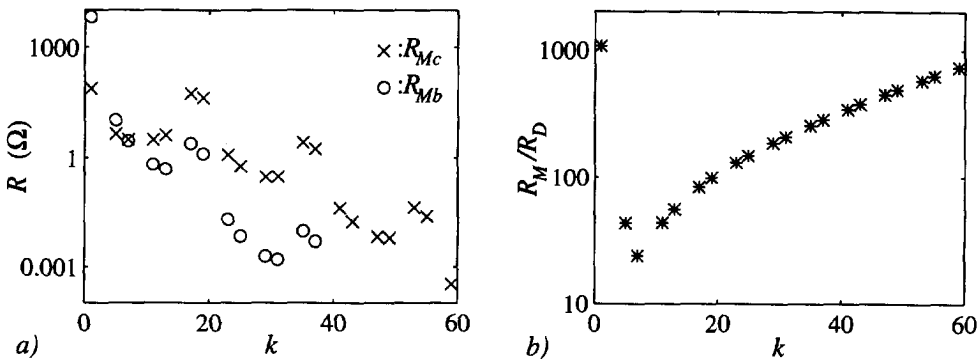


Figure 4.14: a) The magnet loss resistances $R_{Mb,k}$ and $R_{Mc,k}$, and b) the ratio of the magnet loss resistance and the damper resistance $R_{M,k}/R_{D,k}$ as a function of the harmonic number k (for the test model).

Figure 4.14b depicts the ratio of the magnet loss resistance and the damper resistance. It can be seen that the magnet loss resistance is an order of magnitude larger than the damper resistance. Therefore, in a machine with a damper cylinder, the loss in the magnets is small compared to that in the damper cylinder.

The magnet loss resistance $R_{M,k}$ is added to the equivalent circuits of figures 3.8 and 3.10. It is connected in parallel to the inductance L_k , as depicted in figure 4.15. In this figure, the iron loss resistances are omitted because their effect on the terminal voltages and terminal currents is negligible.

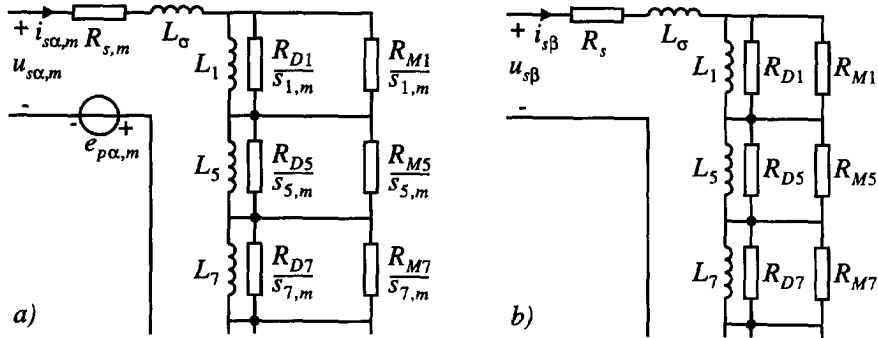


Figure 4.15: The equivalent circuit of the machine a) for a time harmonic during steady-state operation with rectifier load, and b) for the locked-rotor tests.

To obtain the voltage equations during steady-state operation with rectifier and during the locked-rotor tests, the resistances $R_{md,k}$ and $R_{MD,k}$ are introduced. These resistances replace the parallel connection of the damper resistance and the magnet loss resistance:

$$R_{md,k} = \frac{R_{m,k}R_{d,k}}{R_{m,k} + R_{d,k}} ; \quad R_{MD,k} = \frac{R_{M,k}R_{D,k}}{R_{M,k} + R_{D,k}} \quad (4.68)$$

Herewith, the equation for the Fourier coefficients of the steady-state stator voltages of the rectifier-loaded machine (given in subsection 3.5.2, equation (3.88)) becomes

$$\hat{u}_{s,6n+1} = \hat{e}_{p,6n+1} + Z_{6n+1} \hat{i}_{s,6n+1} ; \quad (4.69)$$

$$Z_{6n+1} = R_{s,6n+1} + j(6n+1)\omega_1 L_\sigma + \sum_{k=1,5,7,11,\dots}^{\infty} \frac{j(6n+1)\omega_1 L_k R_{MD,k}}{R_{MD,k} + j s_{k,6n+1} (6n+1)\omega_1 L_k}$$

The impedance during the locked-rotor tests (given in subsection 3.5.3, equation (3.93)) becomes

$$Z(\omega) = 2 \left\{ R_s(\omega) + j\omega L_\sigma + \sum_{k=1,5,7,11,\dots}^{\infty} \frac{j\omega L_k R_{MD,k}}{R_{MD,k} + j\omega L_k} \right\} \quad (4.70)$$

Subsection 4.3.4 explained that the introduction of the sinusoidally distributed damper windings is also useful for a machine without a damper cylinder, because the rotor core

loss can be represented by a rotor core loss resistance connected in parallel to these damper windings. This section shows that the magnet loss in a machine without a damper cylinder can also be represented by magnet loss resistances connected in parallel to these damper windings. In a machine without a damper cylinder, $R_{MDk} = R_{Mk}$ is valid.

4.4.5 Locked-rotor tests of the servomotor

This subsection describes some locked-rotor tests, which partly verify the derived expressions for the magnet loss.

The locked-rotor test (as described in section 3.6) was done with the servomotor, which is a permanent-magnet machine without a damper cylinder (see further appendix A, section A.2). The equivalent circuit of this machine during the locked-rotor tests is given in figure 4.16.

The locked-rotor test was done in two rotor positions:

- 1) The quadrature axis coincides with the axis of stator phase a ($p\theta = \pi/2$). Because a voltage is supplied to the stator phases b and c (as depicted in figure 3.9), the direct axis coincides with the armature winding field axis.
- 2) The direct axis coincides with the axis of stator phase a ($\theta = 0$). Because a voltage is supplied to the stator phases b and c (as depicted in figure 3.9), the quadrature axis coincides with the armature winding field axis.

The resistance of the stator winding was calculated as in section 4.2. The iron loss resistances were calculated as in section 4.3. The values used for the specific iron loss multiplied by the empirical correction factor and the stray loss resistance are $c_{Fe} k_{Fe,0} = 4 \text{ W/kg}$ (at $\omega_0 = 100\pi \text{ rad/s}$ and $\hat{B}_0 = 1 \text{ T}$), and $R_{\sigma Fe} = R_{sFe}/3$.

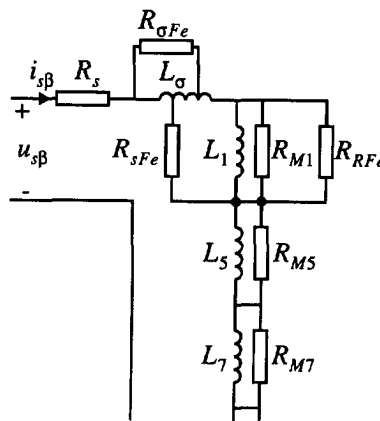


Figure 4.16: The equivalent circuit of the servomotor during the locked-rotor tests.

Figure 4.17 depicts the calculated resistance between the machine terminals during the locked-rotor tests and the contributions to this resistance of iron loss, stator copper loss, and magnet loss. This figure shows that at frequencies above approximately 3 kHz, the magnet loss forms the major part of the losses. This figure also shows that the extra loss due to the increase of the stator resistance is small compared to the other losses. Therefore, the locked-rotor tests neither verify nor refute the calculated increase of the stator resistance, as was the case in subsection 4.3.6.

Figure 4.18 depicts the resistance and inductance measured at the machine terminals during the locked-rotor tests in the direct and the quadrature axis together with the calculated values.

The measured values depend on the amplitude of the current: the larger the amplitude of the current, the larger the measured inductance. This may be caused by hysteresis effects, as explained in subsection 4.3.6 and illustrated in figure 4.12.

In subsection 4.4.1, it was assumed that the effect of eddy currents on the magnetic field in the air gap is negligible. At frequencies above approximately 10 kHz, this assumption is not valid, as is seen from the decrease of both the measured and the calculated inductance in figure 4.18. The calculated inductance decreases at high frequencies, because the impedance of the resistance R_{Mk} in the equivalent circuit of figure 4.16 becomes smaller than the impedance of the inductance L_k . The fact that the calculated inductance decreases shows that by placing the magnet loss resistances in an equivalent circuit, the effect of eddy currents in the magnets on the magnetic field is considered. However, this effect is not considered in a correct way, because the magnet loss resistance was calculated on the assumption that this effect is negligible. Nevertheless, appendix C, section C.2, shows that this way of considering the effect is a simple and useful approximation for frequencies up to 100 kHz.

In the direct axis, the correlation between the measured and the calculated resistance is reasonable. The correlation between the measured and the calculated resistance in the

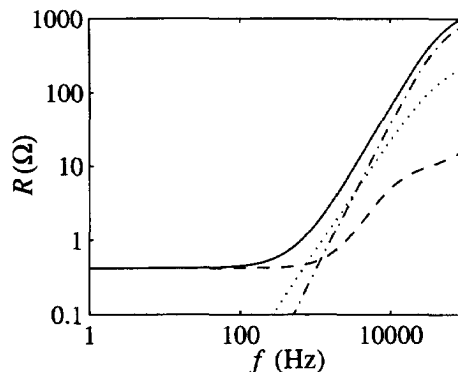


Figure 4.17: The calculated resistance of the servomotor (—) and the contributions to this resistance of iron loss (\cdots), magnet loss ($- \cdot -$), and stator copper loss ($- -$).

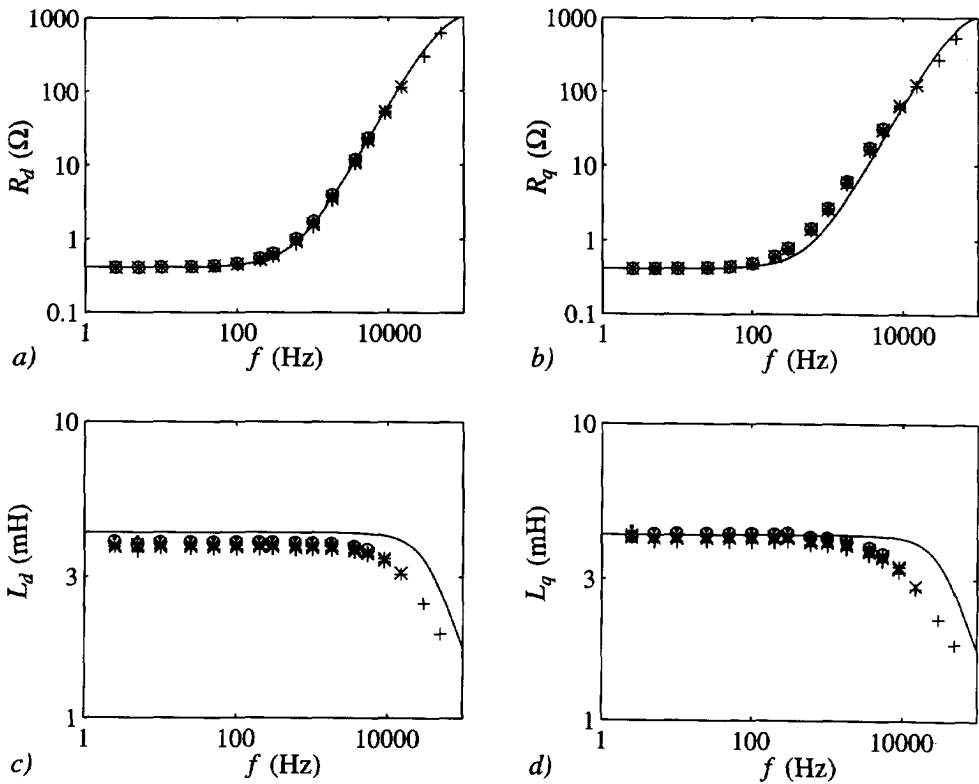


Figure 4.18: a) Resistance and c) inductance in the direct axis and b) resistance and d) inductance in the quadrature axis,

— : calculated, and

+ , x , * , o , \cdot : measured with $I_{sb}=0.2$ A, $I_{sb}=0.5$ A, $I_{sb}=1$ A, $I_{sb}=2$ A, and $I_{sb}=5$ A.

quadrature axis is poorer. This may be so because during these measurements, the machine develops a (large) pulsating torque. The rotor was locked to minimize the power consumed by this torque, but it was impossible to prevent all vibrations. Therefore, the measurements in the quadrature axis may include mechanical loss.

The measured inductance in the direct axis is a little smaller than the calculated inductance, which may have two causes:

- 1) In the calculation, the magnetic permeability of iron is assumed to be infinite, while the real magnetic permeability is finite (as discussed in subsection 4.3.6).
- 2) In the direct axis, there may be saturation due to the magnetic field of the magnets.

That the measured inductance in the direct axis is smaller than the measured inductance in the quadrature axis may also have two causes:

- 1) The rotor iron is not exactly cylindrical. The rotor is almost completely covered with magnets forming poles, but between these poles, there is a small region in which the radius of the rotor iron is a little larger than under the poles. This may

result in a larger inductance in the quadrature axis.

- 2) In the direct axis, there may be saturation because of the magnetic field of the magnets, which is not present in the quadrature axis.

The measured decrease of the inductance starts at a lower frequency than the calculated decrease. More research work is necessary to explain this. The opposite was expected because the assumptions used result in an overrating of the calculated loss and therefore, in an underestimate of the calculated magnet loss resistance.

During the locked-rotor tests, the calculated loss caused by the higher space harmonics is negligible compared to that caused by the fundamental space harmonic. This means that the measurements do not verify the calculation of the loss resulting from the higher space harmonics. It should be realized, that the loss caused by the higher space harmonics is not necessarily negligible when the rotor rotates.

The correlation between measurements and calculations is reasonable. Therefore, it can be concluded that the proposed way of calculating the magnet loss is useful for the fundamental space harmonic and for frequencies above approximately 1 kHz. Below this frequency, the magnet loss is such a small part of the losses, that the derivation is neither verified nor refuted.

4.4.6 Concluding remarks

In this section, a model for the calculation of the eddy-current loss in the magnets has been derived. For space harmonics with a large pole-pitch, this model calculates the eddy-current loss in magnet blocks with a finite width. For space harmonics with a small pole-pitch, the magnet blocks are replaced with a cylinder of magnet material.

For the verification of the derived model, locked-rotor tests have been used. The good correlation between measurements and calculations indicates that the proposed model is useful for the fundamental space harmonic. For the higher space harmonics, the model has been neither verified nor refuted.

The effect of eddy currents in the magnets on the magnetic field in the air gap is not completely negligible at high frequencies. This is seen from the measurements and is affirmed by the calculations of appendix C, section C.2. This effect can be considered by incorporating the magnet loss resistances in the machine model, as illustrated in figure 4.15 and expressed by equation (4.69).

In subsection 4.4.1, it was assumed that the rotor is completely covered with magnets. This assumption was necessary for the derivations of this section. However, it is possible to approximate the loss in a machine the rotor of which is not completely covered with magnets. Because the magnet loss is mainly resistance limited, the loss is proportional to the magnet volume. Therefore, the magnet loss in a machine the rotor of which is partly covered with magnets can be calculated as the magnet loss in a machine the rotor of which is completely covered with magnets multiplied by $2\alpha_m/\alpha_{p,1}$.

4.5 The loss due to the stator slotting

4.5.1 Introduction

Objective

When the rotor of a permanent-magnet machine rotates, the rotor experiences a pulsation of the magnetic flux density because of the stator slotting, even when the machine is without load. Until now, this pulsation has been ignored. However, it causes extra eddy-current loss in the magnets and the damper cylinder. During the locked-rotor tests, this loss is zero. The aim of this section is to approximate this loss.

The following references deal with the pulsation of the magnetic field due to the stator slotting and the resulting loss in permanent-magnet machines.

- The eddy-current loss in a retaining cylinder is calculated by means of finite element methods in several papers, for example in [Mec 93] and [Oya 91].
- In [Hen 94], the loss in a nonmagnetic retaining cylinder is approximately calculated for a given pulsation of the magnetic flux density. The loss is calculated for a machine without load and on the assumption that the effect of the current density in the cylinder on the magnetic field is negligible. Furthermore, it is stated that the pulsation of the magnetic flux density can be calculated by means of a conformal transformation or a finite element calculation.
- In [Bou 80] and [Bou 81], the magnetic vector potential in a slotted air gap is calculated analytically. This is done for a linear model of the machine. The slots are modelled as triangular extensions of the air gap, where the field is one-dimensional. In [Bou 80], this is used to calculate the loss in the magnets, which are replaced with a cylinder of magnet material. In [Bou 81], the loss in a metallic retaining cylinder is also determined.
- Kramer [Kra 83] calculates the scalar magnetic potential in a slotted air gap analytically for a linear model of the machine with rectangular slots. However, at the border of air gap and slot, approximations are necessary.
- Demel [Dem 87] determines the amplitude of the pulsation of the magnetic flux density with measurements and with finite element calculations. He approximates the form of the pulsation, and calculates the resulting loss in the magnets, which are replaced with a cylinder of magnet material.
- In [Wes 83], [Zhu 93c], and [Tak 94], conformal transformations are used to calculate the pulsation of the magnetic flux density due to the stator slotting. Weschta [Wes 83] calculates the resulting loss in the magnets, which are replaced with a cylinder of magnet material. Takahashi [Tak 94] calculates the resulting loss in a nonmagnetic retaining cylinder for a machine without load and on the assumption that the effect of the current density in the cylinder on the magnetic field is negligible.

In this section, the extra loss due to the pulsation of the magnetic flux density because

of the stator slotting is approximated for a given pulsation. As appears from the references mentioned, the pulsation can be calculated in various ways. Here, the conformal transformation described in appendix D is used to calculate the amplitude of the pulsation.

In contrast with some of the references mentioned, this section describes the calculation of the extra loss in the damper cylinder and the magnets for a machine on load. Furthermore, the effect of the current density in the cylinder on the magnetic field is not neglected.

The validity of some of the assumptions used in the derivation is questionable. However, the value of the calculation discussed in this section is that it results in a reasonable first approximation of the extra loss caused by the stator slotting without using extremely complicated methods. Furthermore, the calculations in chapter 7 show that the extra loss due to the stator slotting is not important compared to the other losses. Therefore, it is of no major consequence that some of the assumptions are questionable.

Outline of this section

Firstly, subsection 4.5.2 describes the pulsation of the magnetic flux density because of the stator slotting and discusses the assumptions used in this derivation. In subsection 4.5.3, the losses resulting from this pulsation in the magnets and in the damper cylinder are calculated. Concluding remarks are made in subsection 4.5.4.

4.5.2 The pulsation of the magnetic flux density

In chapter 2, the magnetic flux density in the air gap and the magnets of the machine was calculated on the assumption of a smooth stator surface (without slots). It is assumed that the radial component of this magnetic flux density at the damper radius $B_{r,smooth}(r_d, \alpha_s, t)$ can be used to calculate the radial component of the magnetic flux density at the damper radius in the machine with the real slotted stator $B_{r,slotted}(r_d, \alpha_s, t)$ as

$$B_{r,slotted}(r_d, \alpha_s, t) = B_{r,smooth}(r_d, \alpha_s, t) \left(\frac{1}{k_C} + \gamma(r_d) \cos(6pq\alpha_s) \right) \quad (4.71)$$

This equation is based on the following assumptions and starting-points.

- 1) It is assumed that the pulsation resulting from the stator slotting is a sinusoidal function of the stator coordinate with a wave length equal to the slot pitch.
- 2) It is taken that $\alpha_s = 0$ coincides with the axis of a stator tooth.
- 3) It is taken that $6pq$ is the number of stator slots, where q is the number of slots per pole per phase.
- 4) The amplitude of the pulsation is proportional to the factor $\gamma(r_d)$. It is assumed that the factor $\gamma(r_d)$ can be calculated with equation (D.10) of appendix D. This assumption is only a rough estimate, mainly if the gap between the damper

cylinder and the stator surface is small, as appears from appendix D.

- 5) The Carter factor k_C describes the average reduction of the magnetic flux density because of the stator slotting. In the rest of this thesis, it is assumed to be one, because the difference from one is negligible, as shown in appendix D.

Furthermore, it is assumed that the extra loss resulting from the stator slotting can be approximated by considering only the pulsation on the fundamental space harmonic of the magnetic flux density, that rotates with the same speed as the rotor:

$$B_r(r_d, \alpha_s, \alpha_r, t) = \hat{B}_{r,1}(r_d) \cos(p\alpha_r + \varepsilon) \left(\frac{1}{k_C} + \gamma(r_d) \cos(6pq\alpha_s) \right) \quad (4.72)$$

where

$$\hat{B}_{r,1}(r_d) \cos(p\alpha_r + \varepsilon) = B_{m,1}(r_d, \alpha_r) + B_{rs,1}(r_d, \alpha_r) \quad (4.73)$$

where

- $\hat{B}_{r,1}(r_d) \cos(p\alpha_r + \varepsilon)$ is the fundamental space harmonic of the magnetic flux density which rotates with the same speed as the rotor. The maximum of this harmonic of the magnetic flux density lays at $p\alpha_r = -\varepsilon$. Generally, ε is not equal to zero because of the field of the stator currents.
- $B_{m,1}(r_d, \alpha_r)$ is the fundamental space harmonic of the magnetic flux density produced by the magnets of equation (2.60).
- $B_{rs,1}(r_d, \alpha_r)$ is the fundamental space harmonic of the magnetic flux density produced by the stator currents, that rotates with the same speed as the rotor. This harmonic follows from equation (2.61) when the fundamental time harmonics of the stator currents and $\alpha_s = \alpha_r + \omega_1 t/p - \pi/(2p)$ (as follows from equations (3.2) and (3.81)) are used in this equation.

The damper currents do not contribute to the fundamental space harmonic of the magnetic flux density which rotates with the same speed as the rotor.

Besides, this section is based on the following assumptions.

- The current in the damper cylinder can be calculated by means of the voltage equations of the short-circuited damper windings of section 3.3.
- The rotor of the machine is completely covered with magnets. Subsection 4.5.4 gives a method for calculating the loss in a machine the rotor of which is not completely covered with magnets.

As mentioned earlier, the magnetic field in chapter 2 and the voltage equations in chapter 3 are derived assuming a smooth stator surface. In this section, the effect of the stator slotting on the losses is investigated. However, the effect of the stator slotting on the voltage equations is assumed to remain negligible.

4.5.3 The damper currents caused by the pulsation of the magnetic field

According to equations (3.2) and (3.81), the relation between the angular coordinates of stator and rotor is given by $\alpha_s = \alpha_r + \omega_1 t / p - \pi / (2p)$. If this is substituted in equation (4.72), the result can be worked out to

$$B_r(r_d, \alpha_r, t) = \hat{B}_{r,1}(r_d) \frac{1}{k_C} \cos(p\alpha_r + \varepsilon) + \frac{1}{2} \hat{B}_{r,1}(r_d) \gamma(r_d) \left(\cos((6q-1)p\alpha_r + 6q\omega_1 t - 3q\pi - \varepsilon) + \cos((6q+1)p\alpha_r + 6q\omega_1 t - 3q\pi + \varepsilon) \right) \quad (4.74)$$

The first component of this equation rotates with the same speed as the rotor. Therefore, it does not induce eddy-currents in the damper cylinder and the magnets. The second and the third component induce voltages in the $6q-1$ th and the $6q+1$ th damper winding.

Equation (3.37) gives the voltage equation of the $6q \pm 1$ th damper winding. In this equation, the resistance $R_{d,6q \pm 1}$ is replaced with the resistance $R_{md,6q \pm 1}$ introduced in equation (4.68) to incorporate the effect of eddy currents in the magnets. As explained in subsection 4.4.4, this resistance represents the parallel connection of the damper resistance $R_{d,6q \pm 1}$ introduced in equation (3.45) and the magnet loss resistance $R_{m,6q \pm 1}$ introduced in equation (4.67). In this way, equation (3.37) becomes

$$\vec{0} = R_{md,6q \pm 1} \vec{i}_{d,6q \pm 1} + \frac{d\vec{\Psi}_{d,6q \pm 1}}{dt} \quad (4.75)$$

The flux linkage in this equation consists of three contributions:

- 1) the flux linkage due to the pulsation because of the stator slotting $\vec{\Psi}_{dslot,6q \pm 1}$,
- 2) the flux linkage due to the field of the stator currents $\vec{\Psi}_{ds,6q \pm 1}$, and
- 3) the flux linkage due to the field of the damper currents $\vec{\Psi}_{dd,6q \pm 1}$.

Using these contributions, equation (4.75) can be written as

$$\vec{0} = R_{md,6q \pm 1} \vec{i}_{d,6q \pm 1} + \frac{d\vec{\Psi}_{dslot,6q \pm 1}}{dt} + \frac{d\vec{\Psi}_{ds,6q \pm 1}}{dt} + \frac{d\vec{\Psi}_{dd,6q \pm 1}}{dt} \quad (4.76)$$

In the same way as in subsection 3.3.3, the vector for the flux linkage of the $6q \pm 1$ th damper winding resulting from the pulsation described by equation (4.74) is calculated as

$$\vec{\Psi}_{dslot,6q \pm 1} = \frac{\pi l_s r_d N_{d,6q \pm 1}}{4p(6q \pm 1)} \gamma(r_d) \hat{B}_{r,1}(r_d) \begin{bmatrix} \cos(6q\omega_1 t - 3q\pi \pm \varepsilon) \\ \cos(6q\omega_1 t - 3q\pi + \frac{1}{2}\pi \pm \varepsilon) \end{bmatrix} \quad (4.77)$$

The time derivative of this flux linkage is called the slot voltage $\vec{e}_{dslot,6q \pm 1}$:

$$\begin{aligned} \vec{e}_{dslot,6q\pm 1} &= \frac{d\vec{\Psi}_{dslot,6q\pm 1}}{dt} \\ &= -\frac{3q\omega_1\pi l_s r_d N_{d,6q\pm 1}}{2p(6q\pm 1)} \gamma(r_d) \hat{B}_{r,1}(r_d) \left[\begin{array}{l} \sin(6q\omega_1 t - 3q\pi \pm \varepsilon) \\ \sin(6q\omega_1 t - 3q\pi + \frac{1}{2}\pi \pm \varepsilon) \end{array} \right] \end{aligned} \quad (4.78)$$

In equation (3.47), the flux linkage caused by the stator currents was expressed as $\vec{\Psi}_{ds,6q\pm 1} = M_{sd,6q\pm 1}^T \vec{i}_s$. Furthermore, in equation (3.49), the flux linkage caused by the damper currents was expressed as $\vec{\Psi}_{dd,6q\pm 1} = L_{dd,6q\pm 1} \vec{i}_{d,6q\pm 1}$. With this, equation (4.76) can be written as

$$\vec{0} = R_{md,6q} \vec{i}_{d,6q\pm 1} + \vec{e}_{dslot,6q\pm 1} + \frac{d}{dt} \{ M_{sd,6q\pm 1}^T \vec{i}_s \} + L_{dd,6q\pm 1} \frac{d\vec{i}_{d,6q\pm 1}}{dt} \quad (4.79)$$

Because the effect of the stator slotting on the voltage equations is assumed to be negligible, the stator currents can be calculated from the equations derived for a stator with a smooth stator surface. Using these stator currents and the slot voltage of equation (4.78), the current $\vec{i}_{d,6q\pm 1}$ can be solved from equation (4.79). Therefore, the extra loss caused by the pulsation due to the stator slotting can also be calculated.

It should be noted that this extra loss may be negative when the slot voltage $\vec{e}_{dslot,6q\pm 1}$ opposes the time derivative of the flux linkage caused by the stator currents $\vec{\Psi}_{ds,6q\pm 1}$.

4.5.4 Concluding remarks

In this section, the extra loss due to the stator slotting in the magnets and in the damper cylinder has been calculated. The pulsation of the magnetic flux density has been calculated with a conformal transformation. For the calculation of the loss, the voltage equations introduced in section 3.3 and the magnet loss resistance introduced in section 4.4 have been used.

In subsection 4.5.1, it was assumed that the rotor is completely covered with magnets. However, as in section 4.4, it is possible to approximate the loss in a machine the rotor of which is not completely covered with magnets. Because the magnet loss is mainly resistance limited, the magnet loss is proportional to the magnet volume. Therefore, the magnet loss in a machine the rotor of which is partly covered with magnets can be calculated as the magnet loss in a machine the rotor of which is completely covered with magnets multiplied by $2\alpha_m/\alpha_{p,1}$.

4.6 Summary

In chapters 2 and 3, the voltage equations of the permanent-magnet machine were derived. The derivations in these chapters were based on the assumptions

- that the effect of eddy currents in the iron and in the magnets on the magnetic field in the air gap is negligible, and
- that the effect of stator slotting on the magnetic field is negligible.

This chapter shows that these assumptions are useful for the derivation of the voltage equations, but that more complicated models are necessary for the calculation of the losses in the machine. These models are derived and partly verified in this chapter.

In section 4.2, the frequency-dependence of the stator resistance was described.

Next, section 4.3 introduced expressions for the iron loss, which are considered proportional to $\omega^{1.5}B^2$. This model for the iron loss is different from the commonly used models, but it is simple and it correlates with the results of the locked-rotor tests for the fundamental space harmonic. For the higher space harmonics, the model has been neither verified nor refuted.

Subsequently, in section 4.4, a model for the eddy-current loss in the magnets has been derived. For space harmonics with a large pole pitch, the real width of the magnets has been considered. Also this model has been verified for the fundamental space harmonic by means of locked-rotor tests. For the higher space harmonics, this model has been neither verified nor refuted.

In section 4.5, an approximation of the extra loss due to the stator slotting was given. The pulsation of the magnetic flux density was calculated with a conformal transformation.

In the following chapters, the resulting model will be used to determine the steady-state performance of the rectifier-loaded machine. The voltage equation for the Fourier coefficients of the stator voltages that will be used is given by equation (4.69):

$$\hat{u}_{s,6n+1} = \hat{e}_{p,6n+1} + Z_{6n+1} \hat{i}_{s,6n+1} ; \quad (4.80)$$

$$Z_{6n+1} = R_{s,6n+1} + j(6n+1)\omega_1 L_\sigma + \sum_{k=1,5,7,11,\dots}^{\infty} \frac{j(6n+1)\omega_1 L_k R_{MD,k}}{R_{MD,k} + js_{k,6n+1}(6n+1)\omega_1 L_k}$$

This voltage equation includes the copper loss in the stator, the copper loss in the damper and the eddy-current loss in the magnets.

After calculating the currents and the voltages with these voltage equations, the iron loss will be calculated with the model introduced in section 4.3. The extra loss due to the stator slotting will also be calculated afterwards with the model derived in section 4.5. This is possible, because the influence of the stator slotting and of the iron loss on the terminal voltages and the terminal currents is negligible.

Chapter 5

Calculation of the performance of the generator with rectifier

5.1 Introduction

Objective

In chapters 2 to 4, a model of the permanent-magnet machine was derived. In this chapter, the model is used to determine the performance of the rectifier-loaded permanent-magnet generator. The complete model of the generator with rectifier load will be verified experimentally in the next chapter. In chapter 7, it will be shown that the model can be used to optimize the machine design.

The objective of this chapter therefore is to combine the machine model with a model of the controlled rectifier and to derive a calculation method for the steady-state performance of the rectifier-loaded machine. Figure 5.1 depicts the machine terminal voltages and the controlled rectifier, feeding into a circuit with an inductance, a resistance, and a voltage, which may represent the battery of a series-hybrid vehicle.

The steady-state performance of the rectifier-loaded machine can be determined in several ways. In this thesis, the calculation method introduced by Bolognani and Indri [Bol 78] is used. This calculation method determines the steady-state performance in the frequency domain using Fourier analysis. This is possible because the phenomena are periodic. The calculation method is used in a few references.

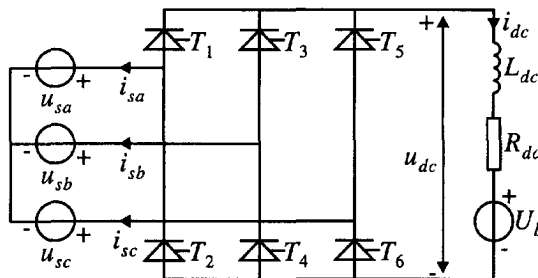


Figure 5.1: The terminal voltages of the generator and the controlled rectifier.

- The method was introduced in [Bol 78], where it was used to analyse a synchronous machine loaded with a three-pulse rectifier. In [Bol 91], Bolognani worked the method out for the analysis of a synchronous machine with six-pulse rectifier. In [Bol 93], the method was applied to analyse a twelve-pulse rectifier connected to the utility grid. In this paper, the possibility of using frequency-dependent parameters was mentioned, but it was not used.
- Hoeijmakers [Hoe 84] used this method to analyse the steady-state performance of a synchronous machine with six-pulse rectifier. He used a machine model with measured frequency-dependent operational inductances, which did not only represent the copper loss, but also the iron loss in the rotor.
- In [Pol 96], the same was done for a permanent-magnet machine with six-pulse rectifier. Here, the measured frequency-dependent operational inductances represented the overall loss in the generator caused by the time harmonics of the stator currents. The iron loss caused by the fundamental time harmonic of the stator currents and the field of the magnets was not calculated. Differences between the direct-axis and the quadrature-axis operational inductances were neglected.

This calculation method is used in this thesis because it has two important advantages.

- 1) It is capable of using frequency-dependent parameters. This is necessary, because in the derived machine model, the effects of space harmonics and eddy currents in the magnets are represented by frequency-dependent parameters.
- 2) The steady-state performance can be calculated without considering the transient interval. Another frequently used calculation method is simulation in the time domain using numerical integration. With this method, the steady state is usually reached after the simulation of a transient interval.

Two disadvantages of the calculation method used in this thesis are the use of large matrices and the use of an iteration process to determine the angle of overlap, as will be explained later in the chapter. However, the advantages are considered decisive.

To use this calculation method, it is necessary to split the machine terminal voltages into voltages across so-called external inductances L_e and so-called internal voltages \bar{e}_s . In this way, figure 5.1 changes into figure 5.2. In this figure, the thyristors are also replaced by switches, as will be explained further. The internal voltages are given by

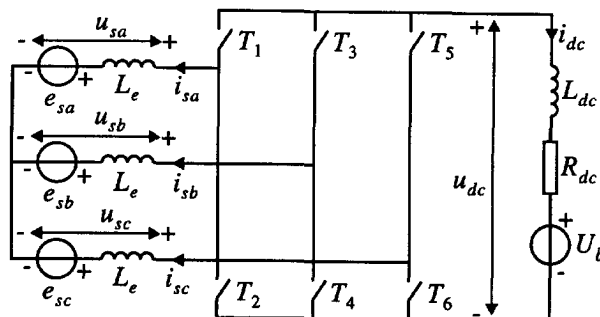


Figure 5.2: Model of the generator with rectifier with external inductance.

$$\vec{e}_s = \vec{u}_s - L_e \frac{d\vec{i}_s}{dt} \quad (5.1)$$

Bolognani does not explain how to choose the value of the external inductance. This choice is also discussed in this chapter.

Outline of the chapter

Firstly, section 5.2 describes the controlled rectifier and the use of Fourier series in this chapter. Next, in section 5.3, the phase currents are calculated for the case where the self-inductance in the direct-current circuit L_{dc} is infinitely large. Subsequently, in section 5.4, the phase currents are calculated for the case where the self-inductance L_{dc} is finite. From this, the voltage across the direct-current circuit u_{dc} and the current in the direct-current circuit i_{dc} can be calculated, which is done in section 5.5. Section 5.6 deals with the choice of the external inductance L_e . Concluding remarks are made in section 5.7.

Assumptions and starting-points

In this chapter, the machine model derived in the previous chapters is used. Therefore, the assumptions used in those chapters are also used here. Furthermore, this chapter is based on the following assumptions.

- The current i_{dc} flows continuously: it is always larger than zero.
- The thyristors can be modelled as ideal switches, as illustrated in figure 5.2.
- The angle of overlap μ is assumed to be smaller than or equal to $\pi/3$.
- The system is in steady state.

5.2 Rough description of the generator with controlled rectifier load

Firstly, subsection 5.2.1 briefly describes the operation principles of a controlled rectifier. For a more extensive description of the operation of rectifier circuits, see other books, for example, [Hof 86]. Subsequently, subsection 5.2.2 introduces the Fourier series which are used in the calculation method.

5.2.1 The operating principles

This section generally describes the operation principles of a controlled rectifier and it introduces some quantities which are used in the rest of the chapter.

In section 5.1, it was assumed that the system is in steady state. Therefore, it is enough to consider one period of the fundamental time harmonic; each period is a repetition of the previous one. In this chapter, the interval $-\pi/3 + \alpha_p < \omega_1 t < 5\pi/3 + \alpha_p$

(where α_p is the delay angle) is considered.

Figure 5.3 depicts a sketch of the three no-load line voltages and the three phase currents of the rectifier-loaded machine. On $\omega_1 t = -\pi/3$, the no-load line voltage $e_{pac} = e_{pa} - e_{pc}$ becomes larger than zero. On $\omega_1 t = -\pi/3 + \alpha_p$ thyristor T_1 is fired and the current starts commutating from phase c to phase a . Often, the terminal voltages lag the no-load voltages, so that the terminal line voltage is still negative on $\omega_1 t = -\pi/3$. However, thyristor T_1 is only fired if the terminal line voltage $u_{sac} = u_{sa} - u_{sc}$ is positive on the firing moment. The angular duration of this commutation is μ . In figures 5.3 and 5.4, this interval has number 1. After the commutation has finished, the current flows through the phases a and b , as can be seen in interval 2 of figures 5.3 and 5.4. Each $\pi/3$, a thyristor is fired on a moment α_p after the zero-crossing of one of the no-load line voltages. The sequential order of triggering is $T_1 - T_6 - T_3 - T_2 - T_5 - T_4$. In this way, a period is divided into twelve intervals, the beginnings and the ends of which coincide with the beginnings and the ends of the commutations. Figures 5.3 and 5.4 depict the twelve intervals. Table 5.1 mentions the twelve intervals and exhibits which thyristors are conducting during these intervals, which are also used in the rest of the chapter.

It should be noted that the delay angle α_p is here related to the no-load voltage, which is directly related to the rotor position, as can be seen in equation (3.16). This introduction of the delay angle α_p is different from the usual introduction of the delay angle or the firing angle. Usually, the delay angle is defined as the angle by which the starting point of commutation is delayed by phase control in relation to rectifier operation without phase control. Therefore, the delay angle is usually related to the terminal voltages. However, here, the delay angle α_p is related to the no-load voltages.

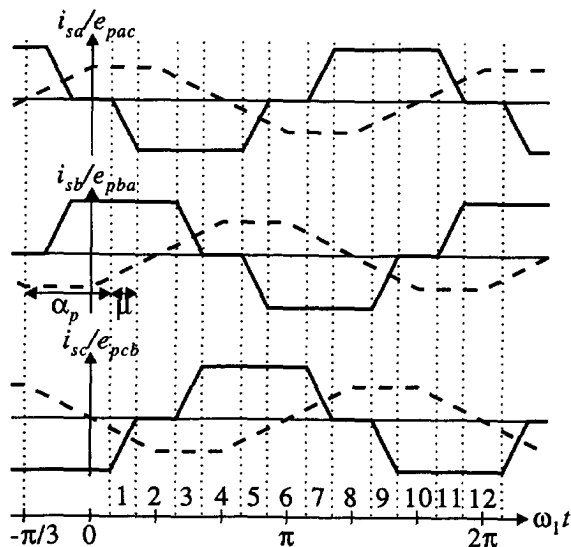


Figure 5.3: Sketch of the three phase currents (—) and the no load line voltages (--) of the PM machine with rectifier load.

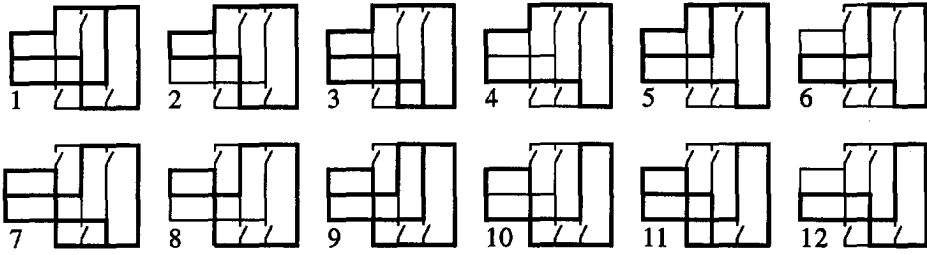


Figure 5.4: Sketch of the current paths during the twelve intervals of a period.

Table 5.1: The twelve intervals of a period with the conducting thyristors.

interval number	time interval	conducting thyristors	
1	$\alpha_p - \frac{1}{3}\pi \leq \omega_1 t < \alpha_p + \mu - \frac{1}{3}\pi$	T_1, T_5	T_4
2	$\alpha_p + \mu - \frac{1}{3}\pi \leq \omega_1 t < \alpha_p$	T_1	T_4
3	$\alpha_p \leq \omega_1 t < \alpha_p + \mu$	T_1	T_6, T_4
4	$\alpha_p + \mu \leq \omega_1 t < \alpha_p + \frac{1}{3}\pi$	T_1	T_6
5	$\alpha_p + \frac{1}{3}\pi \leq \omega_1 t < \alpha_p + \mu + \frac{1}{3}\pi$	T_3, T_1	T_6
6	$\alpha_p + \mu + \frac{1}{3}\pi \leq \omega_1 t < \alpha_p + \frac{2}{3}\pi$	T_3	T_6
7	$\alpha_p + \frac{2}{3}\pi \leq \omega_1 t < \alpha_p + \mu + \frac{2}{3}\pi$	T_3	T_2, T_6
8	$\alpha_p + \mu + \frac{2}{3}\pi \leq \omega_1 t < \alpha_p + \pi$	T_3	T_2
9	$\alpha_p + \pi \leq \omega_1 t < \alpha_p + \mu + \pi$	T_5, T_3	T_2
10	$\alpha_p + \mu + \pi \leq \omega_1 t < \alpha_p + \frac{4}{3}\pi$	T_5	T_2
11	$\alpha_p + \frac{4}{3}\pi \leq \omega_1 t < \alpha_p + \mu + \frac{4}{3}\pi$	T_5	T_4, T_2
12	$\alpha_p + \mu + \frac{4}{3}\pi \leq \omega_1 t < \alpha_p + \frac{5}{3}\pi$	T_5	T_4

5.2.2 The use of Fourier series

In this chapter, Fourier series are used in another way from that in chapters 2 to 4, and in a way slightly different from usual. Therefore, the Fourier series used in this chapter are briefly described in this subsection.

If $f(t)$ is a periodic function of time with period $T=2\pi/\omega_1$, it can be written as a Fourier series:

$$f(t) = \frac{1}{2} \sum_{n=-\infty}^{\infty} \hat{f}_n e^{jn\omega_1 t} \quad (5.2)$$

where the Fourier coefficients \hat{f}_n are calculated as

$$\hat{f}_n = \frac{2}{T} \int_{t=x}^{x+T} f(t) e^{-jn\omega_1 t} dt \quad (5.3)$$

This introduction of Fourier series and Fourier coefficients slightly differs from the usual definition: the factor 1/2 in equation (5.2) and the factor 2 in equation (5.3) are added to the usual definition. The different introduction is used here because in this way, the Fourier coefficients are equal to the complex amplitudes of the harmonics.

Furthermore, a useful property of Fourier series is that if $f(t)$ is a real function,

$$\hat{f}_n = \hat{f}_{-n}^* \quad (5.4)$$

is valid, where \hat{f}_n^* is the complex conjugate of \hat{f}_n .

Using this form of Fourier series, the set of no-load voltages of equation (3.82), the set of stator currents of equation (3.84), and the set of terminal voltages of equation (3.89) during steady-state operation with rectifier load are written as

$$\vec{e}_p = \frac{1}{2} \sum_{n=-\infty}^{\infty} \left(\hat{e}_{p,6n+1} e^{j(6n+1)\omega_1 t} \begin{bmatrix} 1 \\ e^{-j\frac{2}{3}\pi} \\ e^{-j\frac{4}{3}\pi} \end{bmatrix} + \hat{e}_{p,6n+1}^* e^{-j(6n+1)\omega_1 t} \begin{bmatrix} 1 \\ e^{j\frac{2}{3}\pi} \\ e^{j\frac{4}{3}\pi} \end{bmatrix} \right) \quad (5.5)$$

$$\vec{i}_s = \frac{1}{2} \sum_{n=-\infty}^{\infty} \left(\hat{i}_{s,6n+1} e^{j(6n+1)\omega_1 t} \begin{bmatrix} 1 \\ e^{-j\frac{2}{3}\pi} \\ e^{-j\frac{4}{3}\pi} \end{bmatrix} + \hat{i}_{s,6n+1}^* e^{-j(6n+1)\omega_1 t} \begin{bmatrix} 1 \\ e^{j\frac{2}{3}\pi} \\ e^{j\frac{4}{3}\pi} \end{bmatrix} \right) \quad (5.6)$$

$$\vec{u}_s = \frac{1}{2} \sum_{n=-\infty}^{\infty} \left(\hat{u}_{s,6n+1} e^{j(6n+1)\omega_1 t} \begin{bmatrix} 1 \\ e^{-j\frac{2}{3}\pi} \\ e^{-j\frac{4}{3}\pi} \end{bmatrix} + \hat{u}_{s,6n+1}^* e^{-j(6n+1)\omega_1 t} \begin{bmatrix} 1 \\ e^{j\frac{2}{3}\pi} \\ e^{j\frac{4}{3}\pi} \end{bmatrix} \right) \quad (5.7)$$

The internal voltages are also written as Fourier series. This is done by substituting the Fourier series for the stator currents (equation (5.6)) and the terminal voltages (equation (5.7)) in the equation for the internal voltages (equation (5.1)). Furthermore, $\hat{u}_{s,6n+1} = \hat{e}_{p,6n+1} + Z_{i,6n+1} \hat{i}_{s,6n+1}$ (equation (4.80)) is used for the Fourier coefficients of the terminal voltages. The result is

$$\bar{e}_s = \frac{1}{2} \sum_{n=-\infty}^{\infty} \left(\hat{e}_{s,6n+1} e^{j(6n+1)\omega_1 t} \begin{bmatrix} 1 \\ e^{-j\frac{2}{3}\pi} \\ e^{-j\frac{4}{3}\pi} \end{bmatrix} + \hat{e}_{s,6n+1}^* e^{-j(6n+1)\omega_1 t} \begin{bmatrix} 1 \\ e^{j\frac{2}{3}\pi} \\ e^{j\frac{4}{3}\pi} \end{bmatrix} \right) \quad (5.8)$$

where the Fourier coefficients of the internal voltage are calculated as

$$\hat{e}_{s,6n+1} = \hat{e}_{p,6n+1} + Z_{i,6n+1} \hat{i}_{s,6n+1} ; \quad Z_{i,6n+1} = Z_{6n+1} - j(6n+1)\omega_1 L_e \quad (5.9)$$

5.3 An infinitely large self-inductance in the direct-current circuit

5.3.1 Introduction

In this section, the machine current is calculated for the case where the self-inductance in the direct-current circuit L_{dc} is infinitely large. In this case, the current in the direct-current circuit i_{dc} is constant; the magnitude of the current is I_{dc} .

To determine the steady-state performance of the rectifier-loaded permanent-magnet machine, the voltage equations of the machine have to be combined with the switching pattern of the rectifier, and the resulting (differential) equation has to be solved. This section describes a method for doing so.

An ideal calculation method would use all known quantities to determine the unknown quantities. Thus, the ideal calculation method would use the machine parameters, the no-load voltages, the delay angle α_p , the voltage U_b and the resistance R_{dc} to calculate the phase currents and the angle of overlap. However, the calculation method used in this section is not ideal: it uses the machine parameters, the no-load voltages, the delay angle α_p and the angle of overlap to calculate the phase currents and the current i_{dc} . So, the calculation method needs the unknown angle of overlap as an input, and it can not use the known voltage U_b of the voltage source as an input. This causality problem is solved by means of an iteration process. Firstly, the calculation is done with an arbitrary value of the angle of overlap. If the resulting constant component of the voltage u_{dc} is smaller than the calculated voltage across the resistance R_{dc} plus the voltage U_b ($u_{dc,0} < I_{dc} R_{dc} + U_b$), the angle of overlap is decreased and the calculation is repeated. If the resulting constant component of the voltage u_{dc} is larger than the calculated voltage across the resistance R_{dc} plus the voltage U_b ($u_{dc,0} > I_{dc} R_{dc} + U_b$), the

angle of overlap is increased and the calculation is repeated. In this way, the correct value of the angle of overlap is obtained by means of an iteration process.

When the direct-current circuit contains a current source with a constant current, a comparable iteration process may be applied. This is not worked out further, because it is not used in this thesis.

In subsection 5.3.2, the equations describing the machine and the direct-current circuit are combined with the switching pattern of the rectifier. The result is an equation for the time derivative of the current i_{sa} . From this equation, the Fourier coefficients of the phase current are calculated in subsection 5.3.3.

5.3.2 Forming an equation for the time derivative of the phase current

In this subsection, an equation for the time derivative of the current of phase a i_{sa} is formed. This is done, because it appears from the references mentioned in section 5.1 that this equation can be solved. The angle of overlap has a value determined by the iteration process.

Figure 5.5 depicts the circuit during interval number 1. The switches that do not conduct are omitted, and the layout of the circuit is changed to obtain planar meshes. Furthermore, the elements of the direct-current circuit are replaced by a current source with a constant direct current I_{dc} .

The time derivative of the current i_{sa} is determined by solving the mesh equations, which prescribe that the sum of the voltages of a mesh are zero. For the circuit of figure 5.5, it is enough to consider the mesh equation of the mesh which includes phase a :

$$e_{sc} + L_e \frac{di_{sc}}{dt} - L_e \frac{di_{sa}}{dt} - e_{sa} = 0 \quad (5.10)$$

Furthermore, an extra equation is valid for this circuit:

$$i_{sc} = -i_{sa} - i_{sb} = -i_{sa} - I_{dc} \quad (5.11)$$

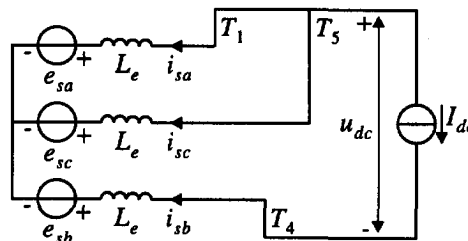


Figure 5.5: The circuit during interval number 1.

Substituting this equation in equation (5.10) results in an equation for the time derivative of the current i_{sa} :

$$2L_e \frac{di_{sa}}{dt} = e_{sc} - e_{sa} \tag{5.12}$$

In the same way, the time derivative of the current i_{sa} during the other intervals can be determined. The results are given in table 5.2. During the intervals 2, 3, 4, 6, 8, 9, 10, and 12, the current i_{sa} is constant so that its time derivative is zero.

To form an equation for the time derivative of the current i_{sa} which is valid during the whole period, the pulse function p is introduced. This pulse function p is one during interval number 1, and zero during the rest of the period:

$$p(\omega_1 t) = \begin{cases} 1 & \text{for } -\frac{1}{3}\pi + \alpha_p \leq \omega_1 t < -\frac{1}{3}\pi + \alpha_p + \mu \\ 0 & \text{for } -\frac{1}{3}\pi + \alpha_p + \mu \leq \omega_1 t < \frac{5}{3}\pi + \alpha_p \end{cases} \tag{5.13}$$

With this pulse function and table 5.2, the time derivative of the current i_{sa} can be written as

$$2L_e \frac{di_{sa}}{dt} = (e_{sc} - e_{sa})(p(\omega_1 t) + p(\omega_1 t - \pi)) + (e_{sb} - e_{sa})(p(\omega_1 t - \frac{2}{3}\pi) + p(\omega_1 t - \frac{5}{3}\pi)) \tag{5.14}$$

Table 5.2: The time derivative of the current during the 12 intervals of a period.

interval number	pulse function that is one	$2L_e \frac{di_{sa}}{dt}$
1	$p(\omega_1 t)$	$e_{sc} - e_{sa}$
2,3,4	-	0
5	$p(\omega_1 t - \frac{2}{3}\pi)$	$e_{sb} - e_{sa}$
6	-	0
7	$p(\omega_1 t - \pi)$	$e_{sc} - e_{sa}$
8,9,10	-	0
11	$p(\omega_1 t - \frac{5}{3}\pi)$	$e_{sb} - e_{sa}$
12	-	0

5.3.3 Solving the Fourier coefficients of the phase current

In the previous subsection, an equation was derived for the time derivative of the current i_{sa} , namely equation (5.14), which is solved in this subsection. This is done by substituting Fourier series for all functions in the equation. The resulting equation can be solved for a finite number of harmonics.

The pulse function p introduced in equation (5.13) can be written as a Fourier series:

$$p(\omega_1 t) = \frac{1}{2} \sum_{n=-\infty}^{\infty} \hat{p}_n e^{jn\omega_1 t} \quad (5.15)$$

where the Fourier coefficients \hat{p}_n are calculated with equation (5.3) as

$$\hat{p}_n = \frac{2}{2\pi} \int_{-\pi/3+\alpha_p}^{-\pi/3+\alpha_p+\mu} e^{-jn\omega_1 t} d\omega_1 t = \frac{j}{\pi n} e^{-jn(-\frac{1}{3}\pi+\alpha_p)} (e^{-jn\mu}-1) \quad (5.16)$$

It should be noted that the Fourier coefficients of the pulse function p can only be determined because the angle of overlap has a value determined by the iteration process.

The Fourier series for the current, the internal voltages and the pulse function p (equations (5.6), (5.8), and (5.15) respectively) are substituted in equation (5.14):

$$\begin{aligned} & \frac{1}{2} \sum_{n=-\infty}^{\infty} \left(2j(6n+1)\omega_1 L_e \hat{L}_{s,6n+1} e^{j(6n+1)\omega_1 t} - 2j(6n+1)\omega_1 L_e \hat{L}_{s,6n+1}^* e^{-j(6n+1)\omega_1 t} \right) \\ &= \frac{1}{4} \sum_{n=-\infty}^{\infty} \left(\hat{L}_{s,6n+1} \left(e^{-j\frac{4}{3}\pi} - 1 \right) e^{j(6n+1)\omega_1 t} + \hat{L}_{s,6n+1}^* \left(e^{j\frac{4}{3}\pi} - 1 \right) e^{-j(6n+1)\omega_1 t} \right) \\ & \quad \cdot \sum_{n=-\infty}^{\infty} \hat{p}_n (1 + e^{jn\pi}) e^{jn\omega_1 t} \\ &+ \frac{1}{4} \sum_{n=-\infty}^{\infty} \left(\hat{L}_{s,6n+1} \left(e^{-j\frac{2}{3}\pi} - 1 \right) e^{j(6n+1)\omega_1 t} + \hat{L}_{s,6n+1}^* \left(e^{j\frac{2}{3}\pi} - 1 \right) e^{-j(6n+1)\omega_1 t} \right) \\ & \quad \cdot \sum_{n=-\infty}^{\infty} \hat{p}_n (1 + e^{jn\pi}) e^{-jn\frac{2}{3}\pi} e^{jn\omega_1 t} \end{aligned} \quad (5.17)$$

The multiplications of the series on the right side of this equation results in

$$\begin{aligned} & \sum_{n=-\infty}^{\infty} \left(j(6n+1)\omega_1 L_e \hat{L}_{s,6n+1} e^{j(6n+1)\omega_1 t} - j(6n+1)\omega_1 L_e \hat{L}_{s,6n+1}^* e^{-j(6n+1)\omega_1 t} \right) = \frac{1}{4} \sum_{k=-\infty}^{\infty} e^{jk\omega_1 t} \\ & \quad \cdot \sum_{m=-\infty}^{\infty} \left(\hat{L}_{s,6m+1} \hat{p}_{k-6m-1} (1 + e^{j(k-6m-1)\pi}) \left\{ e^{-j\frac{4}{3}\pi} - 1 + \left(e^{-j\frac{2}{3}\pi} - 1 \right) e^{-j(k-6m-1)\frac{2}{3}\pi} \right\} \right. \\ & \quad \left. + \hat{L}_{s,6m+1}^* \hat{p}_{k+6m+1} (1 + e^{j(k+6m+1)\pi}) \left\{ e^{j\frac{4}{3}\pi} - 1 + \left(e^{j\frac{2}{3}\pi} - 1 \right) e^{-j(k+6m+1)\frac{2}{3}\pi} \right\} \right) \end{aligned} \quad (5.18)$$

When the right side of this equation is worked out, it appears that the harmonics of which the harmonic number is an integer multiple of 2 or 3 are zero. This could already be expected, because the left side of this equation does not contain these harmonics either. Furthermore, this equation must hold for each time harmonic. By substituting $k=6n+1$ on the right side of this equation, an equation for a series of Fourier coefficients is obtained:

$$j(6n+1)\omega_1 L_e \hat{I}_{s,6n+1} = -\frac{3}{2} \sum_{m=-\infty}^{\infty} \left(\hat{E}_{s,6m+1} \hat{P}_{6(n-m)} + \hat{E}_{s,6m+1}^* e^{j\frac{1}{3}\pi} \hat{P}_{6(n+m)+2} \right) \tag{5.19}$$

By substituting $k=-(6n+1)$ on the right side of equation (5.18), an expression for another series of Fourier coefficients is obtained:

$$-j(6n+1)\omega_1 L_e \hat{I}_{s,6n+1}^* = -\frac{3}{2} \sum_{m=-\infty}^{\infty} \left(\hat{E}_{s,6m+1}^* \hat{P}_{-6(n-m)} + \hat{E}_{s,6m+1} \hat{P}_{-(6(n+m)+2)} e^{-j\frac{1}{3}\pi} \right) \tag{5.20}$$

This equation is the complex conjugate of equation (5.19), as can be seen when it is taken that $\hat{P}_n = \hat{P}_{-n}^*$, which is valid because the pulse function p is a real function (see equation (5.4)).

That these equations are each other's complex conjugates, means that if one of the equations is solved, the solution for the other is also known. Therefore, it is sufficient to solve one of these equations. Here, equation (5.19) is solved.

The Fourier coefficients of the internal voltage in this equation are substituted by equation (5.9):

$$j(6n+1)\omega_1 L_e \hat{I}_{s,6n+1} = -\frac{3}{2} \sum_{m=-\infty}^{\infty} \left((\hat{E}_{p,6m+1} + Z_{i,6m+1} \hat{I}_{s,6m+1}) \hat{P}_{6(n-m)} + (\hat{E}_{p,6m+1}^* + Z_{i,6m+1}^* \hat{I}_{s,6m+1}^*) e^{j\frac{1}{3}\pi} \hat{P}_{6(n+m)+2} \right) \tag{5.21}$$

All unknowns in this equation (the Fourier coefficients of the phase current) are transported to the left side of this equation:

$$j(6n+1)\omega_1 L_e \hat{I}_{s,6n+1} + \frac{3}{2} \sum_{m=-\infty}^{\infty} \left(Z_{i,6m+1} \hat{P}_{6(n-m)} \hat{I}_{s,6m+1} + Z_{i,6m+1}^* e^{j\frac{1}{3}\pi} \hat{P}_{6(n+m)+2} \hat{I}_{s,6m+1}^* \right) = -\frac{3}{2} \sum_{m=-\infty}^{\infty} \left(\hat{E}_{p,6m+1} \hat{P}_{6(n-m)} + \hat{E}_{p,6m+1}^* e^{j\frac{1}{3}\pi} \hat{P}_{6(n+m)+2} \right) \tag{5.22}$$

After introducing

$$a_{nm} = \begin{cases} j(6n+1)\omega_1 L_e & \text{for } n=m \\ 0 & \text{for } n \neq m \end{cases} \tag{5.23}$$

$$b_{nm} = \frac{3}{2} Z_{i,6m+1} \hat{P}_{6(n-m)} \tag{5.24}$$

$$c_{nm} = \frac{3}{2} Z_{i,6m+1}^* P_{6(n+m)+2} e^{j\frac{1}{3}\pi} \quad (5.25)$$

$$d_n = -\frac{3}{2} \sum_{m=-\infty}^{\infty} \left(\hat{e}_{p,6m+1} \hat{p}_{6(n-m)} + \hat{e}_{p,6m+1}^* \hat{p}_{6(n+m)+2} e^{j\frac{1}{3}\pi} \right) \quad (5.26)$$

equation (5.22) can be written as

$$\sum_{m=-\infty}^{\infty} \left((a_{nm} + b_{nm}) \hat{i}_{s,6m+1} + c_{nm} \hat{i}_{s,6m+1}^* \right) = d_n \quad (5.27)$$

This equation contains the Fourier coefficients of the current and their complex conjugates. It can be solved by splitting these Fourier coefficients into real and imaginary parts. Using

$$\hat{i}_{s,6m+1} = x_m + jy_m \quad (5.28)$$

this can be written as a set of equations:

$$\begin{cases} \sum_{m=-\infty}^{\infty} \left(\operatorname{Re}(a_{nm} + b_{nm} + c_{nm}) x_m + \operatorname{Im}(-a_{nm} - b_{nm} + c_{nm}) y_m \right) = \operatorname{Re}(d_n) \\ \sum_{m=-\infty}^{\infty} \left(\operatorname{Im}(a_{nm} + b_{nm} + c_{nm}) x_m + \operatorname{Re}(a_{nm} + b_{nm} - c_{nm}) y_m \right) = \operatorname{Im}(d_n) \end{cases} \quad (5.29)$$

For a finite number of harmonics, $m, n = -N, \dots, N$, this is a set of $4N+2$ equations with $4N+2$ unknowns, which can be written as a matrix equation:

$$\begin{bmatrix} A_{1,1} & \dots & A_{1,4N+2} \\ \vdots & \ddots & \vdots \\ A_{4N+2,1} & \dots & A_{4N+2,4N+2} \end{bmatrix} \begin{bmatrix} x_{-N} \\ \vdots \\ x_N \\ y_{-N} \\ \vdots \\ y_N \end{bmatrix} = \begin{bmatrix} \operatorname{Re}(d_{-N}) \\ \vdots \\ \operatorname{Re}(d_N) \\ \operatorname{Im}(d_{-N}) \\ \vdots \\ \operatorname{Im}(d_N) \end{bmatrix} \quad (5.30)$$

where

$$A_{N+1+n, N+1+m} = \operatorname{Re}(a_{nm} + b_{nm} + c_{nm}) \quad (5.31)$$

$$A_{N+1+n, 3N+2+m} = \operatorname{Im}(-a_{nm} - b_{nm} + c_{nm}) \quad (5.32)$$

$$A_{3N+2+n, N+1+m} = \operatorname{Im}(a_{nm} + b_{nm} + c_{nm}) \quad (5.33)$$

$$A_{3N+2+n, 3N+2+m} = \operatorname{Re}(a_{nm} + b_{nm} - c_{nm}) \quad (5.34)$$

From this matrix equation, x_m and y_m can be solved. When x_m and y_m are solved, the

Fourier coefficients of the current follow with $\hat{i}_{s,6m+1} = x_m + jy_m$ (equation (5.28)). Using the Fourier coefficients of the current, the Fourier coefficients of the terminal voltages can be calculated by means of $\hat{u}_{s,6n+1} = \hat{e}_{p,6n+1} + Z_{6n+1} \hat{i}_{s,6n+1}$ (equation (4.80)).

Although this solution may be very accurate, it remains an approximation, because only a finite number of harmonics can be considered.

It should be noted that the equation for the time derivative of the phase current could only be solved in this way because the angle of overlap had a value before the calculation started.

5.4 A finite self-inductance in the direct-current circuit

5.4.1 Introduction

In this section the current is calculated for the case where the self-inductance in the direct-current circuit L_{dc} is finite. In principle, the method used is the same as in the previous section. However, the equations are much more complicated because the current in the direct-current circuit i_{dc} is not constant. Also, the iteration process to the correct value of the angle of overlap is different.

As in the previous section, an ideal calculation method would use all known quantities to determine the unknown quantities. It would use the machine parameters, the no-load voltages, the delay angle α_p , the parameters of the direct-current circuit, and the voltage U_b to calculate the phase currents and the angle of overlap. However, the calculation method used in this section is not ideal: it uses the machine parameters, the no-load voltages, the delay angle α_p , the parameters of the direct-current circuit, the voltage U_b , and the angle of overlap to calculate the phase currents. So, the calculation process needs the unknown value of the angle of overlap as an input. There is only one correct value for the angle of overlap. When this correct value is used, the output voltage of the rectifier u_{dc} fits to the parameters of the direct-current circuit and the voltage U_b . When another value is used, the calculation method produces nonsense: the output voltage of the rectifier u_{dc} does not fit to the parameters of the direct-current circuit and the voltage U_b . The consequence of this is that the current i_{sa} is not zero during the time phase a does not conduct (during the intervals 6 and 12 in figure 5.3).

This problem is solved by using an iteration process. Firstly, the calculation is done with an arbitrary value for the angle of overlap. If the calculated current i_{sa} during interval number 6 is smaller than zero, the angle of overlap is increased and the calculation is repeated. If the calculated current i_{sa} during interval number 6 is larger than zero, the angle of overlap is decreased and the calculation is repeated. As the value of the current i_{sa} during interval number 6, the current in the middle of this interval is used. This is done because in the middle of the interval, the Gibb's phenomenon [Kwa 91] is smaller than at the borders, and therefore the numerical accuracy of the

calculation is better. Writing this current as a Fourier series as in (5.6) results in

$$i_{sa} \left(\frac{1}{\omega_1} \left(\frac{1}{2} \pi + \alpha_p + \frac{1}{2} \mu \right) \right) = \frac{1}{2} \sum_{m=-\infty}^{\infty} \left(\hat{I}_{s,6m+1} e^{j(6m+1) \left(\frac{1}{2} \pi + \alpha_p + \frac{1}{2} \mu \right)} + \hat{I}_{s,6m+1}^* e^{-j(6m+1) \left(\frac{1}{2} \pi + \alpha_p + \frac{1}{2} \mu \right)} \right) = 0 \quad (5.35)$$

In subsection 5.4.2, the equations describing the machine and the direct-current circuit are combined with the switching pattern of the rectifier. The result is an equation for the time derivative of the current i_{sa} . From this equation, the Fourier coefficients of the phase current are calculated in subsection 5.4.3.

5.4.2 Forming an equation for the time derivative of the phase current

This subsection describes the derivation of an equation for the time derivative of the current of phase a i_{sa} .

The determination of the time derivative of the current i_{sa} if the self-inductance L_{dc} is finite is much more difficult than if this self-inductance is infinitely large. For interval number 1, this determination is given. For the other eleven intervals, the time derivative of the current i_{sa} can be determined in a similar way.

Figure 5.6 depicts the circuit during interval number 1. The switches that do not conduct are omitted, and the layout of the circuit is changed to obtain planar meshes. The time derivative of the current i_{sa} is determined by solving the mesh equations. For the two meshes of figure 5.6 a set of two equations results:

$$\begin{cases} e_{sc} + L_e \frac{di_{sc}}{dt} - L_e \frac{di_{sa}}{dt} - e_{sa} = 0 \\ e_{sb} + L_e \frac{di_{sb}}{dt} + U_b + R_{dc} i_{dc} + L_{dc} \frac{di_{dc}}{dt} - L_e \frac{di_{sc}}{dt} - e_{sc} = 0 \end{cases} \quad (5.36)$$

Furthermore, two extra equations are valid for this network:

$$\begin{cases} i_{sc} = -i_{sa} - i_{sb} \\ i_{dc} = i_{sb} \end{cases} \quad (5.37)$$

These equations are substituted in equation (5.36).

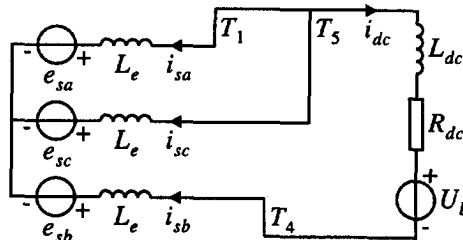


Figure 5.6: The circuit during interval number 1.

From the result, the time derivative of the current i_{sa} can be solved as

$$\frac{di_{sa}}{dt} = \frac{L_{dc}(e_{sc}-e_{sa})}{L_e(3L_e+2L_{dc})} + \frac{e_{sb}+e_{sc}-2e_{sa}+R_{dc}i_{sb}+U_b}{3L_e+2L_{dc}} \quad (5.38)$$

In the same way, the time derivative of the current i_{sa} during the other eleven intervals can be calculated from the mesh equations. The results are given in table 5.3. It can be seen that this table becomes equal to table 5.2 if the self-inductance L_{dc} is made infinitely large.

To form an equation for the time derivative of the phase current i_{sa} which is valid during the whole period, the pulse functions p and h are used. The pulse function p was introduced in equation (5.13). The pulse function h is introduced here, it is one during interval number 2, and zero during the rest of the period:

$$h(\omega_1 t) = \begin{cases} 1 & \text{for } -\frac{1}{3}\pi + \alpha_p + \mu < \omega_1 t < \alpha_p \\ 0 & \text{for } \alpha_p < \omega_1 t < \frac{5}{3}\pi + \alpha_p + \mu \end{cases} \quad (5.39)$$

The following inductances are introduced:

$$L_1 = 2L_e \left(1 + \frac{3L_e}{2L_{dc}} \right) \quad (5.40)$$

$$L_2 = 3L_e + 2L_{dc} \quad (5.41)$$

$$L_3 = 2L_e + L_{dc} \quad (5.42)$$

With these inductances and table 5.3, the time derivative of the current i_{sa} can be written as

$$\begin{aligned} \frac{di_{sa}}{dt} = & \left(\frac{e_{sc}-e_{sa}}{L_1} + \frac{e_{sb}+e_{sc}-2e_{sa}+i_{sb}R_{dc}}{L_2} \right) (p(\omega_1 t) + p(\omega_1 t - \pi)) \\ & + \frac{e_{sb}-e_{sa}+i_{sb}R_{dc}}{L_3} (h(\omega_1 t) + h(\omega_1 t - \pi)) \\ & + \frac{e_{sb}+e_{sc}-2e_{sa}-2i_{sa}R_{dc}}{L_2} (p(\omega_1 t - \frac{1}{3}\pi) + p(\omega_1 t - \frac{4}{3}\pi)) \\ & + \frac{e_{sc}-e_{sa}-i_{sa}R_{dc}}{L_3} (h(\omega_1 t - \frac{1}{3}\pi) + h(\omega_1 t - \frac{4}{3}\pi)) \\ & + \left(\frac{e_{sb}-e_{sa}}{L_1} + \frac{e_{sb}+e_{sc}-2e_{sa}+i_{sc}R_{dc}}{L_2} \right) (p(\omega_1 t - \frac{2}{3}\pi) + p(\omega_1 t - \frac{5}{3}\pi)) \\ & + \frac{U_b}{L_2} (p(\omega_1 t) - p(\omega_1 t - \pi) + 2p(\omega_1 t - \frac{1}{3}\pi) - 2p(\omega_1 t - \frac{4}{3}\pi) + p(\omega_1 t - \frac{2}{3}\pi) - p(\omega_1 t - \frac{5}{3}\pi)) \\ & + \frac{U_b}{L_3} (h(\omega_1 t) - h(\omega_1 t - \pi) + h(\omega_1 t - \frac{1}{3}\pi) - h(\omega_1 t - \frac{4}{3}\pi)) \end{aligned} \quad (5.43)$$

Table 5.3: The time derivative of the current during the 12 intervals of a period.

interval number	pulse function that is one	$\frac{di_{sa}}{dt}$
1	$p(\omega_1 t)$	$\frac{L_{dc}(e_{sc}-e_{sa})}{L_e(3L_e+2L_{dc})} + \frac{e_{sb}+e_{sc}-2e_{sa}+i_{sb}R_{dc}+U_b}{3L_e+2L_{dc}}$
2	$h(\omega_1 t)$	$\frac{e_{sb}-e_{sa}+i_{sb}R_{dc}+U_b}{2L_e+L_{dc}}$
3	$p(\omega_1 t-\frac{1}{3}\pi)$	$\frac{e_{sb}+e_{sc}-2e_{sa}-2i_{sa}R_{dc}+2U_b}{3L_e+2L_{dc}}$
4	$h(\omega_1 t-\frac{1}{3}\pi)$	$\frac{e_{sc}-e_{sa}-i_{sa}R_{dc}+U_b}{2L_e+L_{dc}}$
5	$p(\omega_1 t-\frac{2}{3}\pi)$	$\frac{L_{dc}(e_{sb}-e_{sa})}{L_e(3L_e+2L_{dc})} + \frac{e_{sb}+e_{sc}-2e_{sa}+i_{sc}R_{dc}+U_b}{3L_e+2L_{dc}}$
6	$h(\omega_1 t-\frac{2}{3}\pi)$	0
7	$p(\omega_1 t-\pi)$	$\frac{L_{dc}(e_{sc}-e_{sa})}{L_e(3L_e+2L_{dc})} + \frac{e_{sb}+e_{sc}-2e_{sa}+i_{sb}R_{dc}-U_b}{3L_e+2L_{dc}}$
8	$h(\omega_1 t-\pi)$	$\frac{e_{sb}-e_{sa}+i_{sb}R_{dc}-U_b}{2L_e+L_{dc}}$
9	$p(\omega_1 t-\frac{4}{3}\pi)$	$\frac{e_{sb}+e_{sc}-2e_{sa}-2i_{sa}R_{dc}-2U_b}{3L_e+2L_{dc}}$
10	$h(\omega_1 t-\frac{4}{3}\pi)$	$\frac{e_{sc}-e_{sa}-i_{sa}R_{dc}-U_b}{2L_e+L_{dc}}$
11	$p(\omega_1 t-\frac{5}{3}\pi)$	$\frac{L_{dc}(e_{sb}-e_{sa})}{L_e(3L_e+2L_{dc})} + \frac{e_{sb}+e_{sc}-2e_{sa}+i_{sc}R_{dc}-U_b}{3L_e+2L_{dc}}$
12	$h(\omega_1 t-\frac{5}{3}\pi)$	0

5.4.3 Solving the Fourier coefficients of the phase current

In the previous subsection, an equation was derived for the time derivative of the current i_{sa} , namely equation (5.43), which is solved in this subsection. This is done by substituting Fourier series in the equation. The resulting equation can be solved for a finite number of harmonics. The structure of this solution is the same as in subsection 5.3.3, but the equations are much larger. Therefore, a part of the derivation has been moved to appendix E.

The pulse function h of equation (5.39) can be written as a Fourier series:

$$h(\omega_1 t) = \frac{1}{2} \sum_{n=-\infty}^{\infty} \hat{h}_n e^{jn\omega_1 t} \quad (5.44)$$

where the Fourier coefficients \hat{h}_n are calculated with equation (5.3) as

$$\hat{h}_n = \frac{2}{2\pi} \int_{-\pi/3+\alpha_p+\mu}^{\alpha_p} e^{-jn\omega_1 t} d\omega_1 t = \frac{j}{\pi n} e^{-jn\alpha_p} \left(1 - e^{-jn(-\frac{1}{3}\pi+\mu)} \right) \quad (5.45)$$

Equation (5.43) is worked out by substituting the Fourier series for the pulse functions, the currents and the internal voltages. This is done in appendix E. The resulting equation is given by

$$\begin{aligned} & j(6n+1)\omega_1 \hat{L}_{s,6n+1} \\ & + \sum_{m=-\infty}^{\infty} \left\{ \hat{L}_{s,6m+1} \left(3\hat{p}_{6(n-m)} \left(\frac{Z_{i,6m+1}}{L_1} + \frac{3Z_{i,6m+1} + R_{dc}}{L_2} \right) + \hat{h}_{6(n-m)} \frac{3Z_{i,6m+1} + R_{dc} (1 - e^{-j\frac{2}{3}\pi})}{L_3} \right) \right. \\ & \quad \left. + \hat{L}_{s,6m+1}^* \left(3\hat{p}_{6(n+m)+2}^* \left(\frac{Z_{i,6m+1}^* - R_{dc}}{L_1} \right) e^{j\frac{1}{3}\pi} + \hat{h}_{6(n+m)+2} \frac{3Z_{i,6m+1}^* e^{-j\frac{1}{3}\pi} - j\sqrt{3}R_{dc}}{L_3} \right) \right\} \\ & = 2U_b \left(\hat{p}_{6n+1} \frac{3}{L_2} e^{-j\frac{1}{3}\pi} + \hat{h}_{6n+1} \frac{1}{L_3} (1 + e^{-j\frac{1}{3}\pi}) \right) \\ & - 3 \sum_{m=-\infty}^{\infty} \left\{ \hat{L}_{p,6m+1} \left(\hat{p}_{6(n-m)} \left(\frac{1}{L_1} + \frac{3}{L_2} \right) + \hat{h}_{6(n-m)} \frac{1}{L_3} \right) \right. \\ & \quad \left. + \hat{L}_{p,6m+1}^* \left(\hat{p}_{6(n+m)+2}^* \frac{1}{L_1} e^{j\frac{1}{3}\pi} + \hat{h}_{6(n+m)+2} \frac{1}{L_3} e^{-j\frac{1}{3}\pi} \right) \right\} \end{aligned} \quad (5.46)$$

After introducing

$$\underline{a}_{nm} = \begin{cases} j(6n+1)\omega_1 & \text{for } n=m \\ 0 & \text{for } n \neq m \end{cases} \quad (5.47)$$

$$b_{nm} = 3\hat{p}_{6(n-m)} \left(\frac{Z_{i,6m+1}}{L_1} + \frac{3Z_{i,6m+1} + R_{dc}}{L_2} \right) + \hat{h}_{6(n-m)} \frac{3Z_{i,6m+1} + R_{dc} (1 - e^{-j\frac{2}{3}\pi})}{L_3} \quad (5.48)$$

$$c_{nm} = 3\hat{p}_{6(n+m)+2} \left(\frac{Z_{i,6m+1}^*}{L_1} - \frac{R_{dc}}{L_2} \right) e^{j\frac{1}{3}\pi} + \hat{h}_{6(n+m)+2} \frac{3Z_{i,6m+1}^* e^{-j\frac{1}{3}\pi} - j\sqrt{3}R_{dc}}{L_3} \quad (5.49)$$

$$\begin{aligned} d_n = & 2U_b \left(\hat{p}_{6n+1} \frac{3}{L_2} e^{-j\frac{1}{3}\pi} + \hat{h}_{6n+1} \frac{1}{L_3} (1 + e^{-j\frac{1}{3}\pi}) \right) \\ & - 3 \sum_{m=-\infty}^{\infty} \left\{ \hat{e}_{p,6m+1} \left(\hat{p}_{6(n-m)} \left(\frac{1}{L_1} + \frac{3}{L_2} \right) + \hat{h}_{6(n-m)} \frac{1}{L_3} \right) \right. \\ & \left. + \hat{e}_{p,6m+1}^* \left(\hat{p}_{6(n+m)+2} \frac{1}{L_1} e^{j\frac{1}{3}\pi} + \hat{h}_{6(n+m)+2} \frac{1}{L_3} e^{-j\frac{1}{3}\pi} \right) \right\} \end{aligned} \quad (5.50)$$

equation (5.46) can be written as

$$\sum_{m=-\infty}^{\infty} \left((a_{nm} + b_{nm}) \hat{i}_{s,6m+1} + c_{nm} \hat{i}_{s,6m+1}^* \right) = d_n \quad (5.51)$$

Except for the value of the coefficients in this equation, the equation is equal to that in the previous section (equation (5.27)). The Fourier coefficients of the current can be solved in exactly the same way. Therefore, this solution is not repeated here.

5.5 The quantities in the direct-current circuit

In this section, the current i_{dc} and the voltage u_{dc} are calculated from the Fourier series for the currents and the voltages derived in the previous sections.

5.5.1 The current in the direct-current circuit

Using the pulse functions p and h , the current in the direct-current circuit i_{dc} can be written as

$$\begin{aligned} i_{dc} = & -i_{sa} \left(p(\omega t - \frac{1}{3}\pi) + h(\omega t - \frac{1}{3}\pi) - p(\omega t - \frac{4}{3}\pi) - h(\omega t - \frac{4}{3}\pi) \right) \\ & -i_{sb} \left(p(\omega t - \pi) + h(\omega t - \pi) - p(\omega t) - h(\omega t) \right) \\ & -i_{sc} \left(p(\omega t - \frac{5}{3}\pi) + h(\omega t - \frac{5}{3}\pi) - p(\omega t - \frac{2}{3}\pi) - h(\omega t - \frac{2}{3}\pi) \right) \end{aligned} \quad (5.52)$$

The stator currents and the pulse functions p and h in this equation are replaced by their

Fourier series, equations (5.6), (5.15), and (5.44) respectively:

$$\begin{aligned}
 i_{dc} = & -\frac{1}{4} \sum_{n=-\infty}^{\infty} \left(\hat{L}_{s,6n+1} e^{j(6n+1)\omega_1 t} + \hat{L}_{s,6n+1}^* e^{-j(6n+1)\omega_1 t} \right) \\
 & \cdot \sum_{n=-\infty}^{\infty} (\hat{p}_n + \hat{h}_n) (1 - e^{-jn\pi}) e^{-jn\frac{1}{3}\pi} e^{jn\omega_1 t} \\
 & - \frac{1}{4} \sum_{n=-\infty}^{\infty} \left(\hat{L}_{s,6n+1} e^{-j\frac{2}{3}\pi} e^{j(6n+1)\omega_1 t} + \hat{L}_{s,6n+1}^* e^{j\frac{2}{3}\pi} e^{-j(6n+1)\omega_1 t} \right) \\
 & \cdot \sum_{n=-\infty}^{\infty} (\hat{p}_n + \hat{h}_n) (1 - e^{-jn\pi}) e^{-jn\pi} e^{jn\omega_1 t} \\
 & - \frac{1}{4} \sum_{n=-\infty}^{\infty} \left(\hat{L}_{s,6n+1} e^{-j\frac{4}{3}\pi} e^{j(6n+1)\omega_1 t} + \hat{L}_{s,6n+1}^* e^{j\frac{4}{3}\pi} e^{-j(6n+1)\omega_1 t} \right) \\
 & \cdot \sum_{n=-\infty}^{\infty} (\hat{p}_n + \hat{h}_n) (1 - e^{-jn\pi}) e^{-jn\frac{5}{3}\pi} e^{jn\omega_1 t}
 \end{aligned} \tag{5.53}$$

The multiplications of the series on the right side of this equation can be worked out to

$$\begin{aligned}
 i_{dc} = & -\frac{1}{4} \sum_{k=-\infty}^{\infty} e^{jk\omega_1 t} \cdot \sum_{m=-\infty}^{\infty} \left\{ \hat{L}_{s,6m+1} (\hat{p}_{k-6m-1} + \hat{h}_{k-6m-1}) (1 - e^{-j(k-6m-1)\pi}) \right. \\
 & \cdot \left(e^{-j(k-6m-1)\frac{1}{3}\pi} + e^{-j\frac{2}{3}\pi} e^{-j(k-6m-1)\pi} + e^{-j\frac{4}{3}\pi} e^{-j(k-6m-1)\frac{5}{3}\pi} \right) \\
 & + \hat{L}_{s,6m+1}^* (\hat{p}_{k+6m+1} + \hat{h}_{k+6m+1}) (1 - e^{-j(k+6m+1)\pi}) \\
 & \left. \cdot \left(e^{-j(k+6m+1)\frac{1}{3}\pi} + e^{j\frac{2}{3}\pi} e^{-j(k+6m+1)\pi} + e^{j\frac{4}{3}\pi} e^{-j(k+6m+1)\frac{5}{3}\pi} \right) \right\}
 \end{aligned} \tag{5.54}$$

When this equation is worked out further, it appears that the current i_{dc} only has harmonics of which the harmonic number is an integer multiple of six; the other harmonics are zero. This could already have been expected, because this current is periodic with angular period $\pi/3$. By substituting $k=6n$, the current i_{dc} can be written as the following Fourier series:

$$\begin{aligned}
 i_{dc} = & \frac{1}{2} \sum_{n=-\infty}^{\infty} \hat{L}_{dc,6n} e^{j6n\omega_1 t} ; \\
 \hat{L}_{dc,6n} = & -3 \sum_{m=-\infty}^{\infty} \left(\hat{L}_{s,6m+1} (\hat{p}_{6(n-m)-1} + \hat{h}_{6(n-m)-1}) e^{j\frac{1}{3}\pi} + \hat{L}_{s,6m+1}^* (\hat{p}_{6(n+m)+1} + \hat{h}_{6(n+m)+1}) e^{-j\frac{1}{3}\pi} \right)
 \end{aligned} \tag{5.55}$$

5.5.2 The voltage across the direct-current circuit

The voltage across the direct-current circuit u_{dc} can be calculated in a way comparable to the calculation of the current i_{dc} :

$$\begin{aligned} u_{dc} = & (u_{sa} - u_{sc}) \left(p(\omega t - \frac{1}{3}\pi) + h(\omega t - \frac{1}{3}\pi) - p(\omega t - \frac{4}{3}\pi) - h(\omega t - \frac{4}{3}\pi) \right) \\ & + (u_{sb} - u_{sa}) \left(p(\omega t - \pi) + h(\omega t - \pi) - p(\omega t) - h(\omega t) \right) \\ & + (u_{sc} - u_{sb}) \left(p(\omega t - \frac{5}{3}\pi) + h(\omega t - \frac{5}{3}\pi) - p(\omega t - \frac{2}{3}\pi) - h(\omega t - \frac{2}{3}\pi) \right) \end{aligned} \quad (5.56)$$

The stator terminal voltages and the pulse functions p and h in this equation are replaced by their Fourier series, equations (5.7), (5.15), and (5.44) respectively:

$$\begin{aligned} u_{dc} = & \frac{1}{4} \sum_{n=-\infty}^{\infty} \left(\hat{u}_{s,6n+1} \left(1 - e^{-j\frac{4}{3}\pi} \right) e^{j(6n+1)\omega_1 t} + \hat{u}_{s,6n+1}^* \left(1 - e^{j\frac{4}{3}\pi} \right) e^{-j(6n+1)\omega_1 t} \right) \\ & \cdot \sum_{n=-\infty}^{\infty} (\hat{p}_n + \hat{h}_n) (1 - e^{-jn\pi}) e^{-jn\frac{1}{3}\pi} e^{jn\omega_1 t} \\ & + \frac{1}{4} \sum_{n=-\infty}^{\infty} \left(\hat{u}_{s,6n+1} \left(e^{-j\frac{2}{3}\pi} - 1 \right) e^{j(6n+1)\omega_1 t} + \hat{u}_{s,6n+1}^* \left(e^{j\frac{2}{3}\pi} - 1 \right) e^{-j(6n+1)\omega_1 t} \right) \\ & \cdot \sum_{n=-\infty}^{\infty} (\hat{p}_n + \hat{h}_n) (1 - e^{-jn\pi}) e^{-jn\pi} e^{jn\omega_1 t} \\ & + \frac{1}{4} \sum_{n=-\infty}^{\infty} \left(\hat{u}_{s,6n+1} \left(e^{-j\frac{4}{3}\pi} - e^{-j\frac{2}{3}\pi} \right) e^{j(6n+1)\omega_1 t} + \hat{u}_{s,6n+1}^* \left(e^{j\frac{4}{3}\pi} - e^{j\frac{2}{3}\pi} \right) e^{-j(6n+1)\omega_1 t} \right) \\ & \cdot \sum_{n=-\infty}^{\infty} (\hat{p}_n + \hat{h}_n) (1 - e^{-jn\pi}) e^{-jn\frac{5}{3}\pi} e^{jn\omega_1 t} \end{aligned} \quad (5.57)$$

The multiplications of the series on the right side of this equation can be worked out to

$$\begin{aligned} u_{dc} = & -\frac{1}{4} \sum_{k=-\infty}^{\infty} e^{jk\omega_1 t} \cdot \sum_{m=-\infty}^{\infty} \left\{ \hat{u}_{s,6m+1} (\hat{p}_{k-6m-1} + \hat{h}_{k-6m-1}) (1 - e^{-j(k-6m-1)\pi}) \right. \\ & \cdot \left((1 - e^{-j\frac{4}{3}\pi}) e^{-j(k-6m-1)\frac{1}{3}\pi} + (e^{-j\frac{2}{3}\pi} - 1) e^{-j(k-6m-1)\pi} + (e^{-j\frac{4}{3}\pi} - e^{-j\frac{2}{3}\pi}) e^{-j(k-6m-1)\frac{5}{3}\pi} \right) \\ & + \hat{u}_{s,6m+1}^* (\hat{p}_{k+6m+1} + \hat{h}_{k+6m+1}) (1 - e^{-j(k+6m+1)\pi}) \\ & \left. \cdot \left((1 - e^{j\frac{4}{3}\pi}) e^{-j(k+6m+1)\frac{1}{3}\pi} + (e^{j\frac{2}{3}\pi} - 1) e^{-j(k+6m+1)\pi} + (e^{j\frac{4}{3}\pi} - e^{j\frac{2}{3}\pi}) e^{-j(k+6m+1)\frac{5}{3}\pi} \right) \right\} \end{aligned} \quad (5.58)$$

As was the case in the previous subsection, and as expected, when this equation is worked out further, the voltage u_{dc} appears only to have harmonics of which the harmonic number is an integer multiple of six, the other harmonics are zero. By substituting $k=6n$, the voltage u_{dc} can be written as the following Fourier series:

$$u_{dc} = \frac{1}{2} \sum_{n=-\infty}^{\infty} \hat{u}_{dc,6n} e^{j6n\omega_s t} ;$$

$$\hat{u}_{dc,6n} = 3\sqrt{3} \sum_{m=-\infty}^{\infty} \left(\hat{u}_{s,6m+1} (\hat{p}_{6(n-m)-1} + \hat{h}_{6(n-m)-1}) e^{j\frac{1}{6}\pi} + \hat{u}_{s,6m+1}^* (\hat{p}_{6(n+m)+1} + \hat{h}_{6(n+m)+1}) e^{-j\frac{1}{6}\pi} \right) \quad (5.59)$$

5.6 On the choice of the external inductance

This section deals with the choice of the external inductance L_e . [Bol 80], [Bol 91], and [Bol 93] do not discuss this choice, suggesting that it is free. Hoeijmakers [Hoe 84] says that the external inductance should be chosen as equal to the subtransient inductance of the synchronous machine. He noticed that this produced the best numerical accuracy, but he did not explain why. Here, an explanation of this choice is given, which was already published in [Pol 96].

The external inductance L_e should be chosen as equal to the commutation inductance. The commutation inductance is the inductance opposing the transfer of current from one phase to another during a commutation. In a rectifier-loaded machine, the commutation inductance is the inductance experienced by the important higher time harmonics of the current. It is approximately equal to the leakage inductance L_σ in a machine with a damper cylinder, and to the sum of the inductances L_k and the leakage inductance L_σ in a machine without a damper cylinder (compare figure 4.15a). Generally, this commutation inductance is equal to the subtransient inductance used in [Hoe 84].

It is sensible to choose the external inductance equal to the commutation inductance for the following reason. The terms $Z_{i,6n+1}$ (introduced in equation (5.9)) and the terms b_{nm} and c_{nm} (used in equations (5.27) and (5.51)) become very small for the important time harmonics. Therefore, the matrices in the matrix equations used to solve the Fourier coefficients of the current (the matrix equations (5.27) and (5.51)) become mainly diagonal. This improves the numerical accuracy of the calculation process.

This choice also has physical meaning: the jumps in the terminal voltage caused by commutation are included in the voltage drop across the external inductance L_e , and the internal voltage \bar{e}_s becomes a smooth function of time. In the extreme case that $Z_{i,6n+1} = 0$ is valid for all frequencies, the internal voltage \bar{e}_s becomes equal to the no-load voltage \bar{e}_p .

5.7 Concluding remarks

In chapters 2 to 4 a model of the permanent-magnet generator has been derived. In this chapter, this machine model has been combined with a model of the controlled rectifier. The resulting equations have been solved with a calculation method which calculates the steady-state performance of the rectifier-loaded machine.

In the modelling of the rectifier and the derivation of the calculation method, it has been assumed that

- the current in the direct-current circuit i_{dc} flows continuously,
- the thyristors can be modelled as ideal switches, and
- the angle of overlap μ is smaller than or equal to $\pi/3$.

The derived calculation method solves the equations in the frequency domain using Fourier analysis. Two important characteristics of this method are

- frequency-dependent machine parameters can be used; and
- the steady-state performance can be determined without considering the transient interval.

Furthermore, this chapter has shown that the external inductance L_e should be chosen equal to the commutation inductance.

In the next chapter, the complete model of the rectifier-loaded generator will be verified experimentally.

Chapter 6

Experimental verification of the model of the generator with rectifier

6.1 Introduction

Objective

In chapters 2 to 4, a model of a permanent-magnet generator was derived. In chapter 5, this model was combined with a model of the rectifier. The objective of this chapter is to verify the combination of these models experimentally. In the next chapter, it will be shown that the model derived can be used to optimize the generator design.

The verification of the complete model of the rectifier-loaded generator is done by comparing measured and calculated voltage and current waveforms. Figure 5.1 depicts the circuit in which the voltage and current waveforms have been measured. The permanent-magnet machine used in the experiments is the servomotor, which was also used for the locked-rotor tests described in subsection 4.4.5.

For the comparison of measured and calculated waveforms, the line voltage $u_{sba} = u_{sb} - u_{sa}$ and the phase current i_{sa} are used. The direct-current circuit quantities, the current i_{dc} and the voltage u_{dc} , are not used, because they may (nearly) directly be derived from parts of the phase currents and the line voltages.

In this chapter, there are differences between measured and calculated waveforms, as is always the case. Because these differences may have various causes, it is difficult to explain them. They may be caused by shortcomings of the machine model, by shortcomings of the model of the rectifier, and by measuring errors. In order to improve understanding of the causes of these differences, a second machine model is used, namely a machine model based on measured operational inductances. So, in this chapter, two machine models are used and verified, namely the machine model derived in chapters 2 to 4 and the machine model based on measured operational inductances.

The calculations have been done both considering the real self-inductance L_{dc} and assuming an infinitely large self-inductance L_{dc} in the direct-current circuit. In this way, the usefulness of the calculation assuming an infinitely large self-inductance can be investigated for situations with a finite self-inductance.

Outline of the chapter

Firstly, in section 6.2, the machine model based on measured operational inductances is introduced. Subsequently, section 6.3 deals with four experiments with different values of the self-inductance in the direct-current circuit L_{dc} and with different values of the delay angle α_p . In section 6.4, some conclusions are drawn.

6.2 Machine model based on measured operational inductances

This section gives a brief description of a machine model based on measured operational inductances. This model has been published in [Pol 96]; for a more extensive description, see [Hoe 84].

This section is structured as follows. Firstly, subsection 6.2.1 introduces the machine model based on operational inductances. Next, in subsection 6.2.2, the operational inductances are determined from locked-rotor tests. In subsection 6.2.3, the voltage equation representing this machine model is written as a Fourier series, which can be used in the calculation method of chapter 5.

6.2.1 Introduction of the machine model with operational inductances

This subsection introduces the machine model based on operational inductances. This is done by transforming the stator voltage equation from the time domain to the frequency domain, after which the operational inductances are introduced.

The machine model based on measured operational inductances is based on the following assumptions.

- The stator winding is distributed sinusoidally; space harmonics of the magnetic field of the stator currents are neglected.
- The iron losses in the stator are negligible.
- Nonlinear effects (such as saturation and hysteresis phenomena) are negligible.
- The resistance of a stator phase is not a function of the frequency.

In this machine model, differences between the direct-axis and the quadrature-axis magnetic circuit can be considered [Hoe 84]. However, in this section, the difference is not considered because it is small in the used permanent-magnet machine with surface-mounted magnets.

For the derivation of the model, the starting point is the general equation for the stator voltages, which was already given in equation (3.3). It was assumed that nonlinear effects are negligible. Therefore, the magnetic flux density is a superposition of the different contributions, and the flux linkages of the stator phases of equation (3.3) can be split into two parts:

- 1) A part Ψ'_s dependent on the stator currents. This part includes the flux caused by

the stator currents, but also the fluxes caused by the rotor currents which are induced by the stator currents. These rotor currents may be eddy currents in magnets, eddy currents in the rotor iron, which may be solid, and damper currents.

- 2) A part independent of the stator currents and dependent on the excitation of the rotor. In this thesis, this excitation is the magnetization of the magnets. The time derivative of this part is the no-load voltage \vec{e}_p . In this machine model, the measured no-load voltage is used.

With such a separation, the voltage equation becomes

$$\vec{u}_s = \vec{e}_p + R_s \vec{i}_s + \frac{d\vec{\Psi}'_s}{dt} \tag{6.1}$$

The stator quantities are rotated to the rotor-connected dq -system by means of the well-known Park transformation [Par 29]. In its normalized form, it is given by

$$\begin{bmatrix} i_{sd} \\ i_{sq} \\ i_{s0} \end{bmatrix} = P \vec{i}_s ; \quad \begin{bmatrix} e_{pd} \\ e_{pq} \\ e_{p0} \end{bmatrix} = P \vec{e}_p ; \quad \begin{bmatrix} u_{sd} \\ u_{sq} \\ u_{s0} \end{bmatrix} = P \vec{u}_s ; \quad \begin{bmatrix} \Psi'_{sd} \\ \Psi'_{sq} \\ \Psi'_{s0} \end{bmatrix} = P \vec{\Psi}'_s ; \tag{6.2}$$

$$P = \sqrt{\frac{2}{3}} \begin{bmatrix} \cos(p\theta) & \cos(p\theta - \frac{2}{3}\pi) & \cos(p\theta - \frac{4}{3}\pi) \\ -\sin(p\theta) & -\sin(p\theta - \frac{2}{3}\pi) & -\sin(p\theta - \frac{4}{3}\pi) \\ \frac{1}{2}\sqrt{2} & \frac{1}{2}\sqrt{2} & \frac{1}{2}\sqrt{2} \end{bmatrix} \tag{6.2}$$

Because there is no star-point connection, the zero-components are zero and are omitted in the rest of this section. Application of the Park transformation to equation (6.1) results in

$$\begin{bmatrix} u_{sd} \\ u_{sq} \end{bmatrix} = \begin{bmatrix} e_{pd} \\ e_{pq} \end{bmatrix} + R_s \begin{bmatrix} i_{sd} \\ i_{sq} \end{bmatrix} + \frac{d}{dt} \begin{bmatrix} \Psi'_{sd} \\ \Psi'_{sq} \end{bmatrix} + p\Omega \begin{bmatrix} -\Psi'_{sq} \\ \Psi'_{sd} \end{bmatrix} \tag{6.3}$$

The Fourier transform of this equation is

$$\begin{bmatrix} U_{sd}(\omega) \\ U_{sq}(\omega) \end{bmatrix} = \begin{bmatrix} E_{pd}(\omega) \\ E_{pq}(\omega) \end{bmatrix} + R_s \begin{bmatrix} I_{sd}(\omega) \\ I_{sq}(\omega) \end{bmatrix} + j\omega \begin{bmatrix} \Psi'_{sd}(\omega) \\ \Psi'_{sq}(\omega) \end{bmatrix} + p\Omega \begin{bmatrix} -\Psi'_{sq}(\omega) \\ \Psi'_{sd}(\omega) \end{bmatrix} \tag{6.4}$$

In this equation in the frequency domain, the fluxes can be written as functions of the currents by introducing operational inductances:

$$\begin{cases} \Psi'_{sd}(\omega) = \underline{L}_{do}(\omega) I_{sd}(\omega) \\ \Psi'_{sq}(\omega) = \underline{L}_{qo}(\omega) I_{sq}(\omega) \end{cases} \tag{6.5}$$

where $\underline{L}_{do}(\omega)$ and $\underline{L}_{qo}(\omega)$ are the direct-axis and the quadrature-axis operational

inductance respectively.

Using this in equation (6.4) gives

$$\begin{bmatrix} U_{sd}(\omega) \\ U_{sq}(\omega) \end{bmatrix} = \begin{bmatrix} E_{pd}(\omega) \\ E_{pq}(\omega) \end{bmatrix} + \begin{bmatrix} (R_s + j\omega L_{do}(\omega))I_{sd}(\omega) \\ (R_s + j\omega L_{qo}(\omega))I_{sq}(\omega) \end{bmatrix} + p\Omega \begin{bmatrix} -L_{qo}(\omega)I_{sq}(\omega) \\ L_{do}(\omega)I_{sd}(\omega) \end{bmatrix} \quad (6.6)$$

This equation gives the machine model based on operational inductances. As appears from [Par 29], [Hoe 84] and [Kra 95], machine models based on operational inductances have been used since 1929, mainly in the analysis of synchronous machines. In this thesis, as in [Hoe 84], the term operational inductance is used, because the operational inductance gives a relation between the current and the flux. However, in other work, other names may be used, such as operator [Par 29], or operational impedance [Kra 95].

It should be noted that the operational inductance is introduced as a complex quantity, the imaginary part of which represents losses. The stator iron loss was assumed to be negligible, and the stator resistance was assumed not to be a function of the frequency. Therefore, the imaginary part of the operational inductances represents the rotor losses.

6.2.2 Determination of the operational inductances

This section describes how the operational inductances can be determined from locked-rotor tests. These tests were already described in subsection 3.6, and for the used machine, the results were already given in subsection 4.4.5.

During the locked-rotor tests, $\Omega=0$ is valid, the no-load voltage \bar{e}_p is zero and the voltage and the current are sinusoidal. Using this in voltage equation (6.6) results in

$$\begin{bmatrix} U_{sd}(\omega) \\ U_{sq}(\omega) \end{bmatrix} = \begin{bmatrix} (R_s + j\omega L_{do}(\omega))I_{sd}(\omega) \\ (R_s + j\omega L_{qo}(\omega))I_{sq}(\omega) \end{bmatrix} \quad (6.7)$$

For the determination of the direct-axis operational inductance $L_{do}(\omega)$, the rotor is placed so that the quadrature axis coincides with the axis of stator phase a ($p\theta = \pi/2$). A voltage is supplied to the stator phases b and c , which are connected in series. Therefore, $i_{sc} = -i_{sb}$ and $u_{sb} - u_{sc} = u_{sbc}$ are valid. With the Park transformation (equation (6.2)), the dq -components of the currents and voltages are calculated. Substitution of these dq -components in equation (6.7) results in

$$U_{sbc}(\omega) = 2\{(R_s + j\omega L_{do}(\omega))\}I_{sb}(\omega) = \{R_d(\omega) + j\omega L_d(\omega)\}I_{sb}(\omega) \quad (6.8)$$

where the resistance $R_d(\omega)$ and the inductance $L_d(\omega)$ were introduced as

$$\begin{cases} R_d(\omega) = 2R_s - 2\omega \text{Im}(L_{do}(\omega)) \\ L_d(\omega) = 2\text{Re}(L_{do}(\omega)) \end{cases} \quad (6.9)$$

So, the determination of the direct-axis operational inductance $L_{do}(\omega)$ comes to the

determination of an impedance $R_d(\omega) + j\omega L_d(\omega)$.

After placing the rotor so that the direct axis coincides with the axis of phase a ($\theta=0$), the quadrature-axis operational inductance $L_{qo}(\omega)$ is determined in the same way.

The same test was done in subsection 4.4.5, and the results were depicted in figure 4.18. In figure 6.1 the results are repeated. In this figure, it can be seen that the direct-axis and the quadrature-axis operational inductance are not equal. However, the difference between the direct-axis and the quadrature-axis operational inductance is small, because the machine has a cylindrical rotor with surface-mounted magnets. As mentioned in subsection 6.2.1, this difference is neglected in the calculations throughout the rest of the chapter:

$$L_{do}(\omega) = L_{qo}(\omega) = L_o(\omega) \tag{6.10}$$

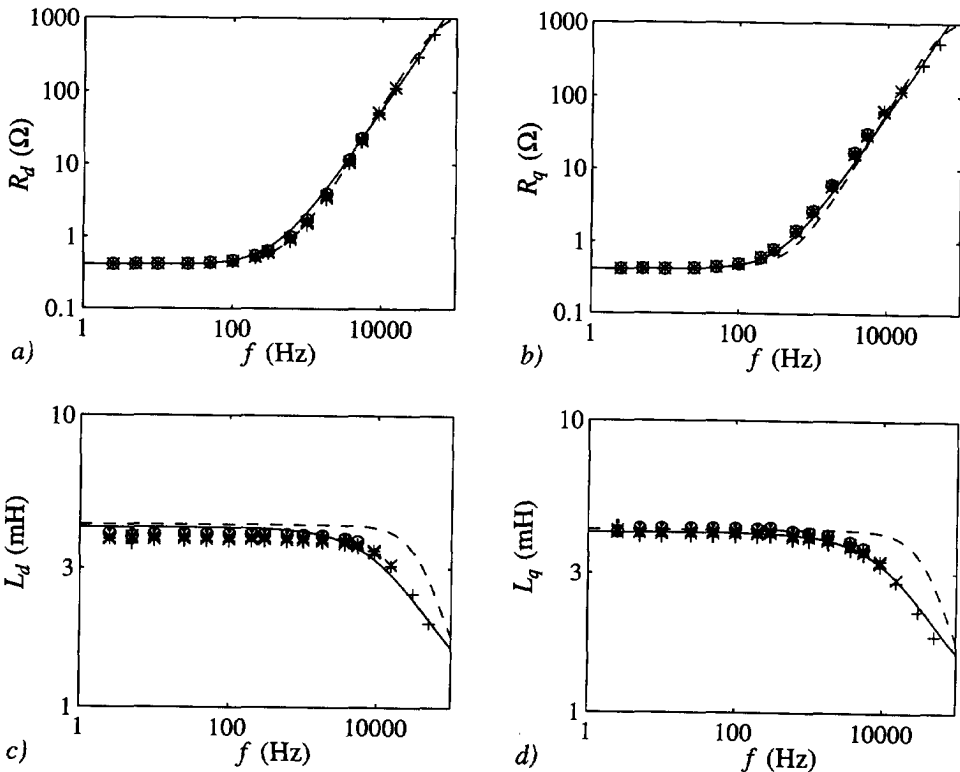


Figure 6.1: a) Resistance and c) inductance in the direct axis and b) resistance and d) inductance in the quadrature axis,

+ , × , * , ○ , ∙ : measured with $I_{sb} = 0.2 \text{ A}$, $I_{sb} = 0.5 \text{ A}$, $I_{sb} = 1 \text{ A}$, $I_{sb} = 2 \text{ A}$, $I_{sb} = 5 \text{ A}$,
 — : values used in the calculation method based on operational inductances, and
 - - : values calculated with the machine model derived in chapters 2 to 4.

The value of the operational inductance $L_o(\omega)$ is determined from the measured values by taking the average of the measured values of the direct-axis and the quadrature-axis operational inductance.

In figure 6.1, it can also be seen that the value of the operational inductance depends on the amplitude of the current. This means that the magnetic circuit is nonlinear, as discussed in the subsections 4.3.6 and 4.4.5. However, as mentioned in subsection 6.2.1, nonlinear effects are ignored. The value of the operational inductance $L_o(\omega)$ is determined from the measurements with $I_{sb} = 2 \text{ A}$. This value is taken because the important time harmonics of the stator currents of the rectifier-loaded machine have amplitudes of a few Ampères. At high frequencies (above 8 kHz), measurements with $I_{sb} = 2 \text{ A}$ were not possible because the power of the amplifier was limited and because the terminal voltages became too high for the insulation. At these frequencies, the values measured with the largest current are used. The resulting values for the resistance and the inductance during the locked-rotor tests (determined with equation (6.9) for the direct axis) are also depicted in figure 6.1.

From this figure, conclusions can be drawn on the commutation inductance, which was introduced in section 5.6. As mentioned there, the commutation inductance of a rectifier-loaded machine is the inductance experienced by the important higher time harmonics of the current. For the permanent-magnet machine used in the experiments, the most important time harmonics have frequencies of 1.8 kHz or 3.6 kHz. According to figure 6.1, the commutation inductance of the machine model derived in chapters 2 to 4 is larger than the commutation inductance of the machine model based on measured operational inductances.

As mentioned earlier, the imaginary part of the operational inductance represents the rotor losses. In the permanent-magnet machine, the rotor losses consist of iron loss and eddy-current loss in the magnets. However, it should be noted that in reality a part of the measured loss arises in the stator iron and contributes to the imaginary part of the operational inductance.

6.2.3 The use of Fourier series in the machine model

In the subsections 6.2.1 and 6.2.2, a machine model based on measured operational inductances was derived. This machine model is represented by a voltage equation in the frequency domain. In this subsection, the voltage equation representing this machine model is written as a Fourier series which can be used in the calculation method described in chapter 5.

In the voltage equation in the dq -system (equation (6.3)), all quantities are replaced by Fourier series. As explained in subsection 5.2.2, Fourier series are used in a slightly different way from usual: the Fourier coefficients are a factor 2 larger than usual. Furthermore, it is taken that this voltage equation only contains time harmonics of which the harmonic number is an integer multiple of six, as follows from the Park transforma-

tion of equations (5.5), (5.6), and (5.7). The result is

$$\begin{bmatrix} u_{sd} \\ u_{sq} \end{bmatrix} = \frac{1}{2} \sum_{n=-\infty}^{\infty} e^{j6n\omega_1 t} \begin{bmatrix} \hat{u}_{sd,6n} \\ \hat{u}_{sq,6n} \end{bmatrix} \tag{6.11}$$

where

$$\begin{bmatrix} \hat{u}_{sd,6n} \\ \hat{u}_{sq,6n} \end{bmatrix} = \begin{bmatrix} \hat{e}_{pd,6n} \\ \hat{e}_{pq,6n} \end{bmatrix} + R_s \begin{bmatrix} \hat{i}_{sd,6n} \\ \hat{i}_{sq,6n} \end{bmatrix} + j6n\omega_1 \begin{bmatrix} \Psi'_{sd,6n} \\ \Psi'_{sq,6n} \end{bmatrix} + \omega_1 \begin{bmatrix} -\Psi'_{sq,6n} \\ \Psi'_{sd,6n} \end{bmatrix} \tag{6.12}$$

This equation is an equation in the frequency domain in the *dq*-system. Therefore, the fluxes in this equation can be replaced by operational inductances multiplied by currents (as in equation (6.6)):

$$\begin{bmatrix} \hat{u}_{sd,6n} \\ \hat{u}_{sq,6n} \end{bmatrix} = \begin{bmatrix} \hat{e}_{pd,6n} \\ \hat{e}_{pq,6n} \end{bmatrix} + (R_s + j6n\omega_1 \underline{L}_o(6n\omega_1)) \begin{bmatrix} \hat{i}_{sd,6n} \\ \hat{i}_{sq,6n} \end{bmatrix} + \omega_1 \underline{L}_o(6n\omega_1) \begin{bmatrix} -\hat{i}_{sq,6n} \\ \hat{i}_{sd,6n} \end{bmatrix} \tag{6.13}$$

In this equation, it was also taken that the direct-axis and the quadrature-axis operational inductance are assumed to be equal, as expressed by equation (6.10).

The Fourier coefficients of this equation are substituted in the Fourier series of equation (6.11), and equation (6.11) is transformed back with the inverse Park transformation (the transpose of the matrix *P* in equation (6.2)). The resulting equation for the Fourier coefficients of the stator terminal voltages is given by

$$\hat{u}_{s,6n+1} = \hat{e}_{p,6n+1} + Z_{6n+1} \hat{i}_{s,6n+1}; \quad Z_{6n+1} = R_s + j(6n+1)\omega_1 \underline{L}_o(6n\omega_1) \tag{6.14}$$

This equation can be used in the calculation method described in chapter 5 in the same way as equation (4.80).

6.3 Comparison of measured and calculated waveforms

This section covers four experiments with different values of the self-inductance in the direct-current circuit L_{dc} and with different values of the delay angle α_p .

6.3.1 Large self-inductance L_{dc} and small delay angle α_p

This subsection covers an experiment with a large self-inductance L_{dc} and with a small delay angle α_p ($\alpha_p = 5^\circ$). For the voltage, the self-inductance and the resistance in the direct-current circuit, $U_b = 367 \text{ V}$, $L_{dc} = 74 \text{ mH}$, and $R_{dc} = 0.29 \Omega$ are valid.

Figure 6.2 depicts the measured and the calculated line voltage and phase current

waveforms. In the calculations, the machine model derived in chapters 2 to 4 has been used. The waveforms have been calculated both assuming an infinitely large self-inductance L_{dc} and considering the real self-inductance L_{dc} . Because this self-inductance L_{dc} is large, the difference between these calculations is invisible. Figure 6.3 also depicts the measured and the calculated waveforms, but here the machine model based on measured operational inductances has been used in the calculation method.

In figure 6.2, the measured angle of overlap is a little smaller than the calculated. This is probably because the modelled commutation inductance is larger than the real commutation inductance. That a smaller commutation inductance results in a smaller angle of overlap is shown in figure 6.3, where the machine model based on measured operational inductances has been used. Probably, the commutation inductance of this machine model correlates better with the real commutation inductance.

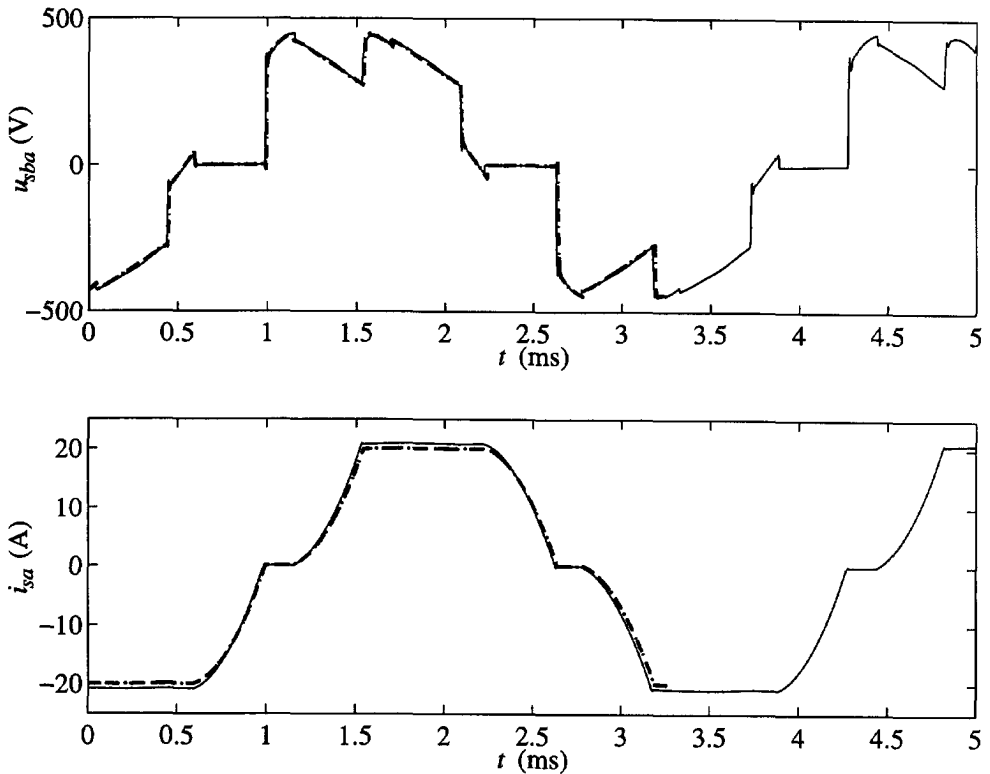


Figure 6.2: Line voltage and phase current waveforms,

— : measured,

- - : calculated considering the real self-inductance L_{dc} , and

.. : calculated assuming an infinitely large self-inductance L_{dc} .

Calculations have been done with the machine model derived in chapters 2 to 4.

Furthermore, from figure 6.2, it can be concluded that the measured current i_{dc} is a little larger than the calculated current i_{dc} . This difference is probably also because the modelled commutation inductance is larger than the real commutation inductance. That a smaller commutation inductance results in a larger current i_{dc} is also shown in figure 6.3, where the machine model based on measured operational inductances has been used. Again, the commutation inductance of this machine model probably correlates better with the real commutation inductance.

The spikes on the measured line voltage at the beginning and the end of the commutation are caused by the snubbers and by the reverse recovery in the thyristors. The spikes on the calculated line voltage at the beginning and the end of the commutation are caused by the Gibb's phenomenon [Kwa 91]. In the figures in this subsection, this phenomenon is hardly visible, but in later subsections, it is clearly visible.

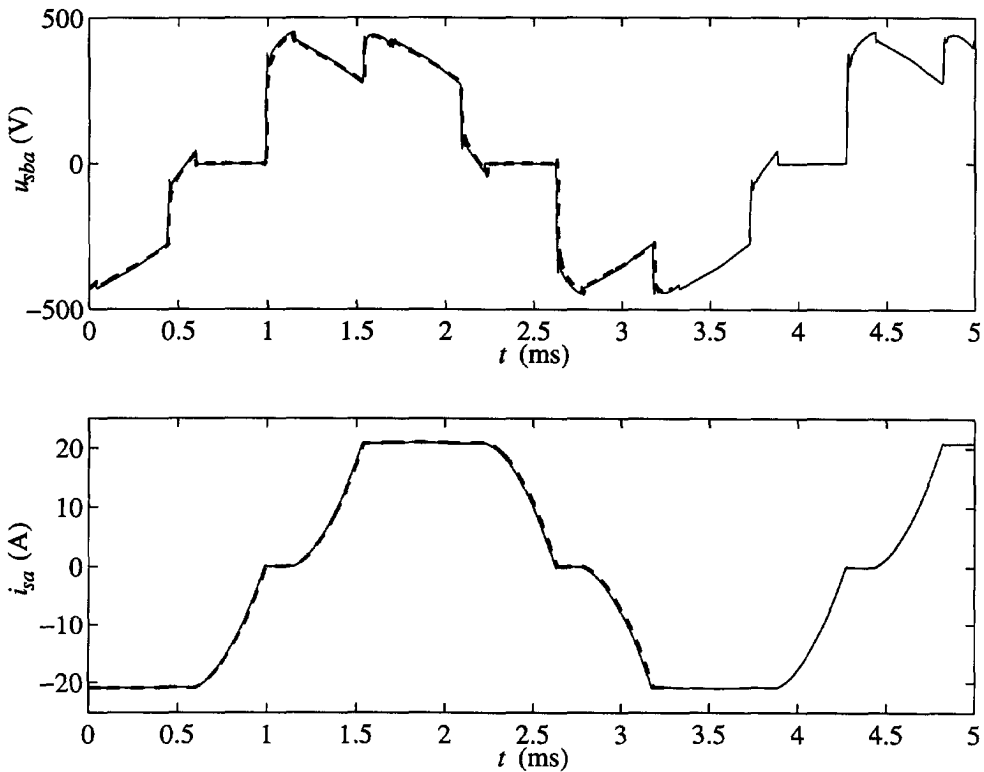


Figure 6.3: Line voltage and phase current waveforms,
 — : measured,
 - - : calculated considering the real self-inductance L_{dc} , and using the machine model based on measured operational inductances.

6.3.2 Large self-inductance L_{dc} and large delay angle α_p

This subsection covers an experiment with a large self-inductance L_{dc} and with a large delay angle α_p ($\alpha_p = 58^\circ$). For the voltage, the self-inductance and the resistance in the direct-current circuit, $U_b = 197$ V, $L_{dc} = 74$ mH, and $R_{dc} = 0.29$ Ω are valid.

Figure 6.4 depicts the measured and the calculated line voltage and phase current waveforms. In the calculations, the machine model derived in chapters 2 to 4 has been used. There is hardly any difference between the calculations assuming an infinitely large self-inductance L_{dc} and the calculations considering the real self-inductance L_{dc} , because the self-inductance L_{dc} is large, as in subsection 6.3.1. Figure 6.5 also depicts the measured and the calculated waveforms, but here the machine model based on measured operational inductances has been used in the calculations.

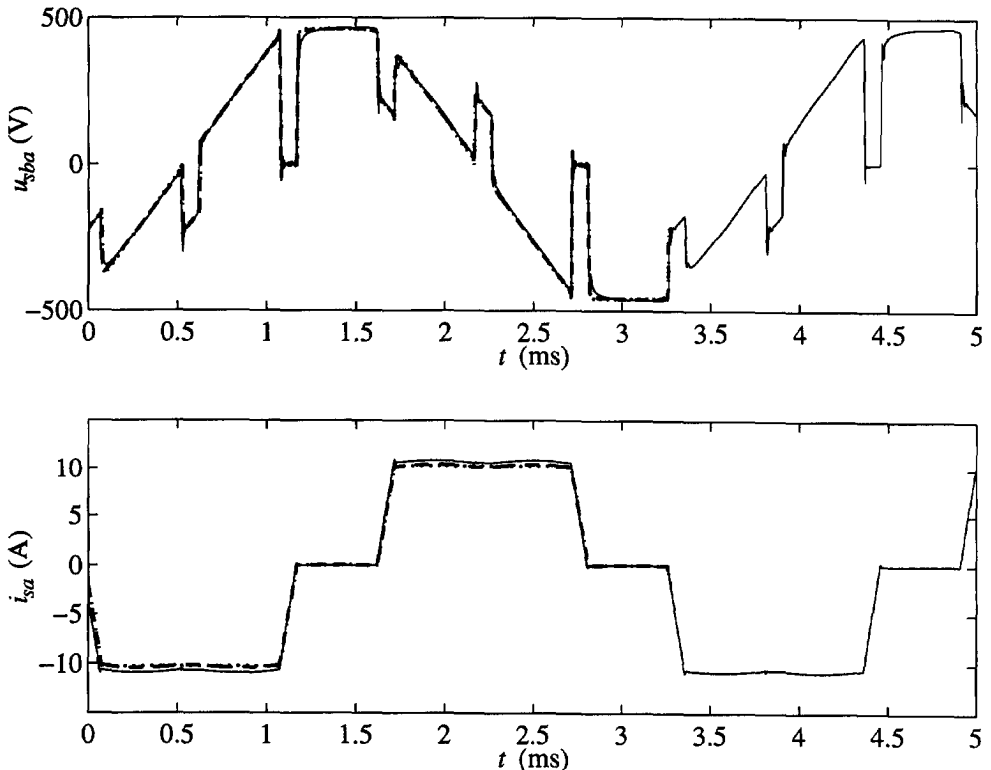


Figure 6.4: Line voltage and phase current waveforms,

— : measured,

- - : calculated considering the real self-inductance L_{dc} , and

.. : calculated assuming an infinitely large self-inductance L_{dc} .

Calculations have been done with the machine model derived in chapters 2 to 4.

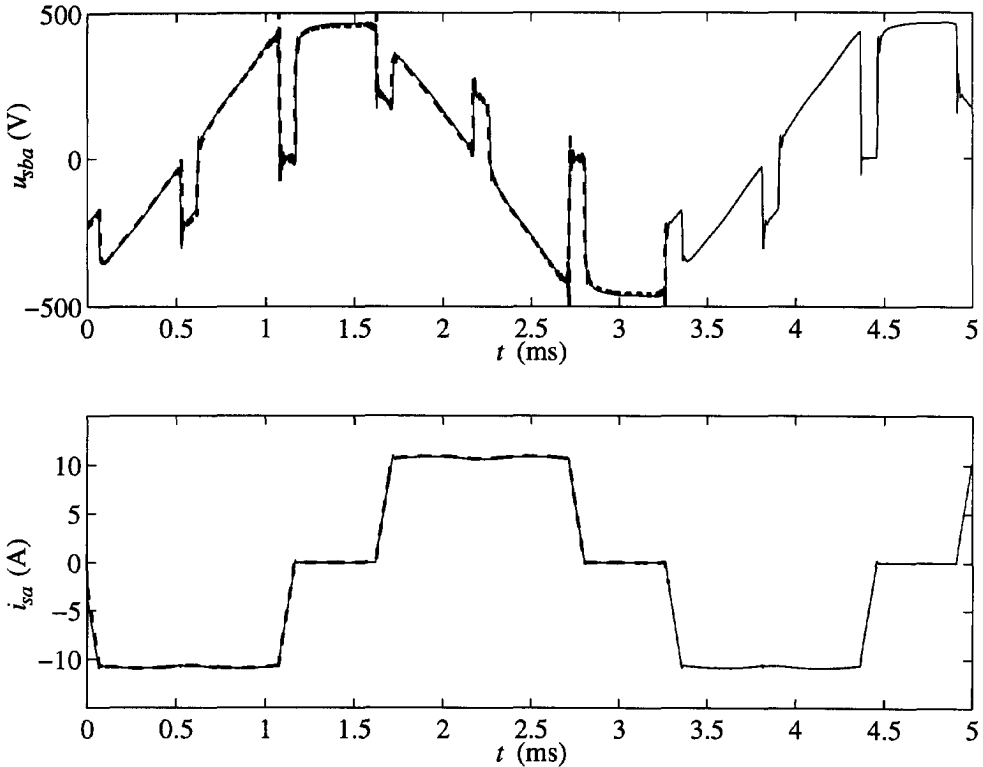


Figure 6.5: Line voltage and phase current waveforms,
 — : measured,
 - - : calculated considering the real self-inductance L_{dc} , and using the machine model based on measured operational inductances.

In figure 6.4, after the commutation interval, the calculated line voltage increases faster than the measured line voltage. In figure 6.5, the measured and the calculated line voltage after the commutation interval correlate much better. This again shows that for the determination of the waveforms, the machine model based on measured operational inductances is better than the machine model derived in chapters 2 to 4.

In figure 6.4, the calculated current i_{dc} is a little smaller than that measured. In figure 6.5, the correlation is better. As explained in subsection 6.3.1, this indicates that the commutation inductance of the machine model derived in chapters 2 to 4 is too large.

6.3.3 Small self-inductance L_{dc} and small delay angle α_p

This subsection deals with an experiment in which the coil in the direct-current circuit is omitted and in which the delay angle α_p is small ($\alpha_p = 6^\circ$). The calculations have been done with $U_b = 369 \text{ V}$, $L_{dc} = 10 \mu\text{H}$, and $R_{dc} = 0.07 \Omega$.

Figure 6.6 depicts the measured and the calculated line voltage and phase current waveforms. In the calculations, the machine model derived in chapters 2 to 4 has been used. The waveforms calculated considering the real self-inductance L_{dc} correlate much better with the measurements than the waveforms calculated assuming an infinitely large self-inductance L_{dc} . This was to be expected, because here the ripple on the current i_{dc} is considerable. Figure 6.7 again depicts the measured and the calculated waveforms, but here the machine model based on measured operational inductances has been used in the calculations.

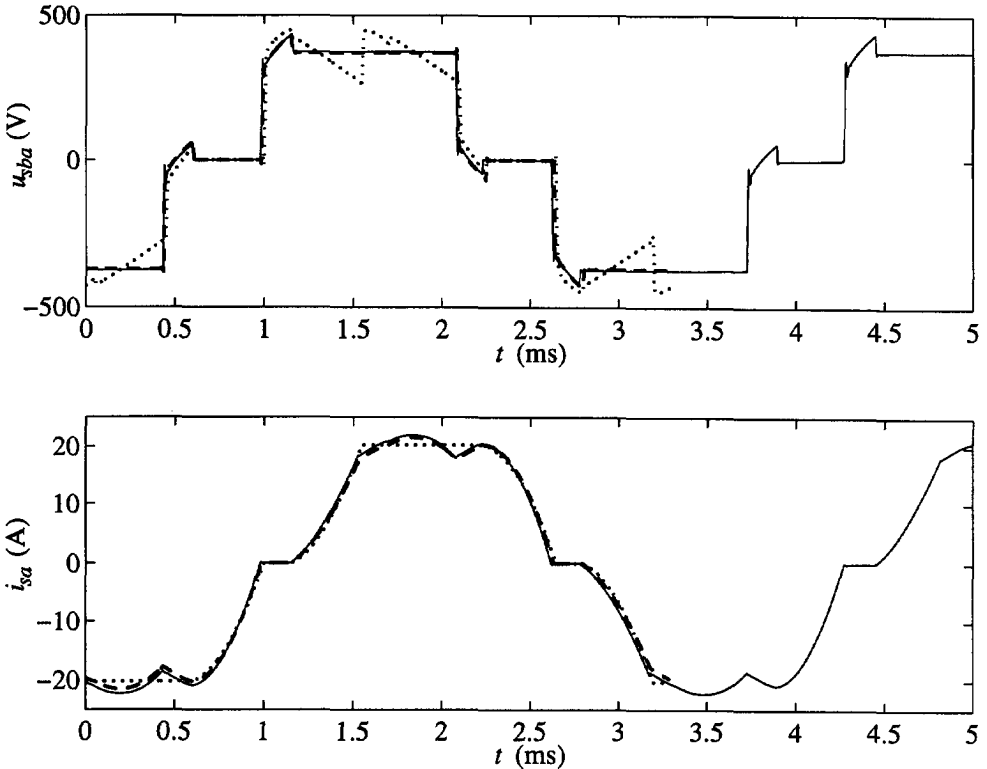


Figure 6.6: Line voltage and phase current waveforms,
 — : measured,
 - - : calculated considering the real self-inductance L_{dc} , and
 .. : calculated assuming an infinitely large self-inductance L_{dc} .
 Calculations have been done with the machine model derived in chapters 2 to 4.

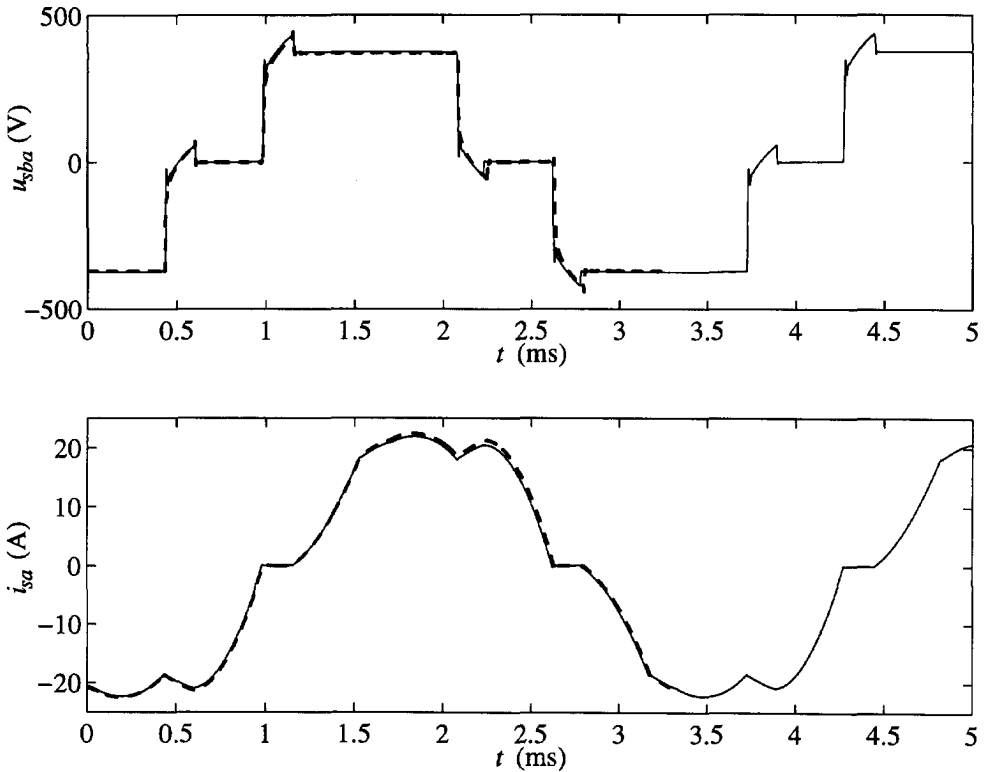


Figure 6.7: Line voltage and phase current waveforms,
 — : measured,
 - - : calculated considering the real self-inductance L_{dc} , and using the machine model based on measured operational inductances.

In figure 6.6, the calculated angle of overlap is larger than that measured. In figure 6.7, the correlation is better. As explained in subsection 6.3.1, this indicates that the commutation inductance of the machine model derived in chapters 2 to 4 is too large.

6.3.4 Small self-inductance L_{dc} and large delay angle α_p

This subsection deals with an experiment in which the self-inductance L_{dc} is omitted and in which the delay angle α_p is large ($\alpha_p = 60^\circ$). The calculations have been done with $U_b = 199$ V, $L_{dc} = 10 \mu\text{H}$, and $R_{dc} = 0.07 \Omega$.

Figure 6.8 depicts the measured and the calculated line voltage and phase current waveforms. In the calculation, the machine model derived in chapters 2 to 4 has been used. The waveforms calculated considering the real self-inductance L_{dc} correlate much better with the measured waveforms than the waveforms calculated assuming an

infinitely large self-inductance L_{dc} . This was to be expected, because here the ripple on the current i_{dc} is very large. Figure 6.9 again depicts the measured and the calculated waveforms, but here the machine model based on measured operational inductances has been used in the calculations.

In figure 6.8, the calculated current i_{dc} is a little smaller than the measured. In figure 6.9, the correlation is better. As explained in subsection 6.3.1, this indicates that the commutation inductance of the machine model derived in chapters 2 to 4 is too large.

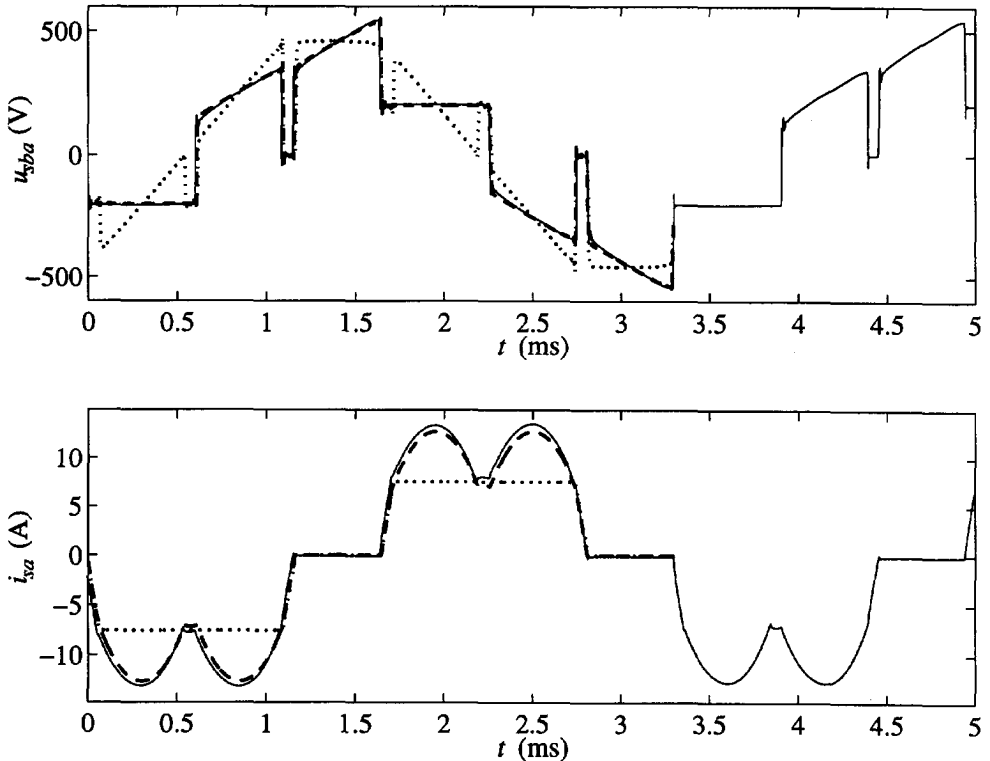


Figure 6.8: Line voltage and phase current waveforms,

— : measured,

-- : calculated considering the finite self-inductance L_{dc} , and

.. : calculated assuming an infinitely large self-inductance L_{dc} .

Calculations have been done with the machine model derived in chapters 2 to 4.

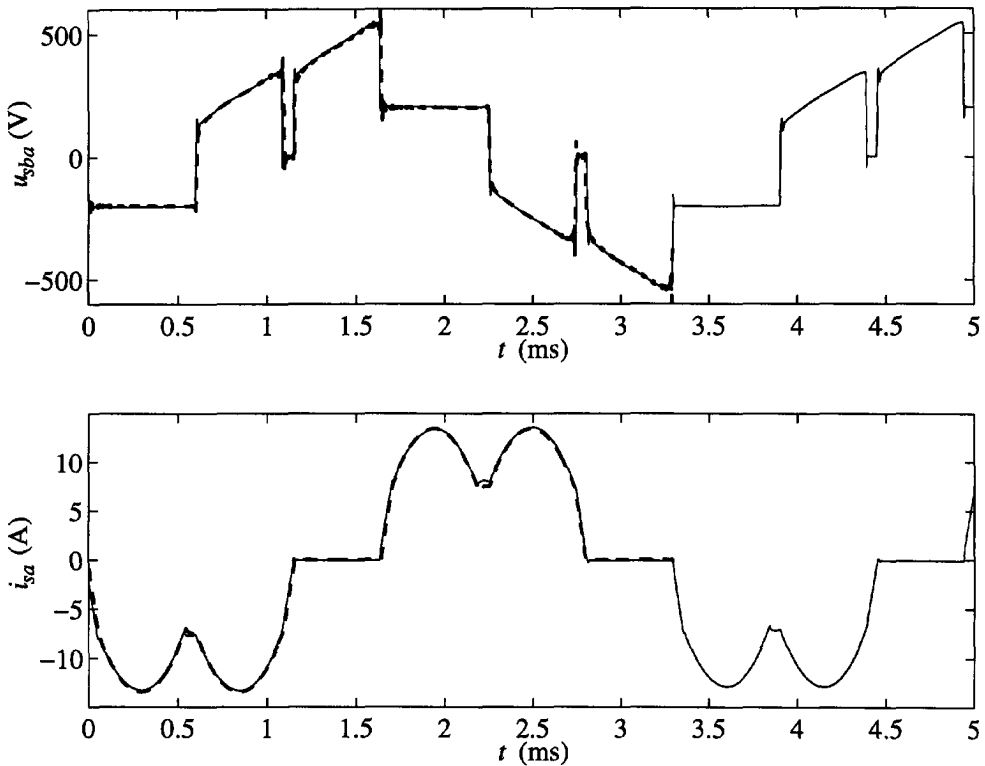


Figure 6.9: Line voltage and phase current waveforms,
 — : measured,
 - - : calculated considering the real self-inductance L_{dc} , and using the machine model based on measured operational inductances.

6.4 Conclusions

In this chapter, measured and calculated voltage and current waveforms are compared. From this, the following conclusions can be drawn.

- 1) The calculation method determining the steady-state performance derived in chapter 5 is good.
- 2) The calculation assuming an infinitely large self-inductance in the direct-current circuit can only be used when the ripple on the current in the direct-current circuit is small. This can be done by using a sufficiently large self-inductance in the direct-current circuit.
- 3) For the calculation of the steady-state performance of the rectifier-loaded generator, the machine model based on measured operational inductances is very accurate.

- 4) For the calculation of the steady-state performance of the generator loaded with a rectifier, the machine model derived in chapters 2 to 4 (which was already partly verified by means of locked-rotor tests) is reasonable.
- 5) The main deficiency of the machine model derived in chapters 2 to 4 is probably that the commutation inductance is too large.

The machine model based on measured operational inductances is very suitable for the determination of the steady-state performance of the rectifier-loaded generator. However, this model can only be used for existing machines. The aim of this thesis is to derive a machine model which can be used for the optimization of the design before the machine is built. This is not possible with the machine model based on measured operational inductances. Therefore, the model based on measured operational inductances is only used to verify the calculation method. For the optimization of the machine design, the model derived from the design parameters in chapters 2 to 4 is used. That it is possible to optimize the machine design using this model is shown in the next chapter.

Chapter 7

On the design of permanent-magnet generators

7.1 Introduction

Objective

In the previous chapters, a model for the determination of the steady-state performance of the rectifier-loaded permanent-magnet generator has been derived. In this chapter, the method is used to investigate some important design aspects of permanent-magnet generators. The effects of the damper cylinder, the magnet width, the rotational frequency, and the damper radius on the losses are investigated. In this way, it is also shown that the derived model is suitable for the optimization of the design of permanent-magnet generators.

The permanent-magnet machine used in this chapter has been built at Eindhoven University of Technology; it is called the Eindhoven machine. The machine dimensions and material properties are given in appendix A, section A.3.

Restrictions

This chapter is restricted to the investigation of the machine in the following circumstances.

- Only the steady-state performance is investigated, because the generator is intended for steady-state applications.
- For the constant component of the current in the direct-current circuit, $i_{dc,0} = 100$ A is valid. In this way, the machine current is approximately the rated current, which is used because the generator system is intended for rated-power applications.
- The value of the voltage of the voltage source in the direct-current circuit U_b is chosen as proportional to the rotational frequency n :

$$U_b = \frac{n}{167 \text{ s}^{-1}} 600 \text{ V} \quad (7.1)$$

This relation between the rotational frequency and the voltage is used to obtain comparable results at different rotational frequencies and to obtain a small delay

- angle. The delay angle is chosen as small in order to limit the reactive power, but it is not chosen as zero because it is used for control of the system.
- The magnet loss is multiplied by $2\alpha_m/\alpha_{p,1}$ because the rotor is not completely covered with magnets, as discussed in subsections 4.4.6 and 4.5.4.
 - The resistance of the damper winding for the fundamental space harmonic $R_{D,1}$ is increased by 50 % because of the end connections, as discussed in section 3.6.
 - It is assumed that the stator conductors have been split into 10 parallel conductors to reduce the increase of the stator copper loss because of skin effect. Furthermore, it is assumed that the voltage induced in these parallel conductors is exactly equal, so that there are no circulating currents in the parallel conductors.
 - To reduce the ripple on the current in the direct-current circuit, a coil in the direct-current circuit is used: $L_{dc}=0.5$ mH.
 - The resistance of the coil in the direct-current circuit is assumed to be negligible: $R_{dc}=0$.
 - In the calculations, the first 37 space harmonics are considered, which is sufficient as will be shown in section 7.3.

Outline of the chapter

Firstly, in section 7.2, the effect of a damper cylinder on the performance of the machine and on the rotor losses is investigated. Next, section 7.3 gives more detailed separations of the generator losses. In section 7.4, some conclusions are drawn.

7.2 The effect of a damper cylinder

This section deals with the effect of a damper cylinder. Firstly, in subsection 7.2.1, the effect of the addition of a damper cylinder on the voltage and current waveforms is investigated. Next, in subsection 7.2.2, the effect of the addition of a damper cylinder on the rotor losses is investigated. Subsequently, subsection 7.2.3 describes the influence of the damper radius on the rotor losses. In closing, subsection 7.2.4 describes why high-speed machines with solid rotor iron need a damper cylinder.

7.2.1 The voltage and current waveforms

Figure 7.1 depicts the calculated waveforms of the line voltage u_{sba} , the phase current i_{sa} , the phase voltage u_{sa} , and the no-load voltage e_{pa} of the Eindhoven machine with and without a damper cylinder. Of course, the damper cylinder has no effect on the no-load voltage. Because these voltage and current waveforms hardly depend on the rotational frequency, they are only depicted for one rotational frequency: $n=333$ s⁻¹.

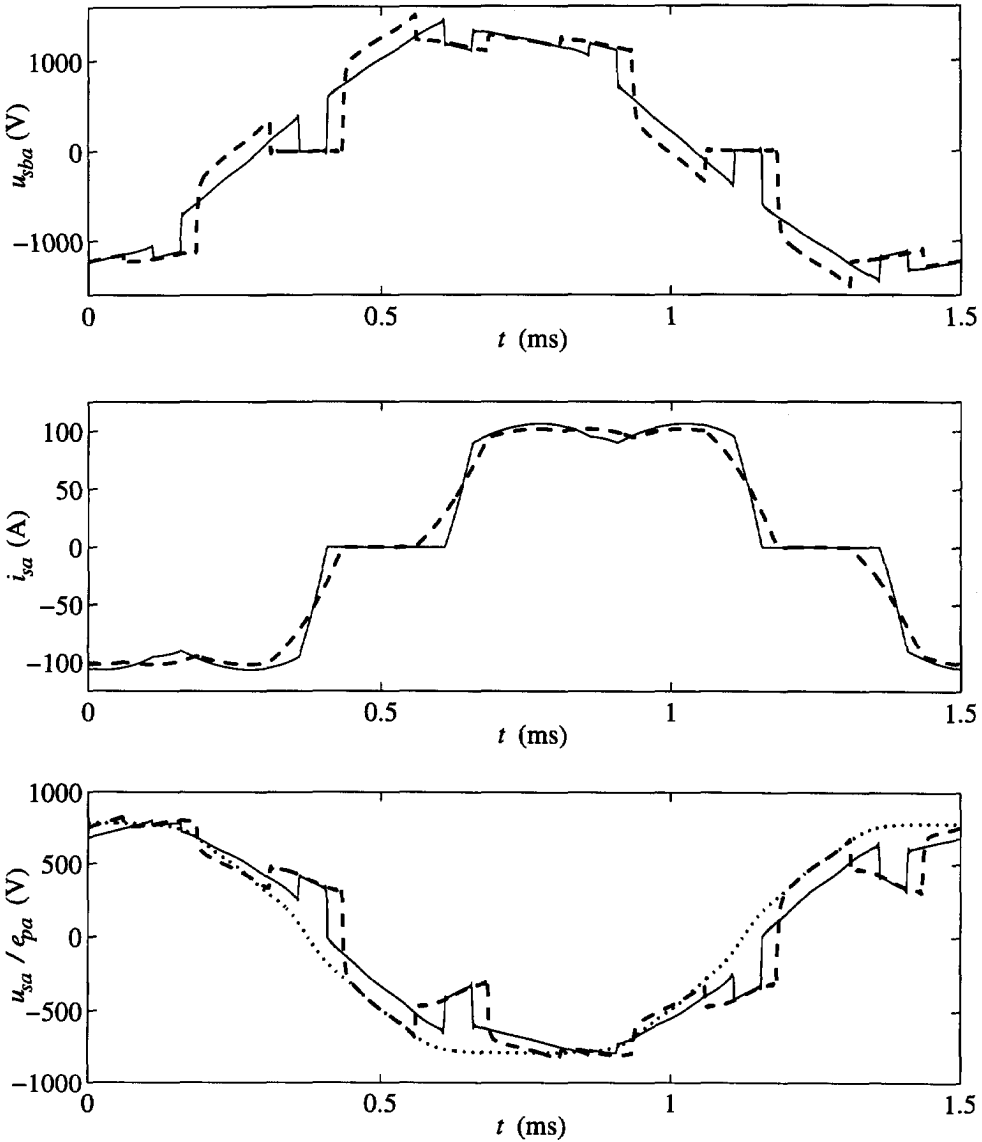


Figure 7.1: Calculated waveforms of the line voltage u_{sba} , the phase current i_{sa} , and the phase voltage u_{sa} of the generator at $n=333 \text{ s}^{-1}$,
 — : with damper cylinder ($\delta_d=0.5 \text{ mm}$), and
 - - : without damper cylinder ($b_m=10 \text{ mm}$).
 The no-load voltage e_{pa} is depicted dotted (..).

The effect of the addition of a damper cylinder on the angle of overlap is that it is reduced from about $\pi/6$ to about $\pi/15$. That the use of a damper cylinder results in a smaller angle of overlap was to be expected, because the commutation inductance of a machine with a damper is smaller than the commutation inductance of a machine without a damper cylinder.

The use of a damper cylinder results in a smaller angle of overlap. However, this does not mean (as is often suggested) that the machine with a damper cylinder supplies less reactive power. The phase angles between the fundamental time harmonics of the terminal current, the terminal voltage, and the no-load voltage hardly depend on the presence of a damper cylinder.

When a normal synchronous machine is loaded with a rectifier, a damper is usually necessary to obtain a sufficiently small angle of overlap. However, from figure 7.1, it can be concluded that the rectifier-loaded permanent-magnet machine does not need a damper to obtain a sufficiently small angle of overlap. This difference can be explained as follows. The effective air gap of a permanent-magnet machine is much larger than the effective air gap of a normal synchronous machine because in a permanent-magnet machine, the magnets also belong to the effective air gap. Therefore, the main inductance of a permanent-magnet machine is much smaller than the main inductance of a synchronous machine. In a machine without a damper, the main inductance is an important part of the commutation inductance. Hence, the commutation inductance of a permanent-magnet machine without a damper is much smaller than the commutation inductance of a normal synchronous machine without a damper.

It is concluded that in a rectifier-loaded permanent-magnet machine, a damper is usually neither necessary to obtain a sufficiently small angle of overlap, nor effective to reduce the reactive power. This is in contrast to what is often said about a synchronous machine with rectifier load.

7.2.2 The addition of a damper cylinder and the rotor losses

Figure 7.2 illustrates the effect of the addition of a damper cylinder on the rotor losses as a function of the rotational frequency n . From this figure, the following conclusions can be drawn.

- 1) At low rotational frequencies, the addition of a damper cylinder results in a large increase of the rotor losses. At very high rotational frequencies, the addition of a damper cylinder results in a decrease of the rotor losses. At medium rotational frequencies, a general statement about the effect of the addition of a damper cylinder on the rotor losses is not possible.
- 2) At rotational frequencies above $n=100 \text{ s}^{-1}$, the rotor loss in a machine with a damper cylinder is mainly inductance-limited: the loss is hardly a function of the rotational frequency.

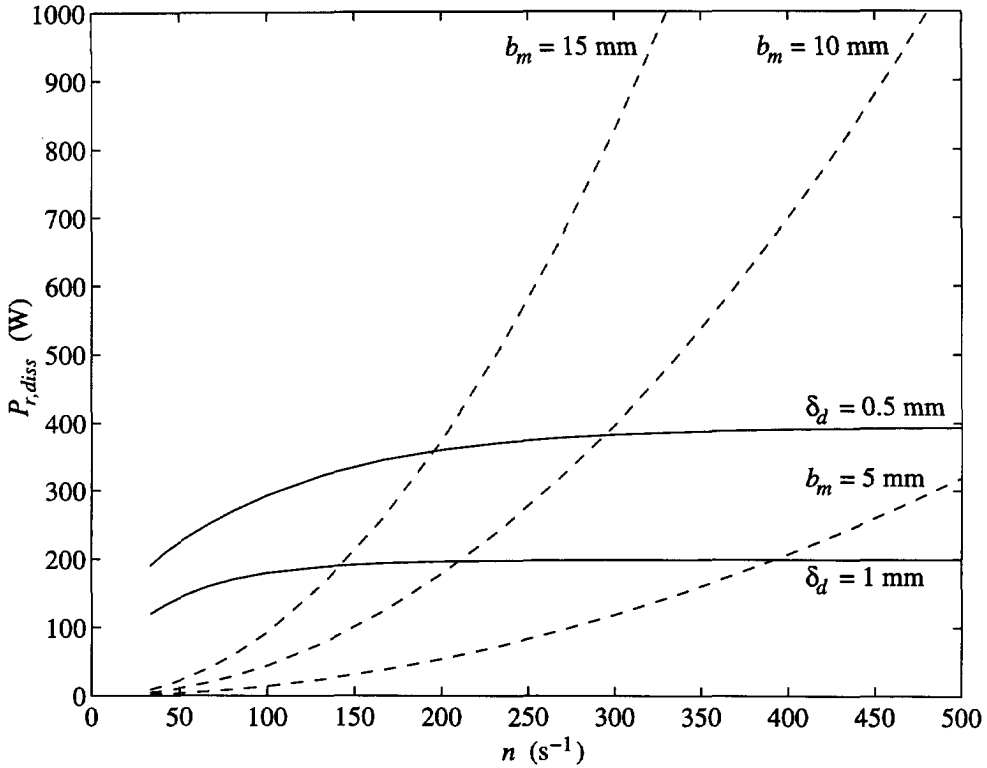


Figure 7.2: Calculated rotor losses as a function of the speed of the generator, —: with a damper cylinder with different values of the thickness of the damper δ_d , and - -: without damper cylinder with different values of the magnet width b_m .

- 3) The rotor losses in a machine with a damper cylinder are roughly inversely proportional to the thickness of the damper cylinder δ_d . However, this is only the case because skin effect in the damper cylinder is neglected. For the thinner damper cylinder ($\delta_d = 0.5$ mm), this is reasonable, because skin effect is not important for the dominating harmonics. However, for the thicker damper cylinder ($\delta_d = 1$ mm), skin effect is not negligible for the dominating harmonics at higher rotational frequencies. Therefore, the curve for $\delta_d = 1$ mm is not reliable at higher rotational frequencies. This shows that it is worthwhile incorporating skin effect in the damper cylinder in the machine model.
- 4) The rotor losses in a machine without a damper cylinder are mainly resistance-limited: the losses roughly increase with the square of the rotational frequency. This affirms that the effect of eddy currents in the rotor on the magnetic field in the air gap is very small.
- 5) The rotor losses in a machine without a damper cylinder are nearly proportional to the square of the magnet width b_m . The magnet loss caused by the space

harmonics with a large pole angle derived in subsection 4.4.2 (equation (4.44)) is proportional to the square of the magnet width b_m . This indicates that the magnet loss caused by the space harmonics with a large pole angle forms an important part of the rotor losses. Therefore, in a machine without a damper cylinder, decreasing the magnet width b_m is a very effective means of decreasing the rotor losses.

7.2.3 The damper radius and the rotor losses

Figure 7.3 illustrates the effect of the damper radius on the rotor losses. The damper radius r_d increases from the rotor radius r_r to the stator radius r_s . The results in this figure are questionable for two reasons.

- 1) As mentioned in section 4.5, the calculation of the extra loss due to the stator slotting is not accurate when the gap between the damper and the stator is small.
- 2) The rotor losses have also been calculated for the case where the damper radius r_d is smaller than the magnet radius $r_m = 69$ mm. In this case, the damper cylinder is in the magnets, which is impossible. To obtain comparable results at different values of the damper radius, the calculations have been done assuming that the magnetic field of the magnets does not depend on the damper radius. Besides, in this case, the model for the calculation of the magnet loss is not valid because the magnet loss resistance of subsection 4.4.3 has been calculated assuming that the damper radius is larger than the magnet radius. Therefore, the calculations have been done assuming an infinitely high resistivity of the magnets.

However, the results of figure 7.3 are given because they are accurate enough to draw two important conclusions from.

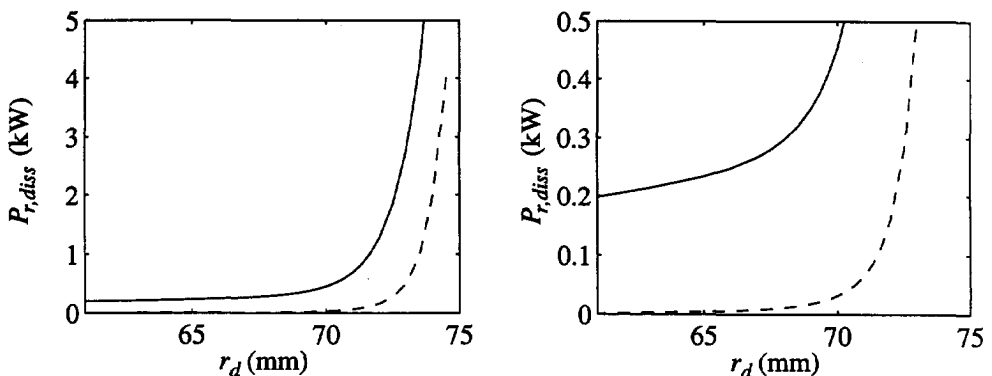


Figure 7.3: Calculated rotor loss $P_{r,diss}$ (—) and the no-load loss (- -) as a function of the damper radius r_d at $n = 333 \text{ s}^{-1}$ with $\delta_d = 0.5 \text{ mm}$. The only difference between the figures is the scale of the vertical axis. The damper radius r_d increases from the rotor radius $r_r = 61 \text{ mm}$ to the stator radius $r_s = 75 \text{ mm}$.

- 1) It is not sensible to use a small distance between the stator and the damper.
- 2) It is worthwhile investigating whether or not it is useful to place the damper cylinder under the magnets instead of surrounding the magnets.

7.2.4 Machines with solid rotor iron

It is necessary to make a remark about an assumption used in the calculations, namely the assumption that the rotor is laminated. Often, the rotor iron of a high-speed machine is solid instead of laminated (as in [Vee 97]) to make the rotor strong enough. In this case, the use of a damper cylinder is advantageous, as can be concluded from the following rough comparison of the loss in a copper damper cylinder and the loss in the solid rotor iron.

In a high-speed machine with solid rotor iron and without a damper cylinder, the solid rotor iron functions as a damper. Because of skin effect, the currents only flow in a thin cylinder at the surface of the rotor iron. Assuming a specific resistance of the solid iron of $\rho_{Fe} = 0.1 \mu\Omega\text{m}$, a relative magnetic permeability of $\mu_{rFe} = 1000$, and a rotational frequency of $n = 333 \text{ s}^{-1}$, the skin depth for the fifth and the seventh time harmonic is $\delta_{skin,Fe} = 0.08 \text{ mm}$. Herewith, the resistivity of the iron damper cylinder is about six times the resistivity of a copper damper cylinder, and the thickness of the iron damper cylinder is about one sixth of the thickness of a copper damper cylinder of $\delta_d = 0.5 \text{ mm}$. For higher time harmonics, the skin depth in iron is even smaller. Therefore, the losses in the solid iron are at least 36 times the losses in a copper damper cylinder at the radius of the rotor iron. In a copper damper cylinder surrounding the magnets, the losses are higher, but they remain much smaller than the losses in the solid rotor iron. In [Vee 97], comparable results are reported.

The model derived in this thesis can also be used for a machine with solid rotor iron and a damper cylinder, because the damper cylinder shields the rest of the rotor, so that the iron loss in the solid rotor is negligible.

7.3 Separation of the generator losses

In table 7.1, the calculated losses of a machine are tabulated for six different situations. The first four columns give the losses with and without a damper cylinder at two different rotational frequencies. The third and the fourth column give the losses in the situation for which the voltage and current waveforms are depicted in figure 7.1. To illustrate the effect of the magnet width in a machine without a damper, the magnet width is halved in the fifth column. To illustrate the effect of the damper radius in a machine with a damper, the damper radius is increased in the sixth column.

In this table, the subscripts *fsh*, *hsh*, *fth*, and *hth* stand for fundamental space

harmonic, higher space harmonics, fundamental time harmonic and higher time harmonics respectively.

The magnet loss due to the higher space harmonics with the harmonic numbers $k=23..37$ $P_{m,hsh,k=23..37}$ is always smaller than 30 mW, which is negligible. Therefore, it is not separately mentioned in the table.

The row in table 7.1 giving the rotor losses affirms the conclusions drawn in subsections 7.2.2 and 7.2.3. Furthermore, the following conclusions can be drawn.

Table 7.1: Calculated losses in a machine with and without damper cylinder at different rotational frequencies n . Also the effect of the magnet width b_m and the damper radius r_d are illustrated.

n	(s ⁻¹)	167	167	333	333	333	333
b_m	(mm)	10	10	10	10	5	10
r_d	(mm)	-	69.5	-	69.5	-	73
$P_{sCu,fth}$	(W)	501	513	559	572	559	572
$P_{sCu,hth}$	(W)	33	93	83	237	82	259
$P_{sFe,fth,fsh}$	(W)	812	805	2293	2268	2289	2266
$P_{sFe,hth,fsh}$	(W)	31	4	89	11	89	9
$P_{sFe,hsh}$	(W)	72	72	204	204	204	204
$P_{\sigma,fth}$	(W)	12	13	35	36	35	36
$P_{\sigma,hth}$	(W)	5	15	15	43	14	47
$P_{stot,diss}$	(W)	1466	1514	3277	3371	3273	3394
P_{rFe}	(W)	7.4	0.0	21.4	0.0	21.4	0.0
$P_{d,fsh,k=1}$	(W)	-	206.7	-	209.1	-	213.7
$P_{d,hsh,k=5..19}$	(W)	-	119.6	-	152.4	-	1724.1
$P_{d,hsh,k=23..37}$	(W)	-	0.4	-	0.6	-	214.8
$P_{m,fsh}$	(W)	106.3	0.3	427.0	0.3	108.9	0.3
$P_{m,hsh}$	(W)	10.3	2.7	41.0	3.5	16.3	3.3
$P_{extra,slotting}$	(W)	-0.3	16.9	-1.2	22.4	-1.3	602.7
$P_{rtot,diss}$	(W)	123.7	346.7	488.2	388.3	145.3	2758.9
$P_{tot,diss}$	(W)	1590	1861	3766	3759	3418	6153

- The stator copper loss caused by the fundamental time harmonic $P_{sCu, fh}$ increases with the rotational frequency because of skin effect in the stator conductors.
- The addition of a damper cylinder results in an increase of the stator copper loss P_{sCu} , mainly of the copper loss caused by higher time harmonics $P_{sCu, hth}$. This is so because addition of a damper cylinder results in an increase of the harmonic content of the current, as can be concluded from figure 7.1.
- As was to be expected from the model, all iron loss components increase with the rotational frequency.
- The stator core loss caused by the fundamental time harmonic and the fundamental space harmonic $P_{sFe, fh, fsh}$ hardly depends on the presence of a damper cylinder.
- The stator core loss produced by the higher space harmonics $P_{sFe, hsh}$ does not depend on the presence of a damper cylinder. This was to be expected, because only the space harmonics of the magnetic field of the magnets are considered, and this magnetic field is not influenced by the damper cylinder.
- The stator core loss produced by the higher time harmonics $P_{sFe, hth, fsh}$ decreases when a damper cylinder is added because the time harmonic fields are reduced by the currents in the damper cylinder.
- The stator iron loss is the largest part of the losses in the generator. If this loss has to be decreased, the use of magnetic materials other than laminated iron should be investigated.
- In a machine with a damper cylinder, the rotor core loss P_{rFe} and the eddy-current loss in the magnets P_m are negligible compared to the loss in the damper cylinder: the damper cylinder shields the rest of the rotor.
- To calculate the damper loss P_d in a machine with a damper cylinder, it is enough to consider a limited number of space harmonics. When the distance between the damper and the stator surface is not too small, it is sufficient to consider the first 19 space harmonics; the contribution of the higher space harmonics is negligible.
- The damper loss due to the fundamental space harmonic $P_{d, fsh, k=1}$ is hardly a function of the damper radius, while the damper loss due to the higher space harmonics $P_{d, hsh}$ strongly depends on the damper radius. This again illustrates that the larger part of the fundamental space harmonic of the magnetic field crosses the air gap, while the larger part of the higher space harmonic of the magnetic field does not.
- In a machine without a damper cylinder, the magnet loss P_m is considerably higher than the rotor core loss P_{rFe} .
- In a machine without a damper cylinder, the most important part of the rotor losses is the magnet loss P_m caused by the fundamental space harmonic. This loss is proportional to the square of the magnet width b_m , as shown in subsection 4.4.2 (equation (4.44)). This agrees with the fifth conclusion of subsection 7.2.2, where it was said that the magnet loss caused by the space harmonics with a large pole angle forms an important part of the rotor losses. Furthermore, it implies that it is not terrible that the magnet loss produced by the higher space harmonics is

- overestimated, as explained in section 4.4.
- In a machine without a damper cylinder, the extra loss due to the stator slotting $P_{extra,slotting}$ appears to be negative. This means that eddy currents induced by the stator slotting oppose the eddy currents due to the stator currents (compare equation (4.79)).
 - In a machine with a damper cylinder, the extra loss due to the stator slotting $P_{extra,slotting}$ is neither negligible nor dominant.

7.4 Conclusions

This chapter illustrates that the model derived in this thesis can be used for the optimization of the design of high-speed permanent-magnet generators. In this chapter, the effects of the damper cylinder, the thickness of the damper cylinder δ_d , the magnet width b_m , the damper radius r_d and the rotational frequency n have been investigated. In the same way, other dimensions that influence the rotor losses can be investigated, such as the slot opening angle β_{so} , the number of pole pairs p , the air gap length $r_s - r_r$, and the magnet length l_m .

In contrast to what is said about a rectifier-loaded synchronous machine, in a rectifier-loaded permanent-magnet machine, a damper is usually neither necessary for obtaining a sufficiently small angle of overlap, nor effective for reducing the reactive power.

A general statement about the usefulness of a damper cylinder is not possible. At high rotational frequencies, the addition of a damper cylinder results in a decrease of the rotor losses, while at low rotational frequencies, it results in an increase of the rotor losses. The decision therefore whether to use a damper cylinder or not should be based on careful calculations.

In a machine with a damper cylinder, the rotor core loss and the eddy-current loss in the magnets are negligible compared to the loss in the damper cylinder: the damper cylinder shields the rest of the rotor. Furthermore, the rotor losses are roughly inversely proportional to the thickness of the damper cylinder if skin effect in the damper cylinder is negligible, which is not always the case. The rotor losses strongly depend on the radius of the damper cylinder. When the distance between the stator surface and the damper is too small, the rotor losses are excessive.

In a machine without a damper cylinder, the magnet loss is roughly proportional to the square of the magnet width. Therefore, decreasing the magnet width is a very effective means of decreasing the rotor losses in a machine without a damper.

When the rotor iron is solid instead of laminated, the use of a damper cylinder will generally be necessary to limit the rotor losses. The machine model derived in this chapter can also be used for these machines with a solid rotor and a damper cylinder.

Chapter 8

Conclusions and recommendations

This thesis deals with the losses in a high-speed permanent-magnet generator with a cylindrical rotor and surface-mounted magnets loaded with a six-pulse controlled bridge rectifier. As described in chapter 1, the objective of the thesis has been to derive a machine model suitable to optimize the machine design. In this optimization, special attention would be paid to the effect of a damper cylinder. Also the effect of using small permanent-magnet blocks on the rotor losses would be investigated.

In chapters 2 to 6, a model of the rectifier-loaded machine has been derived and verified. In chapter 7, some design aspects have been investigated. In this chapter, conclusions are drawn and recommendations for further research are given.

8.1 Conclusions

The machine model

A model of a high-speed permanent-magnet generator has been derived. This model has five characteristics that make it suitable to optimize the machine design.

- 1) The model is analytic.
- 2) The parameters of the model are calculated from the dimensions and material properties of the machine.
- 3) The effect of a damper cylinder can be investigated, because the model may be used for a machine with a damper cylinder and for a machine without a damper cylinder.
- 4) The effect of using small magnet blocks on the rotor losses can be investigated, because the eddy-current loss in the magnets has been modelled as a function of the width of the magnet blocks.
- 5) The model includes the most important electromagnetic losses.

The derivation of the model has been based on the two-dimensional calculation of the magnetic field in the air gap and the magnets. Space harmonics of the magnetic field have been considered because they contribute significantly to the rotor losses. Based on

the calculated magnetic field, voltage equations have been derived. Five kinds of electromagnetic losses have been incorporated into the machine model.

- 1) The copper loss in the stator conductors is calculated considering skin effect.
 - 2) If a damper cylinder is present, the damper loss is considered. The damper cylinder has been modelled as a series of short-circuited sinusoidally-distributed damper windings.
 - 3) The iron loss is considered to be proportional to $\omega^{1.5}B^2$. This model is different from those commonly used, but it is simple and effective.
 - 4) The eddy-current loss in the magnets is considered. The effect of eddy currents in the magnets on the magnetic field in the air gap and the magnets is not completely negligible at high frequencies. It can be approximated by incorporating a magnet loss resistance in the machine model.
 - 5) The loss due to the stator slotting is calculated using a conformal transformation.
- Most of these losses have been represented by resistances in the machine model.

Rectifier load

The model of the permanent-magnet generator has been combined with a model of the controlled rectifier, in which the thyristors are replaced by ideal switches. The resulting equations are solved in the frequency domain to determine the steady-state performance of the rectifier-loaded permanent-magnet machine.

Verification of the derived models

In this thesis, two kinds of measurements have been used to verify the derived models, namely locked-rotor tests and measurements of steady-state voltage and current waveforms of the rectifier-loaded machine.

Locked-rotor tests have been used to verify the machine model. From the comparison of measured voltages, currents, and powers to calculated values,

- 1) the voltage equations of the generator with a damper cylinder,
- 2) the model of the iron loss, and
- 3) the model of the eddy-current loss in the magnets

have been verified for the fundamental space harmonic. For the higher space harmonics, these models have been neither verified nor refuted. Also the model for skin effect in the stator conductors has been neither verified nor refuted. Furthermore, these tests have verified that the effect of eddy currents in the laminated iron on the magnetic field in the air gap and the magnets is negligible, and that the effect of eddy currents in the magnets on the magnetic field in the air gap and the magnets is not completely negligible at high frequencies.

Measurements of voltage and current waveforms have been used to verify the model of the generator loaded with the rectifier. From the comparison of measured voltage and current waveforms to calculated waveforms, it is concluded that the model is suitable for the calculation of voltage and current waveforms.

The model for the loss due to the stator slotting has not been verified.

The generator design

The model of the permanent-magnet machine has been used to investigate some design aspects of permanent-magnet machines. Regarding the usefulness of a damper cylinder, three important conclusions can be drawn.

- 1) In a rectifier-loaded permanent-magnet machine, a damper is generally neither necessary to obtain a sufficiently small angle of overlap, nor effective to reduce the reactive power. This is in contrast to what is often said about a rectifier-loaded synchronous machine.
- 2) In a machine with laminated rotor iron, the effect of a damper cylinder on the rotor losses depends on the rotational frequency. At very high rotational frequencies, the addition of a damper cylinder results in a decrease of the rotor losses, while at lower rotational frequencies, it results in an increase of the rotor losses. Therefore, the decision whether to use a damper cylinder or not should be based on careful calculations.
- 3) In a machine with solid rotor iron, the use of a damper cylinder is generally necessary to limit the rotor losses.

Further, about a machine with a damper cylinder, three conclusions can be drawn.

- 1) The rotor core loss and the eddy-current loss in the magnets are negligible compared to the damper loss: the damper cylinder shields the rest of the rotor.
- 2) The rotor losses are roughly inversely proportional to the thickness of the damper cylinder if skin effect in the damper cylinder is negligible, which is not always the case.
- 3) The rotor losses become excessive when the distance between the stator surface and the damper becomes too small.

Subsequently, one conclusion about a machine with laminated rotor iron and without a damper cylinder is drawn. Decreasing the magnet width is a very effective means of decreasing the rotor losses, because the rotor losses are roughly proportional to the square of the magnet width.

The calculations from which these conclusions were drawn illustrate that the derived model of the permanent-magnet machine is suitable for the optimization of the machine design.

Originality

This thesis is original in its combination of the methods used. When the rotor losses in a permanent-magnet machine with a damper are calculated analytically, stylized current waveforms are often used. When voltage and current waveforms in a machine are calculated analytically, usually machine models are used which do not include effects of space harmonics and losses other than the copper loss. This thesis combines the calculation of voltage and current waveforms with a machine model based on a two-dimensional calculation of the magnetic field including effects of space harmonics and losses other than the copper loss.

Furthermore, this thesis is original in its modelling of the eddy currents in the magnet blocks. Other authors replace the magnets with a cylinder of magnet material. In this thesis, the real width of the magnet blocks is considered.

8.2 Recommendations for further research

Modelling of the machine

The machine model derived in this thesis may be improved or extended by further research into the following five areas.

- 1) In this thesis, skin effect in the damper has not been included. However, this is not appropriate if a thicker damper cylinder is used to reduce the damper loss. Therefore, skin effect in the damper cylinder should be incorporated in the machine model.
- 2) Within this study, the machine model has only been verified for the fundamental space harmonic. For the higher space harmonics, the models have been neither verified nor refuted. In addition, the model for the loss due to the stator slotting has not been verified. More experimental research is necessary in order to do so.
- 3) The modelled commutation inductance of a permanent-magnet machine without a damper cylinder is larger than that measured, see section 6.4. The cause of this difference should be investigated.
- 4) An increase in the distance between the stator surface and the damper cylinder decreases the damper loss. Therefore, it would be worthwhile investigating whether or not it is useful to place the damper cylinder between the magnets and the rotor iron instead of around the magnets. This would especially be interesting if magnets with a very high resistivity or 'laminated' magnets were to be used. The machine model derived in this thesis is not valid when the damper cylinder is placed between the magnets and the rotor iron.
- 5) To reduce the iron loss in the stator, the use of magnetic materials other than laminated iron should be explored.

The generator design

In this thesis, only a few generator design aspects have been investigated. Others should also be explored, such as the form of the stator winding, the slot opening angle, the number of pole pairs, the air gap length, the magnet pole angle, and the magnet length.

References

- Abu 97 S.M. Abu Sharkh, M.R. Harris, N. Taghizadeh Irenji, 'Calculation of rotor eddy-current loss in high-speed PM alternators'. In *Proceedings of the Eighth International Conference on Electrical Machines and Drives*, Cambridge, 1-3 September 1997, pp. 170-174.
- Aca 96 P.P. Acarnley, B.C. Mecrow, J.S. Burdess, N. Fawcett, J.G. Kelly, P.G. Dickinson, 'Design principles for a flywheel energy store for road vehicles'. In *IEEE Transactions on Industry Applications*, vol. 32 (1996), pp. 1402-1408.
- Ådn 91 A.K. Ådnanes, *High efficiency, high performance permanent magnet synchronous motor drives*. PhD-thesis University of Trondheim, 1991.
- Alg 59 P.L. Alger, Angst, G., Davies, E.J., 'Stray-load losses in polyphase induction machines'. In *AIEE Transactions on Power Apparatus and Systems*, vol. 78 (1959), pp. 349-357.
- Alg 65 P.L. Alger, *The nature of induction machines*. New York: Gordon and Breach, 1965.
- And 85 E.C. Andresen, 'Einfluß von Umrichterart, Magnethöhe, Polbedeckung und Wicklungsanordnung auf den Betrieb von Synchronmotoren mit radialen SmCo5-Magneten'. In *etzArchiv*, vol. 7 (1985), pp. 263-270.
- And 87 E.C. Andresen, B. Blöcher, J. Heil, R. Pfeiffer, 'Permanentmagneterregter Synchronmotor mit maschinenkommutiertem Frequenzumrichter'. In *etzArchiv*, vol. 9 (1987), pp. 399-402.
- And 97 E.C. Andresen, R. Keller, 'Variable speed drive with current source inverter supply and permanent magnet synchronous motor compared with cage induction motor'. In *Electrical Engineering*, vol. 80 (1997), pp. 375-381.
- Ama 95 M. Amar, R. Kaczmarek, 'A general formula for prediction of iron losses under nonsinusoidal voltage waveform'. In *IEEE Transactions on Magnetics*, vol. 31 (1995), pp. 2504-2509.
- Ami 95 B. Amin, 'Contribution to iron-loss evaluation in electrical machines'. In *European Transactions on Electrical Power Engineering*, vol. 5 (1995), pp. 325-332.

- Ark 92 A.A. Arkadan, R. Vyas, J.G. Vaidya, M.J. Shah, 'Effect of toothless stator design on core and stator conductors eddy current losses in permanent-magnet generators'. In *IEEE Transactions on Energy Conversion*, vol. 7 (1992), pp. 231-237.
- Ata 94 K. Atallah, D. Howe, 'The calculation of iron losses in brushless permanent-magnet dc motors'. In *Journal of Magnetism and Magnetic Materials*, vol. 133 (1994), pp. 578-582.
- Ber 88 G. Bertotti, 'General properties of power losses in soft ferromagnetic materials'. In *IEEE Transactions on Magnetics*, vol. 24 (1988), pp. 621-630.
- Ber 91 G. Bertotti, A. Boglietti, M. Chiampi, D. Chiarabaglio, F. Fiorillo, M. Lazzari, 'An improved estimation of iron losses in rotating electrical machines'. In *IEEE Transactions on Magnetics*, vol. 27 (1991), pp. 5007-5009.
- Ber 92 B. Bertotti, 'Dynamic generalization of the scalar Preisach model of hysteresis'. In *IEEE Transactions on Magnetics*, vol. 28 (1992), pp. 2599-2601.
- Bin 92 K.J. Binns, P.J. Lawrenson, C.W. Trowbridge, *The analytical and numerical solution of electric and magnetic fields*. Chichester: Wiley, 1992.
- Blö 86 B. Blöcher, *Permanenterregte Synchronmaschine für Speisung durch stromeinprägenden Frequenzumrichter*. PhD-thesis Technische Hochschule Darmstadt, 1986.
- Böd 62 T. Bödefeld, H. Sequenz, *Elektrische Maschinen*. Sixth edition. Vienna: Springer, 1962.
- Bol 69 H. Bolton, 'Transverse edge effect in sheet-rotor induction machines'. In *Proceedings of the IEE*, vol. 116 (1969), pp. 725-731.
- Bol 80 S. Bolognani, G.B. Indri, 'A study of converter-fed synchronous machines by means of Fourier analysis'. In *IEEE Transactions on Industry Applications*, vol. 16 (1980), pp. 203-210.
- Bol 91 S. Bolognani, 'Harmonic analysis of a thyristor bridge-synchronous machine system'. In *Proceedings of the International Conference on the Evolution and Modern aspects of Synchronous Machines*, Zürich, 27-29 August 1991, part 1, pp. 327-332.
- Bol 93 S. Bolognani, M. Fracchia, P. Pozzobon, M. Zigliotti, 'A generalized model for harmonic analysis of natural commutation conversion systems'. In *Proceedings of the Fifth European Conference on Power Electronics and Applications*, Brighton, 13-16 September 1993, vol. 8, pp. 179-184.
- Bou 80 N. Boules, W.-R. Canders, H. Weh, 'Analytische Bestimmung des Nutzungseinflusses auf die Feldverteilung und die Wirbelstromverluste in dauermagneterregten Synchronmaschinen'. In *Archiv für Elektrotechnik*, vol. 62 (1980), pp. 283-293.
- Bou 81 N. Boules, 'Impact of slot harmonics on losses of high-speed permanent-magnet machines with a magnet retaining ring'. In *Electric Machines and Electromechanics*, vol. 6 (1981), pp. 527-539.

- Bou 85 N. Boules, 'Prediction of no-load flux density distribution in permanent-magnet machines'. In *IEEE Transactions on Industry Applications*, vol. 21 (1985), pp. 633-643.
- Buc 78 F.G.G. de Buck, *Ontwerpaanpassing bij inverter-gevoede inductiemotoren*. PhD-thesis State University Gent, 1978.
- Buc 79 F.G.G. de Buck, 'Losses and parasitic torques in electric motors subjected to PWM waveforms'. In *IEEE Transactions on Industry Applications*, vol. 15 (1979), p. 47-53.
- Buc 84 F.G.G. de Buck, P. Gistelink, D. de Backer, 'A simple but reliable loss model for inverter-supplied induction motors'. In *IEEE Transactions on Industry Applications*, vol. 20 (1984), p. 190-202.
- Cam 94 P. Campbell, *Permanent magnet materials and their application*. Cambridge, Cambridge University Press, 1994.
- Can 82 W.-R. Canders, *Berechnung von Schwungradenergiespeichern aus Faserverbundwerkstoff mit elektrischem Energiewandler*. PhD-thesis Technische Universität Carolo-Wilhelmina, Braunschweig, 1982.
- Cha 68 B.J. Chalmers, B.R. Sarkar, 'Induction-motor losses due to nonsinusoidal supply waveforms'. In *Proceedings of the IEE*, vol. 115 (1968), pp. 1777-1782.
- Cha 93 C.C. Chan, 'An overview of electric vehicle technology'. In *Proceedings of the IEEE*, vol. 81 (1993), pp. 1202-1213.
- Cha 96 C.C. Chan, 'Overview of electric vehicles - clean and energy efficient urban transportation'. In *Proceedings of the Sixth Power Electronics and Motion Control Conference*, Budapest, 2-4 September 1996, pp. K/7-K/15.
- Cha 97 C.C. Chan, K.T. Chau, 'An overview of power electronics in electric vehicles'. In *IEEE Transactions on Industrial Electronics*, vol. 44 (1997), pp. 3-13.
- Chu 93 P. Chudi, A. Malmquist, 'A hybrid drive for the car of the future, environmental concept car unites electric drive with gas turbine'. In *ABB Review*, vol. 3 (1993), no. 9, pp. 3-12.
- Chu 96 P. Chudi, A. Malmquist, 'Hybrid drive for low-emission trucks and buses'. In *ABB Review*, vol. 6 (1996), no. 7, pp. 12-18.
- Cla 43 E. Clarke, *Circuit analysis of A-C power systems, Vol. I - Symmetrical and related components*. New York: John Wiley and Sons, Inc., 1943.
- Col 87 R.S. Colby, D.W. Novotny, 'Efficient operation of surface-mounted PM synchronous motors'. In *IEEE Transactions on Industry Applications*, vol. 23 (1987), pp. 1048-1054.
- Cul 72 B.D. Cullity, *Introduction to magnetic materials*. Reading, Massachusetts: Addison-Wesley, 1972.
- Dem 87 W.W. Demel, *Baugröße und Verluste von permanenterregten Synchronmaschinen bei unterschiedlichem Verlauf des Stromes*. PhD-thesis Rheinisch-Westfälische Technische Hochschule Aachen, 1987.

- Eld 95 S.A. Eldhemy, A.A. Mohamed, S.S. Shokralla, 'Calculation of additional losses caused by feeding an induction motor from a non-sinusoidal supply'. In *International Journal of Electrical Engineering Education*, vol. 32 (1995), pp. 51-62.
- Fio 90a F. Fiorillo, A. Novikov, 'Power losses under sinusoidal, trapezoidal and distorted induction waveform'. In *IEEE Transactions on Magnetics*, vol. 26 (1990), pp. 2559-2561.
- Fio 90b F. Fiorillo, A. Novikov, 'An improved approach to power losses in magnetic laminations under nonsinusoidal induction waveform'. In *IEEE Transactions on Magnetics*, vol. 26 (1990), pp. 2904-2910.
- Gle 98 C.N. Glew, 'Stray load losses in induction motors: a challenge to academia'. In *Power Engineering Journal*, vol. 12 (1998), pp. 27-32.
- Gru 78 P. v. Grumbkow, *Optimierung unter Berücksichtigung der Einzeleffekte bei der Berechnung asynchroner Kurzstator - Linearomotoren*. PhD-thesis Technische Universität Carolo-Wilhelmina, Braunschweig, 1978.
- Gün 84 W. Güntensperger, *Schnelllaufende Permanentmagnet-Synchronmaschine mit kleinen Leerlaufverlusten für kinetische Energiespeicher*. PhD-thesis Eidgenössische Technische Hochschule Zürich, 1984.
- Hag 29 B. Hague, *Electromagnetic problems in electrical engineering*. London: Oxford University Press, 1929. (Later edition: *The principles of electromagnetism applied to electrical machines*. New York: Dover, 1962.)
- Hau 89 H.A. Haus, J.R. Melcher, *Electromagnetic fields and energy*. Englewood Cliffs, New Jersey: Prentice Hall, 1989.
- Hen 89 G. Henneberger, W. Schleuter, 'Servoantriebe für Werkzeugmaschinen und Industrieroboter, Teil 2: Bürstenlose Gleichstrommotoren und Zukunftsaussichten'. In *Elektrotechnische Zeitschrift*, vol. 110 (1989), pp. 274-279.
- Hen 94 J.R. Hendershot, T.J.E. Miller, *Design of brushless permanent-magnet motors*. Hillsboro: Magna Physics Publishing, 1994.
- Hoe 84 M.J. Hoeijmakers, *On the steady-state performance of a synchronous machine with convertor - with special attention to wind energy conversion systems*. PhD-thesis, Eindhoven University of Technology, 1984.
- Hoe 93 M.J. Hoeijmakers, P.J. van Duijsen, 'Three-phase equivalent circuits for network simulation of induction machines'. In *Proceedings of the Fifth European Conference on Power Electronics and Applications*, Brighton, 13-16 September 1993, vol. 5, pp. 145-150.
- Hof 86 R.G. Hoft, *Semiconductor power electronics*. New York: Van Nostrand Reinhold Company, 1986.
- IEA 93 International Energy Agency, *Electric vehicles: technology, performance and potential*. Paris: OEDC/IEA, 1993.
- IEC 85 International Electrotechnical Commission, *Letter symbols including conventions and signs for electrical technology. A handbook for everyday use*. Delft: Nederlands Normalisatie-instituut, 1985.

- IEE 72 IEEE, *IEEE standard dictionary of electrical and electronics terms*. New York: Wiley, 1972.
- Jil 94 D.C. Jiles, 'Modelling the effects of eddy current losses on frequency dependent hysteresis in electrically conducting media'. In *IEEE Transactions on Magnetics*, vol. 30 (1994), pp. 4326-4328.
- Kra 83 C. Kramer, *Auslegung und Optimierung eines permanenterregten hochdynamischen Synchron-Stellmotors mittels numerischer und analytischer Feldberechnung*. PhD-thesis, Technische Hochschule Darmstadt, 1983.
- Kra 95 P.C. Krause, O. Wasynczuk, S.D. Sudhoff, *Analysis of electric machinery*. Piscataway, New Jersey: IEEE Press, 1995.
- Krü 92 M. Krüger, *Bordstromversorgung mit schnellaufendem Synchrongenerator*. PhD-thesis Technische Universität Carolo-Wilhelmina, Braunschweig, 1992.
- Krü 94 M. Krüger, 'Kompakte Bordstromversorgung mit schnellaufendem Synchrongenerator'. In *Archiv für Elektrotechnik*, vol. 77 (1994), pp. 213-220.
- Küp 84 K. Küpfmüller, *Einführung in die theoretische Elektrotechnik*. 11th edition. Berlin: Springer-Verlag, 1984.
- Kwa 91 H. Kwakernaak, R. Sivan, *Modern signals and systems*. Englewood Cliffs, New Jersey: Prentice Hall, 1991.
- Lam 66 J. Lammeraner, and M. Štafl, *Eddy currents*. London: Iliffe books, 1966.
- Lan 73 A. Lang, *Einfluß der Streufelder auf Entwurf und Betriebsverhalten asynchroner Linearmotoren*. PhD-thesis Technische Universität Carolo-Wilhelmina, Braunschweig, 1973.
- Lar 70 H. Largiadèr, 'Gesichtspunkte für die Bemessung umrichter gespeister Asynchronmotoren für die Traktion'. In *Brown Boveri Mitteilungen*, vol. 57 (1970), pp. 152-167.
- Lav 78 J.D. Lavers, P.P. Biringer, H. Hollitscher, 'A simple method of estimating the minor loop hysteresis loss in thin laminations'. In *IEEE Transactions on Magnetics*, vol. 14 (1978), pp. 386-388.
- Len 96 K. Lenasi, M. Berlec, D. Makuc, 'Calculation of 2D static fields with conformal transformation method'. In *Proceedings of the Sixth International Conference on Electrical Machines*, 1996, Vigo, vol. 1, pp. 159-162.
- Lev 84 E. Levi, *Polyphase motors*. New York: Wiley, 1984.
- Mac 94 R. Mackay, 'Development of a 24 kW gas turbine-driven generator set for hybrid vehicles', SAE Paper number 940510. In *Electric vehicles driving towards commercialization*, Warrendale (PA): Society of Automotive Engineers, 1997.
- May 86 I.C. Mayergoyz, 'Mathematical models of hysteresis'. In *IEEE Transactions on Magnetics*, vol. 22 (1986), pp. 603-607.
- Mec 93 B.C. Mecrow, A.G. Jack, J.M. Masterman, 'Determination of rotor eddy current losses in permanent magnet machines'. In *Proceedings of the Sixth International Conference on Electrical Machines and Drives*, Oxford, 8-10 September 1993, pp. 299-304.

- Mee 88 R.B. van der Meer, J.S. Rietema, 'Electrical machine for flywheel system EMAFER. Design considerations for an electrical machine in the EMAFER flywheel system'. In *Proceedings of the 23rd Intersociety Energy Conversion Engineering Conference*, 1988, Denver, vol. 2, pp. 47-52.
- Mil 89 T.J.E. Miller, *Brushless permanent-magnet and reluctance motor drives*, Oxford: Clarendon, 1989.
- Mor 94 S. Morimoto, Y. Tong, Y. Takeda, T. Hirasu, 'Loss minimization control of permanent-magnet synchronous motor drives'. In *IEEE Transactions on Industrial Electronics*, vol. 41 (1994), pp. 511-517.
- Mos 72 H. Mosebach, *Effekte der endlichen Länge und Breite bei asynchronen Linearmotoren in Kurzständer- und Kurzläuferbauform*. PhD-thesis Technische Universität Carolo-Wilhelmina, Braunschweig, 1972.
- Mur 83 J.M.D. Murphy, M.G. Egan, 'A comparison of PWM strategies for inverter-fed induction motors'. In *IEEE Transactions on Industry Applications*, vol. 19 (1983), pp. 363-369.
- Off 96 L.J.J. Offringa, R.W.P. Kerkenaar, J.L.F. van der Veen, 'A high-speed 1400 kW permanent-magnet generator with rectifier'. In *Proceedings of the Sixth International Conference on Electrical Machines*, Vigo, 10-12 September 1996, vol. 3, pp. 308-313.
- Oya 91 J. Oyama, T. Higuchi, H. Kotonu, E. Yamada, 'Analysis of a permanent magnet motor with a stainless can in the air gap'. In *Proceedings of the Fourth European Conference on Power Electronics and Applications*, Firenze, September 1991, vol. 3, pp. 440-444.
- Par 29 R.H. Park, 'Two-reaction theory of synchronous machines - Generalized method of analysis, Part I'. In *AIEE Transactions*, vol. 48 (1929), pp. 716-727.
- Pfü 91 H. Pfützner, P. Schönhuber, B. Erbil, G. Harasko, T. Klinger, 'Problems of loss separation for crystalline and consolidated amorphous soft magnetic materials'. In *IEEE Transactions on Magnetics*, vol. 27 (1994), pp. 3426-3432.
- Pol 80 M. Poloujadoff, *The theory of linear induction machinery*. Oxford: Clarendon Press, 1980.
- Pol 96 H. Polinder, M.J. Hoeijmakers, L.J.J. Offringa, W. Deleroi, 'Harmonic analysis of a PM machine with rectifier'. In *Proceedings of the Sixth International Conference on Electrical Machines*, Vigo, 10-12 September 1996, vol. 2, pp. 63-68.
- Pol 97 H. Polinder, M.J. Hoeijmakers, 'Eddy-current losses in the permanent magnets of a PM machine'. In *Proceedings of the Eighth International Conference on Electrical Machines and Drives*, Cambridge, 1-3 September 1997, pp. 138-142.
- Pre 35 F. Preisach, 'Über die magnetische Nachwirkung'. In *Zeitschrift für Physik*, vol. 94 (1935), pp. 277-302.
- Pry 58 R.H. Pry, C.P. Bean, 'Calculation of the energy loss in magnetic sheet materials using a domain model'. In *Journal of Applied Physics*, vol. 29 (1958), pp. 532-533.

- Pul 96 K.R. Pullen, M.R. Etemad, A. Fenocchi, 'The high speed axial flux disc generator - unlocking the potential of the automotive gas turbine' In *Digest of the IEE Colloquium on machines and drives for electric and hybrid vehicles (Digest no. 1996/152)*. London, 28 June 1996, pp. 8/1-4
- Ric 15 R. Richter, 'Über zusätzliche Stromwärme II, Entwurf von Nutzenwicklungen'. In *Archiv für Elektrotechnik*, Vol. 4 (1915), pp. 1-35.
- Ric 67 R. Richter, *Elektrische Maschinen, erster Band*. Third edition. Basel: Birkhäuser, 1967.
- Sch 57 W. Schuisy, *Induktionsmaschinen*. Vienna: Springer, 1957.
- Sch 64 K.K. Schwarz, 'Survey of basic stray losses in squirrel-cage induction motors'. In *Proceedings of the IEE*, vol. 111 (1964), pp. 1565-1574.
- Sch 97 N. Schofield, K. Ng, Z.Q. Zhu, D. Howe, 'Parasitic rotor losses in a brushless permanent magnet traction machine'. In *Proceedings of the Eighth International Conference on Electrical Machines and Drives*, Cambridge, 1-3 September 1997, pp. 200-204.
- Seb 89 T. Sebastian, G.R. Slemon, 'Transient modeling and performance of variable-speed permanent-magnet motors'. In *IEEE Transactions on Industry Applications*, vol. 25 (1989), pp. 101-106.
- Sen 89 P.C. Sen, *Principles of electric machines and power electronics*. New York: Wiley, 1989.
- Sle 90 G.R. Slemon, X. Liu, 'Core losses in permanent-magnet motors'. In *IEEE Transactions on Magnetics*, vol. 26 (1990), pp. 1653-1655.
- Sle 92 G.R. Slemon, *Electric machines and drives*. Reading, Massachusetts: Addison-Wiley, 1992.
- Sou 92 G.C. Sousa, B.K. Bose, J. Cleland, R.J. Spiegel, P.J. Chappell, 'Loss modeling of converter induction machine system for variable speed drive'. In *Proceedings of the 1992 International Conference on Industrial Electronics, Control, Instrumentation and Automation*, vol. 1, pp. 114-120.
- Sto 74 R.L. Stoll, *The analysis of eddy currents*. London: Oxford University Press, 1974.
- Tak 94 I. Takahashi, T. Koganezuwa, G. Su, K. Ohyama, 'A super high speed PM motor drive system by a quasi-current source inverter'. In *IEEE Transactions on Industry Applications*, vol. 30 (1994), pp. 683-690.
- Uda 89 M.R. Udayagiri, T.A. Lipo, 'Simulation of inverter fed induction motors including core losses'. In *IECON '89, Proceedings of the Fifteenth Annual Conference of the IEEE Industrial Electronics Society*, Philadelphia, 6-10 November 1989, pp. 232-236.
- Vai 91 J.G. Vaidya, 'Electrical machines technology for aerospace power generators'. In *Proceedings of the 26th Intersociety Energy Conversion Engineering Conference*, Boston, 4-9 August 1991, pp. 7-12.

- Vee 97 J.L.F. van der Veen, L.J.J. Offringa, A.J.A. Vandenput, 'Minimising rotor losses in high-speed high-power permanent magnet synchronous generators with rectifier load'. In *IEE Proceedings - Electric Power Applications*, vol. 144 (1997), pp. 331-337.
- Ven 82 K. Venkatesan, J.F. Lindsay, 'Comparative study of the losses in voltage and current source inverter fed induction motors'. In *IEEE Transactions on Industry Applications*, vol. 18 (1982), pp. 240-246.
- Wah 91 S. Wahsh, M. El-Bakry, 'Additional core losses in induction machines with PWM inverter'. In *European Transactions on Electrical Power Engineering*, vol. 1 (1991), pp. 189-193.
- Wak 94 E.H. Wakefield, *History of the electric automobile, battery-only electric cars*. Warrendale, PA: Society of Automotive Engineers, 1994.
- Wes 83 A. Weschta, *Entwurf und Eigenschaften permanenterregter Synchron-Servomotoren*. PhD-thesis Universität Erlangen-Nürnberg, 1983.
- Wil 97 S. Williamson, 'Stray losses - a residue of ignorance'. In *Power Engineering Journal*, vol. 11 (1997), p. 3.
- Zhu 92 J.G. Zhu, V.S. Ramsden, P.A. Watterson, 'Finite element calculation of core losses in motors with non-sinusoidal fields'. In *International Conference on Electrical Machines*, Manchester, 15-17 September 1992, pp. 1182-1186.
- Zhu 93a Z.Q. Zhu, D. Howe, E. Bolte, B. Ackermann, 'Instantaneous Magnetic Field distribution in brushless permanent-magnet dc motors, part I: open-circuit field'. In *IEEE Transactions on Magnetics*, vol. 29 (1993), pp. 124-135.
- Zhu 93b Z.Q. Zhu, D. Howe, 'Instantaneous Magnetic Field distribution in brushless permanent-magnet dc motors, part II: armature-reaction field'. In *IEEE Transactions on Magnetics*, vol. 29 (1993), pp. 136-142.
- Zhu 93c Z.Q. Zhu, D. Howe, 'Instantaneous Magnetic Field distribution in brushless permanent-magnet dc motors, part III: effect of stator slotting'. In *IEEE Transactions on Magnetics*, vol. 29 (1993), pp. 143-151.
- Zhu 93d Z.Q. Zhu, D. Howe, 'Instantaneous Magnetic Field distribution in brushless permanent-magnet dc motors, part IV: magnetic field on load'. In *IEEE Transactions on Magnetics*, vol. 29 (1993), pp. 152-158.
- Zhu 93e J.G. Zhu, S.Y.R. Hui, V.S. Ramsden, 'Discrete modelling of magnetic cores including hysteresis, eddy current, and anomalous losses'. In *IEE Proceedings, Part A, Science, Measurement and Technology*, vol. 140 (1993), pp. 317-322.
- Zhu 96 J.G. Zhu, S.Y.R. Hui, V.S. Ramsden, 'A generalized dynamic circuit model of magnetic cores for low- and high-frequency applications - Part I: Theoretical calculation of the equivalent core loss resistance'. In *IEEE Transactions on Power Electronics*, vol. 11 (1996), pp. 246-250.

Appendices

Appendix A Machine parameters

This appendix describes the dimensions and the material properties of the machines used for the measurements and the calculations. Firstly, section A.1 describes the so-called test model. Next, section A.2 gives the nameplate data of the servomotor. Section A.3 describes the Eindhoven machine.

A.1 Parameters of the test model

The test model consists of three parts.

- 1) A three-phase stator with laminated iron (the stator of an induction machine).
- 2) A removable cylindrical rotor with laminated iron without slots.
- 3) A removable copper cylinder in the air gap.

This test model does not have magnets on the rotor, although some figures have been produced assuming magnets on the rotor.

The nameplate data of the three-phase stator are the following.

- | | |
|-----------------------------------------------|---------------------------|
| - rated rotational frequency | $n = 23.5 \text{ s}^{-1}$ |
| - rated power (at $n = 23.5 \text{ s}^{-1}$) | $P = 2.2 \text{ kW}$ |
| - rated stator phase current | $I = 5 \text{ A}$ |
| - rated stator line voltage | $U = 380 \text{ V}$ |

The test model has the following dimensions and properties.

- | | |
|-----------------------------------------------------|---------------------------|
| - total number of turns per phase | $N = 252$ |
| - slot width | $b_{slot} = 8 \text{ mm}$ |
| - stator tooth width | $b_t = 4 \text{ mm}$ |
| - stator yoke height | $h_{sy} = 20 \text{ mm}$ |
| - tooth height | $h_t = 20 \text{ mm}$ |
| - stack length or active length of stator and rotor | $l_s = 110 \text{ mm}$ |
| - number of pole pairs | $p = 2$ |
| - number of slots per pole per phase | $q = 3$ |
| - radius of the stator bore | $r_s = 57.8 \text{ mm}$ |

- chording angle	$\beta_{chord} = 0$
- slot angle	$\beta_{slot} = \pi/18$
- skew angle	$\beta_{skew} = 0$
- slot opening angle	$\beta_{so} = \pi/72$
- rotor radius	$r_r = 50.6 \text{ mm}$
- rotor yoke height	$h_{ry} = 20 \text{ mm}$
- radius of the middle of the damper cylinder	$r_d = 55.0 \text{ mm}$
- thickness of the damper cylinder within the model	$\delta_d = 0.5 \text{ mm}$
- resistivity of the damper cylinder	$\rho_d = 0.0175 \mu\Omega\text{m}$

The damper cylinder is longer than the active length of the stator and the rotor to provide a closing path for the damper currents. The thickness of the damper cylinder within the machine is less than the thickness of the end connections outside to provide closing paths with a small resistance. The end connections have the following dimensions.

- length of the end connections of the damper cylinder	$l_e = 40 \text{ mm}$
- thickness of the end connections of the damper	$\delta_e = 2.0 \text{ mm}$

Other parameters obtained from measurements.

- specific iron loss multiplied by a correction factor	$c_{Fe} k_{Fe,0} = 6 \text{ W/kg}$
- stray loss resistance	$R_{\sigma Fe} = R_{sFe}/3$
- resistance of a stator phase	$R_s = 2.67 \Omega$
- leakage inductance (without air-gap leakage)	$L_{\sigma} = 10 \text{ mH}$

Some calculations are done for this model assuming magnets on the rotor. In this case, the following dimensions and properties of the magnets are assumed.

- permanent magnetization of the sintered NdFeB magnets	$M_{pm} = 796 \text{ kA/m}$
- width of the magnet blocks	$b_m = 10 \text{ mm}$
- magnet length in the direction of the magnetization	$l_m = 4.1 \text{ mm}$
- half of the magnet pole arc angle	$\alpha_m = \pi/5$
- resistivity of the magnets	$\rho_m = 1.3 \mu\Omega\text{m}$

A.2 Parameters of the servomotor

The dimensions and properties of the servomotor were made available for the research, but only on condition that they would not be published. Therefore only the nameplate data are given here. The machine type is Bosch SE-B4 170.050.

- rated torque (at $n = 3.33 \text{ s}^{-1}$)	$M_0 = 14 \text{ Nm}$
- rated current (at $n = 3.33 \text{ s}^{-1}$)	$I_0 = 24 \text{ A}$
- rated rotational frequency	$n = 83.3 \text{ s}^{-1}$

A.3 Parameters of the Eindhoven machine

The Eindhoven machine was designed to meet the following requirements.

- rated rotational frequency $n = 200 \text{ s}^{-1}$
- rated power (at $n = 200 \text{ s}^{-1}$) $P = 80 \text{ kW}$
- rated stator phase current $I = 85 \text{ A}$
- rated line voltage $U = 640 \text{ V}$

The rotor was designed for a rotational frequency of $n = 500 \text{ s}^{-1}$.

The Eindhoven machine has the following dimensions and properties.

- total number of turns per phase $N = 24$
- slot width $b_{slot} = 8 \text{ mm}$
- stator tooth width $b_t = 7 \text{ mm}$
- stator yoke height $h_{sy} = 23 \text{ mm}$
- tooth height $h_t = 20 \text{ mm}$
- stack length or active length of stator and rotor $l_s = 225 \text{ mm}$
- number of pole pairs $p = 2$
- number of slots per pole per phase $q = 3$
- radius of the stator bore $r_s = 75.0 \text{ mm}$
- chording angle $\beta_{chord} = 0$
- slot angle $\beta_{slot} = \pi/18$
- skew angle $\beta_{skew} = 0$
- slot opening width $b_{so} = 2.7 \text{ mm}$
- rotor radius $r_r = 61.0 \text{ mm}$
- rotor yoke height $h_{ry} = 20 \text{ mm}$
- radius of the damper cylinder $r_d = 69.5 \text{ mm}$
- thickness of the damper cylinder within the model $\delta_d = 0.5 \text{ mm}$
- resistivity of the damper cylinder $\rho_d = 0.0175 \mu\Omega\text{m}$
- length of the end connections of the damper $l_e = 5.0 \text{ mm}$
- thickness of the end connections of the damper $\delta_e = 6.0 \text{ mm}$
- permanent magnetization of the sintered NdFeB magnets $M_{pm} = 760 \text{ kA/m}$
- width of the magnet blocks $b_m = 10 \text{ mm}$
- magnet length in the direction of the magnetization $l_m = 8.0 \text{ mm}$
- half of the magnet pole arc angle $\alpha_m = 3\pi/16$
- resistivity of the magnets $\rho_m = 1.3 \mu\Omega\text{m}$

Other estimated parameters which are used in the calculations.

- specific iron loss multiplied by a correction factor $c_{Fe} k_{Fe,0} = 3 \text{ W/kg}$
- stray loss resistance $R_{\sigma Fe} = R_{sFe}/3$
- resistance of a stator phase $R_s = 27 \text{ m}\Omega$
- leakage inductance (without air-gap leakage) $L_{so} = 0.10 \text{ mH}$

Appendix B The number of turns of the space harmonics of a winding

In chapters 2 to 4, the stator winding distribution is used. The numbers of turns of the space harmonics of the winding distribution $N_{s,k}$ follow from the Fourier analysis of the winding distribution. As explained in chapter 2, the number of turns $N_{s,k}$ may be negative for some space harmonics. This appendix describes the relation between a winding and the number of turns of the space harmonics of the winding distribution $N_{s,k}$. In this description, the winding factor is used. Firstly, in section B.1, this winding factor is related to the winding distribution. Next, section B.2 describes the determination of the winding factor of an arbitrary winding.

B.1 The definition of the winding factor

This section starts with an example of a winding. For this example, the numbers of turns of the space harmonics of the winding distribution $N_{s,k}$ are calculated. Next, the winding factor is introduced.

As an example, the numbers of turns of the space harmonics of the winding distribution of a full-pitch winding $N_{s,k}$ in a machine with one slot per pole per phase are calculated. Figure B.1 depicts the full-pitch winding of a two-pole machine. The full-pitch winding has N turns and its axis lays at stator coordinate $\alpha_a = 0$. On the interval $0 < \alpha_s < 2\pi/p$, the winding distribution $n_{sa}(\alpha_s)$ can be written as

$$n_{sa}(\alpha_s) = \begin{cases} \frac{N}{p\beta_{so}} & \text{when } \frac{\pi}{2p} - \frac{\beta_{so}}{2} < \alpha_s < \frac{\pi}{2p} + \frac{\beta_{so}}{2} \\ -\frac{N}{p\beta_{so}} & \text{when } \frac{3\pi}{2p} - \frac{\beta_{so}}{2} < \alpha_s < \frac{3\pi}{2p} + \frac{\beta_{so}}{2} \\ 0 & \text{everywhere else on } 0 < \alpha_s < 2\pi/p \end{cases} \quad (B.1)$$

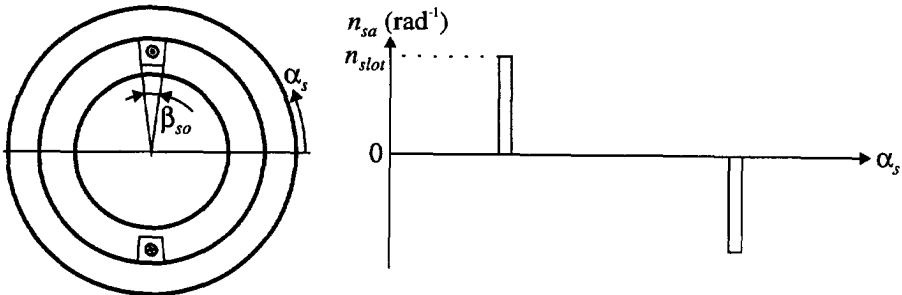


Figure B.1: The winding distribution of a full-pitch winding of a two-pole machine ($p=1$). The winding distribution forms an infinitesimal layer on the stator surface.

where β_{so} is the slot opening angle (in mechanical radians).

The winding distribution $n_{sa}(\alpha_s)$ can also be written as a Fourier series:

$$n_{sa} = \sum_{k=1,3,5,\dots}^{\infty} \frac{1}{2} N_{s,k} \sin(pk\alpha_s) \quad (B.2)$$

where the Fourier coefficients of the winding distribution $\frac{1}{2}N_{s,k}$ are calculated as

$$\frac{1}{2}N_{s,k} = \frac{2p}{2\pi} \int_0^{2\pi/p} n_{sa}(\alpha_s) \sin(pk\alpha_s) d\alpha_s = \frac{2N}{\pi} \sin\left(\frac{1}{2}k\pi\right) \frac{\sin\left(\frac{1}{2}pk\beta_{so}\right)}{\frac{1}{2}pk\beta_{so}} \quad (B.3)$$

For a winding with infinitesimal slot openings, the last part of this equation approaches one, and the Fourier coefficients of the winding distribution $\frac{1}{2}N'_{s,k}$ are given by

$$\frac{1}{2}N'_{s,k} = \frac{2N}{\pi} \sin\left(\frac{1}{2}k\pi\right) \quad (B.4)$$

The winding factor $k_{w,k}$ is introduced as the ratio of $N_{s,k}$ of a real distributed winding to $N'_{s,k}$ of a full-pitch winding in infinitesimal slots. In other books, the winding factor may be introduced in other ways. Slemon [Sle 92] and Miller [Mil 89] introduce the winding factor $k_{w,k}$ as the ratio of the magnetomotive force of the real distributed winding to the magnetomotive force of a full-pitch winding in infinitesimal slots. Richter [Ric 67] introduces the winding factor $k_{w,k}$ as the ratio of the flux linked with the real distributed winding to the flux linked with a full-pitch winding in infinitesimal slots. However, the same winding factor is meant, although it is introduced in different ways.

Using the winding factor $k_{w,k}$, the number of turns of the k th space harmonic of the winding distribution $N_{s,k}$ for a real winding is given by

$$N_{s,k} = k_{w,k} \frac{4N}{\pi} \sin\left(\frac{1}{2}k\pi\right) \quad (B.5)$$

Comparison of this equation with equation (B.3) shows that the winding factor $k_{wslot,k}$ of a full-pitch winding in slots with a real width is given by

$$k_{wslot,k} = \frac{\sin\left(\frac{1}{2}pk\beta_{so}\right)}{\frac{1}{2}pk\beta_{so}} \quad (B.6)$$

Schisky [Sch 57] gives the same expression for the winding factor resulting from slots with a real width.

In the same way, the winding factors of distributed, short-pitched and skewed windings can be derived. This is not done here, because other books describe these derivations extensively. The results are summarized in section B.2.

B.2 Contributions to the winding factor

This section describes the various contributions to the winding factor as a function of the harmonic number k . It is assumed that the machine has an integral-slot winding, which means that the number of slots per pole and phase q is an integer. In this case, the following four contributions to the winding factor $k_{w,k}$ can be distinguished.

- 1) Section B.1 describes how the slot width contributes to the winding factor. This contribution to the winding factor is called the slot factor $k_{wslot,k}$ [Sch 57], and it is given by equation (B.6). Mostly, this slot factor is neglected, because it is nearly equal to one for the important space harmonics.
- 2) Often, a winding is distributed over several slots. The effect of this distribution is considered by the distribution factor or spread factor $k_{wdistribution,k}$ [Sle 92], [Ric 67], [Sch 57], [Böd 62], [Lev 84]. For a three-phase machine, it is given by

$$k_{wdistribution,k} = \frac{\sin(\frac{k\pi}{6})}{q \sin(\frac{k\pi}{6q})} \quad (B.7)$$

- 3) Frequently, windings are short pitched: the winding span is not a whole pole pitch, but, for example, a pole pitch minus a tooth pitch. This effect is considered by the pitch factor or the chording factor $k_{wchord,k}$ [Sle 92], [Ric 67], [Sch 57], [Böd 62], [Lev 84]:

$$k_{wchord,k} = \cos(\frac{1}{2}pk\beta_{chord}) \quad (B.8)$$

where β_{chord} is the chording angle in mechanical radians.

- 4) Sometimes, the rotor and the stator are skewed with respect to each other to reduce higher space harmonics or to reduce cogging torque. In permanent-magnet machines the skew angle is often equal to the slot angle, because in this way the cogging torque is eliminated. The effect of skewing on the Fourier coefficients of the winding distribution is considered by the skew factor $k_{wskew,k}$ [Sch 57], [Lev 84]:

$$k_{wskew,k} = \frac{\sin(\frac{1}{2}pk\beta_{skew})}{\frac{1}{2}pk\beta_{skew}} \quad (B.9)$$

where β_{skew} is the skew angle in mechanical radians.

Often, the skew factor is not considered as a part of the winding factor, because it is not present in the self-inductance of a winding. However, it is present in the mutual inductances between windings which are skewed with respect to each other. It is also present in the no-load voltage of a permanent-magnet machine if the magnets are skewed with respect to the stator.

The winding factor $k_{w,k}$ is the product of the various contributions.

Appendix C The effect of eddy currents on the air-gap field

In chapter 4, the resistances representing the losses in the magnets and the iron are calculated on the assumption that the effect of eddy currents on the air-gap field is negligible. Although this assumption is not always correct, the derived loss resistances are still useful, as is shown in this appendix. This is done for the eddy currents in a laminated core and in the magnets in sections C.1 and C.2 respectively.

For a more elaborate analysis of eddy currents see a book, such as [Sto 74], which is also used in the analysis in this appendix.

C.1 Eddy currents in the iron

In section 4.3, the iron loss is calculated on the assumption that the effect of eddy currents in the iron on the magnetic field in the air gap is negligible. The measurements of subsection 4.3.6 affirm this, but in the measurements of subsection 4.4.5, the effect of eddy currents on the magnetic field is not negligible. This section shows that the effect of eddy currents in laminated iron on the magnetic field in an air gap is negligible for frequencies up to 100 kHz.

In this section, the eddy currents in a laminated core are calculated without neglecting the effect of eddy currents in the laminated core on the magnetic field. An idealized magnetic circuit is used. Firstly, the used assumptions are described. Next, a differential equation for the magnetic field in a lamination core is derived and solved. This solution is used to determine the impedance of an energizing winding. From this conclusions are drawn for the magnetic circuit of an electrical machine.

Assumptions

Figure C.1 is used to explain how the eddy currents in laminated iron are calculated. Figure C.1a depicts the idealized magnetic circuit consisting of an ideal core, a laminated core with length l_{Fe} , and an air gap with length g . That one of the cores is ideal means that the resistivity and magnetic permeability of this core are infinite. The laminations of the laminated core are parallel to the yz -plane. Figure C.1b depicts a cross-section of a lamination.

The derivations in this section are based on the following assumptions.

- All flux remains in the magnetic circuit, leakage flux is negligible.
- In the air gap, the magnetic field only has a component in the y -direction.
- In the air gap, the magnetic field is not a function of x , because of the high magnetic permeability of the cores; the surfaces above and below the air gap are equipotential surfaces.
- End effects are negligible, which means that the laminations can be treated as if they were infinitely long in the y - and the z -direction.

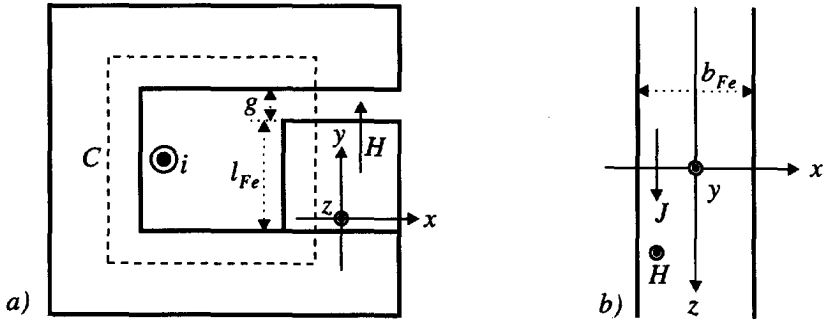


Figure C.1: a) Magnetic circuit consisting of an ideal core, a laminated core with length l_{Fe} and an air gap with length g . b) Cross-section of a lamination.

- The magnetic field in the laminations only has a component in the y -direction. This is not valid at the ends of the laminations, but the end effects are neglected.
- The field varies sinusoidally as a function of time with angular frequency ω .

As a consequence of these assumptions,

- the current density in the laminations only has a component in the z -direction,
- the magnetic field in the laminations is a function of x , and
- the current density in the laminations is a function of x .

The differential equation

A differential equation for the magnetic field strength in the iron is obtained by applying Maxwell's equations to the lamination. In the differential form of the second of Maxwell's equations (equation (3.26)), it is taken that the magnetic flux density only has a y -component and that the electric field strength only has a z -component:

$$\frac{\partial E_z(x)}{\partial x} = \frac{\partial B_{yFe}(x)}{\partial t} \quad (C.1)$$

With $\vec{E} = \rho_{Fe} \vec{J}$ and $\vec{B}_{Fe} = \mu_0 \mu_{rFe} \vec{H}_{Fe}$, this can be written as

$$\frac{\partial J_z(x)}{\partial x} = \frac{\mu_0 \mu_{rFe}}{\rho_{Fe}} \frac{\partial H_{yFe}(x)}{\partial t} \quad (C.2)$$

In the differential form of the first of Maxwell's equations (equation (2.6)), it is taken that the magnetic field strength only has an y -component and that the current density only has a z -component. The result is

$$\frac{\partial H_{yFe}(x)}{\partial x} = J_z(x) \quad (C.3)$$

Differentiating this equation to x and incorporating equation (C.2) results in a differential equation for the magnetic field strength:

$$\frac{\partial^2 H_{yFe}(x)}{\partial x^2} = \frac{\mu_0 \mu_{rFe}}{\rho_{Fe}} \frac{\partial H_{yFe}(x)}{\partial t} \tag{C.4}$$

The magnetic field strength $H_{yFe}(x)$ varies sinusoidally with frequency ω :

$$H_{yFe}(x) = \text{Re}\left\{\hat{H}_{yFe}(x)e^{j\omega t}\right\} \tag{C.5}$$

where $\hat{H}_{yFe}(x)$ is the complex amplitude of the magnetic field strength at position x . For this magnetic field strength, the solution of the differential equation is given by

$$\hat{H}_{yFe}(x) = \hat{H}_{yFe}\left(\frac{1}{2}b_{Fe}\right) \frac{\cosh(\alpha_{Fe} x)}{\cosh\left(\frac{1}{2}\alpha_{Fe} b_{Fe}\right)} \tag{C.6}$$

where $\hat{H}_{yFe}\left(\frac{1}{2}b_{Fe}\right)$ is the complex amplitude of the magnetic field strength at the surface of the plate ($x = \pm \frac{1}{2}b_{Fe}$),

$$\alpha_{Fe} = \frac{1+j}{\delta_{skin,Fe}} \tag{C.7}$$

and $\delta_{skin,Fe}$ is the skin depth of the eddy currents in the laminations, given by

$$\delta_{skin,Fe} = \sqrt{\frac{2\rho_{Fe}}{\mu_0 \mu_{rFe} \omega}} \tag{C.8}$$

The complex amplitude of the average of the magnetic field strength $\hat{H}_{yFe,av}$ is given by

$$\hat{H}_{yFe,av} = \frac{1}{b_{Fe}} \int_{-b_{Fe}/2}^{b_{Fe}/2} \hat{H}_{yFe}(x) dx = \hat{H}_{yFe}\left(\frac{1}{2}b_{Fe}\right) \frac{2}{\alpha_{Fe} b_{Fe}} \frac{\sinh\left(\frac{1}{2}\alpha_{Fe} b_{Fe}\right)}{\cosh\left(\frac{1}{2}\alpha_{Fe} b_{Fe}\right)} \tag{C.9}$$

The problem which remains is to determine the relation between the magnetic field strength and the exciting current i with complex amplitude \hat{i} , see figure C.1a. To determine $\hat{H}_{yFe}\left(\frac{1}{2}b_{Fe}\right)$, the integral form of the first of the Maxwell's equations (equation (2.16)) is applied to the closed path C in figure C.1a. In the laminated core, this closed path is on the surface of a lamination, so the closed path does not enclose eddy currents in the laminations. The result is:

$$l_{Fe} \hat{H}_{yFe}\left(\frac{1}{2}b_{Fe}\right) + g \hat{H}_{yg} = \hat{i} \tag{C.10}$$

where \hat{H}_{yg} is the complex amplitude of the magnetic field strength in the air gap.

The magnetic flux continuity condition prescribes that the magnetic flux flowing through the laminated core also crosses the air gap. It was assumed that the magnetic field in the air gap was not a function of x . Therefore, the magnetic flux density in the air gap is equal to the average of the magnetic flux density in the laminated core:

$$\mu_0 \hat{H}_{yg} = \mu_0 \mu_{rFe} \hat{H}_{yFe,av} \tag{C.11}$$

If this is substituted into equation (C.10), and equation (C.9) is used, the complex

amplitude of the average of the magnetic field strength $\hat{H}_{y_{Fe,av}}$ is solved as

$$\hat{H}_{y_{Fe,av}} = \frac{\hat{I}}{g\mu_{rFe} \left(1 + \frac{l_{Fe}}{g\mu_{rFe}} \frac{\alpha_{Fe} b_{Fe}}{2} \frac{\cosh(\frac{1}{2}\alpha_{Fe} b_{Fe})}{\sinh(\frac{1}{2}\alpha_{Fe} b_{Fe})} \right)} \quad (C.12)$$

The impedance of the energizing winding

The presence of eddy currents in the laminations causes a change in the impedance of the energizing winding. The eddy currents reduce the flux linkage, and they set up ohmic losses. This (frequency-dependent) impedance of the winding is referred to as the reflected impedance, which is given by

$$\underline{Z} = R + j\omega \frac{\Psi}{\hat{I}} = R + R_{Fe} + j\omega L_{Fe} \quad (C.13)$$

where

R is the resistance of the energizing winding,

R_{Fe} is the reflected resistance representing the iron losses, and

L_{Fe} is the reflected inductance, including the effect of eddy currents in the laminations on the flux linkage.

If all flux flows through the laminations and the air gap, the flux linkage Ψ is proportional to the average magnetic field strength of equation (C.12). Therefore,

$$\frac{\Psi}{\hat{I}} = \frac{L}{1 + \frac{l_{Fe}}{g\mu_{rFe}} \frac{\alpha_{Fe} b_{Fe}}{2} \frac{\cosh(\frac{1}{2}\alpha_{Fe} b_{Fe})}{\sinh(\frac{1}{2}\alpha_{Fe} b_{Fe})}} \quad (C.14)$$

where L is a constant with dimension Henry.

The reflected inductance and resistance are depicted in figure C.2. In the calculations for this figure, values have been taken that form an approximation of the values valid for the test model:

- $\rho_{Fe} = 0.3 \mu\Omega\text{m}$,
- $\mu_{rFe} = 5000$,
- $b_{Fe} = 0.5 \text{ mm}$, and
- $l_{Fe}/g = 12$.

Conclusions

From figure C.2, two conclusions can be drawn.

- 1) The effect of eddy currents in the laminated core on the magnetic field in the air gap is visible in the observed frequency range. This may explain small decreases in the measured inductances at high frequencies in subsection 4.3.6. However, for

frequencies up to 100 kHz, the decrease is so small that it is negligible. Therefore, the effect of eddy currents in laminated iron on the magnetic field in the air gap is neglected in this thesis.

- 2) In this section, the eddy current loss in a laminated core excited by a current with a constant amplitude was calculated as a function of the frequency. At low frequencies (up to about 1 kHz), this loss is proportional to ω^2 , and at high frequencies (above about 1 kHz), this loss is proportional to $\omega^{1.5}$. This was already mentioned and used in subsection 4.3.2.

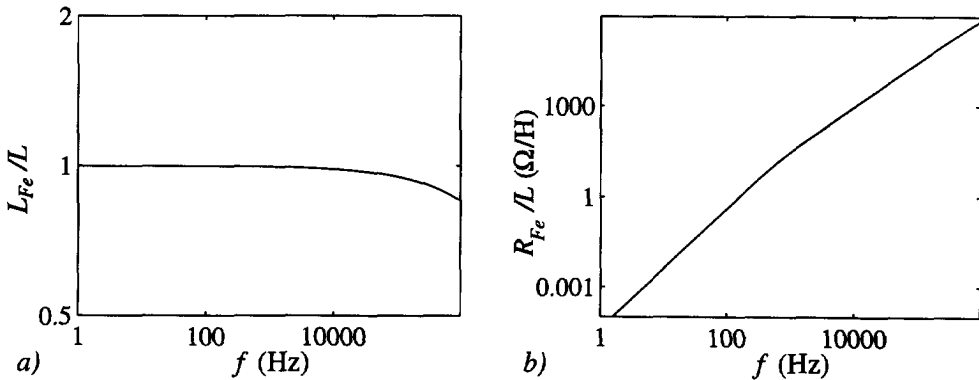


Figure C.2: The reflected inductance a) and resistance b) as a function of the frequency.

C.2 Eddy currents in the magnets

In subsection 4.4.2, a magnet loss resistance has been calculated on the assumption that the effect of eddy currents in the magnets on the magnetic field in the air gap is negligible. However, the measurements of subsection 4.4.5 show that this assumption is not correct at high frequencies. Incorporating the magnet loss resistance in the machine model is an incorrect way of considering the effect of eddy currents on the magnetic field, as explained in subsection 4.4.4. However, this section shows that incorporating the magnet loss resistance in the machine model results in a useful approximation of the eddy current loss in the magnets for frequencies up to 100 kHz.

In this section, the eddy currents in a magnet block are calculated without neglecting the effect of eddy currents in this magnet block on the magnetic field. An idealized magnetic circuit is used. Firstly, the used assumptions are described. Subsequently, a differential equation for the magnetic field in the magnet block is derived and solved. This solution is used to determine the impedance of the energizing winding, which is compared to the impedance calculated using the magnet loss resistance. From this, conclusions are drawn for the magnetic circuit of an electrical machine.

Assumptions

Figure C.3 is used to explain how the eddy currents in the magnet block are calculated. Figure C.3a depicts the idealized magnetic circuit consisting of an ideal core, a magnet block with length l_m , and an air gap with length $g-l_m$. Because the relative magnetic permeability of the magnet is assumed to be one, the effective air gap is g . That the core is ideal means that the resistivity and magnetic permeability of this core are infinite. Figure C.3b depicts a cross-section of the magnet block.

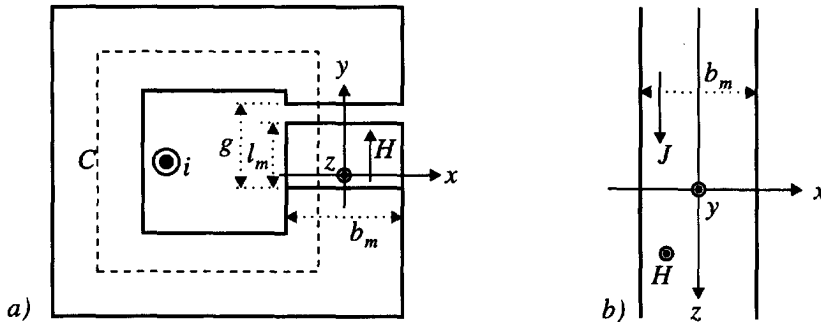


Figure C.3: a) A magnetic circuit consisting of an ideal core, a magnet and an air gap in a rectangular coordinate system. b) A cross-section of the magnet.

The derivations in this section are based on four assumptions.

- All flux remains in the magnetic circuit, leakage flux is negligible.
- The magnetic field in the magnet and the air gap only has a component in the y -direction.
- The magnetic field in the air gap and in the magnet is the same function of x . This is reasonable because of the low magnetic permeability of the magnet.
- The field varies sinusoidally as a function of time with angular frequency ω .
- End effects are negligible, which means that the magnet block is treated as if it were infinitely long in the z -direction.

As a consequence of these assumptions,

- the current density in the magnet only has a component in the z -direction,
- the current density in the magnet block is a function of x , and
- the magnetic flux density in the magnet and in the air gap is a function of x .

Eddy currents are caused by changing magnetic fields. The magnetic field of the magnet is constant, and consequently, it does not cause eddy currents. Therefore, the eddy currents in the magnet can be calculated while the magnetization of the magnet is made zero, which is done in this section.

The differential equation

A differential equation for the magnetic field strength in the iron is obtained by applying Maxwell's equations to the magnet block. In the differential form of the second

of Maxwell's equations (equation (3.26)), it is taken that the magnetic flux density only has an y -component and that the electric field strength only has a z -component:

$$\frac{\partial E_z(x)}{\partial x} = \frac{\partial B_{ym}(x)}{\partial t} \tag{C.15}$$

With $\vec{E} = \rho_m \vec{J}$ and $\vec{B}_m = \mu_0 \vec{H}_m$ (because the magnetization \vec{M} is assumed to be zero), this can be written as

$$\frac{\partial J_z(x)}{\partial x} = \frac{\mu_0}{\rho_m} \frac{\partial H_{ym}(x)}{\partial t} \tag{C.16}$$

Application of the integral form of the first of Maxwell's equations (equation (2.16)) to the dashed closed path C in the magnetic circuit results in

$$(g - l_m)H_{ya}(x) + l_m H_{ym}(x) = i + l_m \int_{-b_m/2}^x J_z(x') dx' \tag{C.17}$$

The magnetic flux continuity condition is valid, which means that the magnetic flux flowing through the magnet, also crosses the air gap. It is assumed that the magnetic flux density in the air gap and the magnetic flux density in the magnets are the same functions of x :

$$\mu_0 H_{ya}(x) = \mu_0 H_{ym}(x) \Rightarrow H_{ya}(x) = H_{ym}(x) \tag{C.18}$$

Incorporating this in equation (C.17) gives

$$gH_{ym}(x) = i + l_m \int_{-b_m/2}^x J_z(x') dx' \tag{C.19}$$

Twice differentiating this equation to x results in

$$\frac{g}{l_m} \frac{\partial^2 H_{ym}(x)}{\partial x^2} = \frac{\partial J_z(x)}{\partial x} \tag{C.20}$$

Using equation (C.16) results in a differential equation for the magnetic field strength:

$$\frac{\partial^2 H_{ym}(x)}{\partial x^2} = \frac{l_m \mu_0}{g \rho_m} \frac{\partial H_{ym}(x)}{\partial t} \tag{C.21}$$

This equation resembles equation (C.4), and the solution has the same form:

$$\hat{H}_{ym}(x) = \hat{H}_{ym}(\frac{1}{2}b_m) \frac{\cosh(\alpha_m x)}{\cosh(\frac{1}{2}\alpha_m b_m)} \tag{C.22}$$

where $\hat{H}_{ym}(\frac{1}{2}b_m)$ is the complex amplitude of the magnetic field strength at the side of the magnet ($x = \pm \frac{1}{2}b_m$),

$$\alpha_m = \frac{1+j}{\delta'_{skin,m}} \quad (C.23)$$

and $\delta'_{skin,m}$ is a corrected skin depth of the eddy currents in the magnet, given by

$$\delta'_{skin,m} = \sqrt{\frac{g}{l_m} \frac{2\rho_m}{\mu_0 \omega}} \quad (C.24)$$

If the air gap is zero ($g=l_m$), the normal formula for the skin depth of a material with a relative magnetic permeability of one is obtained.

A comparable expression for a corrected skin depth is obtained by Lammeraner and Štafl [Lam 66], who calculate the eddy currents in the solid core with air gap of a choke coil.

The complex amplitude of the average of the magnetic field strength is given by

$$\hat{H}_{ym,av} = \frac{1}{b_m} \int_{-b_m/2}^{b_m/2} \hat{H}_{ym}(x) dx = \hat{H}_{ym}(\frac{1}{2}b_m) \frac{2}{\alpha_m b_m} \frac{\sinh(\frac{1}{2}\alpha_m b_m)}{\cosh(\frac{1}{2}\alpha_m b_m)} \quad (C.25)$$

The problem which remains is to determine the relation between the magnetic field strength and the exciting current i with complex amplitude \hat{i} . The magnetic flux density at the side of the magnet follows from equation (C.19) when $x = -\frac{1}{2}b_m$ is used in this equation:

$$\hat{H}_{ym}(\frac{1}{2}b_m) = \frac{\hat{i}}{g} \quad (C.26)$$

Incorporating this in equation (C.25), results in

$$\hat{H}_{ym,av} = \frac{\hat{i}}{g} \frac{2}{\alpha_m b_m} \frac{\sinh(\frac{1}{2}\alpha_m b_m)}{\cosh(\frac{1}{2}\alpha_m b_m)} \quad (C.27)$$

Impedance of the energizing winding

The presence of eddy currents in the magnet causes a change in the impedance of the energizing winding. The eddy currents reduce the flux linkage, and they set up ohmic losses. This change in the impedance of the winding is referred to as the reflected impedance, which is given by

$$\underline{Z} = R + j\omega \frac{\Psi}{\hat{i}} = R + R_m + j\omega L_m \quad (C.28)$$

where

R is the resistance of the energizing winding,

R_m is the reflected resistance representing the eddy current loss in the magnet, and

L_m is the reflected inductance, including the effect of eddy currents in the magnet on

the flux linkage.

If all flux flows through the laminations and the air gap, the flux linkage Ψ is proportional to the average magnetic field strength of equation (C.27). Therefore,

$$\frac{\Psi}{\hat{i}} = \frac{L}{\frac{1}{2}\alpha_m b_m} \frac{\sinh(\frac{1}{2}\alpha_m b_m)}{\cosh(\frac{1}{2}\alpha_m b_m)} \tag{C.29}$$

where L is a constant with dimension Henry.

The reflected inductance and resistance are depicted in figure C.4. In the calculations for this figure, values have been taken that form an approximation of the values valid for the servomotor:

- $\rho_m = 0.5 \mu\Omega\text{m}$,
- $b_m = 5 \text{ mm}$, and
- $g/l_m = 5/3$.

In subsection 4.4.2, a magnet loss resistance was calculated on the assumption that the effect of eddy currents in the magnets on the magnetic field is negligible. In the same way, a magnet loss resistance is calculated for the magnetic circuit of figure C.3a. The resulting reflected resistance and inductance are depicted in figure C.4.

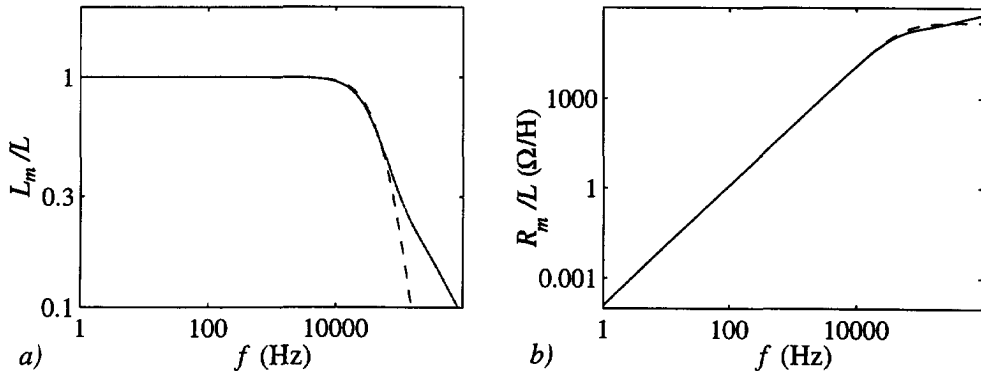


Figure C.4: The reflected inductance a) and resistance b) as a function of the frequency, according to this appendix (—) and to the calculation of section 4.4.2 (- -).

Conclusions

From figure C.4, two conclusions can be drawn.

- 1) As already mentioned in 4.4.5, the effect of eddy currents on the magnetic field in the air gap is not negligible at frequencies above 10 kHz. However, the approximation obtained with the magnet loss resistance of section 4.4.2 remains reasonable for frequencies up to 100 kHz.
- 2) At frequencies up to approximately 20 kHz, the eddy current loss is proportional to ω^2 , at very high frequencies (above approximately 20 kHz) it is proportional to $\sqrt{\omega}$, as already mentioned in subsection 4.4.1.

Appendix D Conformal transformation for a stator slot

D.1 Introduction

This appendix describes the conformal transformation which is used to calculate the amplitude of the pulsation of the magnetic flux density in the air gap because of the stator slotting. Conformal transformations may be useful to calculate magnetic fields like the magnetic field the air gap of a machine with slots, as appears from this appendix and from publications as [Bin 92] and [Len 96]. For a recent and thorough explanation of the use of conformal transformations, see [Bin 92]. In this appendix, the conformal transformation described in [Zhu 93c] is used.

Firstly, section D.2 describes the conformal transformation which is used to calculate the magnetic field under a stator slot. In section D.3, this conformal transformation is used to determine the pulsation of the magnetic flux density caused by the stator slotting.

Assumptions

This appendix is based on the following assumptions.

- The conformal transformation used to calculate the magnetic flux density is based on the idealized single slot model depicted in the z -plane of figure D.1, as in [Wes 83], [Bin 92] and [Zhu 93c]. In this idealized single slot model, it is assumed
 - * that the air gap can be considered linear instead of cylindrical,
 - * that it is sufficient to consider one slot,
 - * that the slot can be considered infinitely deep,
 - * that the slot can be considered rectangular, and
 - * that the magnetic permeability of the iron is infinite.
- The pulsation can be calculated for a machine in which the stator currents are zero.

D.2 The conformal transformation

This section describes the conformal transformation which is used to calculate the magnetic field in the air gap and the slot of a machine with a slotted stator.

Figure D.1 depicts the three planes that are used in the conformal transformation, as is explained further. In the complex z -plane, the idealized slot model is depicted. This figure introduces the points z_1 to z_4 , the distance between the iron surfaces of the stator and the rotor $g = r_s - r_r$, and the width of the slot opening b_{so} .

Because the magnetic permeability of iron is assumed to be infinite, the lines representing the iron surfaces of the stator and the rotor are equipotential lines. The magnetic potentials of the stator at the two sides of the slot are equal because the stator currents are zero. Furthermore, the difference between the magnetic potentials of the

stator and the rotor surfaces because of the magnets is called φ_0 .

The first transformation relates the region of the air gap and the slot in the complex z -plane to the upper half of the complex t -plane. This is done in such a way that the corresponding points in the z -plane and the t -plane are

$$\begin{aligned} z=z_1 &= -b_{so}/2 + jg & \rightarrow & t=t_1 = -a, \\ z=z_2 &= -\infty & \rightarrow & t=t_2 = -1, \\ z=z_3 &= \infty & \rightarrow & t=t_3 = 1, \text{ and} \\ z=z_4 &= b_{so}/2 + jg & \rightarrow & t=t_4 = a. \end{aligned}$$

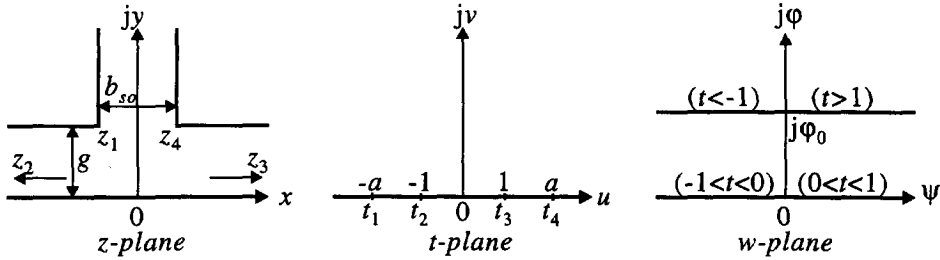


Figure D.1: The three planes used in the conformal transformation.

The points t_1 to t_4 are on the real axis of the t -plane, as depicted in figure D.1. The transformation from the t -plane to the z -plane is given by

$$z = \frac{b_{so}}{\pi} \arcsin\left(\frac{t}{a}\right) + \frac{g}{\pi} \ln \left(\frac{\sqrt{a^2 - t^2} + \frac{2g}{b_{so}} t}{\sqrt{a^2 - t^2} - \frac{2g}{b_{so}} t} \right) \quad (D.1)$$

where a was introduced as

$$a = \sqrt{1 + \left(\frac{2g}{b_{so}}\right)^2} \quad (D.2)$$

In the z -plane, the magnetic potential of the stator surface and the rotor surface is different. Both surfaces are transformed to the real axis of the t -plane. Therefore, the magnetic potential on the real axis of the t -plane is φ_0 between -1 and 1 and zero on the rest.

Next, the upper half of the complex t -plane is transformed to the complex w -plane. In this plane, the field is uniform, which means that the lines $\psi = \text{constant}$ are flux lines, and the lines $\varphi = \text{constant}$ are equipotential lines (figure D.1). The transformation from the t -plane to the w -plane is given by

$$w = \frac{\varphi_0}{\pi} \ln \left(\frac{1+t}{1-t} \right) \quad (D.3)$$

Using the two transformations, the field lines and the equipotential lines in the t -plane

and the z -plane are calculated from the uniform field in the w -plane. The results are depicted in figure D.2. In this figure, a slot pitch of the test model (described in section A.1 of appendix A) is depicted. Although for the test model $b_{so} = 2.5$ mm is valid, in this figure, $b_{so} = 5$ mm is used to obtain clearly visible effects.

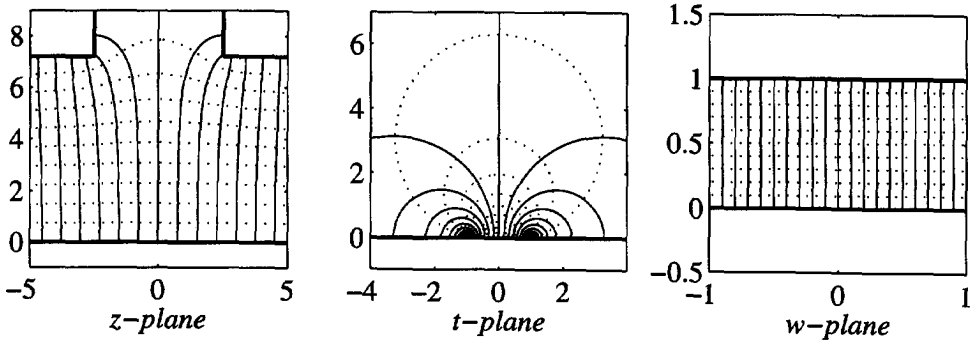


Figure D.2: The field lines (—) and the equipotential lines (..) in the three planes.

D.3 The pulsation of the magnetic flux density

In this section, the pulsation of the magnetic flux density because of the stator slotting is calculated from the conformal transformation described in the previous section.

As far as is known, it is not possible to use the described conformal transformation to calculate the magnetic flux density as an explicit function of z . However, it is possible to calculate the magnitude of the magnetic flux density as a function of t . This is sufficient to obtain a reasonable approximation of the pulsation of the magnetic flux density with simple calculations. The magnitude of the magnetic flux density is calculated as ([Bin 92], [Zhu 93c])

$$|B| = \mu_0 |H| = \mu_0 \left| \frac{dw}{dz} \right| = \mu_0 \left| \frac{dw}{dt} \frac{1}{\frac{dz}{dt}} \right| \quad (D.4)$$

Using equations (D.1) and (D.3), this can be worked out to

$$|B| = \mu_0 \frac{2\phi_0}{\pi(1-t^2)} \frac{1}{\frac{b_{so}}{\pi} \frac{\sqrt{a^2-t^2}}{1-t^2}} = B_0 \frac{1}{\sqrt{1 + \left(\frac{b_{so}}{2g}\right)^2 (1-t^2)}} \quad (D.5)$$

where B_0 was introduced as

$$B_0 = \frac{\mu_0 \phi_0}{g} \quad (D.6)$$

B_0 is the magnetic flux density far from the stator slot in the air gap ($z = \pm \infty$). This can be seen by substituting $t = \pm 1$ in equation (D.1), which results in $z = \pm \infty$, and in equation (D.5), which results in $|B| = B_0$. Two substitutions are necessary because both z and $|B|$ are written as function of t .

Figure D.3a depicts the magnitude of the magnetic flux density as a function of x for different values of y in the air gap. From this figure, two conclusions can be drawn.

- 1) The assumption that the calculation can be based on a single slot model is questionable, because at the axis of a tooth ($x = \pm 5$ mm), the magnetic flux density is still different from B_0 .
- 2) In chapters 2 and 3, the magnetic field in the air gap was calculated on the assumption that the stator surface was smooth: the stator slotting was neglected. According to figure D.3a, the average magnetic flux density at the rotor surface is about $0.99B_0$. (This means that the Carter factor k_C [Ric 67] is about 1.01.) Therefore, the error in the average magnetic flux density made by neglecting the stator slots is about 1 %, which is indeed negligible.

The minimum of the magnetic flux density B_{min} depends on y , and lays at the axis of a stator slot, which coincides with the imaginary axis of the complex z -plane. By means of the transformation given by equation (D.1), the imaginary axis of the z -plane is transformed to the imaginary axis in the t -plane. This is seen from the fact that z is purely imaginary when $t = j\nu$ is substituted in equation (D.1). Herewith, y is calculated as

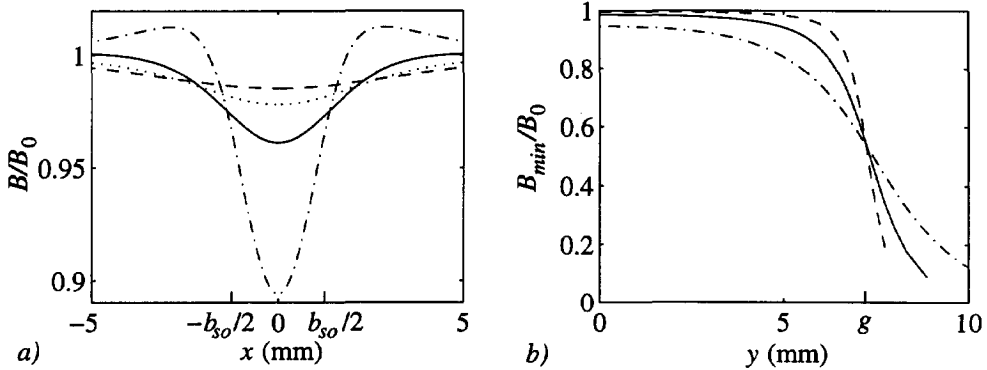


Figure D.3: The magnetic flux density in the air gap of the test model ($g=7.2$ mm)
 a) as a function of the stator coordinate over one slot pitch at different radii
 (- -: $y=0$, \cdots : $y=0.4g$, —: $y=0.6g$, - · -: $y=0.8g$) if $b_{so}=2.5$ mm, and
 b) as a function of the radius at the axis of the slot for different slot openings
 (- · -: $b_{so}=1.25$ mm, —: $b_{so}=2.5$ mm, \cdots : $b_{so}=5$ mm).

$$y = \frac{1}{j} \left(\frac{b_{so}}{\pi} \arcsin\left(\frac{jv}{a}\right) + \frac{g}{\pi} \ln \left(\frac{\sqrt{a^2+v^2} + \frac{2g}{b_{so}} jv}{\sqrt{a^2+v^2} - \frac{2g}{b_{so}} jv} \right) \right) \quad (D.7)$$

The minimum of the magnetic flux density B_{min} is obtained by substituting $t=jv$ into equation (D.5):

$$B_{min} = B_0 \frac{1}{\sqrt{1 + \left(\frac{b_{so}}{2g}\right)^2 (1+v^2)}} \quad (D.8)$$

In this equation, the minimum of the magnetic flux density B_{min} is not written as a function of y , but as a function of v . As far as is known, it is not possible to write v as an explicit function of y by solving v from equation (D.7). Therefore, equation (D.7) is used to iterate to the value for v which agrees with the damper radius $y=r_d-r_r$. Substitution of this value of v in equation (D.8) results in the value for B_{min} at the damper radius.

Figure D.3b depicts this magnetic flux density as a function of y for different values of the slot opening b_{so} . From this figure, it is concluded that to obtain a small pulsation of the magnetic flux density in the damper cylinder, the slot opening b_{so} should be small, and the distance between the stator and the damper cylinder should be large.

In subsection 4.5.2, it is assumed that the described conformal transformation can be used to calculate the pulsation of the magnetic flux density caused by the stator slotting in the following way. The radial component of the magnetic flux density at the damper radius of a machine with a slotted stator $B_{r,slotted}(r_d, \alpha_s, t)$ can be calculated from the radial component of the magnetic flux density at the damper radius of a machine without stator slots $B_{r,smooth}(r_d, \alpha_s, t)$ as

$$B_{r,slotted}(r_d, \alpha_s, t) = B_{r,smooth}(r_d, \alpha_s, t) \left(\frac{1}{k_C} + \gamma(r_d) \cos(6pq\alpha_s) \right) \quad (D.9)$$

This equation is based on the following assumptions and starting-points.

- 1) It is assumed that the pulsation caused by the stator slotting is a sinusoidal function of the stator coordinate with a wave length equal to the slot pitch.
- 2) It is taken that $\alpha_s=0$ coincides with the axis of a stator tooth.
- 3) It is taken that $6pq$ is the number of stator slots.
- 4) It is assumed that the factor $\gamma(r_d)$ follows from the described conformal transformation with equation (D.8) as

$$\gamma(r_d) = \frac{1}{2} \left(1 - \frac{B_{min}}{B_0} \right) = \frac{1}{2} \left(1 - \frac{1}{\sqrt{1 + \left(\frac{b_{so}}{2g} \right)^2 (1 + \nu^2)}} \right) \quad (D.10)$$

- 5) The Carter factor k_C describes the average reduction of the magnetic flux density due to the stator slotting. In the rest of this thesis, it is assumed to be one, because the difference from one is negligible.

In figure D.3a, it can be seen that some of these assumptions are questionable, mainly when the damper cylinder is close to the stator surface.

Appendix E Derivation of equation (5.46)

This appendix describes the derivation of equation (5.46) from equation (5.43).

Substituting the Fourier series for the internal voltages, the currents, and the functions p and h (equations (5.8), (5.6), (5.15), and (5.44)) in equation (5.43) results in

$$\begin{aligned}
 & \frac{1}{2} \sum_{n=-\infty}^{\infty} \left(j(6n+1)\omega_1 \hat{L}_{s,6n+1} e^{j(6n+1)\omega_1 t} - j(6n+1)\omega_1 \hat{L}_{s,6n+1}^* e^{-j(6n+1)\omega_1 t} \right) \\
 &= \frac{1}{4L_1} \sum_{n=-\infty}^{\infty} \left(\hat{L}_{s,6n+1} \left(e^{-j\frac{4}{3}\pi} - 1 \right) e^{j(6n+1)\omega_1 t} + \hat{L}_{s,6n+1}^* \left(e^{j\frac{4}{3}\pi} - 1 \right) e^{-j(6n+1)\omega_1 t} \right) \sum_{n=-\infty}^{\infty} \hat{p}_n (1 + e^{jn\pi}) e^{jn\omega_1 t} \\
 & - \frac{3}{4L_2} \sum_{n=-\infty}^{\infty} \left(\hat{L}_{s,6n+1} e^{j(6n+1)\omega_1 t} + \hat{L}_{s,6n+1}^* \left(e^{j\frac{2}{3}\pi} - 1 \right) e^{-j(6n+1)\omega_1 t} \right) \sum_{n=-\infty}^{\infty} \hat{p}_n (1 + e^{jn\pi}) e^{jn\omega_1 t} \\
 & + \frac{R_{dc}}{4L_2} \sum_{n=-\infty}^{\infty} \left(\hat{L}_{s,6n+1} e^{-j\frac{2}{3}\pi} e^{j(6n+1)\omega_1 t} + \hat{L}_{s,6n+1}^* e^{j\frac{2}{3}\pi} e^{-j(6n+1)\omega_1 t} \right) \sum_{n=-\infty}^{\infty} \hat{p}_n (1 + e^{jn\pi}) e^{jn\omega_1 t} \\
 & + \frac{1}{4L_3} \sum_{n=-\infty}^{\infty} \left(\hat{L}_{s,6n+1} \left(e^{-j\frac{2}{3}\pi} - 1 \right) e^{j(6n+1)\omega_1 t} + \hat{L}_{s,6n+1}^* \left(e^{j\frac{2}{3}\pi} - 1 \right) e^{-j(6n+1)\omega_1 t} \right) \sum_{n=-\infty}^{\infty} \hat{h}_n (1 + e^{jn\pi}) e^{jn\omega_1 t} \\
 & + \frac{R_{dc}}{4L_3} \sum_{n=-\infty}^{\infty} \left(\hat{L}_{s,6n+1} e^{-j\frac{2}{3}\pi} e^{j(6n+1)\omega_1 t} + \hat{L}_{s,6n+1}^* e^{j\frac{2}{3}\pi} e^{-j(6n+1)\omega_1 t} \right) \sum_{n=-\infty}^{\infty} \hat{h}_n (1 + e^{jn\pi}) e^{jn\omega_1 t} \\
 & - \frac{3}{4L_2} \sum_{n=-\infty}^{\infty} \left(\hat{L}_{s,6n+1} e^{j(6n+1)\omega_1 t} + \hat{L}_{s,6n+1}^* e^{-j(6n+1)\omega_1 t} \right) \sum_{n=-\infty}^{\infty} \hat{p}_n e^{-jn\frac{1}{3}\pi} (1 + e^{jn\pi}) e^{jn\omega_1 t} \\
 & - \frac{R_{dc}}{2L_2} \sum_{n=-\infty}^{\infty} \left(\hat{L}_{s,6n+1} e^{j(6n+1)\omega_1 t} + \hat{L}_{s,6n+1}^* e^{-j(6n+1)\omega_1 t} \right) \sum_{n=-\infty}^{\infty} \hat{p}_n e^{-jn\frac{1}{3}\pi} (1 + e^{jn\pi}) e^{jn\omega_1 t} \\
 & + \frac{1}{4L_3} \sum_{n=-\infty}^{\infty} \left(\hat{L}_{s,6n+1} \left(e^{-j\frac{4}{3}\pi} - 1 \right) e^{j(6n+1)\omega_1 t} + \hat{L}_{s,6n+1}^* \left(e^{j\frac{4}{3}\pi} - 1 \right) e^{-j(6n+1)\omega_1 t} \right) \sum_{n=-\infty}^{\infty} \hat{h}_n e^{-jn\frac{1}{3}\pi} (1 + e^{jn\pi}) e^{jn\omega_1 t} \\
 & - \frac{R_{dc}}{4L_3} \sum_{n=-\infty}^{\infty} \left(\hat{L}_{s,6n+1} e^{j(6n+1)\omega_1 t} + \hat{L}_{s,6n+1}^* e^{-j(6n+1)\omega_1 t} \right) \sum_{n=-\infty}^{\infty} \hat{h}_n e^{-jn\frac{1}{3}\pi} (1 + e^{jn\pi}) e^{jn\omega_1 t} \\
 & + \frac{1}{4L_1} \sum_{n=-\infty}^{\infty} \left(\hat{L}_{s,6n+1} \left(e^{-j\frac{2}{3}\pi} - 1 \right) e^{j(6n+1)\omega_1 t} + \hat{L}_{s,6n+1}^* \left(e^{j\frac{2}{3}\pi} - 1 \right) e^{-j(6n+1)\omega_1 t} \right) \sum_{n=-\infty}^{\infty} \hat{p}_n e^{-jn\frac{2}{3}\pi} (1 + e^{jn\pi}) e^{jn\omega_1 t} \\
 & - \frac{3}{4L_2} \sum_{n=-\infty}^{\infty} \left(\hat{L}_{s,6n+1} e^{j(6n+1)\omega_1 t} + \hat{L}_{s,6n+1}^* e^{-j(6n+1)\omega_1 t} \right) \sum_{n=-\infty}^{\infty} \hat{p}_n e^{-jn\frac{2}{3}\pi} (1 + e^{jn\pi}) e^{jn\omega_1 t} \\
 & + \frac{R_{dc}}{4L_2} \sum_{n=-\infty}^{\infty} \left(\hat{L}_{s,6n+1} e^{-j\frac{4}{3}\pi} e^{j(6n+1)\omega_1 t} + \hat{L}_{s,6n+1}^* e^{j\frac{4}{3}\pi} e^{-j(6n+1)\omega_1 t} \right) \sum_{n=-\infty}^{\infty} \hat{p}_n e^{-jn\frac{2}{3}\pi} (1 + e^{jn\pi}) e^{jn\omega_1 t} \\
 & + \frac{U_b}{2} \sum_{n=-\infty}^{\infty} \left(\frac{\hat{p}_n (1 + 2e^{-jn\frac{1}{3}\pi} + e^{-jn\frac{2}{3}\pi})}{L_2} + \frac{\hat{h}_n (1 + e^{-jn\frac{1}{3}\pi})}{L_3} \right) (1 - e^{jn\pi}) e^{jn\omega_1 t}
 \end{aligned} \tag{E.1}$$

Working out the multiplications of the series on the right side of this equation gives

$$\begin{aligned}
 & \sum_{n=-\infty}^{\infty} \left(j(6n+1)\omega_1 \hat{L}_{s,6n+1} e^{j(6n+1)\omega_1 t} - j(6n+1)\omega_1 \hat{L}_{s,6n+1}^* e^{-j(6n+1)\omega_1 t} \right) \\
 &= \sum_{k=-\infty}^{\infty} e^{jk\omega_1 t} \left\{ U_b(1 - e^{jk\pi}) \left(\frac{\hat{P}_k}{L_2} \left(1 + 2e^{-jk\frac{1}{3}\pi} + e^{-jk\frac{2}{3}\pi} \right) + \frac{\hat{H}_k}{L_3} \left(1 + e^{-jk\frac{1}{3}\pi} \right) \right) \right. \\
 &+ \frac{1}{2} \sum_{m=-\infty}^{\infty} \left\{ (1 + e^{j(k-6m-1)\pi}) \hat{L}_{s,6m+1} \left(\frac{\hat{P}_{k-6m-1}}{L_1} \left(e^{-j\frac{4}{3}\pi} - 1 + (e^{-j\frac{2}{3}\pi} - 1) e^{-j(k-6m-1)\frac{2}{3}\pi} \right) \right. \right. \\
 &\quad \left. \left. - \frac{3\hat{P}_{k-6m-1}}{L_2} \left(1 + e^{-j(k-6m-1)\frac{1}{3}\pi} + e^{-j(k-6m-1)\frac{2}{3}\pi} \right) + \frac{\hat{H}_{k-6m-1}}{L_3} \left(e^{-j\frac{2}{3}\pi} - 1 + (e^{-j\frac{4}{3}\pi} - 1) e^{-j(k-6m-1)\frac{1}{3}\pi} \right) \right) \right\} \\
 &+ (1 + e^{j(k+6m+1)\pi}) \hat{L}_{s,6m+1}^* \left(\frac{\hat{P}_{k+6m+1}}{L_1} \left(e^{j\frac{4}{3}\pi} - 1 + (e^{j\frac{2}{3}\pi} - 1) e^{-j(k+6m+1)\frac{2}{3}\pi} \right) \right. \\
 &\quad \left. - \frac{3\hat{P}_{k+6m+1}}{L_2} \left(1 + e^{-j(k+6m+1)\frac{1}{3}\pi} + e^{-j(k+6m+1)\frac{2}{3}\pi} \right) + \frac{\hat{H}_{k+6m+1}}{L_3} \left(e^{j\frac{2}{3}\pi} - 1 + (e^{j\frac{4}{3}\pi} - 1) e^{-j(k+6m+1)\frac{1}{3}\pi} \right) \right) \Bigg\} \quad (E.2) \\
 &+ R_{dc} (1 + e^{j(k-6m-1)\pi}) \hat{L}_{s,6m+1} \left(\frac{\hat{P}_{k-6m-1}}{L_2} \left(e^{-j\frac{2}{3}\pi} - 2e^{-j(k-6m-1)\frac{1}{3}\pi} + e^{-j\frac{4}{3}\pi} e^{-j(k-6m-1)\frac{2}{3}\pi} \right) \right. \\
 &\quad \left. + \frac{\hat{H}_{k-6m-1}}{L_3} \left(e^{-j\frac{2}{3}\pi} - e^{-j(k-6m-1)\frac{1}{3}\pi} \right) \right) \\
 &+ R_{dc} (1 + e^{j(k+6m+1)\pi}) \hat{L}_{s,6m+1}^* \left(\frac{\hat{P}_{k+6m+1}}{L_2} \left(e^{j\frac{2}{3}\pi} - 2e^{-j(k+6m+1)\frac{1}{3}\pi} + e^{j\frac{4}{3}\pi} e^{-j(k+6m+1)\frac{2}{3}\pi} \right) \right. \\
 &\quad \left. + \frac{\hat{H}_{k+6m+1}}{L_3} \left(e^{j\frac{2}{3}\pi} - e^{-j(k+6m+1)\frac{1}{3}\pi} \right) \right) \Bigg\}
 \end{aligned}$$

As expected, when the right side of this equation is worked out, the harmonics of which the harmonic number is an integer multiple of 2 or 3 appear to be zero.

By substituting $k=6n+1$ on the right side of this equation, an equation for a series of Fourier coefficients is obtained:

$$\begin{aligned}
 j(6n+1)\omega \hat{l}_{s,6n+1} &= U_b \left(\hat{p}_{6n+1} \frac{6}{L_2} e^{-j\frac{1}{3}\pi} + \hat{h}_{6n+1} \frac{2}{L_3} (1 + e^{-j\frac{1}{3}\pi}) \right) \\
 &- \sum_{m=-\infty}^{\infty} \left\{ \hat{e}_{s,6m+1} \left(\hat{p}_{6(n-m)} \left(\frac{3}{L_1} + \frac{9}{L_2} \right) + \hat{h}_{6(n-m)} \frac{3}{L_3} \right) \right. \\
 &\quad + \hat{e}_{s,6m+1}^* \left(\hat{p}_{6(n+m)+2} \frac{3}{L_1} e^{j\frac{1}{3}\pi} + \hat{h}_{6(n+m)+2} \frac{3}{L_3} e^{-j\frac{1}{3}\pi} \right) \\
 &\quad + R_{dc} \hat{l}_{s,6m+1} \left(\hat{p}_{6(n-m)} \frac{3}{L_2} + \hat{h}_{6(n-m)} \frac{1}{L_3} (1 - e^{-j\frac{2}{3}\pi}) \right) \\
 &\quad \left. - R_{dc} \hat{l}_{s,6m+1}^* \left(\hat{p}_{6(n+m)+2} \frac{3}{L_2} e^{j\frac{1}{3}\pi} + \hat{h}_{6(n+m)+2} \frac{j\sqrt{3}}{L_3} \right) \right\} \quad (E.3)
 \end{aligned}$$

By substituting $k = -(6n+1)$ into the right side of equation (E.2), an expression for another series of Fourier coefficients is obtained. The resulting expression is the complex conjugate of equation (E.3). Therefore, this expression does not contain extra information and is omitted.

The Fourier coefficients of the internal voltage in equation (E.3) are substituted by equation (5.9). The result can be worked out to

$$\begin{aligned}
 j(6n+1)\omega \hat{l}_{s,6n+1} &+ \sum_{m=-\infty}^{\infty} \left\{ \hat{l}_{s,6m+1} \left(3\hat{p}_{6(n-m)} \left(\frac{Z_{i,6m+1}}{L_1} + \frac{3Z_{i,6m+1} + R_{dc}}{L_2} \right) + \hat{h}_{6(n-m)} \frac{3Z_{i,6m+1} + R_{dc} (1 - e^{-j\frac{2}{3}\pi})}{L_3} \right) \right. \\
 &\quad \left. + \hat{l}_{s,6m+1}^* \left(3\hat{p}_{6(n+m)+2} \left(\frac{Z_{i,6m+1}^* - R_{dc}}{L_1} \right) e^{j\frac{1}{3}\pi} + \hat{h}_{6(n+m)+2} \frac{3Z_{i,6m+1}^* e^{-j\frac{1}{3}\pi} - j\sqrt{3}R_{dc}}{L_3} \right) \right\} \quad (E.4) \\
 &= 2U_b \left(\hat{p}_{6n+1} \frac{3}{L_2} e^{-j\frac{1}{3}\pi} + \hat{h}_{6n+1} \frac{1}{L_3} (1 + e^{-j\frac{1}{3}\pi}) \right) \\
 &\quad - 3 \sum_{m=-\infty}^{\infty} \left\{ \hat{e}_{p,6m+1} \left(\hat{p}_{6(n-m)} \left(\frac{1}{L_1} + \frac{3}{L_2} \right) + \hat{h}_{6(n-m)} \frac{1}{L_3} \right) \right. \\
 &\quad \left. + \hat{e}_{p,6m+1}^* \left(\hat{p}_{6(n+m)+2} \frac{1}{L_1} e^{j\frac{1}{3}\pi} + \hat{h}_{6(n+m)+2} \frac{1}{L_3} e^{-j\frac{1}{3}\pi} \right) \right\}
 \end{aligned}$$

This is the equation that had to be derived, equation (5.46).

Summary

Objective

This thesis deals with the losses in a high-speed permanent-magnet generator with cylindrical rotor and surface-mounted magnets. The generator is loaded with a six-pulse controlled bridge rectifier. Such a generator system may be used in series-hybrid vehicles, aeroplanes, vessels, mobile ground power stations, total energy units, and expanders which recover power from the expansion of compressed natural gas.

The objective of the research is to derive a machine model suitable for optimizing the machine design. The model is mainly intended to minimize the rotor losses. This is important, because high rotor losses heat the rotor, which may result in demagnetization of the magnets.

A way of decreasing the rotor losses may be the use of a damper cylinder. Such a damper cylinder introduces damper loss, but it shields the rest of the rotor, avoiding excessive eddy-current loss in the rotor iron and the magnets. Another way of decreasing the rotor losses is the use of small permanent-magnet blocks. Both methods are explored.

Modelling of the rectifier-loaded generator and model verification

The derivation of the machine model is based on the two-dimensional calculation of the magnetic field in the air gap and the magnets. Space harmonics of the magnetic field are considered, because they contribute significantly to the rotor losses.

The model has five characteristics making it suitable to optimize the machine design.

- 1) The model is analytic.
- 2) Its parameters are calculated from the machine dimensions and material properties.
- 3) It can be used for a machine with and without a damper cylinder.
- 4) It includes the most important electromagnetic losses, namely the stator copper loss, the iron loss, the eddy-current loss in the magnets, and the loss due to the stator slotting. It also includes the damper loss if a damper cylinder is present.
- 5) The eddy-current loss in the magnets is modelled as a function of the width of the magnet blocks.

The model of the permanent-magnet generator is combined with a model of the controlled rectifier. The resulting equations are solved in the frequency domain to determine the steady-state performance of the permanent-magnet machine loaded with a controlled rectifier.

Locked-rotor tests verify the voltage equations of the machine with a damper cylinder, the model for the iron loss, and the model for the eddy-current loss in the magnets for the fundamental space harmonic. For the higher space harmonics, these models are neither verified nor refuted by the locked-rotor tests. Measurements of voltage and current waveforms of the rectifier-loaded generator during normal steady-state operation verify the complete model of the machine with rectifier.

On the generator design

The derived model of the permanent-magnet machine has been used to investigate some design aspects of permanent-magnet machines. From these investigations, the following conclusions can be drawn.

In contrast to what is said about rectifier-loaded synchronous machines, in a rectifier-loaded permanent-magnet machine, a damper is generally neither necessary for obtaining a sufficiently small angle of overlap, nor effective in reducing the reactive power.

In a machine with laminated rotor iron, the effect of a damper cylinder on the rotor losses depends on the rotational frequency. At very high rotational frequencies, the addition of a damper cylinder results in a decrease of the rotor losses, while at lower rotational frequencies, it results in an increase of the rotor losses. Therefore, the decision whether to use a damper cylinder or not should be based on careful calculations. In a machine with solid rotor iron, the addition of a damper cylinder generally results in a decrease of the rotor losses.

In a machine with laminated rotor iron and without a damper cylinder, the greater part of the rotor losses is eddy-current loss in the magnets. In this case, decreasing the magnet width is a very effective means of decreasing the rotor losses, because the eddy-current loss in the magnets is mainly proportional to the square of the magnet width.

In a machine with a damper cylinder, the rotor core loss and the eddy-current loss in the magnets are negligible compared to the damper loss: the damper cylinder shields the rest of the rotor. If skin effect in the damper cylinder is negligible, the rotor losses are roughly inversely proportional to the thickness of the damper cylinder. The damper loss becomes excessive when the distance between the stator surface and the damper becomes too small.

In conclusion

The model of the permanent-magnet machine derived in this thesis is suitable for the optimization of the design of a permanent-magnet machine with rectifier load and for the investigation of the effect of a damper cylinder. The additional value of this model is that it combines the calculation of voltage and current waveforms of a rectifier-loaded machine with a machine model based on the two-dimensional calculation of the magnetic field including the most important electromagnetic losses.

Samenvatting

Doelstelling

Dit proefschrift gaat over de verliezen in een sneldraaiende permanente-magneetgenerator met een cilindrische rotor en magneten in de luchtspleet. De generator is belast met een stuurbare zespulsige bruggelijkrichter. Zo'n generatorsysteem kan gebruikt worden in serie hybride voertuigen, vliegtuigen, schepen, aggregaten, warmte-kracht gekoppelde installaties en turbines die energie terugwinnen uit de expansie van gecomprimeerd gas.

Het doel van het onderzoek is het afleiden van een machinemodel dat gebruikt kan worden om het machineontwerp te optimaliseren. Het model is vooral bedoeld om de rotorverliezen te minimaliseren. Dit is belangrijk omdat hoge rotorverliezen de rotor verhitten, wat tot demagnetisatie van de magneten kan leiden.

Een methode om de rotorverliezen te reduceren is het gebruik van een dempercilinder. Zo'n demper cilinder introduceert demperv verliezen, maar hij schermt de rest van de rotor af, zodat grote wervelstroomverliezen in het rotorijzer en de magneten vermeden worden. Een andere methode om de rotorverliezen te verkleinen is het gebruik van kleine magneetblokjes. Beide methoden worden onderzocht.

Modelvorming van de generator met gelijkrichter en modelverificatie

De afleiding van het machinemodel is gebaseerd op de twee-dimensionale berekening van het magnetisch veld in de luchtspleet en de magneten. Hierin worden ruimtelijke harmonischen van het magnetisch veld meegenomen omdat hun bijdrage aan de rotorverliezen belangrijk is.

Het machinemodel heeft vijf eigenschappen die het geschikt maken om het machineontwerp te optimaliseren.

- 1) Het model is analytisch.
- 2) De parameters van het model worden berekend uit de afmetingen en de materiaaleigenschappen van de machine.
- 3) Het kan gebruikt worden voor een machine met en zonder dempercilinder.
- 4) Het omvat de belangrijkste elektromagnetische verliezen, namelijk de koperverliezen in de stator, de ijzerverliezen, de wervelstroomverliezen in de magneten en de verliezen ten gevolge van de statorgroeven. Het omvat ook de demperv verliezen als een dempercilinder gebruikt wordt.

5) De wervelstroomverliezen in de magneten worden berekend als functie van de breedte van de magneetblokjes.

Het afgeleide model van de permanente-magneet generator wordt gecombineerd met een model van de stuurbare zespulsige bruggelijkrichter. De resulterende vergelijkingen worden opgelost in het frequentiedomein om het gedrag van de permanente-magneet generator met gelijkrichter te bepalen.

Kortsluitproeven met geblokkeerde rotor verifiëren de spanningsvergelijkingen van de machine met dempercilinder, het model voor de ijzerverliezen en het model voor de wervelstroomverliezen in de magneten voor de ruimtelijke grondharmonische. Voor de ruimtelijke hogere harmonischen zijn de modellen geverifieerd noch gevaliseerd. Metingen van spannings- en stroomvormen van de generator met gelijkrichter in normaal bedrijf verifiëren het complete model van machine met gelijkrichter.

Het ontwerp van de generator

Het afgeleide model van de permanente-magneetmachine is gebruikt om enkele belangrijke ontwerpaspecten van permanente-magneetmachines te onderzoeken. Hieruit kunnen de volgende conclusies getrokken worden.

In tegenstelling tot wat beweerd wordt over synchrone machines met gelijkrichter, is een demper in een permanente-magneetmachine met gelijkrichter niet nodig om een voldoende kleine commutatiehoek te krijgen, noch effectief om het reactieve vermogen te reduceren.

In een machine met gelamineerd rotorijzer hangt het effect van een dempercilinder op de verliezen af van het toerental. Bij zeer hoge toerentallen leidt het toevoegen van een dempercilinder tot een reductie van de rotorverliezen, terwijl bij lagere toerentallen het toevoegen van een dempercilinder leidt tot een toename van de rotorverliezen. Daarom moet de beslissing over het gebruik van een dempercilinder gebaseerd worden op zorgvuldige berekeningen. In een machine met massief rotorijzer leidt het toepassen van een dempercilinder over het algemeen tot een reductie van de rotorverliezen.

In een machine met gelamineerd rotorijzer en zonder dempercilinder is het grootste deel van de rotorverliezen wervelstroomverlies in de magneten. In dit geval is het verkleinen van de breedte van de magneetblokjes een zeer effectief middel om de rotorverliezen te reduceren omdat het wervelstroomverlies in de magneten ruwweg evenredig is met het kwadraat van de breedte van de magneten.

In een machine met dempercilinder zijn de ijzerverliezen in de rotor en de wervelstroomverliezen in de magneten verwaarloosbaar ten opzichte van de demperverliezen: de dempercilinder schermt de rest van de rotor af. Als stroomverdringing in de dempercilinder verwaarloosbaar is, is het demperverlies ruwweg omgekeerd evenredig met de dikte van de dempercilinder. De demperverliezen worden zeer groot als de afstand tussen de dempercilinder en het statoroppervlak te klein wordt.

Afsluitend

Het model van de permanente-magneetmachine afgeleid in dit proefschrift is geschikt voor de optimalisatie van het ontwerp van een permanente-magneetmachine met gelijkrichter en voor het onderzoek naar het effect van een dempercilinder. De meerwaarde van dit model is dat het de berekening van de spannings- en stroomvormen van de machine met gelijkrichter combineert met een machinemodel gebaseerd op de twee-dimensionale berekening van het magnetisch veld inclusief de belangrijkste elektromagnetische verliezen.

Curriculum vitae

Henk Polinder is op 4 februari 1968 in Nunspeet geboren. Hij behaalde zijn VWO diploma op het Lambert Franckens College in Elburg in 1986. Daarna ging hij Elektrotechniek studeren aan de Technische Universiteit Delft. In 1992 rondde hij deze studie af en werd toegevoegd onderzoeker bij de vakgroep Vermogenslektronica en Elektrische Machines. Zijn onderzoek naar sneldraaiende permanente-magneetmachines resulteerde in dit proefschrift. Sinds 1996 werkt hij als Universitair Docent bij dezelfde faculteit.

